# The Synthesis and Characterisation of Metal Complexes Containing Chemically Reduced Bipyridyl Ligand Systems




Mark Irwin

Oriel College

University of Oxford

A thesis submitted for the degree of

*Doctor of Philosophy*

Hilary 2013

**DOCTOR OF PHILOSOPHY SCHOOL OF CHEMISTRY**

# DECLARATION OF AUTHORSHIP

**Name: MARK ROBERT FLOYD IRWIN** **Candidate number: 40943**

**College: ORIEL COLLEGE** **Supervisor: DR JOSE GOICOECHEA**

**Title of thesis:**
**THE SYNTHESIS AND CHARACTERISATION OF METAL COMPLEXES CONTAINING CHEMICALLY REDUCED BIPYRIDYL LIGAND SYSTEMS**

**Word Count: ~ 50,000**

*Please tick to confirm the following:*

I have read and understood the University's disciplinary regulations concerning conduct in examinations and, in particular, the regulations on plagiarism (Available at www.admin.ox.ac.uk/proctors/info/pam/section9.shtml). ☐

I have read and understood the Education Committee's information and guidance on academic good practice and plagiarism at www.admin.ox.ac.uk/edc/goodpractice. ☐

The thesis I am submitting is entirely my own work except where otherwise indicated. ☐

It has not been submitted, either partially or in full, for another Honour School or qualification of this University (except where the Special Regulations for the subject permit this), or for a qualification at any other institution. ☐

I have clearly indicated the presence of all material I have quoted from other sources, including any diagrams, charts, tables or graphs. ☐

I have clearly indicated the presence of all paraphrased material with appropriate references. ☐

I have acknowledged appropriately any assistance I have received in addition to that provided by my supervisor. ☐

I have not copied from the work of any other candidate. ☐

I have not used the services of any agency providing specimen, model or ghostwritten work in the preparation of this thesis. (See http://www.admin.ox.ac.uk/statutes/352-051a.shtml#_Toc28142348.) ☐

I agree to retain an electronic copy of this work until the publication of my final examination result, except where submission in hand-written format is permitted. ☐

I agree to make any such electronic copy available to the examiners should it be necessary to confirm my word count or to check for plagiarism. ☐

Candidate's signature: …….. Date: ……..

Nov 2011

# Acknowledgements

Foremost I would like to extend huge thanks to my supervisor, Dr. Jose Goicoechea, for his tireless enthusiasm, patience, encouragement and guidance both during the final year of my undergraduate course and throughout my D.Phil. Without this, my time in the lab would not have been the fantastic experience I enjoyed so much.

I would additionally like to thank Dr. John McGrady and Dr. Tobias Krämer for performing DFT calculations; Prof. Gary Long for assistance with Mössbauer measurements; Dr. Radovan Herchel for help interpreting magnetometry data; Dr. David Watkin, Dr. Amber Thompson and Dr. Richard Cooper for sharing their extensive knowledge of X-ray crystallography; Dr. Jeff Harmer for help with EPR spectroscopy; Dr. Nick Rees for his boundless enthusiasm for NMR and all the undergraduate students who were involved in this project: Ed, Belinda, Rhiannon, Laurence and Becca.

The lab's first (and only) postdoc, Mark Denning, deserves a special acknowledgement not only for passing on many practical techniques, useful tricks and insight when the lab was first starting, but also for his fantastic dance moves and extreme ABBA appreciation.

I would like to thank the D.Phils. who I shared the lab with; Dr Bin$^2$ Zhou, Rob Turberville, Caroline Knapp, Gaby "Quintus" Espinoza-Quintero and Andy Jupp, as well as friendly neighbours Mike "Kellykins" Kelly, Dr.

Joshua Bates and Dr. Tobias Krämer for so many hilarious moments and great memories.

The undergraduates all made the lab a fun, exciting and above all unpredictable place to work in, so I would also like to thank Carl, Tom, Dave, Ed, Rhiannon, CJ, Joe, Belinda, Pete, Amy, Charlie, Laurence, Melissa, Becca and Phil for their big contributions to making the ups and downs of research a much more enjoyable journey.

I would also like to specially thank Hasna Zaher for putting up with my drunken ponderings in a pub on a chemistry drinking trip and sticking with me since.

# Abstract

This thesis describes the synthesis and characterisation of metal complexes that contain chemically reduced bipyridyl ligands. The crystal structures of twenty-six novel complexes are reported alongside detailed discussions on the electronic and spectroscopic effects and trends associated with the different oxidation states within these species.

**Chapter One** introduces the isomers of bipyridine and their redox chemistry, the concept of non-innocent ligands and the spectroscopic techniques that are currently used in determining ligand oxidation states. Subsequently, examples of main group, transition metal, lanthanide and actinide species that contain or may contain reduced forms of the ligand are discussed.

**Chapter Two** details the synthesis and structural characterisation of alkali metal salts of singly and doubly reduced forms of the three commercially available bipyridine isomers. The effects of this reduction are investigated with the aim of developing diagnostic fingerprints for each of the ligand oxidation states.

**Chapter Three** discusses the synthesis of an homologous series of compounds of the form $[M(2,2´\text{-bipy})(mes)_2]^{n-}$ where M = Cr, Mn, Fe, Co, Ni and n = 0, 1. Trends in magnetism, bonding and electronic structure are investigated with reference to theoretical calculations and the diagnostic fingerprints identified in the previous chapter.

**Chapter Four** describes the synthesis and characterisation of three compounds containing the isostructural motif $[Zn_2(4,4´\text{-bipy})(mes)_4]^{n-}$ where n = 0, 1, 2. Structural and spectroscopic changes are discussed and compared to theoretical calculations.

**Chapter Five** contains descriptions of the spectroscopic techniques employed in the above research and synthesis routes to all compounds featured in this thesis.

## List of Abbreviations

The following abbreviations are used in this thesis:

| | |
|---|---|
| 2,2,2-crypt | 4,7,13,16,21,24-hexaoxa-1,10-diazabicyclo[8.8.8]hexacosane |
| 18-crown-6 | 1,4,7,10,13,16-hexaoxacyclooctadecane |
| Å | Ångström |
| AIM | Atoms In Molecules |
| anal. calcd | analysis calculated |
| av | average (mean) |
| bipy | bipyridine |
| °C | degrees Celsius |
| CASSCF | Complete Active Space Self-Consistent Field theory |
| CCD | charged-coupled device |
| Cp* | $C_5(CH_3)_5^-$ |
| CW | continuous wave |
| CYS | cysteine |
| DFT | density functional theory |
| dibenzo-18-crown-6 | dibenzo[a,j]-1,4,7,10,13,16-hexaoxacyclooctadeca-2,11-diene |
| DME | dimethoxyethane |
| DMF | dimethylformamide |
| en | ethylenediamine |
| EPR | electron paramagnetic resonance |
| esd | estimated standard deviation |
| equiv. | equivalents |
| GHz | gigahertz |
| h | hour |
| HMBC | heteronuclear multiple-bond correlation |
| HOMO | highest occupied molecular orbital |

| | |
|---|---|
| HSQC | heteronuclear single-quantum correlation |
| Hz | Hertz |
| IR | infrared |
| K | Kelvin |
| kHz | kilohertz |
| LUMO | lowest unoccupied molecular orbital |
| (m) | medium |
| M | molar |
| mes | mesityl (2,4,6-$Me_3C_6H_2$) |
| mg | milligram |
| MHz | megahertz |
| min | minute |
| mL | millilitre |
| mol | mole |
| mT | millitesla |
| NICS | Nuclear Independant Chemical Shifts |
| nm | nanometers |
| ppm | parts per million |
| PXRD | powder X-ray diffraction |
| py | pyridine |
| RT | room temperature |
| (s) | strong |
| SOMO | singly occupied molecular orbital |
| SQUID | superconducting quantum interference device |
| SXRD | single crystal X-ray diffraction |
| T | Tesla |
| $^t$Bu | *tert*-butyl |

| | |
|---|---|
| $^{t}$Bu-dab | 1,4-di-*tert*-butyl-1,4-diazabutadine |
| THF | tetrahydrofuran |
| TCNE | tetracyanoethene |
| TCNQ | 7,7,8,8-tetracyano-p-quinodimethane |
| Tol | toluene |
| UV-Vis | ultraviolet-visible spectrophotometry |
| (w) | weak |
| XAFS | X-ray absorption fine structure |
| XANES | X-ray absorption near edge structure |

# Contents

**1 Introduction** **1**

1.1 Bipyridine as a Ligand . . . . . 1

1.1.1 Isomers of Bipyridine . . . . . 1

1.1.2 Bonding of Bipyridines . . . . . 2

1.2 Redox Chemistry of Bipyridine Isomers . . . . . 3

1.3 Non-Innocent Ligands . . . . . 5

1.3.1 Definitions . . . . . 5

1.3.2 Techniques to Probe Oxidation State . . . . . 7

1.3.3 Examples of Non-Innocent Ligands . . . . . 9

1.4 2,2´-Bipyridine . . . . . 20

1.4.1 Main Group Compounds . . . . . 21

1.4.2 Lanthanide Compounds . . . . . 24

1.4.3 Actinide Compounds . . . . . 29

1.4.4 Transition Metal Compounds . . . . . 32

1.5 4,4´-Bipyridine . . . . . 34

1.6 2,4´-Bipyridine . . . . . 37

1.7 Project Aims . . . . . 40

1.8 References . . . . . 41

**2 Alkali Metal Salts of Bipyridine Anions** **51**

2.1 Introduction . . . . . 51
2.2 General Synthesis . . . . . 53
2.3 2,2´-Bipyridine . . . . . 55
2.3.1 2,2´-Bipyridyl Radical Anion . . . . . 55
2.3.1.1 Synthesis . . . . . 56
2.3.1.2 Structural Characterisation . . . . . 56
2.3.1.3 Spectroscopic Characterisation . . . . . 60
2.3.2 2,2´-Bipyridyl Dianion . . . . . 62
2.3.2.1 Synthesis . . . . . 62
2.3.2.2 Structural Characterisation . . . . . 63
2.3.2.3 Spectroscopic Characterisation . . . . . 64
2.3.3 Electronic Structure and Bond Metric Parameters . . . . . 66
2.4 2,4´-Bipyridine . . . . . 68
2.4.1 2,4´-Bipyridyl Radical Anion . . . . . 69
2.4.1.1 Synthesis . . . . . 69
2.4.1.2 Structural Characterisation . . . . . 69
2.4.1.3 Spectroscopic Characterisation . . . . . 71
2.4.2 2,4´-Bipyridyl Dianion . . . . . 73
2.4.2.1 Synthesis . . . . . 73
2.4.2.2 Structural Characterisation . . . . . 73
2.4.2.3 Spectroscopic Characterisation . . . . . 76
2.4.3 Electronic Structure and Bond Metrics . . . . . 77
2.5 4,4´-Bipyridine . . . . . 80
2.5.1 4,4´-Bipyridyl Radical Anion . . . . . 80
2.5.1.1 Synthesis . . . . . 80
2.5.1.2 Structural Characterisation . . . . . 81
2.5.1.3 Spectroscopic Characterisation . . . . . 83

2.5.2 4,4´-Bipyridyl Dianion . . . . . 85
2.5.2.1 Synthesis . . . . . 85
2.5.2.2 Structural Characterisation . . . . . 86
2.5.2.3 Spectroscopic Characterisation . . . . . 88
2.5.3 Electronic Structure and Bond Metrics . . . . . 88
2.6 Summary of Chapter 2 . . . . . 90
2.7 References . . . . . 91

**3 Reduction of T.M. Complexes of 2,2´-Bipyridine 95**
3.1 Introduction . . . . . 95
3.1.1 Structurally Characterised Compounds Containing Reduced 2,2´-Bipyridyl Ligands . . . . . 96
3.1.1.1 Main Group Compounds . . . . . 96
3.1.1.2 Lanthanide Compounds . . . . . 99
3.1.1.3 Actinide Compounds . . . . . 101
3.1.2 Transition Metal Compounds . . . . . 104
3.1.3 Non-Innocent Behaviour . . . . . 105
3.2 Neutral Compounds: $[M(2,2´\text{-bipy})(mes)_2]^0$ . . . . . 106
3.2.1 General Synthesis . . . . . 106
3.2.2 Synthesis and Structural Characterisation . . . . . 107
3.2.2.1 $Cr(2,2´\text{-bipy})(mes)_2\cdot THF$ . . . . . 107
3.2.2.2 $Mn(2,2´\text{-bipy})(mes)_2$ . . . . . 107
3.2.2.3 $Fe(2,2´\text{-bipy})(mes)_2$ . . . . . 107
3.2.2.4 $Co(2,2´\text{-bipy})(mes)_2\cdot THF$ . . . . . 109
3.2.2.5 $Ni(2,2´\text{-bipy})(mes)_2$ . . . . . 113
3.3 Reduced Compounds: $[M(2,2´\text{-bipy})(mes)_2]^-$ . . . . . 113
3.3.1 General Synthesis . . . . . 113
3.3.2 Synthesis and Structural Characterisation . . . . . 115

3.3.2.1 [K(dibenzo-18-crown-6)·THF][Cr(2,2´-bipy)(mes)$_2$] . 115
3.3.2.2 [K(18-crown-6)][Mn(2,2´-bipy)(mes)$_2$] . . . . . 115
3.3.2.3 [K(2,2,2-crypt][Fe(2,2´-bipy)(mes)$_2$] . . . . . 116
3.3.2.4 [K(2,2,2-crypt)][Co(2,2´-bipy)(mes)$_2$] . . . . . 120
3.3.2.5 [K(2,2,2-crypt)][Ni(2,2´-bipy)(mes)$_2$] . . . . . 120
3.4 Results and Discussion . . . . . 123
3.4.1 Trends in Bond Metrics . . . . . 123
3.4.2 Magnetism and Spectroscopy . . . . . 125
3.4.3 Mössbauer Spectroscopy . . . . . 132
3.4.4 EPR Spectroscopy . . . . . 135
3.4.5 Infrared and Raman Spectroscopy . . . . . 138
3.4.6 Trends in Electronic Structure . . . . . 141
3.4.7 Attempts to Synthesise Complexes of the Bipyridyl Dianion . 147
3.5 Summary of Chapter 3 . . . . . 148
3.6 References . . . . . 148

**4 Reduction of Zinc Complexes of 4,4´-Bipyridine 151**
4.1 Introduction . . . . . 151
4.2 $Zn_2$(4,4´-bipyridine)(mes)$_4$ . . . . . 154
4.2.1 Synthesis . . . . . 155
4.2.2 Structural Characterisation . . . . . 155
4.2.3 Spectroscopic Characterisation . . . . . 156
4.3 $Zn_2$(4,4´-bipyridine)(mes)$_4$ Radical Monoanion . . . . . 160
4.3.1 Synthesis . . . . . 160
4.3.2 Structural Characterisation . . . . . 160
4.3.3 Spectroscopic Characterisation . . . . . 160
4.4 $Zn_2$(4,4´-bipyridine)(mes)$_4$ Dianion . . . . . 163
4.4.1 Synthesis . . . . . 163

4.4.2 Structural Charactersation . . . . . 163
4.4.3 Spectroscopic Characterisation . . . . . 165
4.5 Electronic Structure and Bond Metrics . . . . . 167
4.6 Summary of Chapter 4 . . . . . 173
4.7 References . . . . . 173

**5 Experimental** **176**
5.1 Manipulation of Compounds . . . . . 176
5.2 Physical Measurements . . . . . 178
5.2.1 Single Crystal X-ray Diffraction . . . . . 178
5.2.2 Powder X-ray Diffraction . . . . . 181
5.2.3 Superconducting Quantum Interference Device Magnetometry (SQUID) . . . . . 182
5.2.4 Electron Paramagnetic Resonance . . . . . 184
5.2.5 Infrared Spectroscopy . . . . . 185
5.2.6 Raman Spectroscopy . . . . . 187
5.2.7 Nuclear Magnetic Resonance . . . . . 188
5.2.8 Mössbauer Spectroscopy . . . . . 190
5.2.9 Elemental Microanalysis . . . . . 191
5.3 Density Functional Theory Calculations . . . . . 192
5.4 Preparation of Materials . . . . . 194
5.4.1 Solvents . . . . . 194
5.4.2 Reagents . . . . . 194
5.4.3 Synthesis of Precursors . . . . . 194
5.4.3.1 Synthesis of (mes)MgBr . . . . . 196
5.4.3.2 Synthesis of (mes)Li . . . . . 196
5.4.3.3 Synthesis of $KC_8$ . . . . . 196
5.4.3.4 Synthesis of $Mn_3(mes)_6$·toluene . . . . . 197

5.4.3.5 Synthesis of $Fe_2(mes)_4$ . . . 197
5.4.3.6 Synthesis of $Co(mes)_2(PEt_2Ph)_2$ . . . 198
5.4.3.7 Synthesis of Ni(2,2´-bipy)$(mes)_2$ . . . 198
5.4.3.8 Synthesis of $Zn(mes)_2$ . . . 199
5.5 Synthesis of Compounds 1 to 22 . . . 199
5.5.1 Compound 1: K(2,2´-bipy)(en) . . . 199
5.5.2 Compound 2: $Rb_2$(2,2´-bipy)$(en)_2$ . . . 200
5.5.3 Compound 3: K(2,4´-bipy)(en) . . . 201
5.5.4 Compound 4: $K_4$(2,4´-bipy)$_2(en)_{3.5}$ . . . 201
5.5.5 Compound 5: $Rb_4$(2,4´-bipy)$_2(en)_{3.5}$ . . . 202
5.5.6 Compound 6: Na(4,4´-bipy)(en) . . . 203
5.5.7 Compound 7: $Na_2$(4,4´-bipy)$(en)_2$ . . . 203
5.5.8 Compound 8: Cr(2,2´-bipy)$(mes)_2$ . . . 203
5.5.9 Compound 9: Mn(2,2´-bipy)$(mes)_2$ . . . 204
5.5.10 Compound 10: Fe(2,2´-bipy)$(mes)_2$ . . . 205
5.5.11 Compound 11: Co(2,2´-bipy)$(mes)_2$ . . . 206
5.5.12 Compound 12: Ni(2,2´-bipy)$(mes)_2$ . . . 207
5.5.13 Compound 13: [K(dibenzo-18-crown-6)][Cr(2,2´-bipy)$(mes)_2$] . 208
5.5.14 Compound 14: [K(18-crown-6)][Mn(2,2´-bipy)$(mes)_2$] . . . 208
5.5.15 Compound 15: [K(2,2,2-crypt)][Fe(2,2´-bipy)$(mes)_2$] . . . 209
5.5.16 Compound 16: [K(2,2,2-crypt)][Co(2,2´-bipy)$(mes)_2$] . . . 210
5.5.17 Compound 17: [K(2,2,2-crypt)][Ni(2,2´-bipy)$(mes)_2$] . . . 211
5.5.18 Compound 18: [K(2,2,2-crypt)][Fe$(mes)_3$] . . . 212
5.5.19 Compound 19: $Zn_2$(4,4´-bipy)$(mes)_4$ . . . 212
5.5.20 Compound 20: [K(18-crown-6)$(THF)_2$][$Zn_2$(4,4´-bipy)$(mes)_4$] . 213
5.5.21 Compound 21: $[K(18\text{-crown-6})]_2[Zn_2(4,4´\text{-bipy})(mes)_4]$ . . . 214
5.5.22 Compound 22: [K(18-crown-6)(THF)][Zn$(mes)_3$] . . . 215

5.6 References . . . . . 215

**A X-ray Data Collection and Refinement Parameters** **219**

**B List of Publications** **225**

**C Posters Presented at Conferences** **226**

# List of Figures


1.1 The isomers of bipyridine . . . . . 2

1.2 Related pyridyl-based ligands . . . . . 3

1.3 The σ and π bonding between a transition metal and a bipyridine ligand 4

1.4 The synthesis and chemical reduction of 4,4´-bipyridine . . . . . 4

1.5 Types of interconversion . . . . . 7

1.6 Examples of ligands commonly found to exhibit non-innocent behaviour 10

1.7 Redox states for 1,2-diketone bis(2,6-diisopropylphenyl)glyoxal . . . . 11

1.8 1,4-diaza-1,3-butadiene and *o*-diiminobenzene ligand bases . . . . . 12

1.9 The first structurally characterised azo-based radical system . . . . . 14

1.10 7,7,8,8-tetracyano-*p*-quinodimethane (TCNQ) . . . . . 15

1.11 Tetrazine examples . . . . . 16

1.12 The simplified proposed mechanism of catechol dioxygenase . . . . . 16

1.13 Topaquinone . . . . . 17

1.14 Simplified P450 radical rebound mechanism . . . . . 18

1.15 Proposed mechanism for the catalytic cyclisation of dienes . . . . . 19

1.16 Distribution of inter-pyridyl ring bond lengths for 2,2´-bipy . . . . . 21

1.17 Crystal structure of $Si(2,2´\text{-bipy})_2$ . . . . . 22

1.18 Crystal structure of the $[Al(2,2´\text{-bipy})_2]^-$ anion . . . . . 23

1.19 Crystal structure of $[B(2,2´\text{-bipy})^{\cdot}Cl_2]$ . . . . . 23

1.20 Crystal structures of [B(2,2´-bipy)Cl] and [B(2,2´-bipy)Ph] . . . . . 24

1.21 Crystal structure of Sm(2,2´-bipy)$Cp^*_2$ . . . . . 25

1.22 Crystal structures of La complexes containing 2,2´-bipyridine . . . . . 26

1.23 Crystal structure of Yb(2,2´-bipy)$Cp^*_2$ . . . . . 28

1.24 Substituted bipyridine systems employed by Andersen and co-workers 28

1.25 Crystal structure of U(2,2´-bipy)$_4$ . . . . . 30

1.26 Crystal structure of U(2,2´-bipy)Cp*($C_8H_8$) . . . . . 31

1.27 Crystal structure of U(2,2´-bipy)($Tp^{Me_2}$)$_2$ . . . . . 31

1.28 Crystal structure of Th(2,2´-bipy)($\eta^5$-1,2,4($^t$Bu)$_3C_5H_2$)$_2$ . . . . . 32

1.29 Resonance canonical proposed by Chisholm and co-workers . . . . . 33

1.30 Resonance canonical proposed by Brookhart and co-workers . . . . . 33

1.31 Distribution of inter-pyridyl ring bond lengths for 4,4´-bipyridine . . 35

1.32 Crystal structure of [1,1´-diethyl-4,4´-bipyridilium]$_2$[$Fe_4Pt(CO)_{16}$] . . 36

1.33 Structures of 4,4´-bipyridine containing molecular squares . . . . . 37

1.34 The coordination modes of 2,4´-bipyridine . . . . . 38

1.35 Distribution of inter-pyridyl ring bond lengths for 2,4´-bipyridine . . 39

2.1 Crystal structure of **1a** . . . . . 57

2.2 Crystal structure of **1b** . . . . . 59

2.3 Solid and solution phase EPR spectra of **1** . . . . . 60

2.4 Crystal structure of **2** . . . . . 63

2.5 Powder X-ray diffraction pattern of **2** . . . . . 65

2.6 DFT calculated 2,2´-bipyridine LUMO . . . . . 66

2.7 Graph of 2,2´-bipyridyl moiety bond lengths . . . . . 68

2.8 Crystal structure of **3** . . . . . 70

2.9 Powder X-ray diffraction pattern of **3** . . . . . 71

2.10 Solid and solution phase EPR spectra of **3** . . . . . 72

2.11 Crystal structures of **4** and **5** . . . . . 75

2.12 Powder X-ray diffraction pattern of **5** . . . . . 76

2.13 DFT calculated 2,4´-bipyridine LUMO . . . . . 77
2.14 Graph of 2,4´-bipyridyl moiety bond lengths . . . . . 78
2.15 Powder X-ray diffraction pattern of **6** . . . . . 81
2.16 Crystal structure of **6a** . . . . . 82
2.17 Crystal structure of **6b** . . . . . 84
2.18 Solid and solution phase EPR spectra of **6** . . . . . 85
2.19 Crystal structure of **7a** . . . . . 87
2.20 DFT calculated 4,4´-bipyridine LUMO . . . . . 88
2.21 Graph of 4,4´-bipyridyl moiety bond lengths . . . . . 90

3.1 The LUMO of neutral 2,2´-bipyridine . . . . . 96
3.2 Crystal structure of $Si(2,2´\text{-bipy})_2$ . . . . . 97
3.3 Crystal structure of the $[Al(2,2´\text{-bipy})_2]^-$ anion . . . . . 98
3.4 Crystal structures of $BCl_2(2,2´\text{-bipy})$ $BCl(2,2´\text{-bipy})$ and $BPh(2,2´\text{-bipy})$ 98
3.5 Crystal structure of $Cp^*_2Sm(2,2´\text{-bipy})$ . . . . . 99
3.6 Crystal structures of $La(Tp^{Me_2})_2(2,2´\text{-bipy})$ and $Cp^*_2Yb(2,2´\text{-bipy})$ . 100
3.7 Crystal structure of $U(2,2´\text{-bipy})_4$ . . . . . 101
3.8 Crystal structures of $Cp^*(C_8H_8)U(2,2´\text{-bipy})$ and $(Tp^{Me_2})_2U(2,2´\text{-bipy})$ 102
3.9 Crystal structure of $(\eta^5\text{-}1,2,4(t\text{-Bu})_3C_5H_2)_2Th(2,2´\text{-bipy})$ . . . . . 103
3.10 Crystal structures of transition metal examples . . . . . 105
3.11 Crystal structure of **8** . . . . . 108
3.12 Crystal structure of **9** . . . . . 108
3.13 Powder X-ray diffraction pattern of **9** . . . . . 109
3.14 Crystal structure of **10** . . . . . 110
3.15 Powder X-ray diffraction pattern of **10** . . . . . 110
3.16 Crystal structure of **11** . . . . . 111
3.17 Powder X-ray diffraction pattern of **11** . . . . . 112
3.18 Crystal structure of **12** . . . . . 113

3.19 Powder X-ray diffraction pattern of **12** . . . . . 114
3.20 General scheme for the synthesis of $[M(2,2´\text{-bipy})(mes)_2]^-$ products . 114
3.21 Crystal structure of **13** . . . . . 116
3.22 Crystal structure of **14a** . . . . . 117
3.23 Crystal structure of **14b** . . . . . 118
3.24 Crystal structure of **15** . . . . . 119
3.25 Crystal structure of **18** . . . . . 119
3.26 Powder X-ray diffraction pattern of **15** . . . . . 120
3.27 Crystal structure of **16** . . . . . 121
3.28 Powder X-ray diffraction pattern of **16** . . . . . 121
3.29 Crystal structure of **17** . . . . . 122
3.30 Powder X-ray diffraction pattern of **17** . . . . . 122
3.31 Relative energies of the *d* orbitals in tetrahedral and octahedral geometries . . . . . 124
3.32 Trends in bond metrics . . . . . 126
3.33 Effective magnetic moments of compounds **8** to **11** and **13** to **17** . . . 130
3.34 Mössbauer spectra of **10** and **15** . . . . . 133
3.35 EPR spectra of **9**, **11** and **13** to **16** . . . . . 137
3.36 Solution-state EPR spectrum of **17** . . . . . 138
3.37 IR spectra of compounds **8** to **12** . . . . . 139
3.38 IR spectra of compounds **13** to **17** . . . . . 140
3.39 Raman spectra of compounds **8** to **12** . . . . . 140
3.40 Raman spectra of compounds **13** to **17** . . . . . 141
3.41 Mulliken spin densities for the transition metal complexes in **8**, **13**, **9** and **14** . . . . . 142
3.42 The singly occupied bipyridyl π* based orbitals of **14** and **15** . . . . . 146
3.43 The singly occupied bipyridyl π* based orbitals of **13** and **16** . . . . . 146

4.1 Structure of $[Cu_2(4,4´\text{-bipy})_4]\cdot(\text{d-Hcam})_2\cdot(4,4´\text{-bipy})_2\cdot 12(H_2O)$ . . . . 152
4.2 The structure of one of two interpenetrated networks in MOF-5 . . . 153
4.3 Structures of 4,4´-bipyridine containing molecular squares . . . . . 154
4.4 Schematic of reactions described in Chapter 4 . . . . . 155
4.5 Crystal structure of **19** . . . . . 156
4.6 Powder X-ray diffraction pattern of **19** . . . . . 157
4.7 Dissociation equilibrium for **19** . . . . . 157
4.8 One-dimensional NOESY spectrum of **19** . . . . . 158
4.9 Crystal structure of **20a** . . . . . 161
4.10 Powder X-ray diffraction pattern of **20a** and **20b** . . . . . 161
4.11 Solid and solution phase EPR spectra of **20** . . . . . 163
4.12 Crystal structure of **21** . . . . . 164
4.13 Powder X-ray diffraction pattern of **21** . . . . . 165
4.14 Crystal structure of **22** . . . . . 166
4.15 Powder X-ray diffraction pattern of **22** . . . . . 166
4.16 Comparison of NMR spectra of **19** and **21** . . . . . 168
4.17 Resonance canonicals of the 4,4´-bipyridyl dianion in **21** . . . . . 168
4.18 DFT calculated 4,4´-bipyridine LUMO . . . . . 170

5.1 Schematic of a Schlenk line . . . . . 177
5.2 Schematic diagram of a four circle single crystal X-ray diffractometer 179
5.3 Diagrammatic explanation of Bragg's Law . . . . . 179
5.4 Schematic diagram of a transmission X-ray diffractometer . . . . . 182
5.5 SQUID instrument superconducting coil configuration . . . . . 183
5.6 The Zeeman effect . . . . . 185
5.7 Simplified schematic of an EPR instrument . . . . . 186
5.8 Simplified schematic of an IR spectrometer . . . . . 187
5.9 Raman transitions . . . . . 188

5.10 Simplified schematic of a Mössbauer spectrometer . . . . . 191

# Chapter 1

# Introduction

## 1.1 Bipyridine as a Ligand

Since its discovery in 1888, 2,2´-bipyridine (2,2´-bipy) has become one of the most ubiquitous and well-documented ligands in coordination chemistry.[1] There is a large amount of literature concerning the spectroscopic and electronic properties of the isolated ligand, and it has been incorporated into a vast number of complexes.[2] Two other readily available isomers of bipyridine exist (2,4´- and 4,4´-bipyridine) as well as many other related compounds. This research project has focused on complexes that contain chemically reduced forms of bipyridine with a view to exploiting the unusual electron-rich properties of the reduced ligand to synthesise compounds with interesting electronic properties and/or unusual metal oxidation states.

### 1.1.1 Isomers of Bipyridine

There are six structural isomers of bipyridine: 2,2´-, 2,3´-, 2,4´-, 3,3´-, 3,4´- and 4,4´-bipyridine (Figure 1.1). The ubiquity of 2,2´-bipyridine in the chemical literature stems from its ability to chelate metal centres in a wide variety of complexes, while 4,4´-bipyridine is frequently employed as a rigid linker in polymers and metal-organic

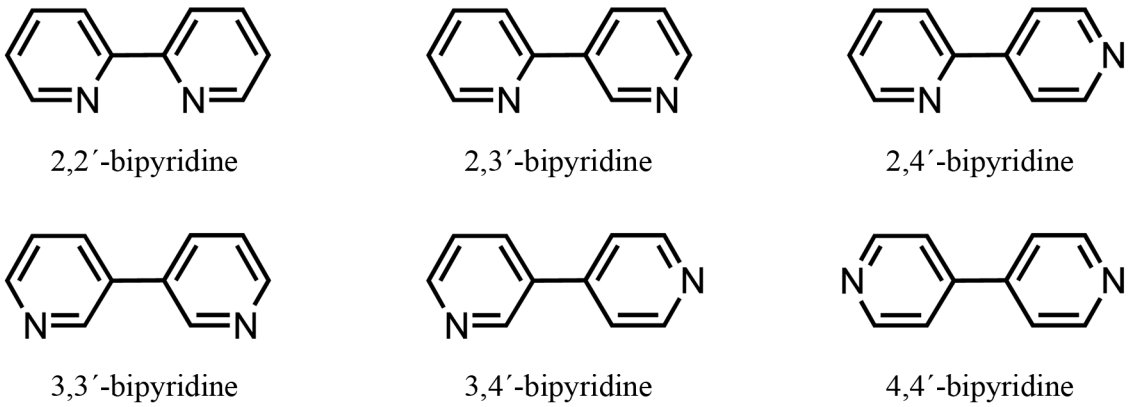
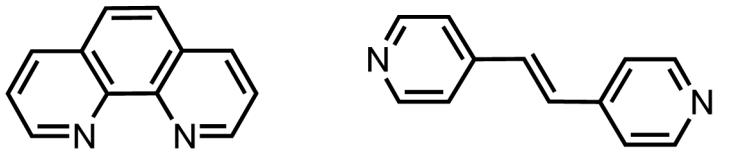



Figure 1.1: The isomers of bipyridine.

frameworks.[3–5] 2,4′-bipyridine is the only other commercially available isomer, but is far less widely studied, possibly because of its inability to act as a chelating ligand or as a linker with a predictable geometry. A survey of crystallographically characterised structures in the Cambridge Structural Database (CSD) bears out this trend, listing 6652 compounds containing 2,2′-bipyridine and 5115 compounds containing the 4,4′- isomer.[6] This is in stark contrast to the other isomers which are far less numerous. There are 58 listed structures containing the 2,4′-bipyridine moiety while the 2,3′-, 3,3′- and 3,4′- isomers are present in only 2, 32 and 7 structures, respectively. This is despite the fact that the 2,3′- and 3,3′- isomers are the only known naturally occurring forms of bipyridine.[7,8] Structurally similar compounds such as 1,10-phenanthroline or trans-1,2′-bis(4-pyridyl) ethylene (Figure 1.2) are also well known (incorporated in 6301 and 820 structures in the CSD, respectively) while substituted bipyridine compounds such as 4,4′-dimethyl-2,2′-bipyridine are also readily available, if less abundant (394 structures in the CSD).[6]

### 1.1.2 Bonding of Bipyridines

Bipyridine ligands are able to interact in two different ways with metal cations. For many alkali metal complexes, including those discussed in Chapter 2, such interactions




1,10-phenanthroline trans-1,2′-bis(4-pyridyl) ethylene

Figure 1.2: Related pyridyl-based ligands.

are almost entirely ionic (due to the angular distribution function of the spherical metal valence s orbitals).[9] These metal cations, having little preference for specific bonding orientations, interact by electrostatic attractions either with the electron-rich nitrogen sites, or by an interaction with the electron-rich π manifolds above and below the pyridyl ring systems. In the alkali metal cation containing systems described in this thesis, specific effort has been made to refer to these electrostatic contributions as 'interactions' rather than 'bonds', reflecting the very low levels of covalency.[10]

By contrast, when a bipyridine ligand is coordinated to a transition metal cation, the presence of occupied and vacant d orbitals on the metal allows primary σ-donation of electron density from the nitrogen lone pair. This may be augmented by π-backbonding from the transition metal to a π* antibonding orbital on the bipyridine ring system (Figure 1.3). However, the ability of bipyridine ligands to act as π-acceptors has been the subject of some debate, with recent computational research suggesting that the effect may not be as strong as previously postulated.[11–15] The implications of this are discussed in more detail later in the chapter and throughout this thesis.

## 1.2 Redox Chemistry of Bipyridine Isomers

The accessibility of reduced states of bipyridine has been known for 50 years. The first example of a reduced bipyridine radical was reported by Bruin and co-workers in 1962, who observed that a deep blue colour developed upon addition of sodium

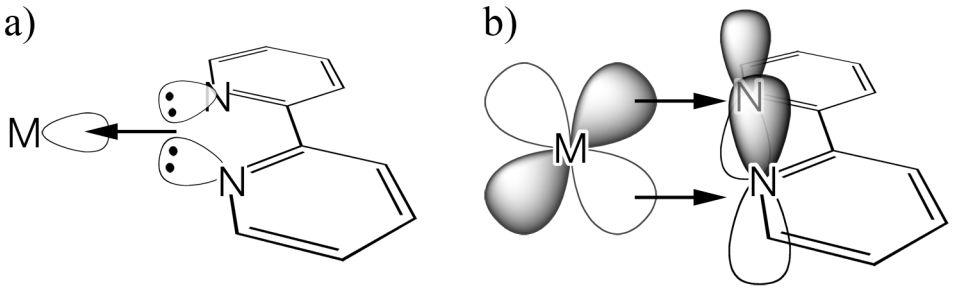



Figure 1.3: (**a**) σ and (**b**) π bonding between a transition metal and a bipyridine ligand.

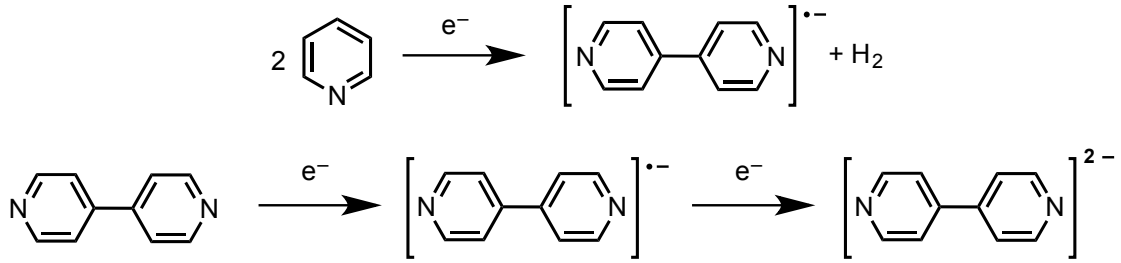



Figure 1.4: The synthesis and chemical reduction of 4,4´-bipyridine.

to pyridine.[16] This was caused by the *in situ* reduction of pyridine by sodium metal to form pyridyl radicals which combine with other solvent molecules to form a 4,4´-bipyridine radical and hydrogen gas. Loss of the radical electron to the solvent yielded the neutral 4,4´-bipyridine species. Alternatively, further reduction by alkali metal yielded the 4,4´-bipyridyl dianion (Figure 1.4). The singly reduced radical species was characterised using solution EPR spectroscopy by Carrington *et al.* in the same year, revealing the hyperfine structure associated with the 4,4´-bipyridyl radical anion.[17] Subsequently, a vast amount of information has been published on both experimental and theoretical studies of the reduced forms of bipyridine. This includes IR,[18] Raman,[19–24] UV-vis,[25–27] and EPR spectroscopic data,[28–32] in addition to electrochemical and computational studies.[33–41]

However, closer inspection of the spectroscopic data often reveals contradictory reports, potentially due to the difficulties of manipulating such air- and moisture-sensitive species. One prominent example concerns the solution EPR spectrum of

the 2,2´-bipyridyl radical anion. dos Santos Veiga and co-workers have stated that they are unable to reproduce the EPR spectrum reported by Zahlan and co-workers and although they observe a spectrum similar to that reported by Konig, there is disagreement over hyperfine coupling constants.[16,28,31] A second example is found in the UV-vis spectrum of the 2,2´-bipyridyl radical reported by Konig and Kremer,[27] who reference three other articles they believe to either omit or erroneously report data.

Please note that from this point forward, 'bipyridine' will be used to refer to the neutral form of an isomer whilst 'bipyridyl' will be used when discussing a reduced state.

## 1.3 Non-Innocent Ligands

### 1.3.1 Definitions

The term 'oxidation state' is used throughout this thesis to describe the (frequently hypothetical) charge that an atom would possess if all bonding interactions were purely ionic. This is defined by the IUPAC as: "the charge an atom might be imagined to have when electrons are counted according to an agreed-upon set of rules."[42] These rules state that the oxidation state of a free element is zero while that of a monoatomic ion is equal to the charge of the ion. Additionally, the algebraic sum of the oxidation states of all atoms in a molecule must add up to the net charge on that molecule. For a molecular system or ligand where charge is delocalised across multiple atoms, the oxidation state of the system as a whole may be considered, with the zero point now taken as the neutral, uncharged system or ligand. It should be noted that the terms 'oxidation state' and 'valence state' or 'valence number' are frequently used erroneously to mean the same thing, which was the subject of a recent article in the literature.[43] Whilst oxidation state is used as defined above, IUPAC defines valence as:

"the maximum number of univalent atoms (originally hydrogen or chlorine atoms) that may combine with an atom of the element under consideration, or with a fragment, or for which an atom of this element can be substituted".[42] As such, whilst oxidation state is a description of the number of electrons on an atom or molecule, valence refers instead to coordination numbers of univalent atoms. This is an important distinction, not least because valence number is necessarily positive, whilst oxidation state may be both positive or negative.

Although the concept of oxidation state and its weaknesses are frequently debated,[44–46] the term is helpful, both in providing a general tool for electron counting (for example the balancing of charges in an equation) and also as a guide to electronic configurations and hence the likely reactivity or physical properties of a system.[47] It is also crucial in the context of non-innocent ligands.

The descriptor 'non-innocent' was first used by Jørgenson in 1966 to describe the difficulty in assigning oxidation states in a complex containing both redox active ligands and a redox active central metal cation: "Ligands are innocent when they allow the oxidation states of central atoms to be defined",[48] Conversely, the presence of a 'suspect' or 'non-innocent' ligand can lead to significant difficulty in unambiguously stating oxidation levels of metal and ligand. The archetypal example is the NO ligand, capable of existing in three oxidation states: $(NO)^+$, $(NO)^{\cdot}$ and $NO^-$, and is incorporated in the $[Fe(NO)(H_2O)_5]^{2+}$ ion which is responsible for the colour produced in the 'brown ring' analytical test for nitrites and nitrates.[49] In this system three possible assignments could be plausible: Fe(I) / $(NO)^+$, Fe(II) / $(NO)^{\cdot}$, and Fe(III) / $(NO)^-$, and it was only relatively recently with the use of electron paramagnetic resonance (EPR) and Mössbauer spectroscopic measurements that the presence of Fe(III) was demonstrated.[50]

However, the term 'non-innocent ligand' can be a poor choice of words because while a ligand may exhibit redox activity in one complex, this certainly does not

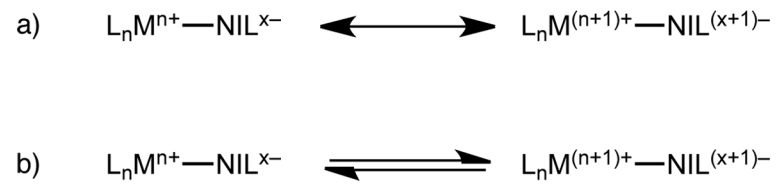



Figure 1.5: Types of interconversion: (**a**) Resonance canonicals (**b**) Valence tautomers.

guarantee that it will act similarly in all other complexes. This led Ward and McCleverty to refine the term, referring to a ligand's ability to demonstrate 'non-innocent behaviour' rather than suggesting that 'non-innocent ligands' exist universally.[51]

For the generic interconversion between $L_n(M^{n+})(NIL^{x-})$ and $L_n(M^{(n+1)+})(NIL^{(x+1)-})$ (NIL = non-innocent ligand) there are two distinct energy surfaces. Transitions that proceed without a barrier to conversion are termed 'resonance forms' and can be drawn as several contributing structures. These exist in an equilibrium position between the contributing resonance canonical forms (Figure 1.5a). Alternatively, if there *is* a barrier to conversion then the structures are termed 'valence tautomers', with each structure representing a separate energy minimum (Figure 1.5b). In the latter case it is (theoretically) possible to isolate each form while in the former case it is by definition impossible because only one state physically exists.

### 1.3.2 Techniques to Probe Oxidation State

As mentioned in section 1.1.2, complexes incorporating transition metals may demonstrate significant covalent bonding between ligands and the central metal atom by means of strong σ-donation and π-backbonding. In such situations oxidation states are seldom precise and often the metal is described as having a 'formal oxidation state', referring to its oxidation state were all interactions purely ionic.[52] In many systems the magnitude of such effects is not so pronounced and it is meaningful to examine the oxidation state of a central metal. However, when a metal is coordinated to a non-innocent ligand the consequence can be misassignment of the

metal oxidation state. For example, Ga(II) was proposed in the system [Ga(II)($^t$Bu-dab$^{2-}$)($^t$Bu-dab)] where $^t$Bu-dab = 1,4-di-*tert*-butyl-1,4-diazabutadine.[53–55] However, more careful examination of the published EPR spectra (the basis of the original assignment) revealed inconsistencies in hyperfine couplings and show a better description is [Ga(III)($^t$Bu-dab)$^{\cdot-}$($^t$Bu-dab)$^{2-}$].[56] Another example centres around the complex [Re(2,2´-bipy)(CO)$_3$Cl]$^-$ which was originally assumed to contain Re(0),[57] while subsequent EPR studies revealed a more conventional Re(I) cation and a reduced bipyridine ligand.[58] A similar oxidation state reassignment was published for [Cu(dpp)$_2$] (dpp = 2,9-diphenyl-1,10-phenanthroline) which was originally reported to contain Cu(0),[59] but again EPR studies showed the presence of a reduced ligand and Cu(I) rather than Cu(0).[60] These cases alone demonstrate that while EPR techniques are powerful tools in the analysis of non-innocent behaviour, interpretation of spectra is not necessarily straightforward and other complementary techniques are essential for the accurate characterisation of suspect complexes.

The choice of characterisation technique is inevitably limited by the nature of the species under investigation. For example, Mössbauer spectroscopy may be used to determine the oxidation state of a nucleus with high precision, but is very limited with regards to the nuclei that may be studied.[61] In complexes that are potentially capable of displaying non-innocent behaviour, study of both the central metal ion and the suspect ligand can aid assignment of oxidation states. Among the most frequently encountered techniques are UV/vis, IR, Raman, NMR and EPR spectroscopy, SQUID magnetometry, cyclic voltammetry and X-ray diffraction.[62–69] Less frequently used (presumably a consquence of lower availablility) is X-ray absorption fine structure (XAFS) spectroscopy. The technique observes X-ray absorption as a function of energy, with each oxidation state of each element providing a unique fingerprint. Thus, by fitting sample spectra to known absorption profiles it is possible to determine unknown oxidation states in samples and to detect ratios of different oxidation states

of the same element when present. This has some overlap with the information provided by Mössbauer spectroscopy although the requirement for a tunable energy X-ray source has meant that these measurements typically require a dedicated synchrotron beam station.

### 1.3.3 Examples of Non-Innocent Ligands

The study of non-innocent ligands has grown substantially in recent years and the area has been the subject of multiple reviews.[70–74] Figure 1.6 shows examples of common ligand architectures from both inorganic and biological chemistry that may exhibit non-innocent behaviour.

The first examples, **I** and **II**, represent two of the first identified ligands that have been shown to demonstrate non-innocent behaviour, with **I** specifically described by Jørgenson as "the simplest case of a suspect ligand".[48] The three different charge states found: $NO^+$, $NO^{\cdot}$ and $NO^-$, are easily distinguished by structural techniques, with X-ray diffraction proving a particularly effective tool to measure M–N–O angles.[75] However, as can be seen from the other examples in Figure 1.6, distinction by significant structural variation may not be a viable approach in many cases.

The role of NO as a signaling agent in biological systems has been extensively investigated.[76] The production and regulation of NO is known to involve iron coordination complexes. A frequently discussed haem complex (Fe-porphyrin) has recently been investigated, in which multiple accessible oxidation state combinations of both metal and ligand are accessible.[77] Calculations show the $R_nFe(II)–NO^+$and $R_nFe(III)–NO^-$ states to have very similar energies (with the latter marginally more favourable) and the authors postulate that small steric or electronic perturbations in protein active sites would be sufficient to dictate ligand oxidation state; a crucial step for NO uptake, release and transfer.

The dioxide, superoxide and peroxide non-innocent ligand series (**II**),[78–81] are also

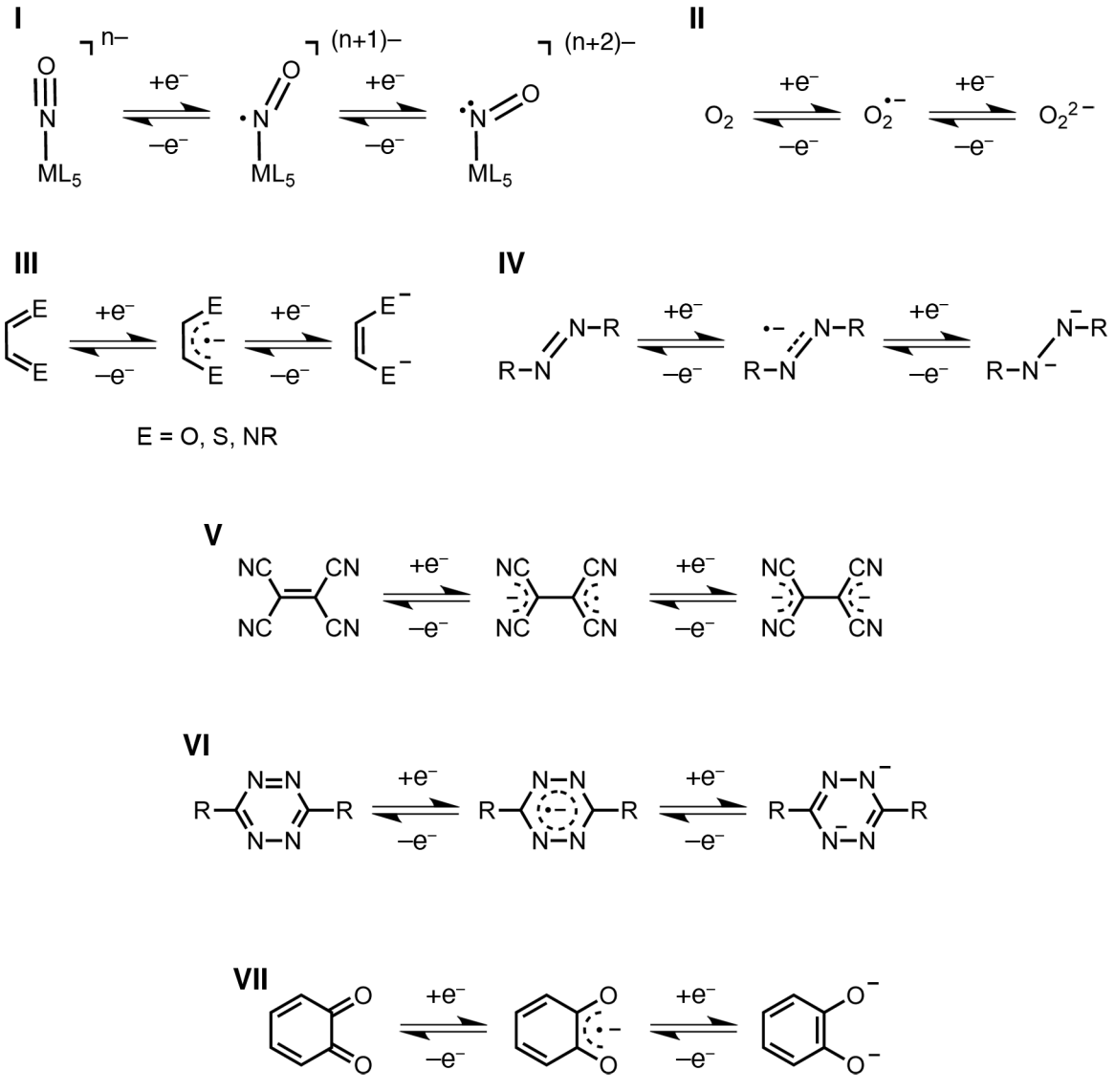



Figure 1.6: Examples of ligands commonly found to exhibit non-innocent behaviour.

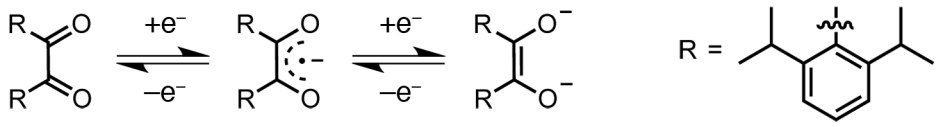



Figure 1.7: Redox states for 1,2-diketone bis(2,6-diisopropylphenyl)glyoxal.[86]

of substantial biological importance, particularly in the process of oxygen transport. Conflicting opinions as to the precise electronic structure of oxymyoglobin and oxyhaemoglobin have caused debate in the literature: the coordination complexes are diamagnetic, which may be explained (in a manner which parallels the NO example earlier) either as $R_nFe(II)–(O_2)$,[82] or $R_nFe(III)–(O_2^{\cdot-})$,[83] with the spins in the latter tautomer being antiferromagnetically coupled. More recent computational analysis suggests the latter is the better description, showing the $O_2$ ligand exhibiting non-innocent behaviour.[84]

Example **III** represents three related redox systems. In all cases successive reductions lead first to a delocalised radical and then to separated charges localised on the more electronegative heteroatoms. During this process the C–C bond contracts as it gains increasing double bond character while the C–E bonds are found to elongate.[85,86] For example, in 1,2-diketone bis(2,6-diisopropylphenyl)gloxyl (Figure 1.7, where E = O), the C–C bond length reduces from 1.51 Å in the neutral species to 1.45 Å in the radical anion and to 1.39 Å in the dianion, accompanied by elongations of the C–O bond lengths from 1.21 Å to 1.29 Å and 1.35 Å, in the respective states.[86] Table 1.1 shows two further examples with varying E groups which illustrate the same trend. Because of this incremental change in bond metrics, high quality single crystal X-ray diffraction data is required to aid determination of these ligand oxidation states.

These systems are able to bind to transition metals in a bidentate manner. In **III** (E = N), α-diimine ligands are generally derived from two structures: 1,4-diaza-1,3-butadiene or *o*-diiminobenzene (Figure 1.8) and both are known to display non-

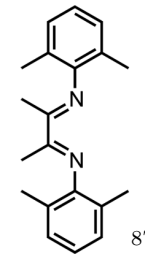
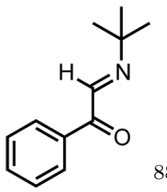
| | C–C | | | C–E[a] | | |
|---|---|---|---|---|---|---|
| Oxidation State: | 0 | –1 | –2 | 0 | –1 | –2 |
|  87 | 1.47 | 1.38 | 1.36 | 1.29 | 1.34 | 1.40 |
|  88 | 1.52 | 1.42 | 1.36 | 1.29/1.22 | 1.33/1.30 | 1.43/1.37 |

Table 1.1: Bond lengths in Å for examples of other **III** type redox systems. [a]Bond distances for the final example are given in the format C–NR / C–O.

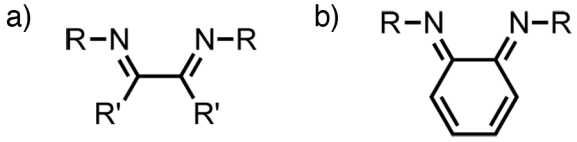



Figure 1.8: (**a**) 1,4-diaza-1,3-butadiene and (**b**) *o*-diiminobenzene ligand bases.

innocent behaviour when coordinated to transition metals.[89–95]

Dithiolates (**III**, E = S) behave in an analogous manner,[96–99] with considerable biochemical research focusing on the effects of their presence at catalytic sites of Mo and W complexes in oxotransferases.[100] Of note is a recent paper by Weighart and co-workers describing the lack of substantial deviation in bond metrics between the neutral and reduced forms of benzene-1,2-dithiolate, seemingly caused by a favourable delocalisation of radical and anion position around the aromatic ring.[101] As a result, the use of other techniques such as sulfur K-edge X-ray absorption and EPR are discussed in the context of tools to identify oxidation states of this ligand in transition metal complexes.

Non-innocent behaviour has been also observed in several other related ligands including α-iminopyridines,[102,103] α-iminoketones,[88] α-iminophenolates[104–110] and thiophenolates,[111–113] that all demonstrate the same fundamental redox steps (albeit with differing heteroatoms) outlined in **III**.

Azo groups and their reduced hydrazido forms (**IV**) exhibit three readily accessible oxidation states and hence have considerable potential for non-innocent behaviour, particularly in cases where the radical species may be stabilised by delocalisation of the unpaired electron.[114,115] One example of this is 2,2´-azobispyridine which exists in two stereoisomeric forms, each of which is found in multiple coordination environments (Table 1.2) and which has been extensively studied in the areas of dye development and nitrogen fixation.[115–119] Recently the first structurally characterised example of an azoaromatic radical anion was published as the product of reacting the pro-ligand with $[(Ph_3P)_4Cu](PF_6)$.[120] The ligand based radical is stabilised by coordination to two Cu(I) sites (Figure 1.9). UV/vis spectroelectrochemical analysis, single crystal X-ray diffraction and EPR spectroscopy were used to determine the existence and location of the radical, with the latter revealing a single resonance with a $g$ value of 2.0077 showing no evidence of any contribution from a copper centred spin. Comparison with previously published X-ray data of the same complex with a net 2+ charge (with an innocently behaving ligand),[121] shows the expected elongation of the N=N bond from 1.248(1) Å to 1.345(7) Å upon reduction, concomitant with lowering of bond order.

Another heavily studied example of a non-innocent ligand is tetracyanoethylene (TCNE) (**V**). This, and the related compound 7,7,8,8-tetracyano-*p*-quinodimethane (TCNQ, Figure 1.10a) both incorporate four strong acceptor groups, providing considerable stabilisation by delocalisation of charge in the reduced forms of the ligands. This is reflected in the low reduction potentials which are around +0.2 V,[122] affording non-innocent behaviour in a variety of complexes.[123]

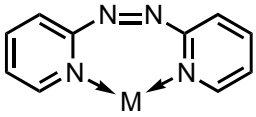
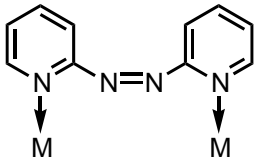
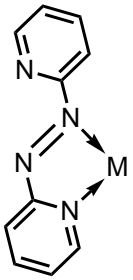
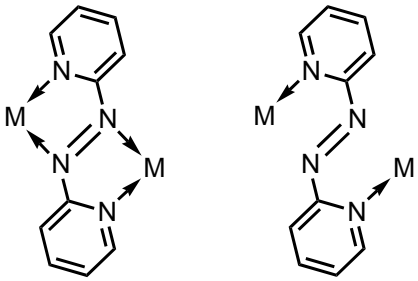
| Ligand conformation: | One metal site: | Two metal sites: |
|---|---|---|
| *cis* |  |  |
| *trans* |  |  |

Table 1.2: Coordination environments of 2,2´-azobispyridine.[115]

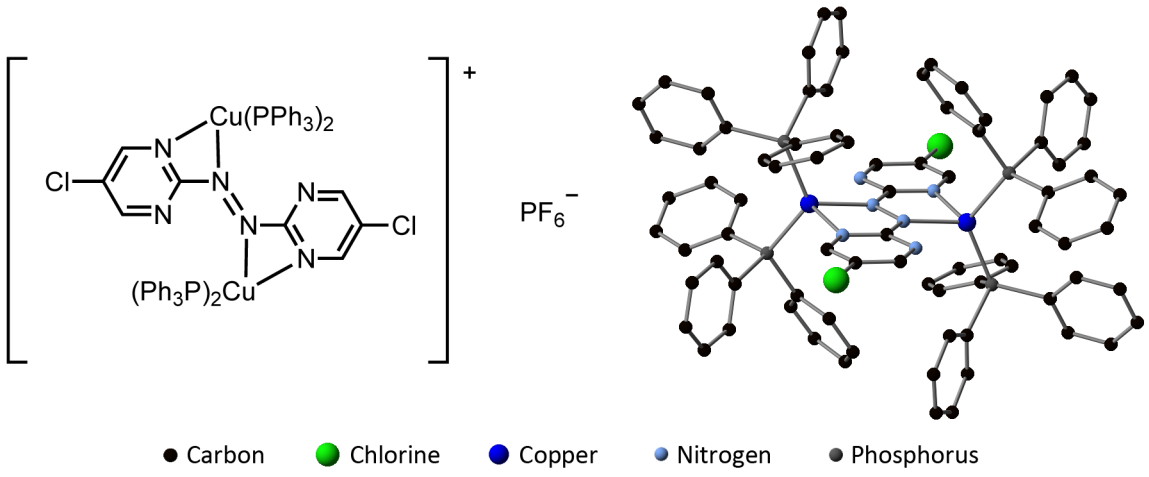



Figure 1.9: The first structurally characterised azo-based radical system and crystal structure of the cation.[120]

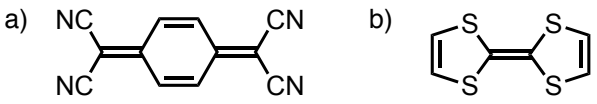



Figure 1.10: (**a**) 7,7,8,8-tetracyano-*p*-quinodimethane (TCNQ) and (**b**) tetrathiafulvalene.

When TCNE or TCNQ is mixed with a suitable electron donor, such as tetrathiafulvalene (Figure 1.10b) in acetonitrile, crystals containing alternating layers of the two reagents are precipitated. Such compounds demonstrate anisotropic low-resistance semiconducting properties and have been described as organic metals.[124–126] Electron transfer between the two species allows both to gain aromaticity, permitting intermolecular electron transfer between adjacent molecules throughout the crystal.

The chemistry of 1,2,4,5-tetrazines (**VI**) represents a growing research interest with applications in conducting polymers in the field of molecular electronics.[127–132] The R groups depicted in Figure 1.6 are typically a pyridine-like heterocycle containing one or more nitrogen atoms to either allow bidentate binding of multiple metal cations, or act as a linker in a similar manner to 4,4´-bipyridine (Figure 1.11a).[133] One interesting publication from Kaim and co-workers reveals the crystal structure of a neutral ligand and its singly reduced radical form, illustrating the variation in bond metrics associated with the presence of the radical on the tetrazine ring (Figure 1.11b).[134] EPR measurements show hyperfine splitting constants consistent with interactions with the nuclear spin of the $^{14}$N ring atoms, the $^{63/65}$Cu(I) centres and also the $^{31}$P nuclei of the phosphine ligands.

The final example in Figure 1.6, **VII**, is perhaps the oldest and best known example of an organic non-innocent ligand. The *o*-quinone / *o*-semiquinone / catecholate redox system and its ability to act in a non-innocent manner was first documented in 1973 when the ligand centred radical was identified using UV/vis and EPR spectroscopic measurements. Since that time the ligands have become better known for their role in multiple biological processes including photosynthesis,[135] and enzyme

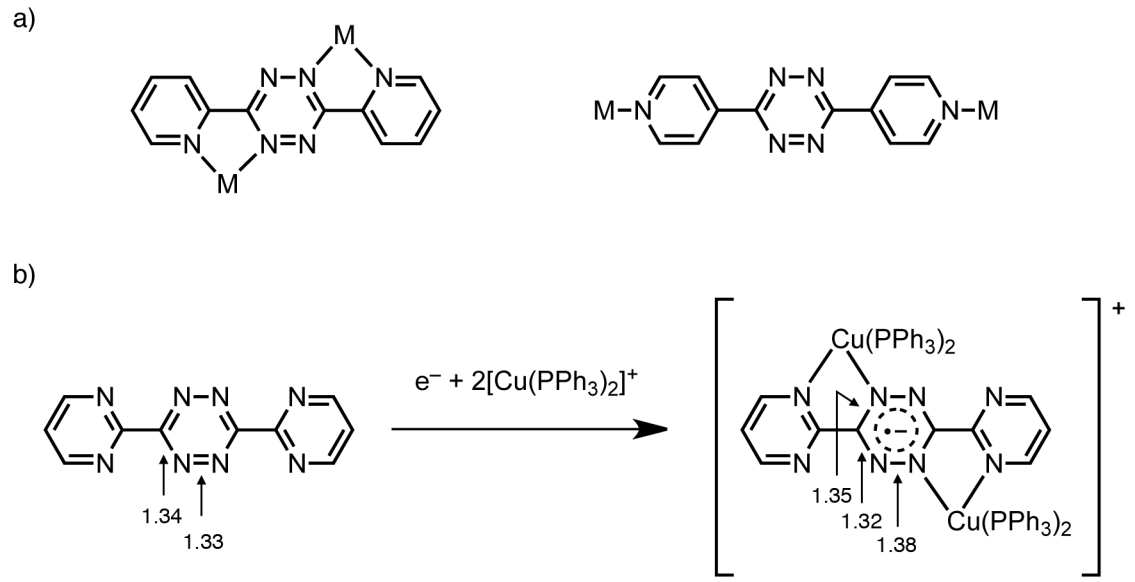



Figure 1.11: (**a**) Two examples of 1,2,4,5-tetrazines illustrating their coordination modes. (**b**) Bond metric changes as a result of ligand reduction.[134] All distances are given in Å.

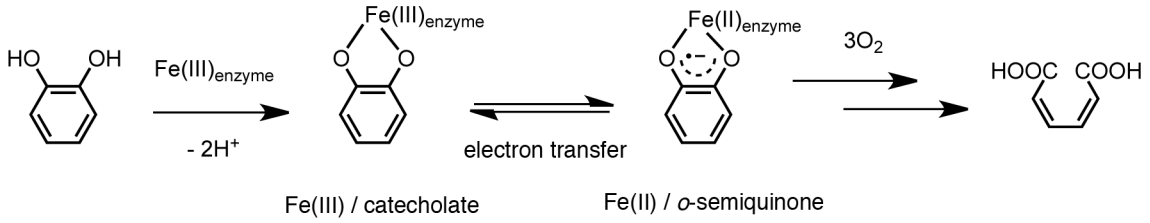



Figure 1.12: The simplified proposed mechanism of catechol dioxygenase.[141]

functions related to nutrition,[136] pathology and toxicology.[137–139]

Two proteins containing Fe and Cu complexes incorporating the catecholate ligand are believed to exploit its non-innocent behaviour. Figure 1.12 shows a simplified reaction scheme for the iron based catechol dioxygenase which is able to split the C–C bond between α-diols by an intramolecular electron exchange.[140–142]

An analogous mechanism has been proposed for the Cu(II) site in amine oxidase, thought to be responsible for the the conversion of primary amines to aldehydes using topaquinone (Figure 1.13) as a cofactor.[143] The topaquinone cofactor is oxidised to a semiquinone which was detectable using EPR spectroscopy. In the absence of the

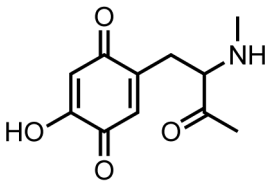



Figure 1.13: Topaquinone.

cofactor no reaction is observed to take place and is consistent with the requirement of a Cu(I) oxidation state to bind and activate oxygen.[144]

While the ligands described in this section represent some of the most commonly encountered examples that may exhibit non-innocent behaviour, this list is by no means exhaustive and recent reviews show an increasing number of reactions are being investigated, particularly in biochemistry, looking for previously missed non-innocent behaviour as an explanation for reactivity or substrate selection.[71,72,74]

The cytochrome P450 family of enzymes, widely studied and present in all organisms, catalyse the splitting of dioxygen and subsequent insertion of an oxygen atom into an unactivated hydrocarbon bond.[145] Although the active site and specifically the location of an iron atom in a porphyrin ring is well known, the exact mechanism that allows this reaction to take place is still not fully understood, and multiple competing theories exist.[146–148] However, the broad reaction process is widely accepted to proceed by a radical rebound mechanism, shown in a simplified form in Figure 1.14.[149] This process relies on non-innocent behaviour of the supporting haem porphyrin, which has been investigated using EPR spectroscopy, among other techniques.[150]

Inorganic examples of catalytic cycles dependent upon the redox activity of ligands have also been observed.[151] One investigation examined the cyclisation of dienes as catalysed by a bis(imino)pyridine Fe complex.[152] Although the complex was initially thought to contain Fe(0), multiple spectroscopic tools and theoretical calculations have been used to demonstrate that Fe(II) is a better descripton and that the ligand is instead doubly reduced, acting as an electron store during the catalytic cycle (Figure

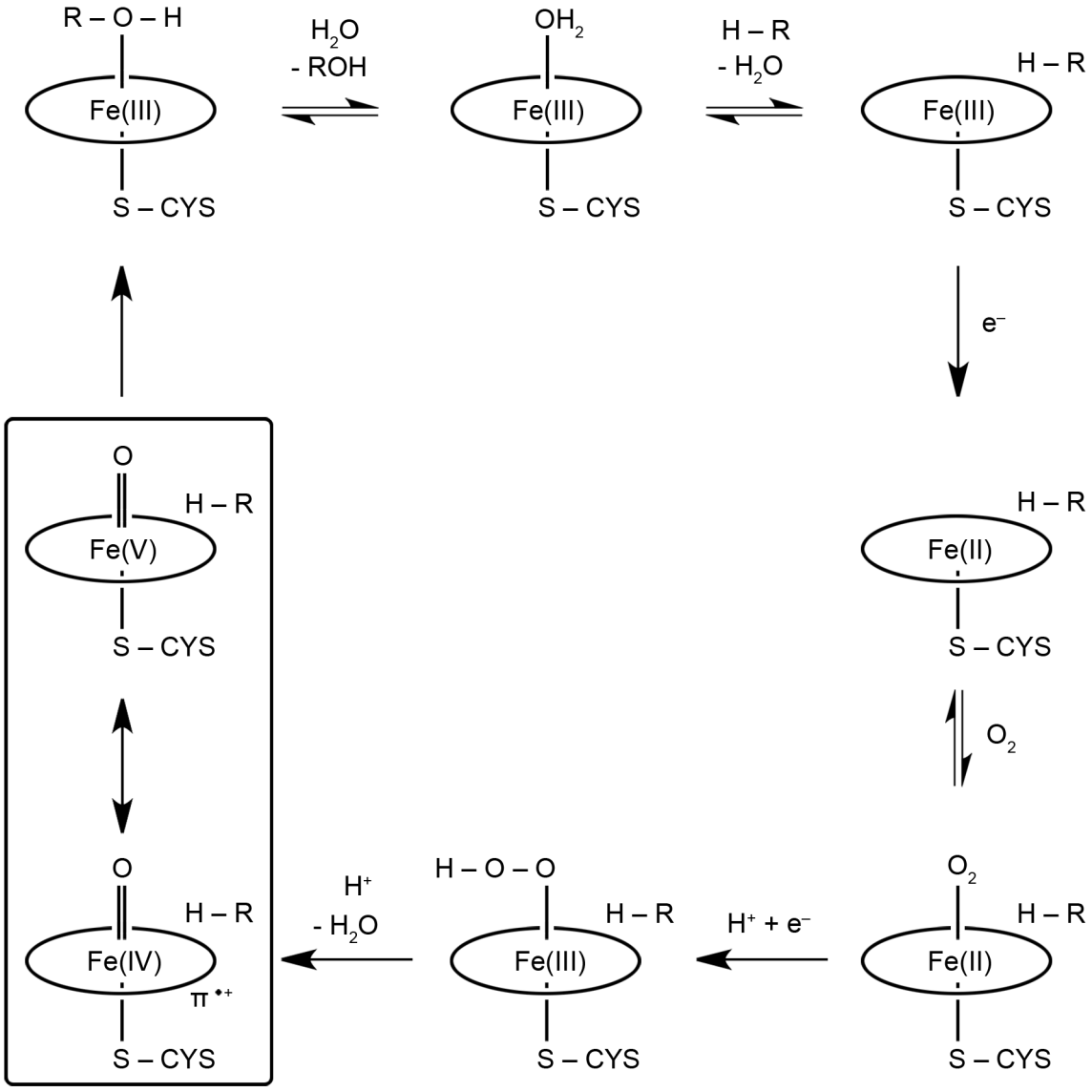



Figure 1.14: Simplified mechanism of the P450 catalysed hydrolysis of a hydrocarbon, highlighting the radical rebound steps.[150]

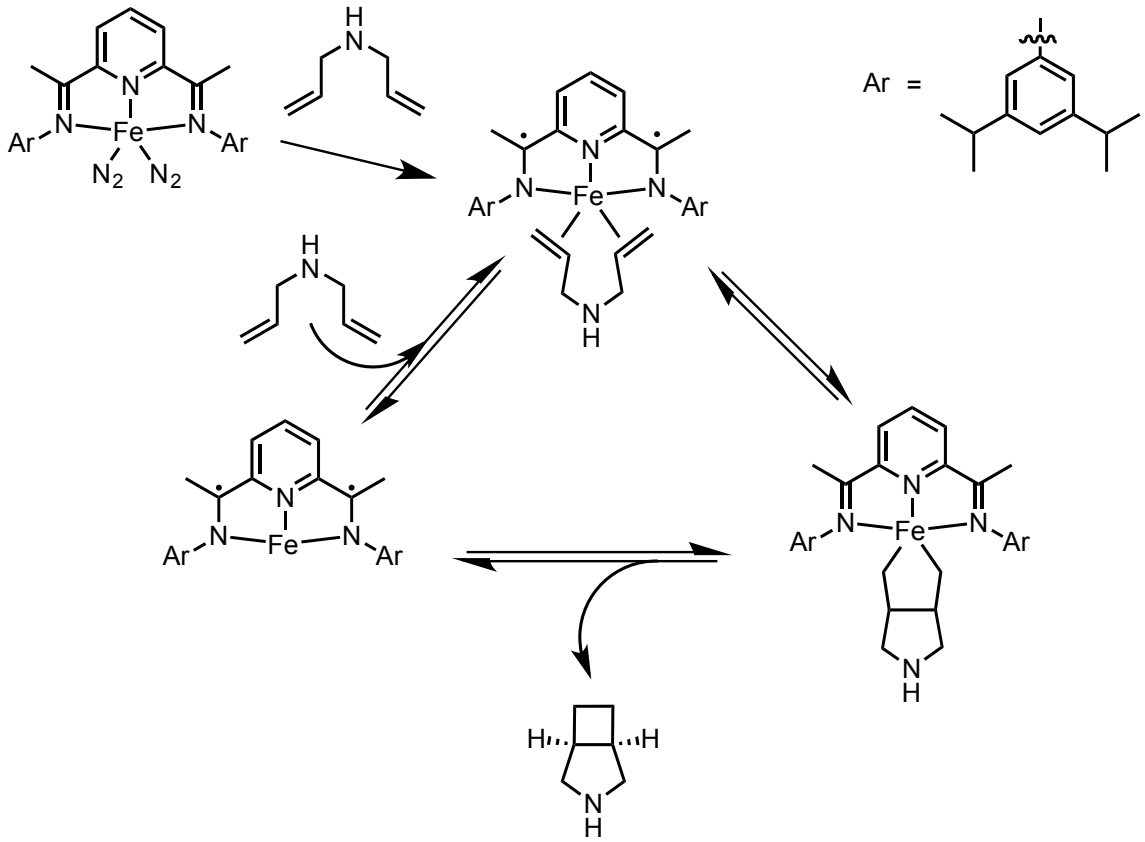



Figure 1.15: Proposed mechanism for the catalytic cyclisation of dienes involving a non-innocent ligand. The active species is Fe(II) rather than Fe(0) throughout the cycle.[152]

1.15).

A second example comes from a very recently published study of the complex Re(2,2´-bipy)$(CO)_3$Cl.[153] This compound is known to electrochemically reduce carbon dioxide catalytically to carbon monoxide under protic conditions, with the activated catalyst believed to be [Re(2,2´-bipy)$(CO)_3]^-$. The authors document the synthesis of the anion by reaction of the parent compound with two equivalents of $KC_8$. IR and NMR spectroscopy, and comparisons of bond metric data from crystal structures to those published in work described in Chapter 2 of this thesis, provide evidence for the reduction of the bipyridine ligand and not the Re(I) metal centre.

## 1.4 2,2´-Bipyridine

As mentioned at the start of this introduction, 2,2´-bipyridine is extensively employed in the field of coordination chemistry because of its ability to act as a bidentate ligand towards a range of main group, transition metal and f-block elements. A large number of these complexes have been structurally characterised and recorded in the CSD allowing a discussion of bond metrics. Chapter 2 examines in detail the structural effects of bipyridine reduction, but at this point it is sufficient to state that the largest structural change observed is a contraction of the inter-pyridyl bond: the structure of uncoordinated 2,2´-bipyridine was reported by Chisholm and co-workers to have an inter-ring bond length of 1.490(3) Å.[154] For a singly reduced bipyridyl radical this value is 1.429(av) Å and for a doubly reduced bipyridyl ligand the observed inter-ring bond length is 1.399(6) Å.[155] Once structure solutions showing high $R$ factors, disordered models, room temperature data collections, powder pattern derived results and other sources of error or inconsistency are excluded, the mean value for coordinated 2,2´-bipyridine ligands recorded in the CSD is 1.476 Å. Figure 1.16 shows a histogram plot of these data. It is immediately obvious that the vast majority of bond distances fall within a narrow range of around 1.45 to 1.50 Å. However, there are a number of structures with bond lengths shorter than might be expected, within the 1.40 to 1.43 Å range.

It is interesting to note that while alkali metal compounds containing reduced bipyridine isomers have been well characterised (particularly in solution), there are substantially fewer main group, transition metal or f-block examples described in the literature.

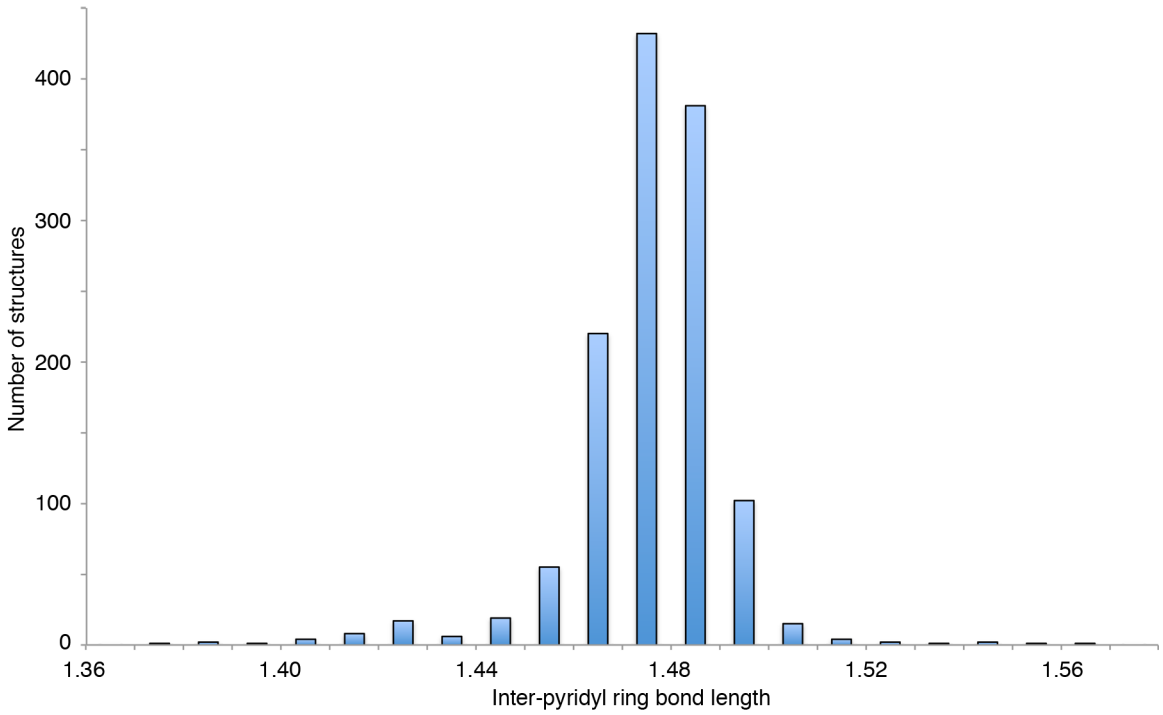



Figure 1.16: Histogram showing the distribution of inter-pyridyl ring bond lengths (in Å) in structures containing 2,2´-bipyridine.[6]

### 1.4.1 Main Group Compounds

Excluding the alkali metal salts discussed in Chapter 2, there are five main group complexes incorporating reduced forms of 2,2´-bipyridine for which crystal structures exist. The first example was studied in 1979 and details the synthesis of Si(2,2´-bipy)$_2$ using a vapour deposition technique.[156] The X-ray data were collected using instruments with significantly less capability than modern diffractometers and consequently the structure (Figure 1.17) is less well determined (only the silicon atom is refined anisotropically). High esd values prohibit a conclusive interpretation of bonding, but inter-ring bond lengths of 1.34(1) and 1.35(1) Å are certainly indicative of doubly reduced ligands and support the authors' conclusion that the system exists as Si(IV) and two dianionic bipyridyl ligands. Unfortunately no other characterisation techniques are presented to corroborate this assignment.

Other structures are newer and more comprehensively characterised. In 2003

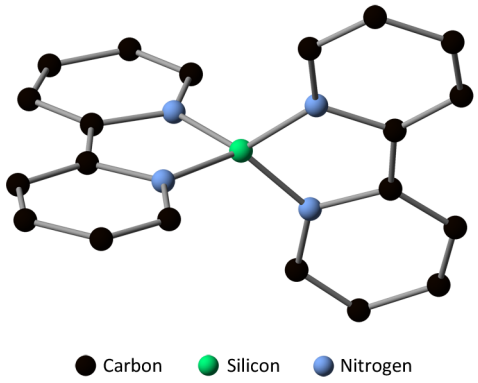



Figure 1.17: Crystal structure of Si(2,2´-bipy)$_2$. Hydrogen atoms have been omitted for clarity.[156]

[Li(THF)$_4$][Al(2,2´-bipy)$_2$] was synthesised by the reaction of Ti(2,2´-bipy)$_3$ with $AlCl_3$ in THF and subsequent crystallisation from $Et_2O$.[157] The [Al(2,2´-bipy)$_2$]$^-$ anion is a pseudo-tetrahedral complex (Figure 1.18), with inter-pyridyl bond lengths of 1.365 and 1.371 Å (no esd values available). The authors note that these bond metrics are highly similar to those found in alkali metal salts of the dianion (see Chapter 2) and formally classify the complex as containing an aluminium(III) centre and two dianionic ligands. However, $^1$H NMR studies show that weak resonances associated with the bipyridyl protons exhibit broadened shifts between 6.7 and 4.9 ppm while DFT calculations indicate that a sub '+3' charge is present on the aluminium site. These results suggest the existance of some amount of radical, monoanionic character on the ligands, and the authors conclude that the oxidation states of aluminium and bipyridine ligands are likely non-integer values.

The three remaining main group complexes were very recently reported by Russell, Norman and co-workers, and involve the coordination of 2,2´-bipyridyl species to boron centres.[158,159] Reaction of $B_2(NMe_2)_2Cl_2$ with 2,2´-bipyridine in *n*-hexane followed by slow evaporation of solvent yielded crystals of [B(2,2´-bipy)Cl$_2$]$^\bullet$ (Figure 1.19). The bipyridyl fragment has a reported inter-ring bond length of 1.413(3) Å which is typical of a singly reduced, radical ligand. This view was corroborated using EPR spectroscopy, and DFT calculations which show almost all radical spin density

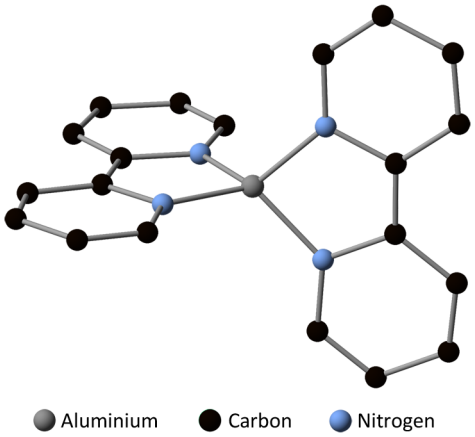



Figure 1.18: Crystal structure of the $[Al(2,2´\text{-bipy})_2]^-$ anion in $[Li(THF)_4][Al(2,2´\text{-bipy})_2]$. Hydrogen atoms have been omitted for clarity.[157]

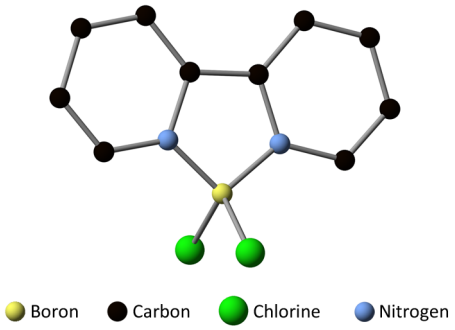



Figure 1.19: Crystal structure of $[B(2,2´\text{-bipy})\cdot Cl_2]$.[158] Hydrogen atoms have been omitted for clarity.

lies on the ligand. The EPR spectrum shows extremely detailed fine structure and the authors note that even after excluding lower abundancy isotope contributions ($^{10}$B and $^{37}$Cl) the expected number of lines is 11340, of which about 150 are resolved. This fine detail arises because of the contributions of many inequivalent nuclei: $4 \times 2 \times {}^{1}\text{H}$ ($I = 1/2$), $2 \times {}^{14}\text{N}$ ($I = 1$), $1 \times {}^{11}\text{B}$ ($I = 3/2$) and $1 \times {}^{35}\text{Cl}$ ($I = 3/2$). Expected line splitting is given by: $\prod_i (2n_i I_i + 1)$ where $n$ is the number of equivalent nuclei and $I$ is the nuclear spin of the nucleus. Thus for this system, the calculated spectrum is composed of: $(2 \times 2 \times 1/2 + 1)^4 (2 \times 2 \times 1 + 1)(2 \times 1 \times 3/2 + 1)(2 \times 2 \times 3/2 + 1) = 3^4 \times 5 \times 4 \times 7 = 11340$ lines. As a result of this, modelling the data was not attempted.

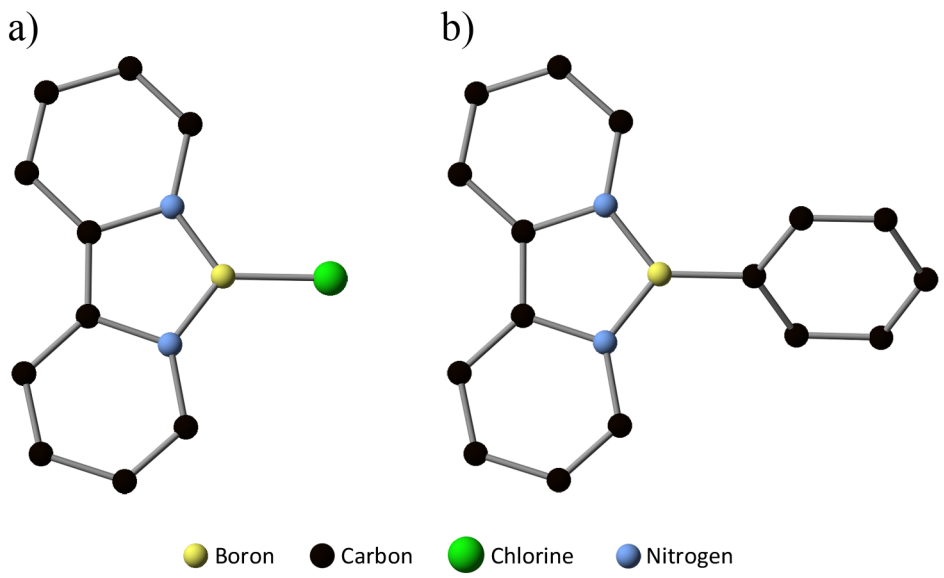



Figure 1.20: The crystal structures of (**a**) B(2,2´-bipy)Cl and (**b**) B(2,2´-bipy)Ph. Hydrogen atoms have been omitted for clarity.[159]

The reaction of $Li_2$(2,2´-bipy) with $BCl_3$ or $BPhCl_2$, followed by slow evaporation of solvent was reported to give rise to the related compounds B(2,2´-bipy)Cl and B(2,2´-bipy)Ph, respectively (Figure 1.20).[159] The inter-pyridyl bond lengths in these structures are 1.379(2) and 1.380(av) Å, consistent with a doubly reduced species. DFT calculations support this assignment and additionally show a decrease in aromaticity of the two bipyridine rings relative to those of free bipyridine, together with increasing aromaticity in the N–B–N containing 5 membered ring.

### 1.4.2 Lanthanide Compounds

Traditionally believed to have very small levels of covalency in bonding interactions with ligands, lanthanide compounds have nonetheless proven to pose interesting questions with regard to complexes containing non-innocent ligands, and in particular 2,2´-bipyridine.

In the decade following the publication of the first crystallised main group complex of a reduced bipyridyl, the first structure of a lanthanide complex was also docu-

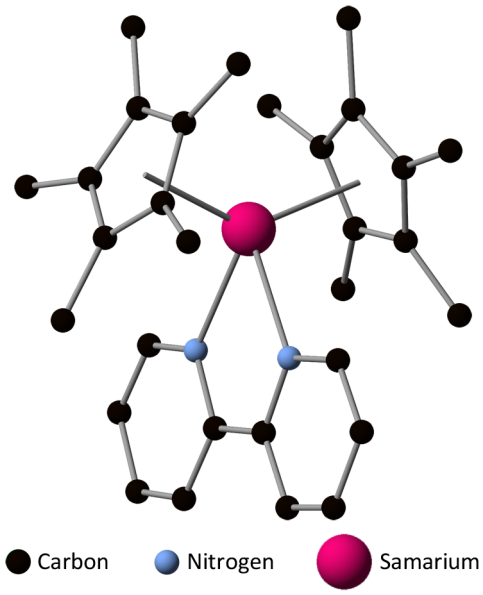



Figure 1.21: Crystal structure of Sm(2,2´-bipy)$Cp^*_2$ ($Cp^*$ = $C_5Me_5$). Hydrogen atoms have been omitted for clarity.[160]

mented. Evans and co-workers crystallographically characterised Sm(2,2´-bipy)$Cp^*_2$ ($Cp^*$ = $C_5Me_5$) from the reaction of $Cp^*_2Sm(THF)_2$ and 2,2´-bipyridine in toluene (Figure 1.21).[160] In this complex there exist two potential electronic structures: Sm(II) accompanied by a neutral bipyridine ligand, or Sm(III) with a charge balancing radical bipyridyl ligand. The authors note the diagnostic inter-pyridyl bond length of 1.429(4) Å suggests the latter case is correct, an assignment which is corroborated by reference to the $^{13}C$ NMR shifts of the $Cp^*$ ligands (which are consistent with the presence of an Sm(III) cation) and IR absorption frequencies, which fit the diagnostic bands for a bipyridyl radical, first identified by Nakamoto and co-workers.[18]

The synthesis and structural characterisation of two interesting bipyridine lanthanum complexes was reported in 2003 by Marques and co-workers. These are La(2,2´-bipy)($Tp^{Me_2}$)$Cl_2$ and La(2,2´-bipy)($Tp^{Me_2}$)$_2$, where $Tp^{Me_2}$ = hydrotris(3,5-dimethylpyrazolyl)borate. The first contains a neutral 2,2´-bipyridine ligand which is reduced to form the second (Figure 1.22).[161] The inter-pyridyl bond length in the neutral species is 1.484(8) Å while in the reduced species it contracts to 1.45(2) Å.

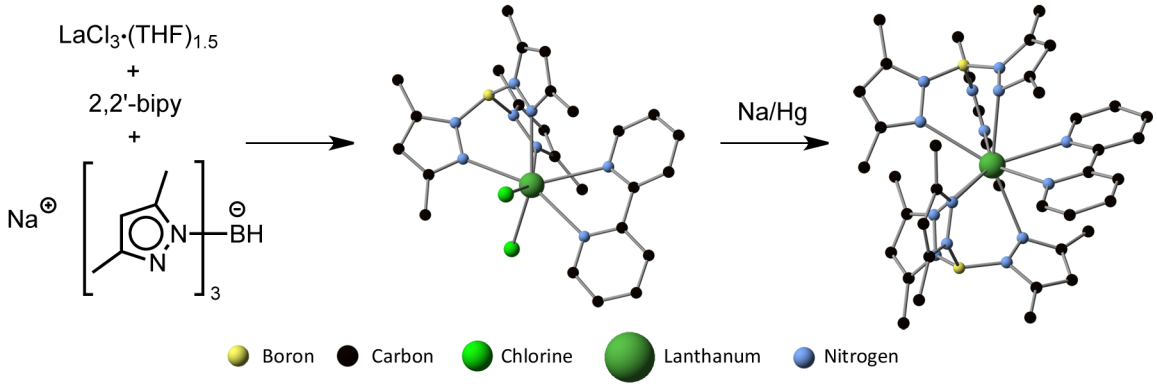



Figure 1.22: Synthetic route and crystal structures of La complexes containing 2,2´-bipyridine. The neutral species is La(2,2´-bipy)($Tp^{Me_2}$)$Cl_2$, which is reduced to La(2,2´-bipy)($Tp^{Me_2}$)$_2$. $Tp^{Me_2}$ = hydrotris(3,5-dimethylpyrazolyl)borate. Hydrogen atoms are omitted for clarity in addition to a THF solvent molecule present in the lattice of the reduced compound.[161]

Although the latter bond distance has a statistically large esd, stronger evidence for the presence of a bipyridine centred radical comes from magnetic susceptibility measurements where a temperature independent paramagnetic response of 1.5 $\mu_B$ was recorded. The discrepency between this and the spin-only formula calculated value of 1.73 $\mu_B$ is ascribed to the presence of either an anti-ferromagnetic interaction between adjacent complexes in a crystallite, or by the presence of traces of a contaminant resulting from a small amount of sample oxidation/decomposition. The authors also note that while the $^1$H NMR spectrum of the neutral species exhibits sharp resonances, the reduced species shows highly broadened peaks, again consistent with the presence of a radical species.

Perhaps the most rigorously investigated lanthanide complexes of reduced bipyridyl ligands come from Andersen and co-workers who have published three increasingly analytical papers discussing the electronic structure of Yb(2,2´-bipy)$Cp^*_2$ (Figure 1.23) and several related compounds. The first paper identifies the potential for non-innocent behaviour analogous to that described for the related samarium complex above, arising from either Yb(II) or Yb(III) oxidation states that may be present in the

complex.[162] A single crystal X-ray diffraction structure provides evidence to support a reduced bipyridyl ligand (inter-pyridyl bond length: 1.383(av) Å), and is corroborrated by comparison of the IR spectrum with the Nakamoto diagnostic absorption bands,[18] and by the observation of broadened resonances in the $^1$H NMR spectrum. However, SQUID magnetic susceptability measurements reveal that the system is far more complex than initially anticipated. In the case of an Yb(II) complex containing an innocent bipyridine ligand, the sample would be expected to be diamagnetic. For the Yb(III) alternative, the authors describe the expected two-regime response arising as a result of inaccessibility of low lying energy levels at temperatures below 30 K, but which become fully accessible above 90 K, resulting in two separate Curie-Weiss regions with differing paramagnetic responses. Instead of this response, the system was found to exhibit a continuously varying magnetic moment with temperature, and at all points susceptibility was substantually lower than that which might be expected from coupled, non-interacting spins on the Yb(III) cation and the bipyridyl radical (0.5 to 2.5 $\mu_B$ observed compared to 4.3 – 5.6 $\mu_B$ calculated). Virtually identical responses were found for the related compounds Yb(2,2´-bipy)$(Me_4C_5H)_2$ and Yb(1,10-phenanthroline)$Cp^*_2$. Variable field measurements provided evidence of antiferromagnetic ordering at low temperatures, but no associated quantum mechanical theory existed to model this interaction. However, f-orbitals typically act as core orbitals with little participation in bonding interactions and antiferromagnetic coupling (to the degree required to explain such low magnetic susceptibiliies) would suggest a substantial bonding interaction. The possibility of a temperature dependant equilibrium between Yb(II) and Yb(III) complexes was examined and determined highly unlikely by XANES analysis of the compound, which showed no changes in signal intensity ratio between 10 and 400 K.[163]

A second paper published several years later examined the effects of substituent groups on the bipyridyl moiety (Figure 1.24).[164] These compounds were examined

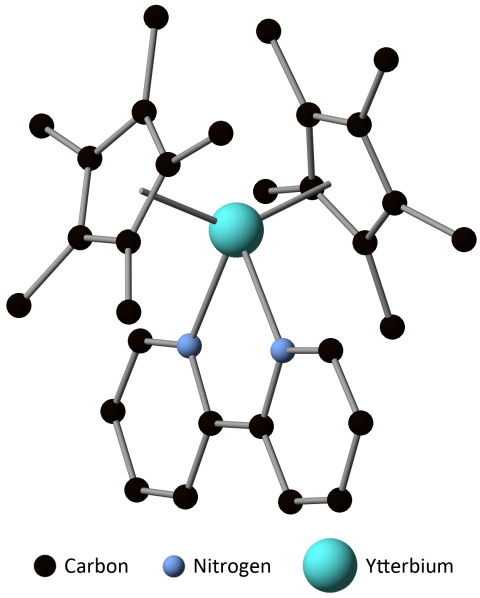



Figure 1.23: Crystal structure of Yb(2,2´-bipy)$Cp^*_2$. Hydrogen atoms have been omitted for clarity.[162]

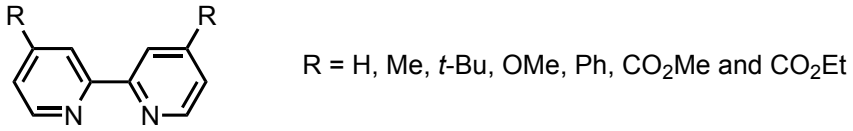



Figure 1.24: Substituted bipyridine systems employed by Andersen and co-workers.

using extensive magnetic susceptability measurements, X-ray crystallography and variable temperature $^1$H NMR. All compounds were found to exhibit similar paramagnetic properties to those described above and the authors noted an elegant correlation between molar magnetic susceptibility and the displacement of resonance positions, relative to those of the related innocent compound [Yb(2,2´-bipy)$Cp^*_2$]I. Orbital analysis studies revealed that symmetry related 4f and 5d orbitals allowed hybridisation and subsequent interaction with the bipy radical orbital providing a potential route to allow stronger antiferromagnetic interactions.

The third paper from Andersen and co-workers further examines the magnetic effects of substituted bipyridine ligands, as well as a series of related diazabutadiene systems.[165] XANES data were used to probe the oxidation state of the Yb atom

in all compounds and reveals varying Yb(II) and Yb(III) contributions across the compounds, all of which were found to be invariant with temperature (again ruling out the possibility of temperature dependant equilibria between Yb(II) and Yb(III) complexes in all cases). EPR and SQUID measurements, together with CASSCF theoretical calculations, are used to argue that the ground state for these complexes is multiconfigurational (with intermediate valence), and that the observed magnetism arises as a result of the previously described intramolecular coupling as well as a smaller intermolecular contribution. The authors conclude that electron–electron repulsion in Yb(II) is greater than in Yb(III), but because of the lack of covalent bonding between Yb and the coordinated bipyridine molecule, charge transfer is not permitted. Instead, hybridisation of the Yb(II) and Yb(III) states to form a mixed valency ground state with associated partial negative charge on the ligand is driven by the lowering of the total energy of the molecule.

### 1.4.3 Actinide Compounds

The chemistry of actinides is dominated by uranium chemistry and this element is similarly present in the majority of actinide complexes that contain reduced forms of bipyridyl ligands.

The first recorded structure was published in 1975 by Del-Piero and co-workers. U(2,2´-bipy)$_4$ contains four unique inter-bipyridyl bond lengths of 1.416(av) Å (Figure 1.25).[166] Originally discussed as a formal U(0) complex, and although there are relatively large esd values associated with this crystal structure, it is entirely consistent with the presence of a U(II) or higher charged cation with an appropriate number of reduced ligands, and indeed has been discussed as such in the literature.[167,168] However, without further characterisation it is not possible to be more definitive.

More recently, multiple spectroscopic techniques were used to conclusively prove the existance of bipyridyl based radicals in two analogous compounds. The reac-

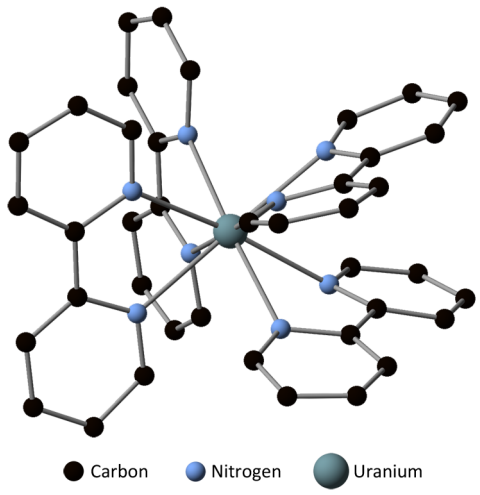



Figure 1.25: Crystal structure of U(2,2´-bipy)$_4$. Hydrogen atoms were not modelled in the literature structure.[166]

tion of (Cp*U($C_8H_8$))$_2$($\mu$-$C_8H_8$) with either of 2,2´-bipyridine or 4,4´-dimethyl-2,2´-bipyridine yielded two equivalents of Cp*($C_8H_8$)U(2,2´-bipy) or Cp*($C_8H_8$)U(4,4´-dimethyl-2,2´-bipy), respectively, and one equivalent of $C_8H_8$ as depicted in Figure 1.26.[169] Crystal structures of these species both have shortened inter-pyridyl bond distances of 1.427(3) Å for the 2,2´-bipyridyl containing structure and 1.436(4) Å for the disubstituted analogue, suggesting that the ligands are singly reduced radicals. Broadened NMR spectra resonances and IR bands falling within the diagnostic regions identified by Nakamoto were used as confirmation of this, while DFT calculations revealed the SOMO orbital to be largely bipyridine based, with the U site carrying a +4 charge and the bipyridyl ligand a –1 charge. The authors believe reduction arises as a result of displacement of the bridging $(C_8H_8)^{2-}$ ligand by neutral bipyridine followed by electron transfer to form the reaction products. This is argued on the basis of relative reduction potentials of 2,2´-bipyridine / 2,2´-bipyridyl radical anion, and $C_8H_8$ / $C_8H_8{}^{2-}$ (–2.10 and 1.68 V, respectively, versus SCE) which would require prior complexation of the bipyridine to lower its redox potential, then allowing the reaction to take place.

A second paper detailing the synthesis of a different uranium coordination complex

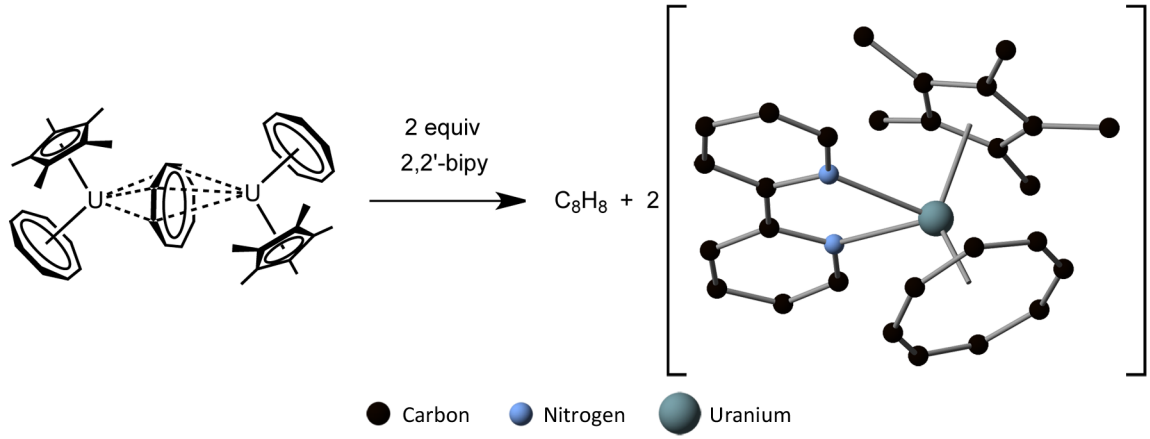



Figure 1.26: Synthetic route to and crystal structure of U(2,2´-bipy)Cp*($C_8H_8$). Hydrogen atoms have been omitted for clarity.[169]

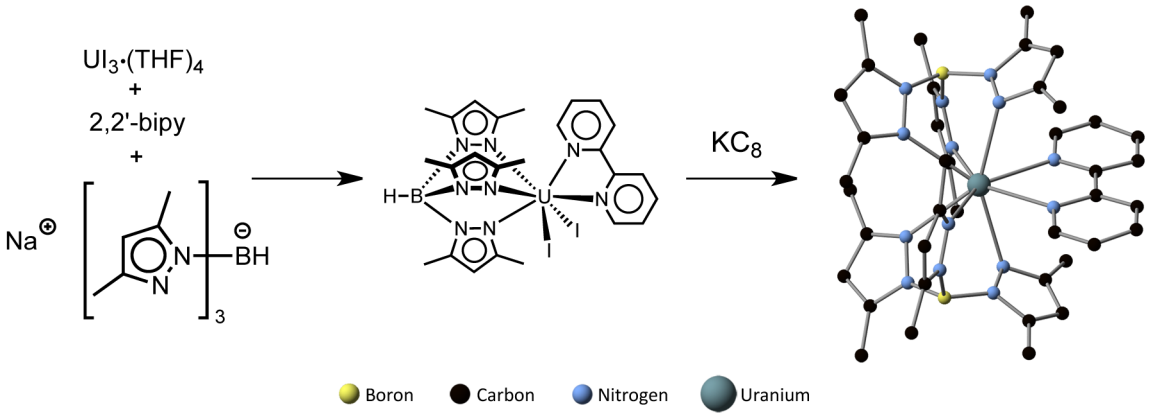



Figure 1.27: Synthetic route and crystal structure of U(2,2´-bipy)($Tp^{Me_2}$)$_2$. $Tp^{Me_2}$ = hydrotris(3,5-dimethylpyrazolyl)borate. Hydrogen atoms are omitted for clarity as well as two THF solvent molecules present in the lattice.[170]

incorporating a bipyridyl radical ligand was published in the same year.[170] Bart and co-workers detail the synthesis and reduction of a uranium analogue of the La(2,2´-bipy)($Tp^{Me_2}$)$Cl_2$ complex described in the previous section (Figure 1.27). Crystallographic characterisation of the reduced compound reveals an inter-pyridyl distance of 1.409(13) Å while a $^1$H NMR spectrum reveals resonance shifts that are also consistent with the presence of a bipyridyl radical.

The only crystallographically characterised non-uranium actinide complex containing a reduced bipyridine ligand is a very recently published thorium complex.

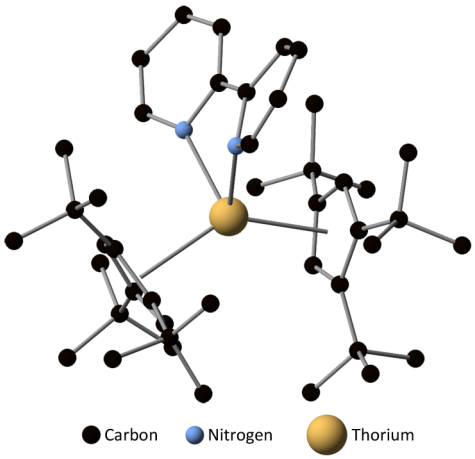



Figure 1.28: Crystal structure of Th(2,2´-bipy)($\eta^5$-1,2,4($^t$Bu)$_3$C$_5$H$_2$)$_2$. Hydrogen atoms have been omitted for clarity.[171]

Walter and co-workers describe the reaction of Th($\eta^5$-1,2,4($^t$Bu)$_3$C$_5$H$_2$)$_2$Cl$_2$ with 2,2´-bipyridine and an excess of KC$_8$ to form Th(2,2´-bipy)($\eta^5$-1,2,4($^t$Bu)$_3$C$_5$H$_2$)$_2$ (Figure 1.28).[171] Unlike the $^1$H NMR spectra of the uranium compounds above, in this instance the authors noted a diamagnetic response with resonance shifts slightly offset from those of neutral bipyridine. Coupled with a very short inter-pyridyl bond length of 1.382(8) Å, the system is described as Th(IV) complexed to a dianionic bipyridyl ligand.

### 1.4.4 Transition Metal Compounds

By contrast with main-group and f-block compounds, the numbers of transition metal compounds containing reduced bipyridine ligands where oxidation states of both metal and ligand are comprehensively analysed are far fewer. The earliest example is the sodium salt of [(CO)$_4$Cr(2,2´-bipy)]$^-$, for which EPR and UV-Vis spectroscopic measurements were used along with DFT calculations to suggest the presence of a bipyridyl radical anion, complexed to a Cr(0) metal.[172–175]

Of note is the absence of any crystallographically characterised transition metal complexes where a negative charge is assigned to the bipyridine ligand. This may be

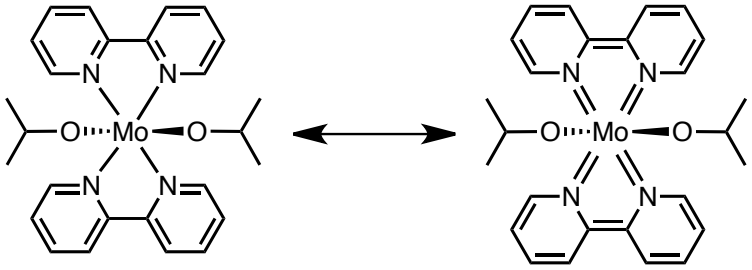



Figure 1.29: Resonance canonical proposed by Chisholm and co-workers.

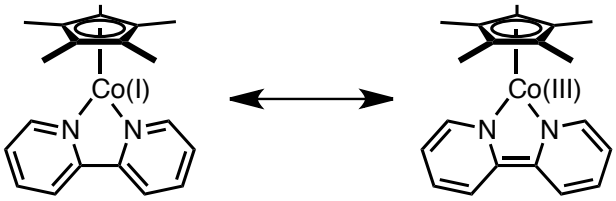



Figure 1.30: Resonance canonical proposed by Brookhart and co-workers.

due to ambiguity in charge assignment, a result of multiple accessible oxidation states at both the central metal and the bipyridine ligand. Although in other areas of the periodic table, the presence of a reduced bipyridyl monoanion or dianion is readily apparent, there are several instances where the assignment is less trivial.

The structure of Mo(*i*-PrO)$_2$(2,2´-bipy)$_2$ reported by Chisholm and co-workers, has an inter-pyridyl ring bond length of 1.425(4) Å,[154] suggesting that ligand reduction could have taken place. However, this explaination was not considered and instead the unusual bond metric was explained by reference to the resonance canonical in Figure 1.29 and thus implies extensive donation from the electron rich metal to the π* orbital of bipyridine.

Similarly, Brookhart and co-workers noted that the reaction of Co($C_5Me_5$)($\eta^2$-$H_2C$=CHSi$Me_3$)$_2$ with 2,2´-bipyridine to yield Co($C_5Me_5$)(2,2´-bipy), gave rise to crystals exhibiting a shorter than expected inter-pyridyl ring bond length of 1.419(3) Å.[176] The authors interpret this as a consequence of the π-acceptor ability of 2,2´-bipyridine and also suggest a resonance canonical that allows for increased double bond character between the pyridine rings (Figure 1.30).

A final example comes from Tilley and co-workers who crystallographically characterised [K(dibenzo-18-crown-6)][Ru($C_5Me_5$)(2,2´-bipy)] (dibenzo-18-crown-6 = dibenzo[a,j]-1,4,7,10,13,16-hexaoxacyclooctadeca-2,11-diene).[177] In this complex the 2,2´-bipyridyl moiety exhibits an inter-pyridyl ring bond length of 1.401(9) Å. The authors do not specifically discuss this highly shortened bond but observe that NMR measurements of a freshly prepared sample yield reasonable spectra while samples stood in solvent for several hours show significant symptoms of paramagnetism. Both of these suggest the formation of a bipyridyl dianion (that is partially oxidised to the radical as it decomposes in solvent).

In all three cases discussed above there is evidence to suggest the formation of complexes that incorporate a reduced bipyridyl ligand, but in the absence of EPR spectroscopy and magnetic susceptibility measurements, it is not possible to state categorically that this is the case. It is important to note that, as will be seen in Chapter 2, the reduction of bipyridine causes population of the same π* orbital that would act as an acceptor in the case of extensive backbonding. This is an important observation as both effects would potentially give rise to the same changes in bond metrics. This is discussed further in Chapter 3.

## 1.5 4,4´-Bipyridine

The ubiquity of 2,2´-bipyridine as a chelating ligand is mirrored by the multitude of structures that incorporate 4,4´-bipyridine as a rigid linker. In common with the previously described 2,2´-isomer, the inter-ring bond length shows the greatest change upon ligand reduction. As will be discussed in Chapter 2, in a neutral uncoordinated species, a bond distance of 1.487 Å is reported,[178] while in the singly reduced bipyridyl anion this length is shortened to 1.425(av) Å and in the doubly reduced analogue it is 1.363(av) Å.[179] A survey of crystallographically characterised compounds in the

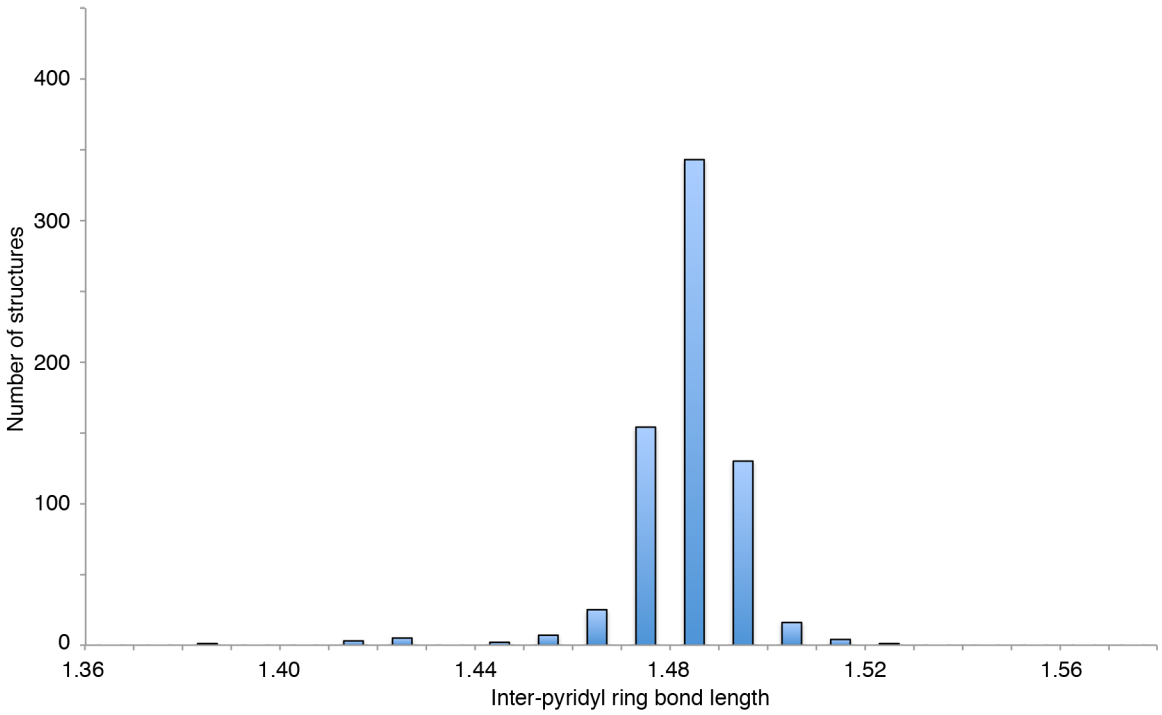



Figure 1.31: Histogram showing the distribution of inter-pyridyl ring bond lengths (in Å) in structures containing 4,4´-bipyridine.[6]

Cambridge Structural Database reveals a mean bond length of 1.484 Å and an even narrower range of bond lengths of between 1.47 and 1.50 Å.[6] The histogram shown in Figure 1.31 illustrates this and shows the presence of a smaller group of structures with bond lengths between 1.38 and 1.43 Å. Almost all of these structures are the results of the research documented in this thesis, with the only exception being a recently published polyoxometalate based coordination polymer.[180] Unfortunately, the refinement is dominated by the large tungsten containing clusters with the result that, despite having a low R factor (4.0%), esd values for C–C bonds are too large to be statistically meaningful. Additionally, the incorporation of water molecules within the lattice would seem to preclude the possibility of a bipyridiyl radical, which are typically highly air- and moisture-sensitive.

The structure of a related compound does however contain a relevant bond metric. The viologen [1,1´-diethyl-4,4´-bipyridilium]$I_2$ was reacted with the disodium salt of

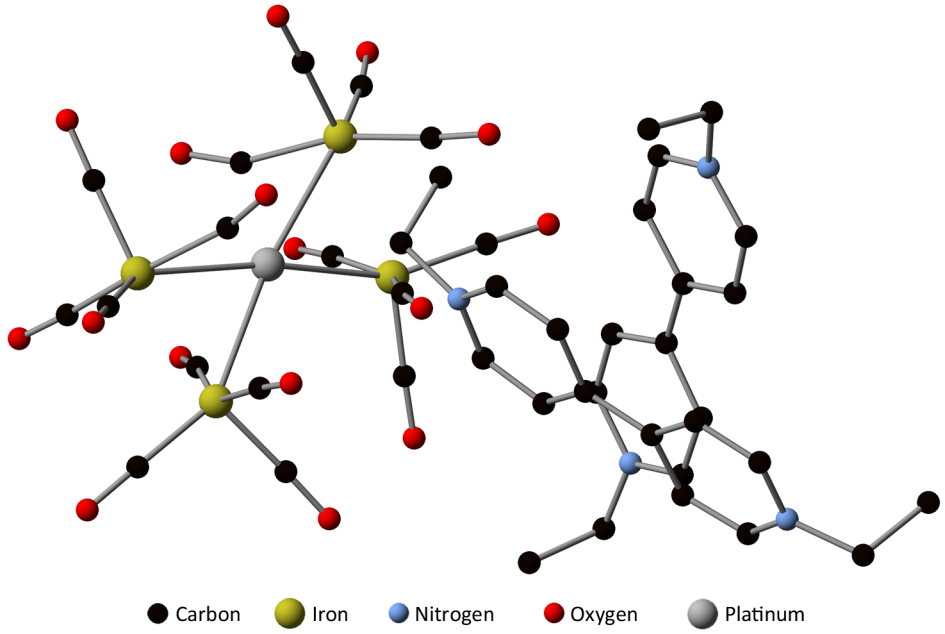



Figure 1.32: Crystal structure of [1,1´-diethyl-4,4´-bipyridilium]$_2$[$Fe_4Pt(CO)_{16}$]. The bipyridilium molecules are symmetry related but both are included to highlight dimer stacking. Hydrogen atoms have been omitted for clarity.[181]

$[FePt_4(CO)_{16}]^{2-}$ to generate [1,1´-diethyl-4,4´-bipyridilium]$_2$[$Fe_4Pt(CO)_{16}$], with the aim of exploiting the multiple redox states of the bipy-like ligand together with those of the cluster to form new semiconductors (Figure 1.32).[181] Note that the normal charge on the bipyridilium molecule is +2 because of the presence of two pseudo quaternary nitrogen atoms. In this example they appear to carry a +1 charge. Structural characterisation using single crystal X-ray diffraction revealed an inter-pyridyl ring bond length of 1.421 Å (no esd value available; the two bipyridilium cations are symmetry related), suggesting the presence of a radical ligand. The authors use EPR spectroscopy to determine that this is indeed the case, and are able to show that the radicals exist in pairs in close proximity (4.15 Å separation) in the crystal lattice with their spins aligned to create a triplet state.

Although (outside of work described in the chapters of this thesis) there are no crystal structures containing reduced forms of 4,4´-bipyridine, the literature does contain many examples of complexes of the ligand that exhibit redox chemistry. One

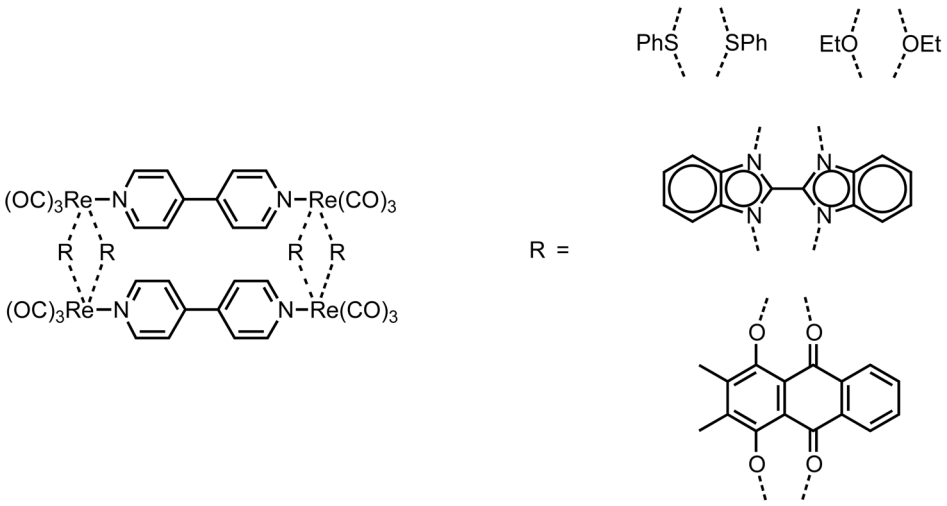



Figure 1.33: Structures of 4,4-bipyridine containing molecular squares.

interesting example concerns the reduction of molecular square or rectangular shaped systems.[182–184] Several related coordination complexes, each incorporating two 4,4´-bipyridine ligands have been synthesised (Figure 1.33). These are found to undergo reversible single, double and triple reductions while retaining connectivity. Reduction was effected either by use of a potentiostat, or more quantitatively by the use of sodium amalgam in conjunction with 2,2,2-crypt. Reduction products were characterised in solution using a mixture of cyclic voltammetry, fluorescence spectroscopy and spectroelectrochemistry, the latter allowing continuous monitoring of IR and UV/vis absorption at a range of applied potentials.

## 1.6 2,4´-Bipyridine

The final isomer of bipyridine investigated in the course of this thesis is 2,4´-bipyridine. Unlike the 2,2´- and 4,4´- isomers, 2,4´-bipyridine is far less frequently encountered in the literature and has no well defined single coordination mode: while the nitrogen at the 4´ position is typically bonded to a cation, the remaining nitrogen atom may be coordinated to another point in the same isolated molecule, act as a bridge in a polymer, or not be bonded to anything (Figure 1.34).

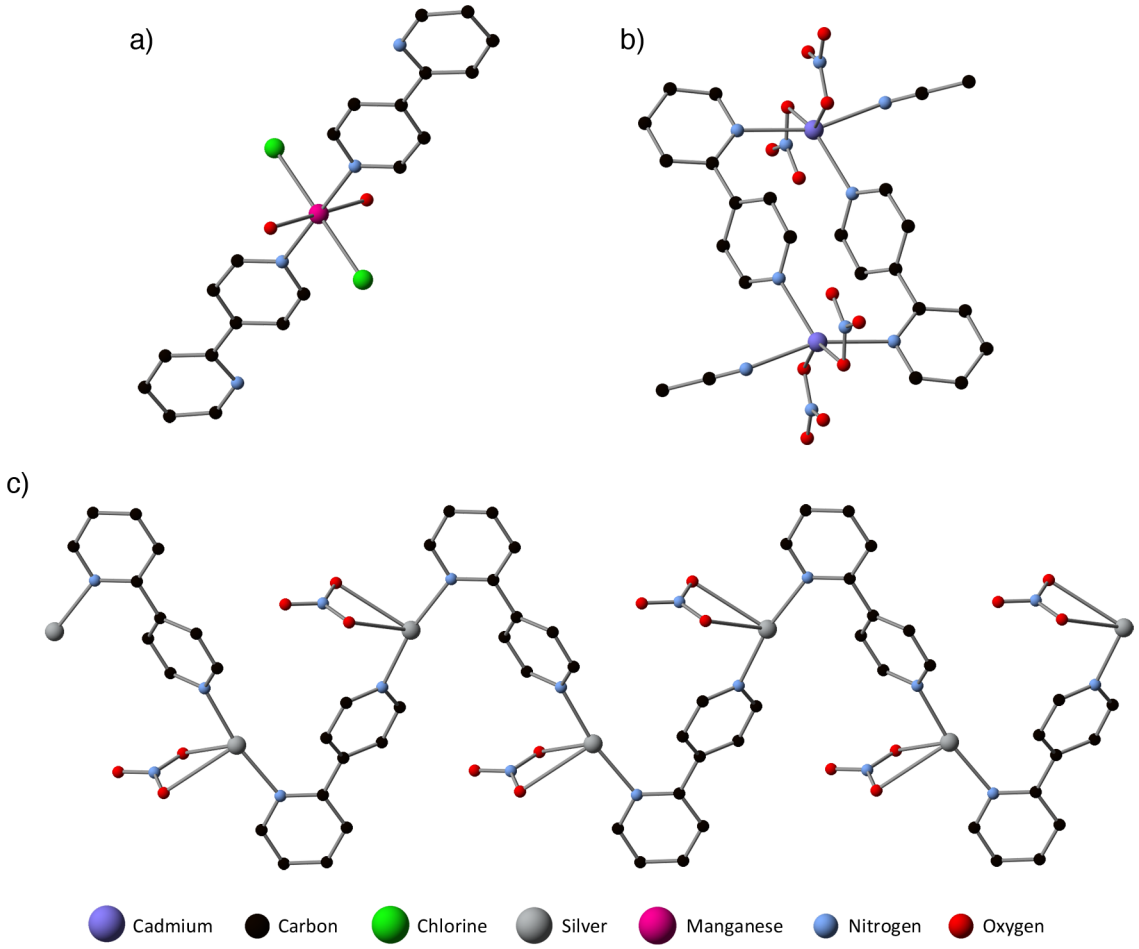



Figure 1.34: The coordination modes of 2,4´-bipyridine: (**a**) Mono-coordinated within an isolated molecule as seen in $Mn(2,4´\text{-bipy-N}´)_2Cl_2(H_2O)_2$.[185] (**b**) Bonded at both nitrogen atoms in a discrete molecule, as seen in the molecular square $[Cd(2,4´\text{-bipy})(NO_3)_2MeCN]_2$.[186] (**c**) Bonded at both nitrogen atoms as part of an extended structure, exemplified by $[Ag(2,4´\text{-bipy})(NO)_3]_n$.[187] Hydrogens have been omitted from all structures for clarity.

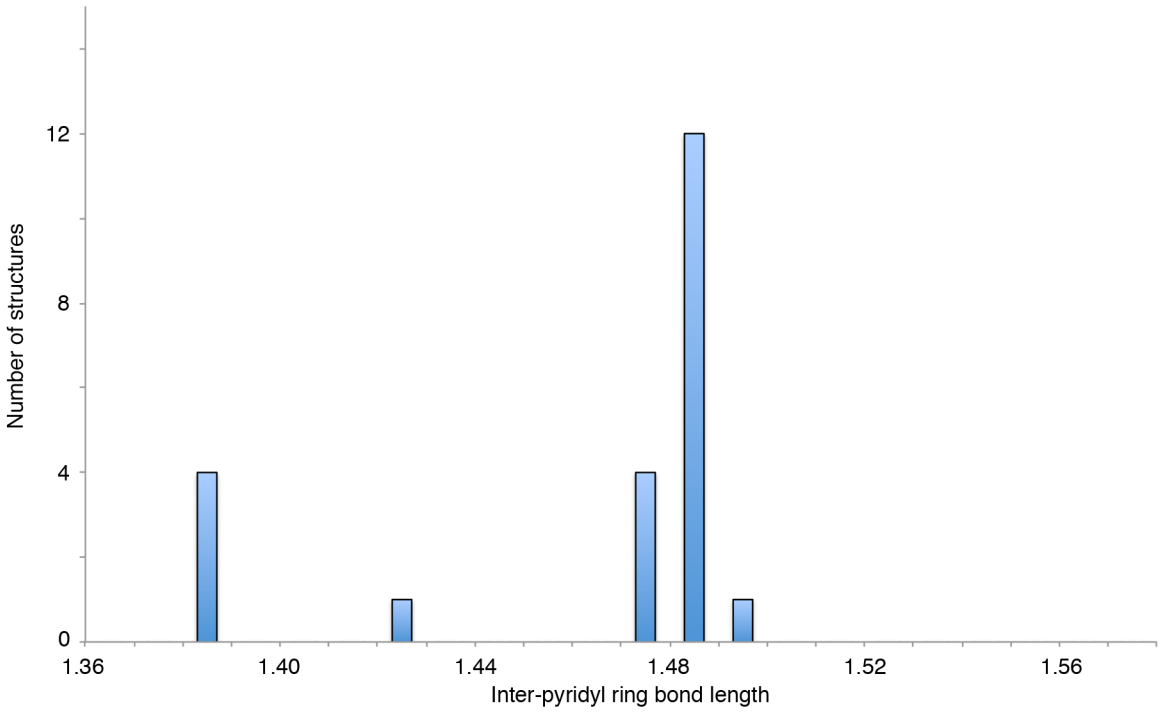



Figure 1.35: Histogram showing the distribution of inter-pyridyl ring bond lengths (in Å) in structures containing 2,4´-bipyridine.[6]

Although the number of structures in the CSD containing this isomer is far fewer, an analysis of bond metrics similar to those in the previous two sections is still meaningful. For uncoordinated 2,4´-bipyridine, the interpyridyl ring bond length has been reported as 1.484(av) Å, which shortens to 1.429(3) Å in the singly reduced radical, and further contracts to 1.386(av) Å in the doubly reduced species.[155] Examination of a histogram (Figure 1.35) of the length of this bond in high quality structures in the CSD reveals a familiar (if less well populated) narrow range of values (1.47 to 1.50 Å).[6] The entirety of the results not found within this range are from the work detailed in this thesis, and are discussed in Chapter 2. Due to the low total numbers of structures containing the 2,4´-bipyridine isomer, the inclusion of complexes containing a reduced ligand species has a considerable effect on the mean bond length of the dataset, reducing it to 1.464 Å.

## 1.7 Project Aims

The broad aim of this project is to investigate the effects of chemical reduction on the structural properties of bipyridine ligands and to evaluate whether this may be used to identify complexes where the ligand isomers exhibit non-innocent behaviour. This is broken down into two distinct parts:

1. The existing chemical literature provides little by way of established bond metric data for the reduced states of the three bipyridine isomers so an initial investigation of non-ambiguous radical anion and dianionic complexes is necessary. To this end, Chapter 2 details the synthesis and characterisation of alkali metal salts of the reduced species, augmenting the existing spectroscopic information in the literature and providing a series of diagnostic tools that may be used to help determine unknown ligand oxidation states in more complex systems.

2. The tools identified in Chapter 2 are subsequently evaluated for the two most common bipyridine isomers. It is acknowledged that strong π-backbonding from an electron rich metal to the π* orbital of bipyridine could lead to the same changes in bond metrics that are demonstrated by the alkali metal salts; however Wieghardt recently postulated that bipyridine may not actually be as good a π acceptor as is widely thought,[13–15] and questioned the relative magnitudes of donation versus reduction. Chapter 3 details the synthesis of a homologous series of top row transition metal complexes of the form M(2,2´-bipy)(mes)$_2$(M = Cr, Mn, Fe, Co, Ni; mes = 2,4,6-$Me_3C_6H_2$), together with their singly reduced analogues, all of which have been crystallographically, magnetically and spectroscopically characterised. The results are discussed both with reference to the usefulness of the diagnostic tools of Chapter 2, but also with regards to trends within the series. In particular this permits discussion of the magnitude of π-backbonding and the validity of using single crystal X-ray diffraction as a guide

to ligand oxidation state. Chapter 4 details the synthesis and characterisation of three isostructural complexes of the form $[(mes)_2Zn\text{-}(4,4'\text{-bipy})\text{-}Zn(mes)_2]^{n-}$ (n = 0, 1, 2), representing the first structurally characterised complexes of the 4,4´-bipyridyl radical anion and dianion. Comparisons are made between the data for these species and the alkali metal salts of Chapter 2 and the validity of the diagnostic tests based on the latter are verified.

## 1.8 References


[1] Sykes, A.; Constable, E. C. *Homoleptic Complexes of 2,2'-Bipyridine*; Academic Press Limited: London, 1989; Vol. 34.

[2] Kaes, C.; Katz, A.; Hosseini, M. W. *Chem. Rev.* **2000**, *100*, 3553.

[3] Wilkinson, G.; Gillard, R. D.; McCleverty, J. A.; Reedijk, J. *Heterocyclic Nitrogen-donor Ligands in Comprehensive Coordination Chemistry: The Synthesis, Reactions, Properties and Applications of Coordination Compounds*; Pergamon Press: Oxford, U.K., 1987; Vol. 2.

[4] James, S. L. *Chem. Soc. Rev.* **2003**, *32*, 276.

[5] Rosi, N. L.; Eddaoudi, M.; Kim, J.; O'Keeffe, M.; Yaghi, O. M. *CrystEngComm* **2002**, 401.

[6] *Numbers taken from the Cambridge Structural Database (CSD) Version 5.33 Update 2*; Feb 2012.

[7] Schumacher, J. N.; Green, C. R.; Best, F. W.; Newell, M. P. *J. Agric. Food. Chem.* **1977**, *25*, 310.

[8] Foder, G. B.; Colasanti, B. *Alkaloids: Chemical and Biological Perspectives*; Pelletier, S. W., Ed.; Wiley: New York, 1985; Vol. 3.

[9] Ma, J. C.; Dougherty, D. A. *Chem. Rev.* **1997**, *97*, 1303.

[10] Bickelhaupt, F. M.; Solà, M.; Fonseca Guerra, C. *J. Chem. Theory Comput.* **2006**, *2*, 965.

[11] Dieck, H. T.; Franz, K.-D.; Hohmann, F. *Ber.* **1975**, *108*, 163.

[12] Leyssens, T.; Peeters, D.; Orpen, A. G.; Harvey, J. N. *Organometallics* **2007**, *26*, 2637.

[13] Scarborough, C. C.; Wieghardt, K. *Inorg. Chem.* **2011**, *50*, 9773.

[14] Scarborough, C. C.; Sproules, S.; Weyhermuller, T.; DeBeer, S.; Wieghardt, K. *Inorg. Chem.* **2011**, *50*, 12446.

[15] Bowman, A. C.; Sproules, S.; Wieghardt, K. *Inorg. Chem.* **2012**, *51*, 3707.

[16] Zahlan, A.; Heineken, F. W.; Bruin, M.; Bruin, F. *J. Chem. Phys.* **1962**, *37*, 683.

[17] Carrington, A.; dos Santosveiga, J. *Mol. Phys.* **1962**, *5*, 21.

[18] Saito, Y.; Takemoto, J.; B, H.; Nakamoto, K. *Inorg. Chem.* **1972**, *11*, 2003.

[19] Kawashima, H.; Kato, T.; Shida, T. *J. Raman Spectrosc.* **1991**, *22*, 187.

[20] Castella-Ventura, M.; Kassab, E.; Buntinx, G.; Poizat, O. *PCCP* **2000**, *2*, 4682.

[21] Danzer, G. D.; Golus, J. A.; Strommen, D. P.; Kincaid, J. R. *J. Raman Spectrosc.* **1990**, *21*, 3.

[22] Bradley, P. G.; Kress, N.; Hornberger, B. A.; Dallinger, R. F.; Woodruff, W. H. *J. Am. Chem. Soc.* **1981**, *103*, 7441.

[23] Oe, S.; Fukushima, K. *J. Mol. Struct.* **1990**, *223*, 337.

[24] Kihara, H.; Gondo, Y. *J. Raman Spectrosc.* **1986**, *17*, 263.

[25] Konig, E.; Herzog, S. *J. Inorg. Nucl. Chem.* **1970**, *32*, 585.

[26] Mahon, C.; Reynolds, W. L. *Inorg. Chem.* **1967**, *6*, 1927.

[27] Konig, E.; Kremer, S. *Chem. Phys. Lett.* **1970**, *5*, 87.

[28] Veiga, J. D. S.; Reynolds, W. L.; Bolton, J. R. *J. Chem. Phys.* **1966**, *44*, 2214.

[29] Henning, J. C. M. *J. Chem. Phys.* **1966**, *44*, 2139.

[30] Van Voorst, J. D. W.; Zijlstra, W. G.; Sitters, R. *Chem. Phys. Lett.* **1967**, *1*, 321.

[31] Konig, E.; Fischer, H. *Z. Naturforsch. A.* **1962**, *A 17*, 1063.

[32] Kaim, W. *Ber.* **1981**, *114*, 3789.

[33] Brown, O. R.; Butterfield, R. J. *Electrochim. Acta* **1982**, *27*, 321.

[34] Ne, T.; Re, H.; Bard, A. J. *J. Am. Chem. Soc.* **1973**, *95*, 6582.

[35] Yang, L.; Wimmer, F. L.; Wimmer, S.; Zhao, J. X.; Braterman, P. S. *J. Organomet. Chem.* **1996**, *525*, 1.

[36] Braterman, P. S.; Song, J. I. *J. Org. Chem.* **1991**, *56*, 4678.

[37] Kalyanaraman, V.; Rao, C. N. R.; George, M. V. *J. Chem. Soc. B* **1971**, 2406.

[38] Roullier, L.; Laviron, E. *Electrochim. Acta* **1978**, *23*, 773.

[39] Ould-Moussa, L.; Poizat, O.; Castella-Ventura, M.; Buntinx, G.; Kassab, E. *J. Phys. Chem.* **1996**, *100*, 2072.

[40] Castella-Ventura, M.; Kassab, E. *J. Raman Spectrosc.* **1998**, *29*, 511.

[41] Diez, R. P.; Jubert, A. H.; Ottavianelli, E. *J. Mol. Struct.* **1993**, *106*, 241.

[42] McNaught, A. D.; Wilkinson, A. *IUPAC. Compendium of Chemical Terminology (the "Gold Book").*, 2nd ed.; Blackwell Scientific Publications, Oxford, 1997.

[43] Parkin, G. *J. Chem. Educ.* **2006**, *83*, 791.

[44] Resta, R. *Nature* **2008**, *453*, 735.

[45] Jansen, M.; Wedig, U. *Angew. Chem. Int. Ed.* **2008**, *47*, 10026.

[46] Aullón, G.; Alvarez, S. *Theor. Chem. Acc.* **2009**, *123*, 67.

[47] Chaudhuri, P.; Verani, C. N.; Bill, E.; Bothe, E.; Weyhermüller, T.; Wieghardt, K. *J. Am. Chem. Soc.* **2001**, *123*, 2213.

[48] Jørgensen, C. K. *Coord. Chem. Rev.* **1966**, *1*, 164.

[49] Wiberg, N.; Holleman, A.; Wiberg, E. *Inorganic Chemistry*; Academic Press Inc, 2001.

[50] Wanat, A.; Schneppensieper, T.; Stochel, G.; van Eldik, R.; Bill, E.; Wieghardt, K. *Inorg. Chem.* **2002**, *41*, 4.

[51] Ward, M.; McCleverty, J. *J. Chem. Soc., Dalton Trans.* **2002**, 275.

[52] Kaupp, M.; von Schnering, H. G. *Angew. Chem. Int. Ed. Engl.* **1995**, *34*, 986.

[53] Cloke, F. G. N.; Hanson, G. R.; Henderson, M. J.; Hitchcock, P. B.; Raston, C. L. *J. Chem. Soc., Chem. Commun.* **1989**, 1002.

[54] Henderson, M. J.; Kennard, C. H. L.; Raston, C. L.; Smith, G. *J. Chem. Soc., Chem. Commun.* **1990**, 1203.

[55] Cloke, F. G. N.; Dalby, C. I.; Henderson, M. J.; Hitchcock, P. B.; Kennard, C. H. L.; Lamb, R. N.; Raston, C. L. *J. Chem. Soc., Chem. Commun.* **1990**, 1394.

[56] Kaim, W.; Matheis, W. *J. Chem. Soc., Chem. Commun.* **1991**, 597.

[57] Hawecker, J.; Lehn, J.-M.; Ziessel, R. *J. Chem. Soc., Chem. Commun.* **1983**, 536.

[58] Kaim, W.; Kohlmann, S. *Chem. Phys. Lett.* **1987**, *139*, 365.

[59] Masood, M. A.; Zacharias, P. S. *J. Chem. Soc., Dalton Trans.* **1991**, 111.

[60] Stang, P. *Chem. Eur. J.* **1998**, *4*, 19.

[61] Gütlich, P.; Bill, E.; Trautwein, A. X. *Mössbauer Spectroscopy and Transition Metal Chemistry: Fundamentals and Applications*, 1st ed.; Springer Berlin Heidelberg, 2011.

[62] Balch, A. L. *J. Am. Chem. Soc.* **1973**, *95*, 2723.

[63] Kaim, W. *Coord. Chem. Rev.* **1987**, *76*, 187.

[64] Griffith, W. P. *Transition Met. Chem.* **1993**, *18*, 250.

[65] Pierpont, C. G.; Lange, C. W. *Progress in Inorganic Chemistry*; John Wiley & Sons Inc: Pierpont, Cg, Univ Colorado, Dept Chem & Biochem, Boulder, Co 80309 Usa., 1994; Vol. 41, p 331.

[66] Carugo, O.; Djinovic, K.; Rizzi, M.; Castellani, C. B. *J. Chem. Soc., Dalton Trans.* **1991**, 1551.

[67] Pierpont, C. G. *Coord. Chem. Rev.* **2001**, *216*, 99.

[68] Bhattacharya, S.; Gupta, P.; Basuli, F.; Pierpont, C. G. *Inorg. Chem.* **2002**, *41*, 5810.

[69] Kaim, W.; Fiedler, J. *Chem. Soc. Rev.* **2009**, *38*, 3373.

[70] Butin, K. P.; Beloglazkina, E. K.; Zyk, N. V. *Russ. Chem. Rev.* **2005**, *74*, 531.

[71] Kaim, W.; Schwederski, B. *Coord. Chem. Rev.* **2010**, *254*, 1580.

[72] Kaim, W. *Inorg. Chem.* **2011**, *50*, 9752.

[73] Lyaskovskyy, V.; de Bruin, B. *ACS Catalysis* **2012**, *2*, 270.

[74] Kaim, W. *Eur. J. Inorg. Chem.* **2012**, 343.

[75] Enemark, J.; Feltham, R. *Coord. Chem. Rev.* **1974**, *13*, 339.

[76] Murad, F. *Angew. Chem. Int. Ed.* **1999**, *38*, 1856.

[77] Praneeth, V. K. K.; Paulat, F.; Berto, T. C.; George, S. D.; Näther, C.; Sulok, C. D.; Lehnert, N. *J. Am. Chem. Soc.* **2008**, *130*, 15288.

[78] Schaefer, W. P. *Inorg. Chem.* **1968**, *7*, 725.

[79] Marsh, R. E.; Schaefer, W. P. *Acta Crystallogr. Sect. B - Struct. Sci.* **1968**, *24*, 246.

[80] Schmidt, S.; Heinemann, F. W.; Grohmann, A. *Eur. J. Inorg. Chem.* **2000**, *2000*, 1657.

[81] Cramer, C. J.; Tolman, W. B. *Acc. Chem. Res.* **2007**, *40*, 601.

[82] Pauling, L.; Weiss, J. *Nature* **1964**, *203*, 182.

[83] Weiss, J. *Nature* **1964**, *202*, 83.

[84] Chen, H.; Ikeda-Saito, M.; Shaik, S. *J. Am. Chem. Soc.* **2008**, *130*, 14778.

[85] Fabre, M.; Jaud, J.; Hliwa, M.; Launay, J.-P.; Bonvoisin, J. *Inorg. Chem.* **2006**, *45*, 9332.

[86] Spikes, G. H.; Milsmann, C.; Bill, E.; Weyhermüller, T.; Wieghardt, K. *Inorg. Chem.* **2008**, *47*, 11745.

[87] Ghosh, M.; Sproules, S.; Weyhermüller, T.; Wieghardt, K. *Inorg. Chem.* **2008**, *47*, 5963.

[88] Lu, C. C.; Bill, E.; Weyhermüller, T.; Bothe, E.; Wieghardt, K. *Inorg. Chem.* **2007**, *46*, 7880.

[89] de Bruin, B.; Bill, E.; Bothe, E.; Weyhermuller, T.; Wieghardt, K. *Inorg. Chem.* **2000**, *39*, 2936.

[90] Dutta, S. K.; Beckmann, U.; Bill, E.; Weyhermuller, T.; Wieghardt, K. *Inorg. Chem.* **2000**, *39*, 3355.

[91] Chłopek, K.; Bill, E.; Weyhermüller, T.; Wieghardt, K. *Inorg. Chem.* **2005**, *44*, 7087.

[92] Blanchard, S.; Neese, F.; Bothe, E.; Bill, E.; Weyhermuller, T.; Wieghardt, K. *Inorg. Chem.* **2005**, *44*, 3636.

[93] Mealli, C.; Ienco, A.; Phillips, A. D.; Galindo, A. *Eur. J. Inorg. Chem.* **2007**, *2007*, 2556.

[94] Muresan, N.; Chlopek, K.; Weyhermuller, T.; Neese, F.; Wieghardt, K. *Inorg. Chem.* **2007**, *46*, 5327.

[95] Muresan, N.; Weyhermuller, T.; Wieghardt, K. *Dalton Trans.* **2007**, 4390.

[96] Wang, K.; Stiefel, E. I. *Science* **2001**, *291*, 106.

[97] Harrison, D. J.; Nguyen, N.; Lough, A. J.; Fekl, U. *J. Am. Chem. Soc.* **2006**, *128*, 11026.

[98] Kapre, R.; Ray, K.; Sylvestre, I.; Weyhermueller, T.; George, S. D.; Neese, F.; Wieghardt, K. *Inorg. Chem.* **2006**, *45*, 3499.

[99] Kapre, R.; Bothe, E.; Weyhermuller, T.; George, S. D.; Wieghardt, K. *Inorg. Chem.* **2007**, *46*, 5642.

[100] Tunney, J.; McMaster, J.; Garner, C. *Comprehensive Coordination Chemistry II*; McCleverty, J.; Meyer, T., Eds.; Elsevier-Pergamon, Oxford, 2004; Vol. 8, p 459.

[101] Ray, K.; Weyhermüller, T.; Neese, F.; Wieghardt, K. *Inorg. Chem.* **2005**, *44*, 5345.

[102] Lu, C. C.; Bill, E.; Weyhermueller, T.; Bothe, E.; Wieghardt, K. *J. Am. Chem. Soc.* **2008**, *130*, 3181.

[103] Wile, B. M.; Trovitch, R. J.; Bart, S. C.; Tondreau, A. M.; Lobkovsky, E.; Milsmann, C.; Bill, E.; Wieghardt, K.; Chirik, P. J. *Inorg. Chem.* **2009**, *48*, 4190.

[104] Verani, C. N.; Gallert, S.; Bill, E.; Weyhermuller, T.; Wieghardt, K.; Chaudhuri, P. *Chem. Commun.* **1999**, 1747.

[105] Chun, H.; Weyhermuller, T.; Bill, E.; Wieghardt, K. *Angew. Chem. Int. Ed.* **2001**, *40*, 2489.

[106] Chun, H.; Verani, C. N.; Chaudhuri, P.; Bothe, E.; Bill, E.; Weyhermüller, T.; Wieghardt, K. *Inorg. Chem.* **2001**, *40*, 4157.

[107] Bachler, V.; Olbrich, G.; Neese, F.; Wieghardt, K. *Inorg. Chem.* **2002**, *41*, 4179.

[108] Min, K. S.; Weyhermuller, T.; Wieghardt, K. *Dalton Trans.* **2003**, 1126.

[109] Kokatam, S.; Weyhermuller, T.; Bothe, E.; Chaudhuri, P.; Wieghardt, K. *Inorg. Chem.* **2005**, *44*, 3709.

[110] Haneline, M. R.; Heyduk, A. F. *J. Am. Chem. Soc.* **2006**, *128*, 8410.

[111] Ghosh, P.; Begum, A.; Bill, E.; Weyhermuller, T.; Wieghardt, K. *Inorg. Chem.* **2003**, *42*, 3208.

[112] Ghosh, P.; Begum, A.; Herebian, D.; Bothe, E.; Hildenbrand, K.; Weyhermuller, T.; Wieghardt, K. *Angew. Chem. Int. Ed.* **2003**, *42*, 563.

[113] Ghosh, P.; Bill, E.; Weyhermuller, T.; Wieghardt, K. *J. Am. Chem. Soc.* **2003**, *125*, 3967.

[114] Blackmore, K. J.; Lal, N.; Ziller, J. W.; Heyduk, A. F. *J. Am. Chem. Soc.* **2008**, *130*, 2728.

[115] Kaim, W. *Coord. Chem. Rev.* **2001**, *219-221*, 463.

[116] Albini, A.; Kisch, H. In *Theoretical Inorganic Chemistry II*; Topics in Current Chemistry, Vol. 65; Springer Berlin / Heidelberg, 1976; p 105.

[117] Kisch, H.; Holzmeier, P.; Stone, F.; West, R., Eds.; Advances in Organometallic Chemistry, Vol. 34; Academic Press, 1992; p 67.

[118] Sellmann, D.; Fürsattel, A. *Angew. Chem. Int. Ed.* **1999**, *38*, 2023.

[119] Kurosawa, M.; Nankawa, T.; Matsuda, T.; Kubo, K.; Kurihara, M.; Nishihara, H. *Inorg. Chem.* **1999**, *38*, 5113.

[120] Doslik, N.; Sixt, T.; Kaim, W. *Angew. Chem. Int. Ed.* **1998**, *37*, 2403.

[121] Kaim, W.; Kohlmann, S.; Jordanov, J.; Fenske, D. *Z. Anorg. Allg. Chem.* **1991**, *598*, 217.

[122] Peover, M. E. *Trans. Faraday Soc.* **1962**, *58*, 2370.

[123] Kaim, W.; Moscherosch, M. *Coord. Chem. Rev.* **1994**, *129*, 157.

[124] Ferraris, J.; Cowan, D. O.; Walatka, V.; Perlstein, J. H. *J. Am. Chem. Soc.* **1973**, *95*, 948.

[125] Frere, P.; Skabara, P. J. *Chem. Soc. Rev.* **2005**, *34*, 69–98.

[126] Kirtley, J. R.; Mannhart, J. *Nat. Mater.* **2008**, *7*, 520.

[127] Hanack, M.; Lange, A.; Grosshans, R. *Synth. Met.* **1991**, *45*, 59.

[128] Hanack, M.; Gul, A.; Subramanian, L. R. *Inorg. Chem.* **1992**, *31*, 1542.

[129] Hanack, M.; Polley, R. *Inorg. Chem.* **1994**, *33*, 3201.

[130] Pohmer, J.; Hanack, M.; Barcina, J. O. *J. Mater. Chem.* **1996**, *6*, 957.

[131] Stuzhin, P. A.; Vagin, S. I.; Hanack, M. *Inorg. Chem.* **1998**, *37*, 2655.

[132] Li, Z.; Ding, J.; Song, N.; Lu, J.; Tao, Y. *J. Am. Chem. Soc.* **2010**, *132*, 13160.

[133] Kaim, W. *Coord. Chem. Rev.* **2002**, *230*, 127.

[134] Glöckle, M.; Hübler, K.; Kümmerer, H.-J.; Denninger, G.; Kaim, W. *Inorg. Chem.* **2001**, *40*, 2263.

[135] Ishikita, H.; Morra, G.; Knapp, E.-W. *Biochemistry* **2003**, *42*, 3882.

[136] Furie, B.; Bouchard, B. A.; Furie, B. C. *Blood* **1999**, *93*, 1798.

[137] Sadler, G. G.; Gordon, N. R. *Inorg. Chim. Acta* **1991**, *180*, 271.

[138] He, M.; Sheldon, P. J.; Sherman, D. H. *PNAS* **2001**, *98*, 926.

[139] Arreguin, S.; Nelson, P.; Padway, S.; Shirazi, M.; Pierpont, C. *J. Inorg. Biochem.* **2009**, *103*, 87.

[140] Borowski, T.; Siegbahn, P. E. M. *J. Am. Chem. Soc.* **2006**, *128*, 12941.

[141] Pau, M. Y. M.; Davis, M. I.; Orville, A. M.; Lipscomb, J. D.; Solomon, E. I. *J. Am. Chem. Soc.* **2007**, *129*, 1944.

[142] Bugg, T. D.; Ramaswamy, S. *Curr. Opin. Chem. Biol.* **2008**, *12*, 134.

[143] Brazeau, B. J.; Johnson, B. J.; Wilmot, C. M. *Arch. Biochem. Biophys.* **2004**, *428*, 22.

[144] Dooley, D. M.; McGuirl, M. A.; Brown, D. E.; Turowski, P. N.; Mclntire, W. S.; Knowles, P. F. *Nature* **1991**, *349*, 262.

[145] Guengerich, F. P. *Chem. Res. Toxicol.* **2008**, *21*, 70.

[146] Newcomb, M.; Le Tadic-Biadatti, M.-H.; Chestney, D. L.; Roberts, E. S.; Hollenberg, P. F. *J. Am. Chem. Soc.* **1995**, *117*, 12085.

[147] Harris, N.; Cohen, S.; Filatov, M.; Ogliaro, F.; Shaik, S. *Angew. Chem. Int. Ed.* **2000**, *39*, 2003.

[148] Hackett, J. C.; Brueggemeier, R. W.; Hadad, C. M. *J. Am. Chem. Soc.* **2005**, *127*, 5224.

[149] He, X.; de Montellano, P. R. O. *J. Biol. Chem.* **2004**, *279*, 39479.

[150] Auclair, K.; Hu, Z.; Little, D. M.; Ortiz de Montellano, P. R.; Groves, J. T. *J. Am. Chem. Soc.* **2002**, *124*, 6020.

[151] Chirik, P. J.; Wieghardt, K. *Science* **2010**, *327*, 794.

[152] Bouwkamp, M. W.; Bowman, A. C.; Lobkovsky, E.; Chirik, P. J. *J. Am. Chem. Soc.* **2006**, *128*, 13340.

[153] Benson, E. E.; Kubiak, C. P. *Chem. Commun.* **2012**, *48*, 7374.

[154] Chisholm, M. H.; Huffman, J. C.; Rothwell, I. P.; Bradley, P. G.; Kress, N.; Woodruff, W. H. *J. Am. Chem. Soc.* **1981**, *103*, 4945.

[155] Gore-Randall, E.; Irwin, M.; Denning, M. S.; Goicoechea, J. M. *Inorg. Chem.* **2009**, *48*, 8304.

[156] Morancho, R.; Pouvreau, P.; Constant, G.; Jaud, J.; Galy, J. *J. Organomet. Chem.* **1979**, *166*, 329.

[157] Nikiforov, G. B.; Roesky, H. W.; Noltemeyer, M.; Schmidt, H. G. *Polyhedron* **2004**, *23*, 561.

[158] Mansell, S. M.; Adams, C. J.; Bramham, G.; Haddow, M. F.; Kaim, W.; Norman, N. C.; McGrady, J. E.; Russell, C. A.; Udeen, S. J. *Chem. Commun.* **2010**, *46*, 5070.

[159] Mansell, S. M.; Norman, N. C.; Russell, C. A. *Dalton Trans.* **2010**, *39*, 5084.

[160] Evans, W.; Drummond, D. *J. Am. Chem. Soc.* **1989**, *111*, 3329.

[161] Roitershtein, D.; Domingos, A.; Pereira, L. C. J.; Ascenso, J. R.; Marques, N. *Inorg. Chem.* **2003**, *42*, 7666.

[162] Schultz, M.; Boncella, J. M.; Berg, D. J.; Tilley, T. D.; Andersen, R. A. *Organometallics* **2002**, *21*, 460.

[163] Booth, C. H.; Walter, M. D.; Daniel, M.; Lukens, W. W.; Andersen, R. A. *Phys. Rev. Lett.* **2005**, *95*, 267202.

[164] Walter, M. D.; Berg, D. J.; Andersen, R. A. *Organometallics* **2006**, *25*, 3228.

[165] Booth, C. H.; Walter, M. D.; Kazhdan, D.; Hu, Y. J.; Lukens, W. W.; Bauer, E. D.; Maron, L.; Eisenstein, O.; Andersen, R. A. *J. Am. Chem. Soc.* **2009**, *131*, 6480.

[166] Del Piero, G. Z. A. B. G., G.; Perego *Cryst. Struct. Commun.* **1975**, *4*, 521.

[167] Mehdoui, T.; Berthet, J.-C.; Thuéry, P.; Salmon, L.; Rivière, E.; Ephritikhine, M. *Chem. Eur. J.* **2005**, *11*, 6994.

[168] Bart, S. C.; Heinemann, F. W.; Anthon, C.; Hauser, C.; Meyer, K. *Inorg. Chem.* **2009**, *48*, 9419.

[169] Takase, M. K.; Fang, M.; Ziller, J. W.; Furche, F.; Evans, W. J. *Inorg. Chim. Acta* **2010**, *364*, 167.

[170] Kraft, S. J.; Fanwick, P. E.; Bart, S. C. *Inorg. Chem.* **2010**, *49*, 1103.

[171] Ren, W.; Zi, G.; Walter, M. D. *Organometallics* **2012**, *31*, 672.

[172] Kaizu, Y.; Kobayashi, H. *Bull. Chem. Soc. Jpn.* **1970**, *43*, 2492.

[173] Kaizu, Y.; Kobayashi, H. *Bull. Chem. Soc. Jpn.* **1972**, *45*, 470.

[174] Vlcek, A.; Baumann, F.; Kaim, W.; Grevels, F.; Hartl, F. *J. Chem. Soc., Dalton Trans.* **1998**, 215.

[175] Zalis, S.; Daniel, C.; Vlcek, A. *J. Chem. Soc., Dalton Trans.* **1999**, 3081.

[176] Lenges, C. P.; White, P. S.; Marshall, W. J.; Brookhart, M. *Organometallics* **2000**, *19*, 1247.

[177] Mork, B. V.; McMillan, A.; Yuen, H.; Tilley, T. D. *Organometallics* **2004**, *23*, 2855.

[178] Kraft, S.; Hanuschek, E.; Beckhaus, R.; Haase, D.; Saak, W. *Chem. Eur. J.* **2005**, *11*, 969.

[179] Denning, M. S.; Irwin, M.; Goicoechea, J. M. *Inorg. Chem.* **2008**, *47*, 6118.

[180] Kong, X.-J.; Ren, Y.-P.; Zheng, P.-Q.; Long, Y.-X.; Long, L.-S.; Huang, R.-B.; Zheng, L.-S. *Inorg. Chem.* **2006**, *45*, 10702.

[181] Femoni, C.; Iapalucci, M.; Longoni, G.; Tiozzo, C.; Wolowska, J.; Zacchini, S.; Zazzaroni, E. *Chem. Eur. J.* **2007**, *13*, 6544.

[182] Dinolfo, P. H.; Williams, M. E.; Stern, C. L.; Hupp, J. T. *J. Am. Chem. Soc.* **2004**, *126*, 12989.

[183] Dinolfo, P. H.; Hupp, J. T. *J. Am. Chem. Soc.* **2004**, *126*, 16814.

[184] Bhattacharya, D.; Sathiyendiran, M.; Luo, T. T.; Chang, C. H.; Cheng, Y. H.; Lin, C. Y.; Lee, G. H.; Peng, S. M.; Lu, K. L. *Inorg. Chem.* **2009**, *48*, 3731.

[185] Kruszynski, R.; Bartczak, T. J.; Adamczyk, A.; Czakis-Sulikowska, D.; Kałużna, J. *Acta Crystallogr. Sect. E* **2001**, *57*, m183.

[186] Khlobystov, A. N.; Brett, M. T.; Blake, A. J.; Champness, N. R.; Gill, P. M. W.; O'Neill, D. P.; Teat, S. J.; Wilson, C.; Schröder, M. *J. Am. Chem. Soc.* **2003**, *125*, 6753.

[187] Tong, M.-L.; Chen, X.-M.; Ye, B.-H.; Ng, S. W. *Inorg. Chem.* **1998**, *37*, 5278.

# Chapter 2

# Alkali Metal Salts of Bipyridine Radical Anions and Dianions

## 2.1 Introduction

The 2,2´- and 4,4´- isomers of bipyridine (bipy) are among the most ubiquitous ligands in coordination chemistry. As discussed in the introduction, when complexed to transition metals their capacity to act as non-innocent ligands can make the precise determination of metal and ligand oxidation states extremely challenging. The earliest evidence for the existence of reduced forms of bipyridine was published 50 years ago, when Carrington used electron paramagnetic resonance (EPR) spectroscopy to examine the radicals produced by addition of alkali metals to pyridine.[1] Subsequently, multiple authors have used a variety of techniques to spectroscopically characterise the radical anions and, to a lesser extent, the dianions that make up the bipyridine reduction products. Published data includes IR,[2] Raman,[3–8] UV-vis,[9–11] and EPR spectroscopic data,[12–17] as well as electrochemical and computational studies.[18–26] For the 2,2´-bipy isomer in particular, structural measurements of the reduced species have also been reported.[27–30]

| | Neutral 2,2´-Bipyridine | 2,2´-Bipyridyl Radical Monoanion |
|---|---|---|
| Ring deformation mode: 900 – 1000 $cm^{-1}$ | No bands | strong: 950 $cm^{-1}$ |
| C=C, C=N stretching: 1490 – 1650 $cm^{-1}$ | strong: 1600 – 1610 $cm^{-1}$ | multiple strong bands: 1490 – 1575 $cm^{-1}$ |

Table 2.1: Diagnostic peaks in the IR spectrum for determining the oxidation state of 2,2´-bipyridine.[2]

| Half equation: | Standard potential: |
|---|---|
| stilbene + $e^-$ → [stilbene]$^{\bullet-}$ | –2.21 V |
| biphenyl + $e^-$ → [biphenyl]$^{\bullet-}$ | –2.60 V |
| styrene + $e^-$ → [styrene]$^{\bullet-}$ | –2.65 V |

Table 2.2: Standard electrode potentials (E°) for selected aromatic compounds.[31]

Distinguishing between the different oxidation states of bipyridine is important, particularly in situations where bipy ligands are complexed to metal centres that themselves are capable of existing in multiple oxidation states. Perhaps the most widely cited attempt to provide a diagnostic tool for the identification of the oxidation state of a bipy moiety is a paper by Nakamoto and co-workers, where the authors describe infrared (IR) absorption bands that can be used to distinguish the different oxidation states of 2,2´-bipyridine.[2] The results from this paper are summarised in Table 2.1.

Most of the samples that have been reported are generated *in situ* by the use of alkali metals. The use of the group 1 metals to reduce similar systems is well known and Table 2.2 shows several examples of related organic systems together with their electrode potentials. One interesting conclusion from the electrochemical measurements of the bipyridine isomers is that while alkali metals are able to drive the formation of the radical monoanionic species, a second reduction is also accessible, to yield bipyridyl dianions, as shown in Tables 2.3 and 2.4.

As a result of this, an early project aim was to synthesise and structurally characterise a series of alkali metal salts of the 2,2´-, 2,4´- and 4,4´-bipyridine reduction

| Half equation: | Standard potential |
|---|---|
| $Na^+ + e^- \rightarrow Na$ | –2.71 V |
| $K^+ + e^- \rightarrow K$ | –2.93 V |
| $Rb^+ + e^- \rightarrow Rb$ | –2.98 V |
| $Cs^+ + e^- \rightarrow Cs$ | –2.92 V |

Table 2.3: Standard electrode potentials (E°) for the alkali metals.[32]

| | 2,2´-bipyridine | 2,4´-bipyridine | 4,4´-bipyridine |
|---|---|---|---|
| bipy + $e^- \rightarrow$ bipy$^{\bullet-}$ | –1.47 V | –1.34 V | –1.17 V |
| bipy$^{\bullet-}$ + $e^- \rightarrow$ bipy$^{2-}$ | –1.88 V | –2.05 V | –1.66 V |

Table 2.4: Standard electrode potentials (E°) for the stepwise reduction of bipyridine isomers.[18,20,33] Data have been re-referenced to the SCE using literature values from Bratsch and Lagowski.

products to establish bond metric parameters that could be used as a tool to aid in the assignment of ligand oxidation state in less trivial complexes. A secondary aim was to extend the work of Nakamoto and provide a series of diagnostic IR and Raman bands that may be used to aid identification of the the oxidation state of the 2,4´- and 4,4´-bipy isomers.

## 2.2 General Synthesis

The same general synthetic approach was taken for the formation of all of the compounds described in this chapter. Approximately 100 mg of 2,2´-bipy, 2,4´-bipy or 4,4´-bipy were reacted with one or two equivalents of an alkali metal and stirred in ethylenediamine (en) for 14 hours in a capped sample vial in an inert atmosphere glovebox. During this time the colourless solutions acquired a deep purple colour consistent with the reduction of bipyridine. The solution was then filtered into a crystallisation ampoule through a Pasteur pipette containing packed glass wool at the constriction. Prior to use, the glass wool packed pipette was placed in an ampoule and heated under vacuum to remove all traces of air and moisture. The filtered solution was transferred in a sealed ampoule to a Schlenk line where it was layered with a suit-

able anti-solvent (benzene, toluene or diethylether as required, to induce the formation of crystals) and in some cases placed in a 8 – 10 °C fridge to further aid crystallisation. It is worth noting at this point that although the reduction of ethylenediamine by alkali metals to form the amide and hydrogen gas is thermodynamically favourable, it is kinetically very slow. Amide formation is readily apparent, as the typical deep purple reaction solutions become dark brown. This affords a window of opportunity in which the reduction of bipyridine may take place without reducing the reaction solvent. Whilst sodium and potassium reactions occurred largely without detectable solvent reduction, the reaction time available was found to substantially decrease with decreasing first ionisation energies of the group one metal used. Rubidium reactions often produced a small quantity of an amorphous brown precipitate whilst caesium would react with ethylenediamine almost immediately upon contact, as evidenced by the rapid evolution of hydrogen. Ethylenediamine was chosen as a solvent because of its ability to solvate electrons at room temperature, though due to the potential for solvent reduction, other alternatives were also examined. Dimethylformamide (DMF) was found to solvate electrons and caesium ions but reaction kinetics were slowed to the point that sample decomposition would frequently take place before reactions reached completion. Additionally, the hygroscopic nature of DMF made it difficult to remove water traces to the degree required for these reactions. Tetrahydrofuran (THF), while useful in the reactions detailed in subsequent chapters, also proved to have very slow reaction kinetics.

The bonding between bipyridyl moieties and alkali metal cations in the salts produced is predominantly ionic. Lattices are held together through electrostatic attractions between the positively charged metal cations and either the lone pairs on nitrogen atoms in a σ-type interaction, or the negatively charged π manifold of the bipyridyl anion via a π-type interaction.

## 2.3 2,2´-Bipyridine

Of the three most readily available isomers of bipyridine, the 2,2´- isomer is by far the most frequently studied because of its ability to chelate to metal centres.[34] This isomer has been extensively used in the field of coordination chemistry and the chemical literature contains a wealth of information about both the electrochemical and spectroscopic properties of the isolated ligand, as well as extensive characterisation for the vast number of complexes that it forms with metal centres. As noted in the introduction, the CSD structural database (at the time of writing) lists 6652 structures incorporating the ligand, a number greater than the combined entries for the other 5 isomers.[35]

### 2.3.1 2,2´-Bipyridyl Radical Anion

The reduction of 2,2´-bipyridine to form a radical species has been known for several decades.[36,37] Throughout this period it has been investigated using a variety of techniques: IR,[2] Raman,[3–6] UV-vis,[9–11] and electron paramagnetic resonance (EPR) spectroscopic data have been published,[12–17] typically from either *in situ* prepared salts or in coordination compounds. The electrochemical generation of the radical has also been explored.[18,19] However, closer inspection of published data often reveals contradictions, possibly as a result of the extreme air- and moisture-sensitivity of this species and the difficulties associated with its manipulation and isolation. In spite of the wealth of data available in the chemical literature, there is little structural data available for this species, particularly for 'charge-separated' compounds. While an alkali-metal salt of the 2,2´-bipy dianion has been reported,[27] no analogous structure is available for the radical monoanion. Lanthanide complexes where a bipyridine ligand is assigned a singly reduced radical state are known.[28,29] There are also several reports by Andersen and co-workers where critical magnetometry studies are used to

unequivocally prove the presence of a bipyridyl radical in $(Cp^*)_2Yb(2,2´\text{-bipy})$ ($Cp^* = C_5(CH_3)_5^-$).[38–40] Following the publication of the work described in this chapter, a boron complex containing a bipyridyl radical anion in $BCl_2(bipy)$ has also been documented, supported by EPR measurements and extensive DFT calculations.[30] Additionally, there are several transition metal complexes reported where bond metrics suggest the presence of a reduced bipyridine species but instead the structural distortion is explained in terms of extensive π-backbonding into the π* orbital on the ligand.[41–44] This is discussed in more detail in Chapter 1.

#### 2.3.1.1 Synthesis

K(2,2´-bipy)(en) (**1**) was prepared by the reaction of 2,2´-bipy with one equivalent of potassium metal in ethylenediamine. This yielded an intensely coloured purple solution from which dark-purple air- and moisture-sensitive crystals containing the 2,2´-bipyridyl radical anion, $2,2´\text{-bipy}^{\bullet-}$ were isolated four days after layering with toluene.

#### 2.3.1.2 Structural Characterisation

Two compositionally identical polymorphs of **1** were found to crystallise from en/toluene solutions: K(2,2´-bipy)(en) (**1a**) and $K_4(2,2´\text{-bipy})_4(en)_4$ (**1b**), both exhibiting similar bond metric parameters in the bipyridyl moiety. Phase **1b** appears to be the major product based upon visual analyses and single-crystal X-ray diffraction studies of multiple crystals. Some batches of the reaction products were found to only show evidence for the presence of **1b**. Although loss of crystallinity upon sample grinding prevented the collection of powder X-ray diffraction data in order to precisely determine polymorph ratios, bulk sample composition has been corroborated by elemental microanalysis. The minor phase, **1a**, consists of a single crystallographically unique potassium cation coordinated to a 2,2´-bipyridyl radical and an ethylenediamine

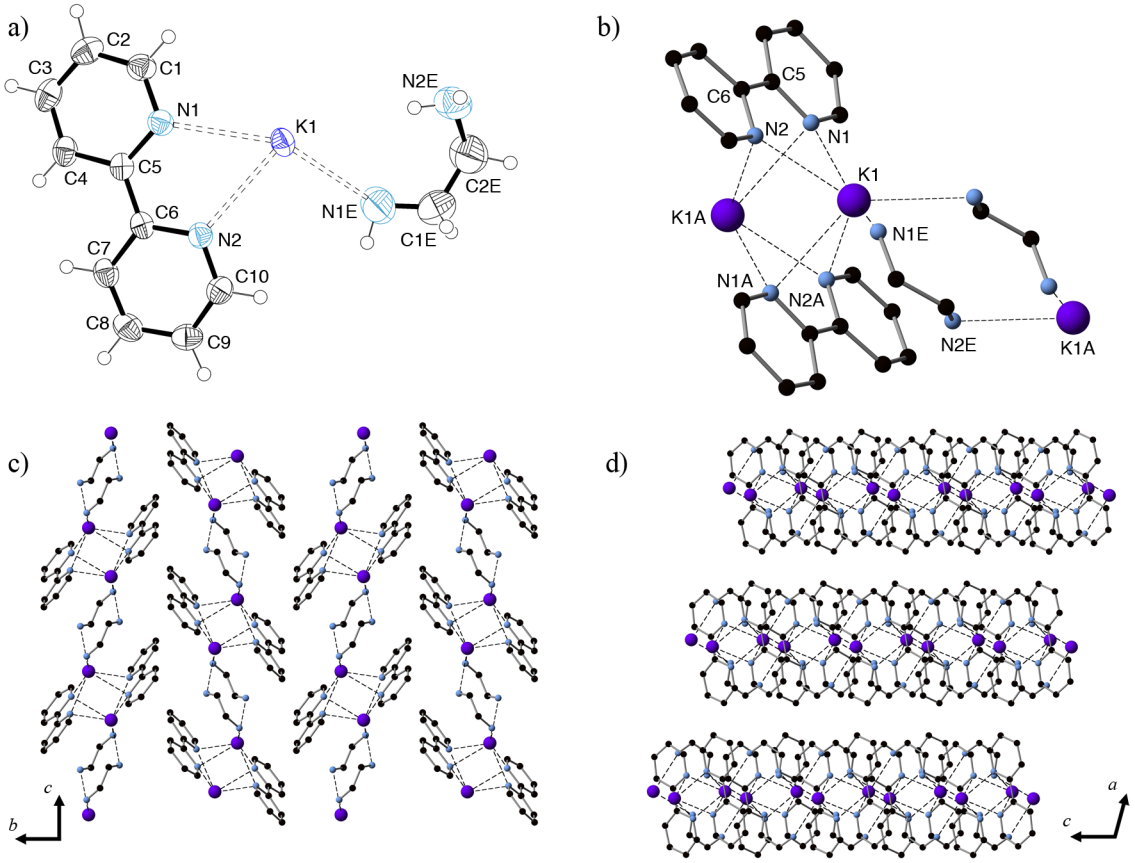



Figure 2.1: (**a**) Thermal ellipsoid representation of the atoms in the asymmetric unit of **1a**. Anisotropic displacement ellipsoids pictured at the 50% probability level. (**b**) Interactions within the asymmetric unit forming the one-dimensional chain-like structure. (**c**) Packing diagram viewed along the crystallographic *a* axis highlighting the absence of interactions between chains. (**d**) Packing diagram viewed along the crystallographic *b* axis. Note that in (b), (c) and (d), hydrogen atoms have been omitted for clarity.

molecule (Figure 2.1). The structure consists of dimeric units containing two potassium atoms bridged by two 2,2´-bipyridyl radical anions. Terminally bound ethylenediamine molecules bridge adjacent dimers giving rise to one-dimensional chains that run parallel to the unit cell *c* axis with no obvious inter-chain interactions present.

The nitrogen sites N1 and N2 interact with two potassium cations K1 and K1A (generated by symmetry). These have distances from K1 of 2.820(2) Å and 2.841(2) Å, respectively and as such may be considered as electrostatic interactions with the nitrogen lone pairs.[45] The equivalent distances to K1A are both 2.960(2) Å and

have a greater interaction with the π* SOMO due to the 'side-on' position of the potassium atom. This interaction appears to extend to C5 and C6, which also have relatively short contacts to K1A of 3.337(2) Å and 3.314(2) Å, respectively. Dimers are linked to adjacent units by bridging ethylenediamine molecules; the K1 to N1E distance is 2.851(3) Å at one dimer and the K1A to N2E distance at the linked dimer is 2.892(2) Å. As with the other structures discussed in this chapter, the ability of ethylenediamine to act both as a flexible linker and as a bidentate chelating ligand is crucial in the formation of the isolated crystalline structures and can give rise to the multiple polymorphs observed for some of these reaction products. Whilst there is much discussion in the literature of the effects of ether-based Lewis bases in the formation of alkali-metal networks,[46–49] the relative rarity of en-like solvents in such complexes has limited similar analysis.[50–54] Crystals of **1a** were found to crack when cooled below 200 K, attributed to strain caused by a phase transition.

The second and more commonly encountered polymorph, **1b**, has a more complex structure. The asymmetric unit contains four crystallographically unique potassium cations, four 2,2´-bipyridyl radical anions and four ethylenediamine linkers that serve to bridge adjacent tetramers (Figure 2.2). This gives rise to a two-dimensional sheet-like structure, with sheets in the crystallographic *ab* plane stacking along the *c* axis. This extended structure shows no obvious interaction between adjacent sheets.

Tetrameric units are held together by both 'end-on' and 'side-on' interactions between the potassium cations and the bipyridyl anions. Each potassium site is coordinated to one bipyridyl radical by two nitrogen lone pair interactions and to one or two additional bipyridyl anions via the π ring system. K1 is joined by two ethylenediamine linkers to K2 of an adjacent tetramer and K3 is joined by two ethylenediamine linkers to K4 of a different adjacent tetramer (distances are between 2.876(2) Å and 2.951(2) Å with mean distance 2.916 Å). These interactions form the two-dimensional sheets that stack together to generate the complete structure.

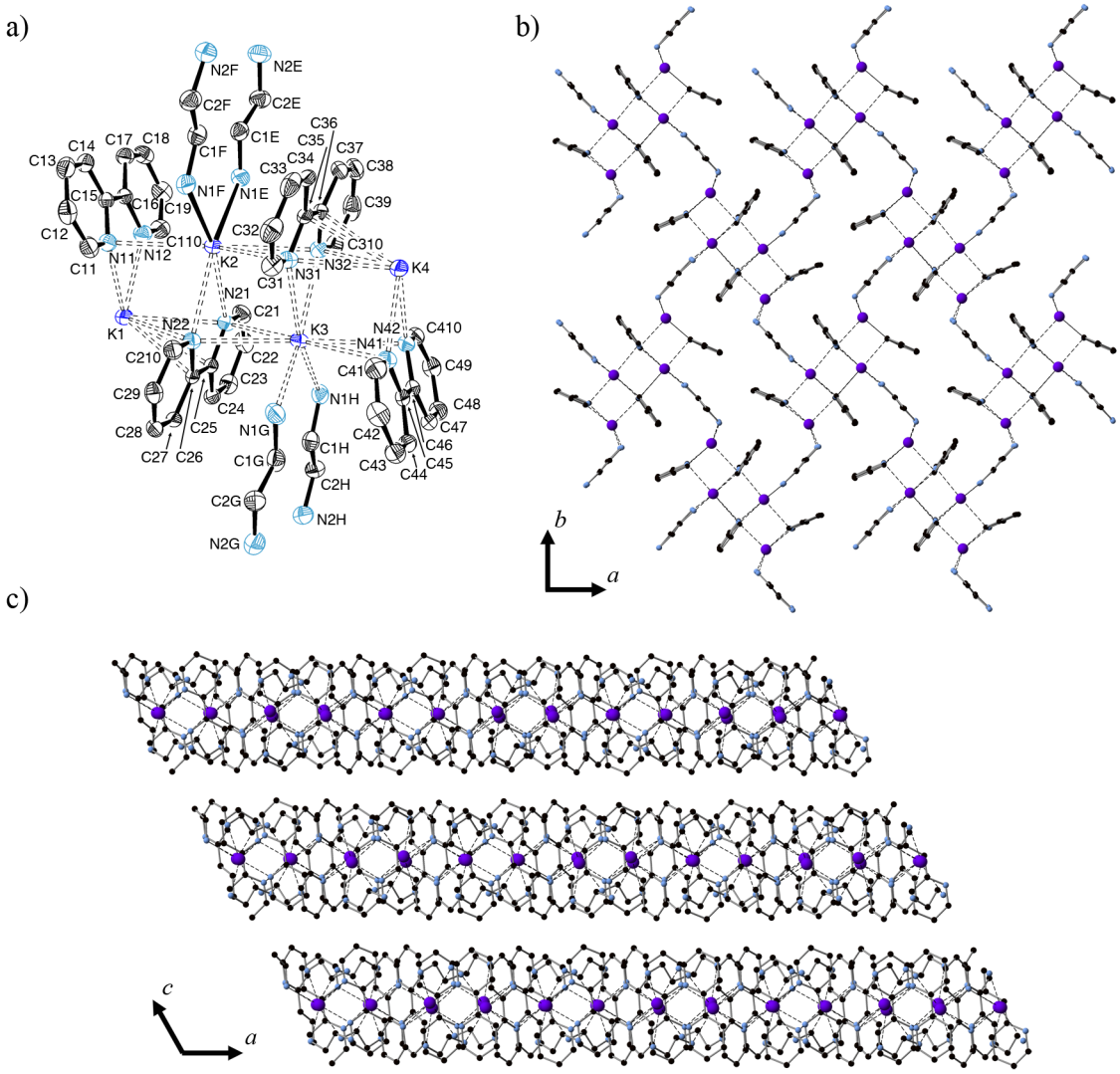



Figure 2.2: (**a**) Thermal ellipsoid representation of the atoms in the asymmetric unit of **1b**. Anisotropic displacement ellipsoids pictured at the 50% probability level. (**b**) The structure of a single sheet in the crystallographic *ab* plane. (**c**) View along the crystallographic *a* axis showing the lack of interaction between adjacent sheets. Note that hydrogen atoms are omitted for clarity.

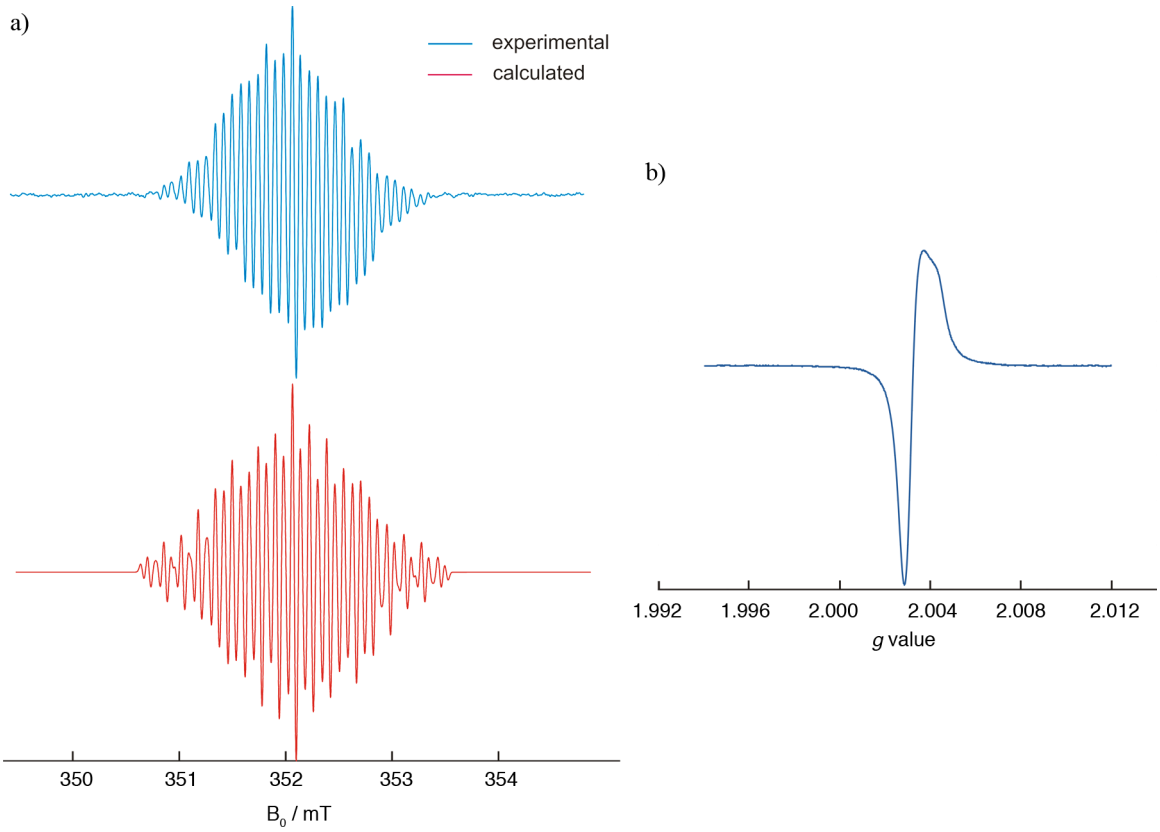
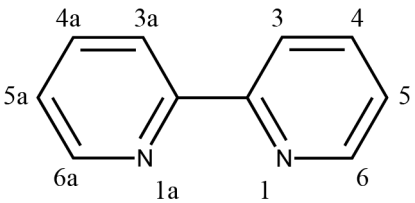



Figure 2.3: (**a**) Comparison of experimental and calculated solution-phase EPR spectra for **1**. (**b**) Solid state EPR spectrum for **1**.

#### 2.3.1.3 Spectroscopic Characterisation

*In situ* EPR measurements of sodium and lithium salt solutions containing 2,2´-bipyridyl radicals provided some of the first evidence of the existence of the radical anion,[12] owing to the technique's ability to measure responses from very low concentrations of paramagnetic compounds. Both solid and solution EPR measurements of **1** were used to test for and confirm the presence of the 2,2´-bipyridyl radical anion. Solution spectra reveal a resonance with a $g$ value of 2.0035 and significant hyperfine splitting from coupling of the unpaired electron with two $^{14}$N ($I = 1$) and eight $^{1}$H ($I = 1/2$) nuclear spins (Figure 2.3a). The $g$ value is very similar to that of a free electron ($g = 2.002319$) and is typical for an unpaired electron delocalised over an an aromatic system. DFT calculated isotopic Fermi contact coupling constants




| Sites: | DFT Calculated: | Least-Squares Fit: |
|---|---|---|
| 1, 1a | 8.74 | 9.03 |
| 3, 3a | –4.65 | –4.32 |
| 4, 4a | –0.98 | –1.77 |
| 5, 5a | –14.54 | –15.87 |
| 6, 6a | 2.42 | 0.32 |

Table 2.5: Comparison of DFT calculated and least-squares fitted hyperfine coupling constants for the solution EPR response of **1**. All frequencies are in MHz.

were found to compare well to those determined from least-squares fittings of the data (Table 2.5).[55] These values are also similar to those previously reported in the literature.[12–17]

EPR measurements of a solid sample of **1** show an asymmetric resonance centred on $g = 2.0033$, again close to the $g$ value of a free electron (Figure 2.3b). The anisotropy of the resonance may arise due to two possible effects:

1. The sample measured is a mixture of polymorphs **1a** and **1b**, each of which may give rise to slightly different resonances which partially overlap in the observed spectrum.

2. If **1b** is by far the major product as is believed, then differing parallel and perpendicular contributions to the $g$ value may arise due to the highly ordered crystal structure which causes the bipyridyl radicals to be stacked perpendicular to the $ab$ plane.

In either case the results are conclusive in showing the presence of the radical in both solution and solid states.

Outside of EPR, one of the most commonly used spectroscopic tools in the determination of bipyridine oxidation state is IR. While several papers on the subject have been published, the most detailed was reported by Nakamoto and co-workers, who describe a series of diagnostic regions in the IR spectrum that may be used to differentiate between neutral 2,2´-bipy and the reduced radical species in more complicated

coordination complexes.[2] The first region is between 900 and 1000 $cm^{-1}$ which shows no absorption bands when measuring neutral 2,2´-bipyridine. By contrast, compound **1** shows an absorption at 939 $cm^{-1}$ which is in good agreement with the value of 944 $cm^{-1}$ observed for Li(bipy)·$n$THF. This vibrational mode corresponds to a ring deformation. The second region Nakamoto identifies is the C=C and C=N stretching area between 1475 and 1625 $cm^{-1}$. Neutral species of 2,2´-bipyridine are expected to show a strong absorption band at around 1600 to 1610 $cm^{-1}$ while radical anions are predicted to exhibit medium or strong bands between 1490 and 1575 $cm^{-1}$. In the spectrum of **1** we observe two strong bands at 1495 and 1561 $cm^{-1}$ which are again in good agreement with the previously mentioned lithium salt, where these bands were observed at 1486 and 1554 $cm^{-1}$.[2,41]

### 2.3.2 2,2´-Bipyridyl Dianion

A two electron reduction of neutral 2,2´-bipyridine affords the dianionic species which was recently characterised crystallographically as alkali metal salts in three forms including the polymer $[(2,2´\text{-bipy})^{2-}(Na^{+}(dme))_2]_\infty$ (dme = dimethoxyethane).[27] Later in the same year an example of the dianion in the lanthanide complex (Yb(2,2´-bipy)$(THF)_2)_3$ was also reported.[56] The synthesis of an alkali metal salt containing the 2,2´-bipyidyl dianionic species was desired to allow for comparison of spectroscopic data with existing literature values, and to perform additional studies.

#### 2.3.2.1 Synthesis

$Rb_2$(2,2´-bipy)$(en)_2$ (**2**) was prepared by the reaction of 2,2´-bipy with two equivalents of rubidium metal in ethylenediamine. The resulting dark purple coloured solution yielded black-purple rod-like air- and moisture-sensitive crystals containing the 2,2´-bipyridyl dianion, 2,2´-bipy$^{2-}$, several days after layering with toluene.

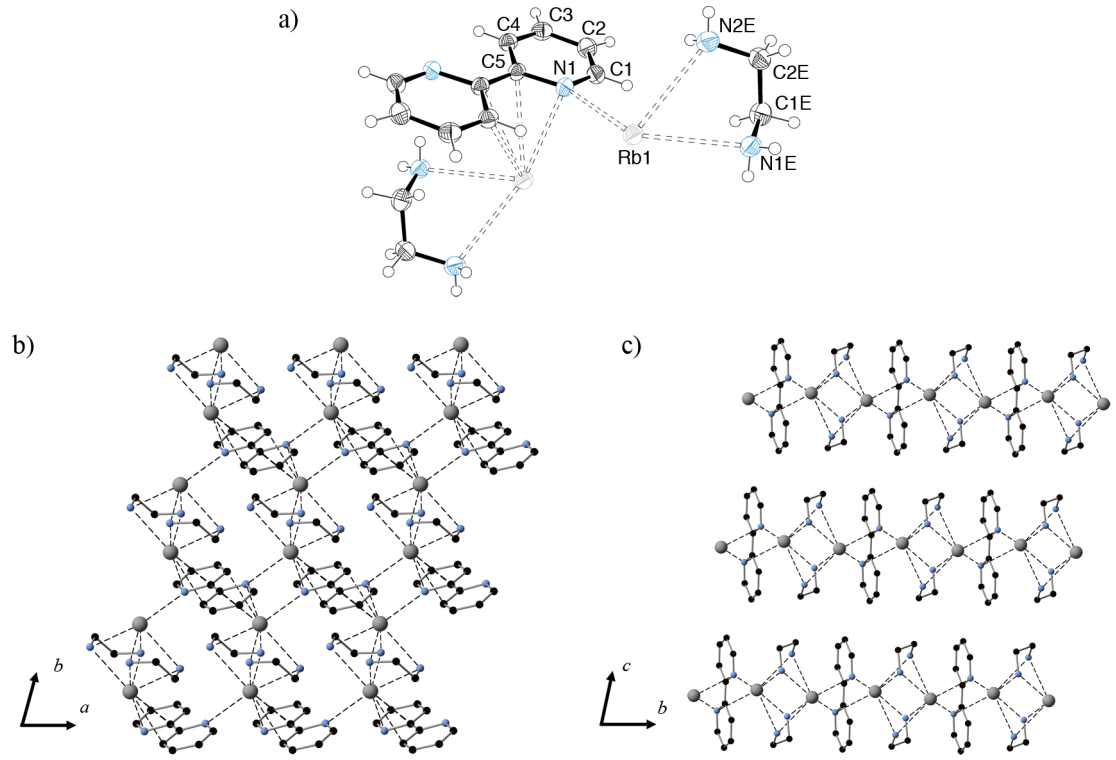



Figure 2.4: (**a**) Thermal ellipsoid representation of the atoms in the asymmetric unit of **2**. Anisotropic displacement ellipsoids pictured at the 50% probability level. (**b**) The structure of a single sheet running parallel to the *ab* plane. (**c**) Packing diagram viewed along the crystallographic *a* axis highlighting the absence of interactions between sheets. Note that in (b) and (c) hydrogen atoms have been omitted for clarity.

#### 2.3.2.2 Structural Characterisation

As mentioned at the start of this section, prior to this work the crystal structures of three sodium salts of the 2,2´-bipyridyl dianion had previously been published by Bock and co-workers, all of which resulted from direct reduction of bipyridine by the alkali metal.[27] The asymmetric unit of **2** contains a single rubidium cation, half a bipyridyl dianion and a single ethylenediamine molecule (Figure 2.4).

In all three structures published by Bock and co-workers, the bipyridyl dianion adopts a *cis* conformation, the opposite geometry to that observed in **2**. For a gaseous 2,2´-bipy$^{2-}$ ion the *trans* conformation is favourable due to the increased distance between like partial charges localised on the two electronegative nitrogen atoms. The

existence of crystalline forms of both stereoisomers suggests that in the solid state, the thermodynamic benefit of increased distance between nitrogen atoms can be outweighed by electrostatic attraction. The *trans* orientation of 2,2´-bipy$^{2-}$ in **2** allows for interaction with four neighbouring rubidium cations. There are two nitrogen lone pair interactions (one from each nitrogen) to different, symmetry generated rubidium cations with a distance of 2.946(3) Å. An additional interaction between the π manifold of the bipyridyl dianion and symmetry related metal cations above and below the bipyridyl plane has a Rb1 to N1 bond distance of 2.976(3) Å as well as several close contacts to C4, C5 and the symmetry generated C5A of 3.225(3), 3.236(3) and 3.131(3) Å, respectively. Together these interactions form one-dimensional chains which are bridged by pairs of ethylenediamine molecules between rubidium cations. These are coordinated in a doubly chelating fashion with bond lengths of 3.081(3) and 3.164(3) Å to one rubidium and 3.180(3) and 3.110(3) Å to the neighbouring site in an adjacent chain (Figure 2.4b). The resultant two-dimensional sheets form parallel to the crystallographic *ab* plane and stack along the unit cell *c* axis with no obvious interactions present between adjacent sheets.

Bulk sample composition has been confirmed by elemental microanalysis and powder X-ray diffraction measurements (Figure 2.5).

#### 2.3.2.3 Spectroscopic Characterisation

While a large volume of data has been published on the 2,2´-bipyridyl radical anion, information on the dianion is far rarer. Owing to the presence of a centre of inversion in the bipyridyl *trans* stereoisomer (point group $C_{2h}$), no coincidental peaks in IR and Raman spectra are expected because of the mutual-exclusion rule. This is largely observed, with the very small number of peaks common to both being attributed to the presence of ethylenediamine molecules in the crystal structure. There are several potentially diagnostic peaks in the IR spectrum: two strong bands at 1560 and 1590

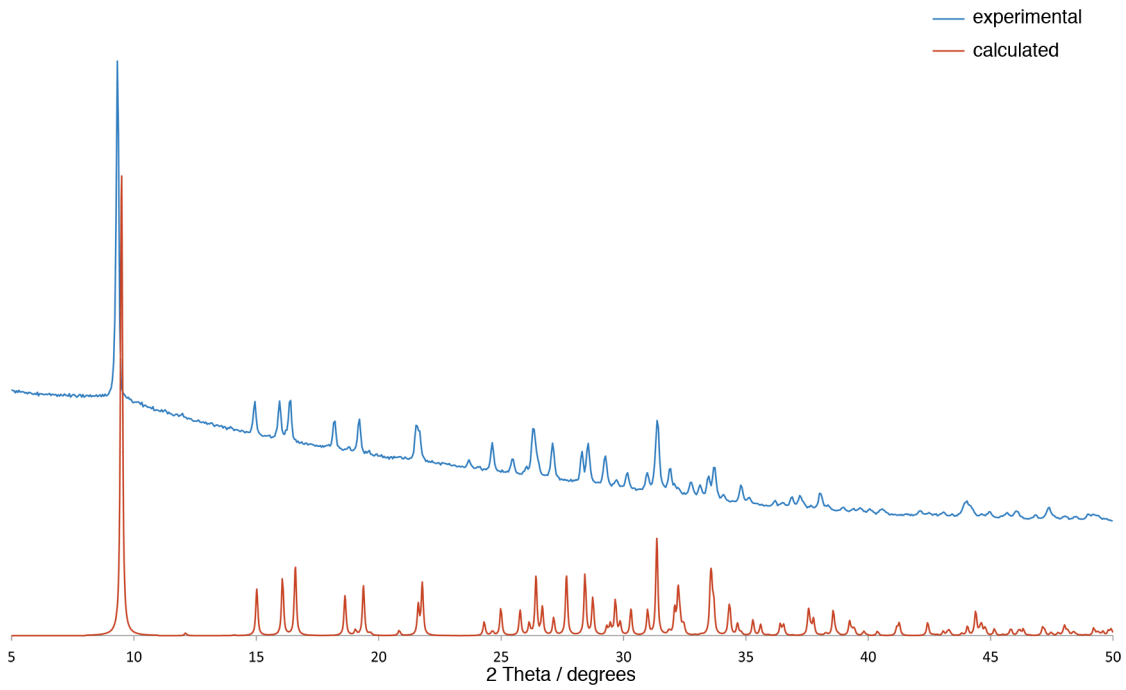



Figure 2.5: Comparison of calculated and experimental powder X-ray diffraction patterns for **2**.

$cm^{-1}$ from C=C and C=N stretches are much more intense and shifted to higher wavenumbers than those observed for the radical species. Additionally, three peaks occurring at 801, 830 and 867 $cm^{-1}$ have no counterpart in the spectra of the neutral or singly-reduced species. The Raman spectrum shows several strong peaks, with the band at 957 $cm^{-1}$ having potential diagnostic value as it was also observed at 956 $cm^{-1}$ in $Li_2$(2,2´-bipy).[5]

It is interesting to note that an EPR measurement of a solid sample of **2** (which should be diamagnetic) showed a weak resonance with a $g$ value of 2.0033. This is attributed to the presence of trace amounts of the singly reduced species **1** which was formed either as a reaction byproduct or while manipulating the sample and is only detectable due to the highly sensitive nature of the EPR technique (capable of detecting paramagnetic compounds at concentrations as low as $10^{-9}$ M).[57]

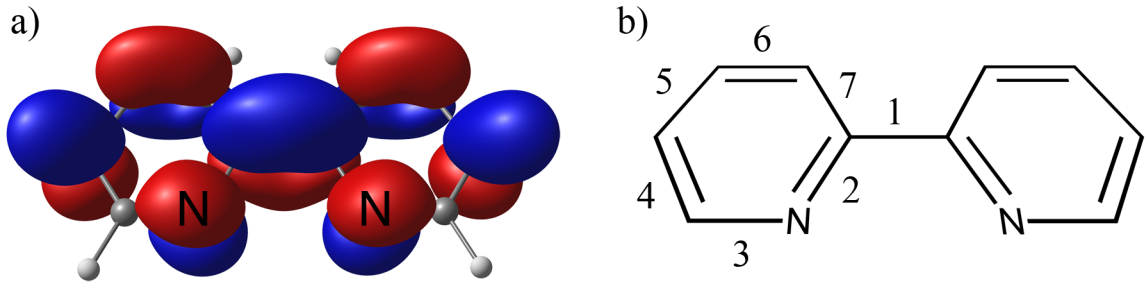



Figure 2.6: (**a**) DFT calculated 2,2´-bipy LUMO showing the alternating bonding and antibonding interactions in the π manifold. (**b**) Numbering scheme used in describing bond metric changes.

### 2.3.3 Electronic Structure and Bond Metric Parameters

Examination of the crystallographic structures of neutral bipyridine, **1a**, **1b**, and **2** shows clear correlations between bond metric parameters and the oxidation state of the bipyridine moiety. The first reduction causes population of the lowest unoccupied molecular orbital (LUMO) of the neutral species to form a singly occupied molecular orbital (SOMO) in the radical species. A further reduction fills this orbital; the highest occupied molecular orbital (HOMO) of the dianionic species. Density functional theory (DFT) calculations have revealed that this orbital is non-degenerate with net π*-antibonding character.[58] The calculated orbitals are largely unchanged by oxidation state with the LUMO of the neutral species being very similar to the SOMO calculated for the radial anion, which in turn strongly resembles the HOMO of the doubly reduced species. The calculated LUMO of the neutral species is pictured in Figure 2.6, together with a numbering scheme for the 2,2´-bipy bonds.

It is important to note that the orbital contains eight nodes such that upon population any bonds with a local bonding interaction would be expected to have increased bond order (and hence shorten). Conversely, any bonds with a local antibonding interaction will have reduced bond order (manifested as longer bond lengths). Thus bonds 1 and 6 are expected to shorten while bonds 2, 5 and 7 are expected to elongate. These predicted variations are indeed observed experimentally and substantial C–C

| | 2,2´-bipy | | 2,2´-bipy$^{\bullet-}$ | | | 2,2´-bipy$^{2-}$ | |
|---|---|---|---|---|---|---|---|
| Bond: | literature[41] | [DFT] | **1a** | **1b** | [DFT] | **2** | [DFT] |
| 1 | 1.490(3) | [1.494] | 1.431(3) | 1.429(av) | [1.436] | 1.399(6) | [1.400] |
| 2 | 1.346(2) | [1.357] | 1.390(av) | 1.388(av) | [1.403] | 1.436(4) | [1.442] |
| 3 | 1.341(2) | [1.350] | 1.337(av) | 1.337(av) | [1.341] | 1.343(4) | [1.339] |
| 4 | 1.384(2) | [1.397] | 1.373(av) | 1.382(av) | [1.405] | 1.381(5) | [1.412] |
| 5 | 1.383(3) | [1.397] | 1.404(av) | 1.404(av) | [1.419] | 1.429(5) | [1.440] |
| 6 | 1.385(2) | [1.395] | 1.365(av) | 1.364(av) | [1.382] | 1.358(5) | [1.376] |
| 7 | 1.394(2) | [1.407] | 1.428(av) | 1.428(av) | [1.438] | 1.452(4) | [1.453] |

Table 2.6: Bond lengths for neutral 2,2´-bipyridine and its reduced forms in **1a**, **1b** and **2**. When multiple crystallographically unique bonds are present in a structure, mean lengths are given. Values in square brackets were obtained from geometry optimised structures using DFT calculations. All bond lengths are in Å.

and C–N bond length changes were noted upon reduction. These are summarised in Table 2.6 and Figure 2.7. The effect is greatest for bond 1, the inter-ring bond, which shortens from 1.490(3) Å in the neutral species,[41] to 1.431(3) and 1.429(2) Å in **1a** and **1b**, respectively, as it gains π character. The second reduction causes a further decrease in bond length to 1.399(6) Å when the interaction effectively becomes a double-bond, showing a variation of 0.091 Å or 6% relative to the neutral species. This bond distance is very similar to those in the three known alkali-metal salts of the bipyridyl dianion: 1.375(4), 1.376(5), and 1.380(av) Å,[27] as well as that in the reported lanthanide complex (Yb(2,2´-bipy)(THF)$_2$)$_3$: 1.407(av) Å.[56] The inter-ring bond lengths of the radical species **1a** and **1b** are also very much in line with previously reported complexes: (Cp*)$_2$Sm(2,2´-bipy), 1.429(4) Å;[28] (Cp*)$_2$Yb(2,2´-bipy), 1.426(5) Å;[38] Mo(O$^i$Pr)$_2$(2,2´-bipy)$_2$, 1.425(av) Å;[41] and ($\eta^6$-Tol)Fe(2,2´-bipy) (Tol = toluene),[44] 1.417(3) Å; all of which may be considered as formally containing a bipyridyl radical anion. Similar arguments and comparisons may be made for the other bipyridine bonds. Both the bond metric values and resultant trends are consistent with those computed from unrestricted geometry optimised DFT calculations.

In addition to the above consideration of bond metrics, variation of the bipyridine inter-ring torsion angle was also investigated. As the LUMO of the neutral species is

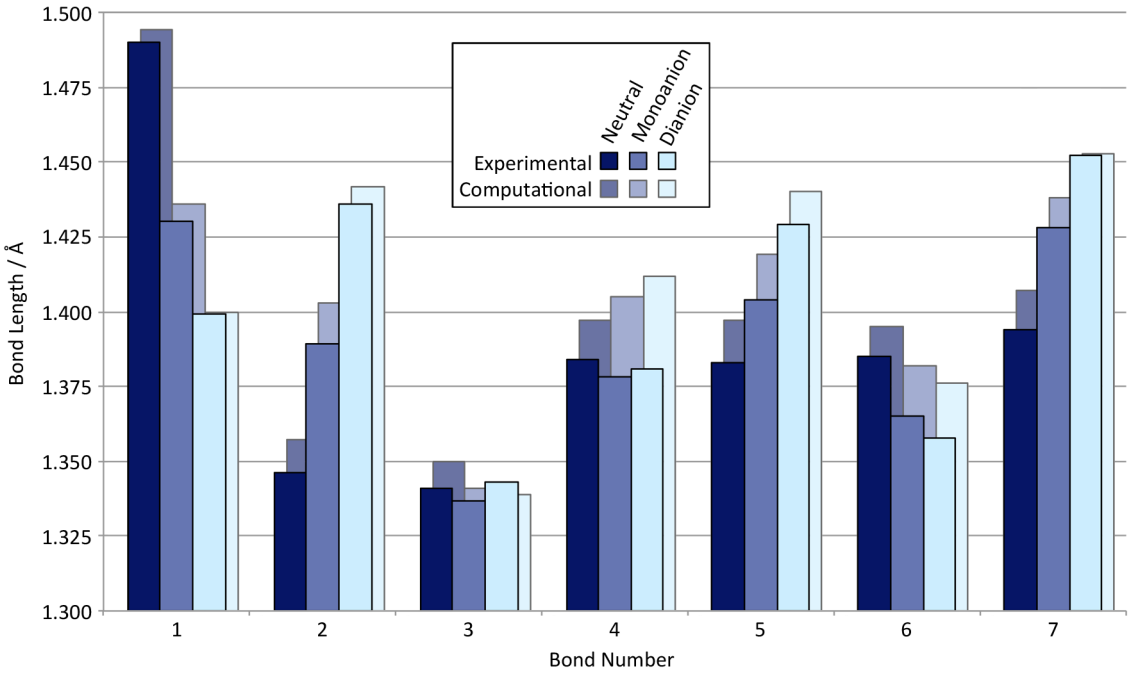



Figure 2.7: Graphical comparison of experimental and calculated bond lengths in 2,2´-bipyridine and its reduced forms in **1a**, **1b** and **2**.

incrementally populated, bond 1 gains π character, leading to increased coplanarity of the ring system. However, the 2,2´- isomer of bipyridine is a poor candidate to demonstrate this due to its bidentate bonding mode which favours a coplanar geometry. Values observed from single-crystal X-ray diffraction studies are generally small, with the mean torsion angle from 5801 structures in the CSD being 4.5°.[35] The angles observed for **1a**, **1b** and **2** are 5.6°, 1.8° and 0° respectively and as such it is not reasonable to use this value diagnostically to determine ligand oxidation states.

## 2.4 2,4´-Bipyridine

In contrast to both the 2,2´- and 4,4´- isomers of bipyridine, for which there is a large volume of spectroscopic and structural information available, 2,4´-bipyridine is far less frequently reported in the chemical literature, presumably because of its inability to bind as either a bidentate ligand or a rigid linker. This is evidenced in the

number of complexes available through the Cambridge Structural Database, where the 6652 2,2´-bipy containing structures and the 5115 4,4´-bipy containing structures vastly outnumber the 58 structures reported with 2,4´-bipyridine ligands.[35]

### 2.4.1 2,4´-Bipyridyl Radical Anion

Compared to the two other commercially available isomers, 2,4´-bipyridine is far less frequently encountered in the literature and publications concerning its reduced forms are rarer still. A surface enhanced Raman study of an electrode mounted sample of neutral 2,4´-bipyridine at different potentials was published in 1990,[7] and more recently an electrochemical study was reported,[20] but outside of these papers there is very little information available concerning the reduced forms of 2,4´-bipyridine. To augment existing literature information for the other isomers, crystalline samples of alkali metal salts of both the radical anion and the dianion have been synthesised and structurally and spectroscopically characterised.

#### 2.4.1.1 Synthesis

Reaction of 2,4´-bipy with one equivalent of potassium metal in ethylenediamine yields K(2,4´-bipy)(en) (**3**), an intensely coloured dark purple solution. Dark-purple air- and moisture-sensitive plate-like crystals containing the 2,4´-bipyridyl radical anion, 2,4´-bipy$^{\bullet-}$, were isolated several days after layering with toluene or ether.

#### 2.4.1.2 Structural Characterisation

The asymmetric unit of **3** contains a 2,4´-bipyridyl radical anion, a potassium cation and an ethylenediamine solvent molecule (Figure 2.8a) Each potassium site is co-ordinated to four atoms: two terminally bonded ethylenediamine molecules (one at N1E and one at N2E), and two bipyridyl radical anions, both at the 4´ position (N2); one as a interaction with the nitrogen lone pair and the other in a ‘side-on’

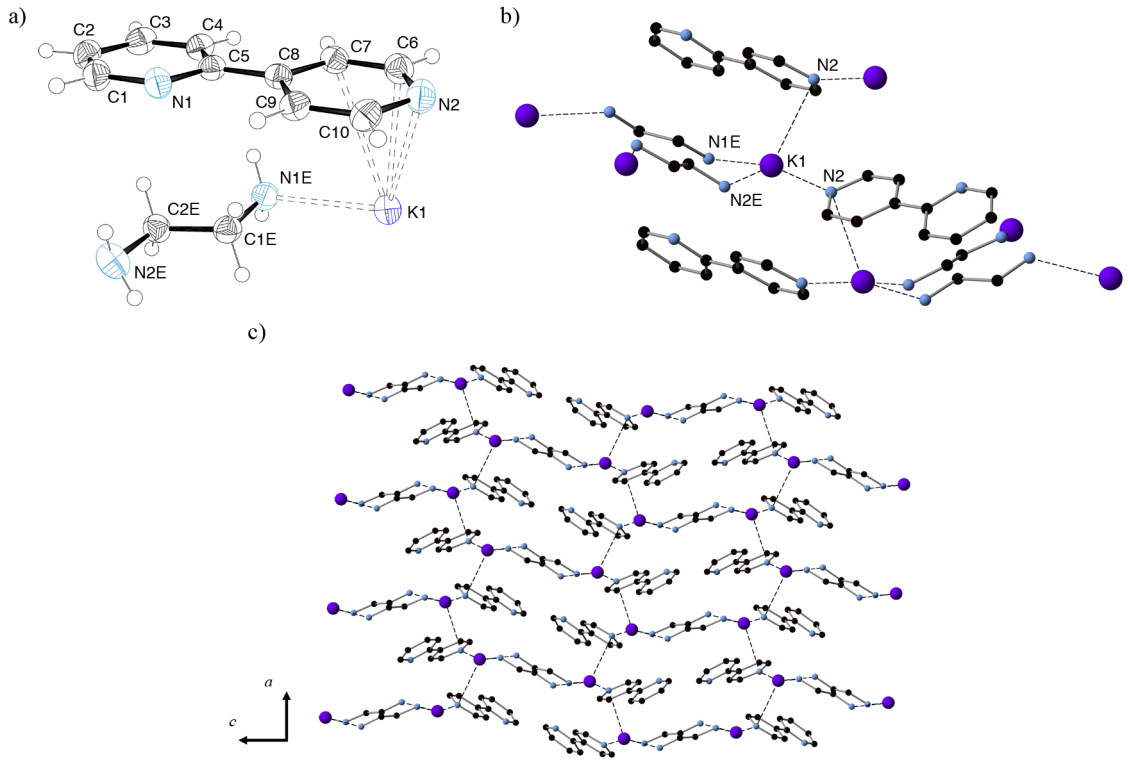



Figure 2.8: (**a**) Thermal ellipsoid representation of the atoms in the asymmetric unit of **3**. Anisotropic displacement ellipsoids pictured at the 50% probability level. (**b**) The interactions giving rise to the extended framework. (**c**) Packing diagram viewed along the crystallographic *b* axis showing the bridging ethylenediamine and 2,4´-bipy radical anion linkers. Note that hydrogen atoms have been omitted from (b) and (c) for clarity.

manner to the π manifold (Figure 2.8b). These bond lengths are 2.798(2), 2.882(2), 2.800(2) and 3.249(2) Å, respectively. The latter 'side-on' interaction may also extend to carbon atoms C6 and C7 with close contact distances of 3.078(2) and 3.348(2) Å, respectively. In this way, each ethylenediamine and 2,4´-bipy anion bridge separate symmetry generated potassium atoms to create the extended crystal structure which has a heavily distorted diamondoid type structure. It is interesting to note that the 2 position (N1) of the 2,4´-bipyridyl radical is not involved in the bonding in any way.

Bulk composition has been confirmed by powder X-ray diffraction and elemental microanalysis (Figure 2.9).

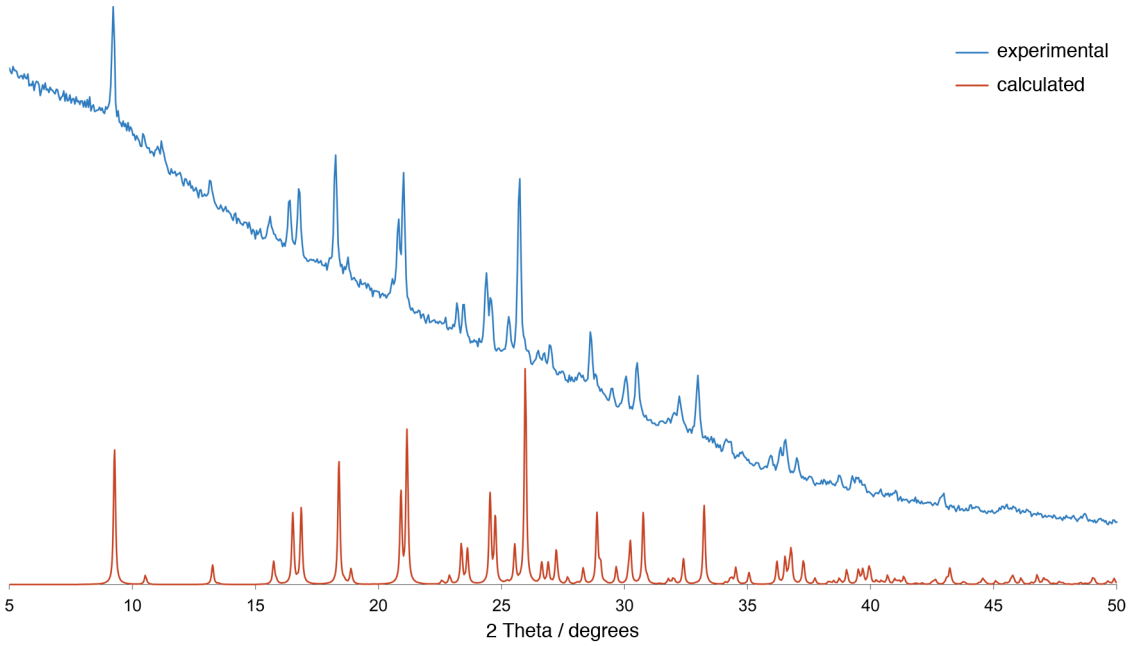



Figure 2.9: Comparison of calculated and experimental powder X-ray diffraction patterns for **3**.

#### 2.4.1.3 Spectroscopic Characterisation

Solid and solution EPR spectroscopic measurements on **3** clearly prove the existence of the bipyridine radical anion (Figure 2.10). The solution-phase spectrum shows a complex hyperfine coupling pattern that arises due to the coupling of magnetic moments between the delocalised electron, two inequivalent $^{14}$N nuclei ($I = 1$) and eight inequivalent $^{1}$H nuclei ($I = 1/2$). Theoretically, this would give rise to 2304 lines, though these are not all observable due to detector resolution limits and concomitant line broadening. The resonance is centreed at a $g$ value of 2.0037 which is identical to that of the 2,2´-bipy isomer ($g = 2.0035$) and very similar to that of a free electron ($g = 2.002319$). DFT calculated isotopic Fermi contact coupling constants were found to compare well to those determined from least-squares fits of the data (Table 2.7).[55] The solid-state spectrum shows a single resonance centred at $g = 2.0037$. No hyperfine interactions are observed (as is expected) and the resonance shape is symmetrical.

IR measurements on **3** show a strong band in the 900 – 1000 cm$^{-1}$ region at

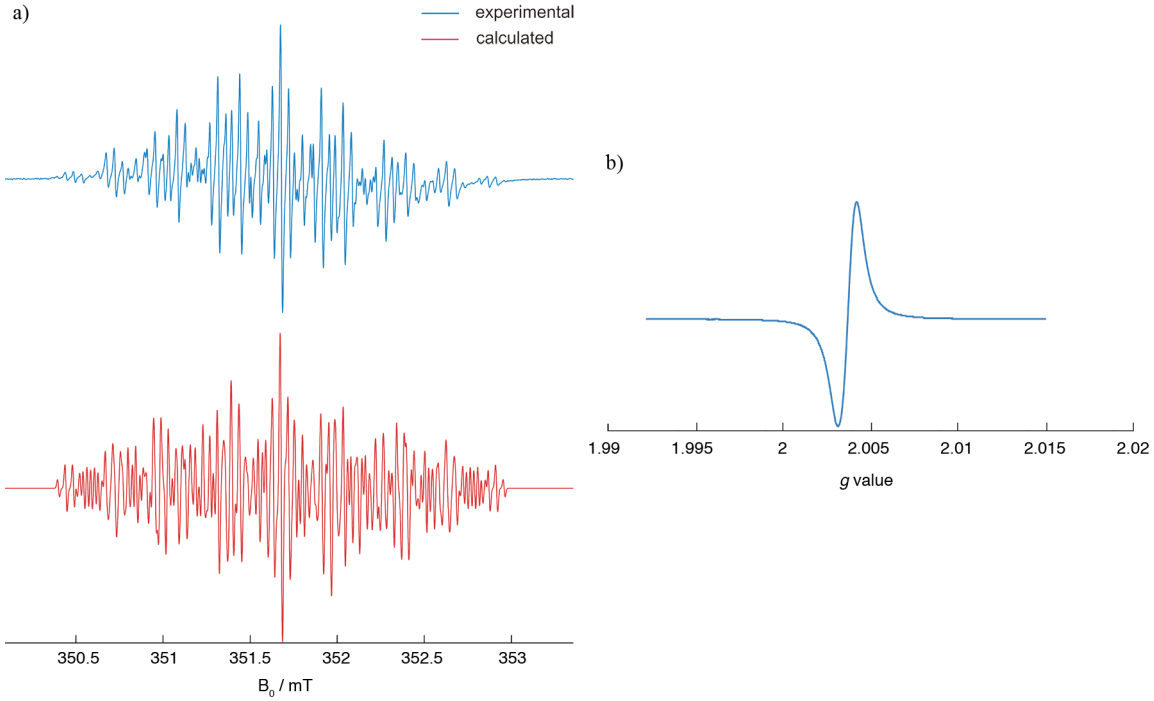
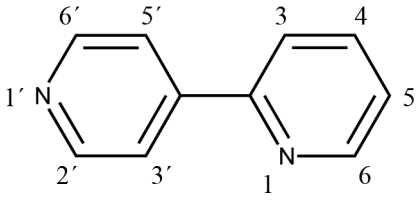



Figure 2.10: (**a**) Comparison of experimental and calculated solution EPR spectra for **3**. (**b**) Solid state EPR spectrum for **3**.




| Site: | DFT Calculated: | Least-Squares Fit: |
|---|---|---|
| 1 | 9.23 | 6.56 |
| 3 | –3.88 | –3.52 |
| 4 | –1.95 | –2.88 |
| 5 | –14.40 | –12.42 |
| 6 | 2.58 | 1.28 |
| 1′ | 13.69 | 10.10 |
| 2′ | –0.35 | –1.15 |
| 3′ | –6.66 | –6.56 |
| 5′ | –6.68 | –7.99 |
| 6′ | 0.22 | 1.21 |

Table 2.7: Comparison of DFT calculated and least-squares fitted hyperfine coupling constants for the solution EPR response of **3**. All frequencies are in MHz.

944 $cm^{-1}$ corresponding to a ring deformation mode, and a C=C or C=N stretch at 1559 $cm^{-1}$, neither of which are present in the spectrum of the parent compound. Conversely, several bands in the spectrum of the neutral species at 730, 773, 851, 1043 and 1066 $cm^{-1}$ are not present in the singly reduced radical anion spectrum and may also be useful in the diagnosis of bipyridine oxidation state. Raman measurements show similar peak positions with differing intensities but which are comparable to the surface enhanced spectra reported in the literature.[7] This is reasonable as the $C_s$ point group of planar 2,4´-bipyridine allows for IR and Raman excitations of all vibrational modes.

## 2.4.2 2,4´-Bipyridyl Dianion

The work carried out here provides the first detailed study of the doubly reduced form of 2,4´-bipyridine. Similar reactions to those mentioned previously allowed isolation of two isostructural salts containing the dianionic species which will be discussed together in the following subsections.

### 2.4.2.1 Synthesis

$K_4$(2,4´-bipy)$_2$(en)$_{3.5}$ (**4**) was prepared by the reaction of 2,4´-bipy with two equivalents of potassium metal in ethylenediamine. This yielded an intensely coloured dark purple solution from which dark-purple/black air- and moisture-sensitive needle-like crystals containing the 2,4´-bipyridyl dianion, 2,4´-bipy$^{2-}$ were isolated several days after layering with toluene. $Rb_4$(2,4´-bipy)$_2$(en)$_{3.5}$ (**5**) was prepared in an analogous manner, forming purple rod-like crystals.

### 2.4.2.2 Structural Characterisation

Both **4** and **5** share a common structure and will be discussed in tandem. From here on in the potassium salt will be referenced unless otherwise stated. Figures 2.11a

and b show the asymmetric units of both salts and highlight their similarities. The asymmetric unit of **4** contains four potassium cations, two 2,4´-bipyridine dianions and three and a half crystallographically unique ethylenediamine molecules. The extended structure consists of two-dimensional sheets that lie parallel to the *ac* plane of the unit cell. Within each sheet are chains of 2,4´-bipyridyl dianions held together by potassium cations. N11 and N21 (both at the 2 position of different 2,4´-bipy moieties) each interact with three metal atoms. One interaction is in the plane of the bipyridine rings with N11 interacting with K2 and N21 interacting with K1 (these interaction distances are 2.860(2) and 2.834(2) Å, respectively). The two remaining interactions are to cations above and below the ring system and show short contacts between ring nitrogen and carbon atoms. For example, K1 interacts with N11, C15, C16 and C110 with inter-atomic distances of between 2.832(2) and 3.259(2) Å while on the opposite face of the ring system, K3 interacts with N11, C14, C15, and C16 with distances between 2.945(2) and 3.497(2) Å. N12 and N22 (both at the 4´ position of 2,4´-bipy) are each bonded to two potassium ions. A σ-type interaction links a cation in the plane of the bipyridine system in each case, binding N12 to K3 and N22 to K4 with bond lengths of 2.925(2) and 2.816(2) Å, respectively. In addition, a cation lies above the plane of these sites, again with short contacts to ring carbon atoms. In this way K2 interacts with N12, C18, and C19 with contact distances between 2.861(2) and 3.157(2) Å while K1 is bonded to N22, C27, C28, and C29 with distances that range between 2.998(2) and 3.478(2) Å (Figure 2.11c). These interactions form potassium-bipyridyl chains with the K3 sites of one chain linked to the K4 sites of an adjacent chain by ethylenediamine bridges to create two-dimensional sheets. These ethylenediamine bridges are almost all coordinated in a bidentate manner with K3 and K4 bridged by N1E, N2E and N1G with distances ranging between 2.864(2) and 3.068(2) Å. The exception is N2G which only interacts with K4, at a distance of 2.858(2) Å. Potassium cations in adjacent sheets are held together by further bridging

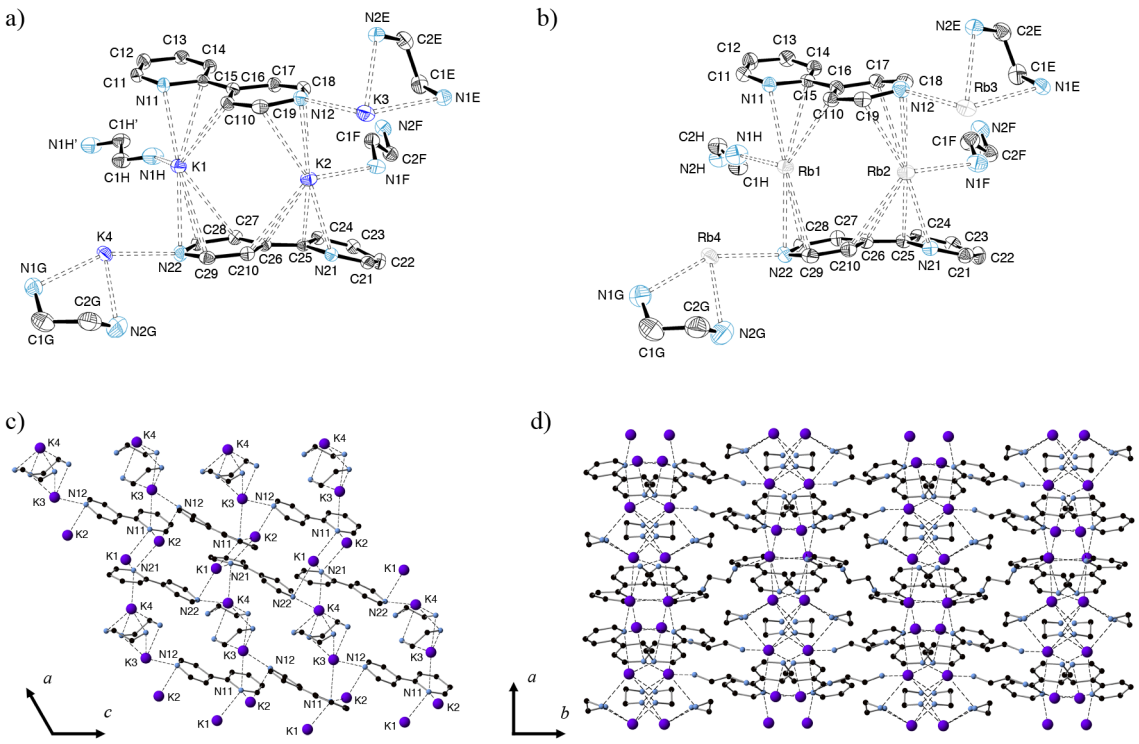



Figure 2.11: (**a**) Thermal ellipsoid representation of the atoms in the asymmetric unit of **4**. Anisotropic displacement ellipsoids pictured at the 50% probability level. (**b**) Thermal ellipsoid representation of the atoms in the asymmetric unit of **5**. Anisotropic displacement ellipsoids pictured at the 50% probability level. (**c**) The structure of a single sheet of **4** in the crystallographic *ac* plane highlighting the role played by ethylenediamine molecules in cross-linking chains of potassium cations and bipyridyl anions. (**d**) View along the crystallographic *c* axis showing the role of ethylenediamine in holding adjacent sheets together. Note that hydrogen atoms have been omitted from all structures for clarity.

ethylenediamine molecules: N1H and K1 with bond length 2.962(2) Å (the second half of the ligand is generated by symmetry) together with K2 and N1F and K3 and N2F at opposite ends of the same ligand with bonding distances of 2.934(2) and 3.074(2) Å, respectively. These interactions cause the stacking of sheets to reveal the three-dimensional crystal structure.

The compositional purity of both samples was confirmed by elemental microanalysis and a powder X-ray diffraction pattern was collected for **5** to check for phase purity (Figure 2.12).

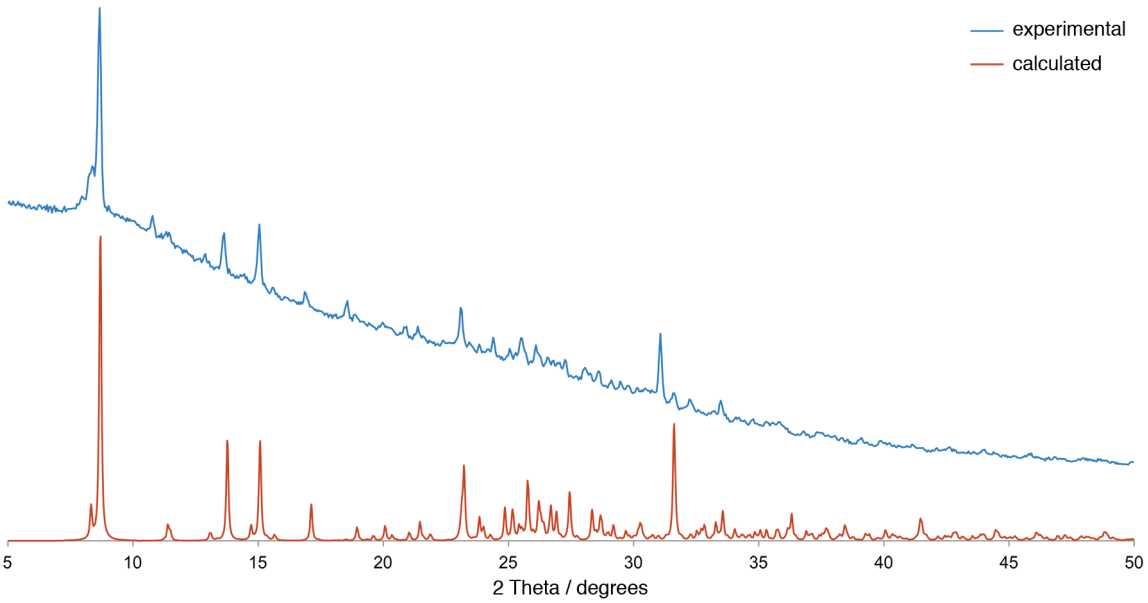



Figure 2.12: Comparison of calculated and experimental powder X-ray diffraction patterns for **5**.

#### 2.4.2.3 Spectroscopic Characterisation

The IR spectra of **4** and **5** are very similar as would be expected for closely related structures which vary only in the nature of the metal cation. Two strong bands appear in the 900 – 1000 $cm^{-1}$ region that are not present in the spectra of the neutral or singly reduced species at 900 and 950 $cm^{-1}$ for **4** and at 902 and 951 $cm^{-1}$ for **5**. Two strong peaks arising from in-plane bending modes are found at 1257 and 1290 $cm^{-1}$ for **4** and at 1255 and 1291 $cm^{-1}$ for **5**. This area contains only very weak peaks for the neutral species and a weak band at 1267 $cm^{-1}$ for the radical monoanionic species. As such it may be used diagnostically to distinguish the oxidation state of 2,4´-bipyridine. The C=C and C=N stretching region contains two further strong peaks at 1574 and 1607 $cm^{-1}$ for **4** and at 1576 and 1604 $cm^{-1}$ for **5**. These lie approximately 10 $cm^{-1}$ higher than similar bands for the single reduced species and as such are less useful in a diagnostic context. The Raman spectra of **4** and **5** are again very similar to the IR spectra as the $C_s$ symmetry of the 2,4´-bipy ligand means that all possible vibrational modes are both IR and Raman active. Non-coincident

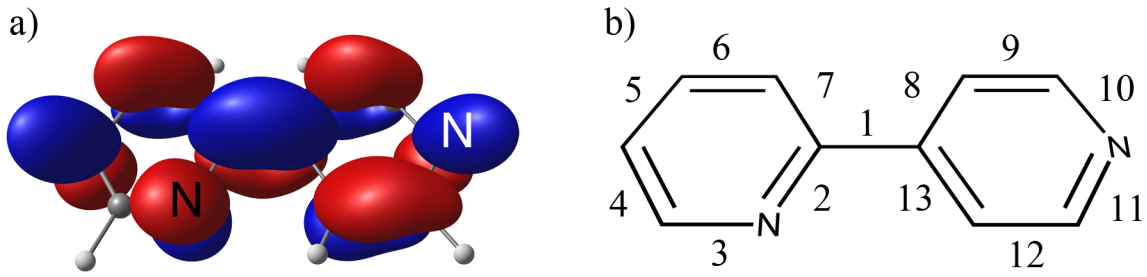



Figure 2.13: (**a**) DFT calculated 2,4´-bipy LUMO showing the alternating bonding and antibonding interactions in the π manifold. (**b**) Numbering scheme used in describing bond metric changes.

peaks between IR and Raman spectra are attributed to the different bonding modes of ethylenediamine in the crystal lattices or to trace impurities.

As was found with the 2,2´-bipyridyl dianion, EPR measurements on solid samples of **4** and **5** give rise to very weak resonances ($g$ = 2.0035 and 2.0038, respectively) at or around the $g$ value of **3** ($g$ = 2.0037). This is again assumed to be the result of a trace of the 2,4´-bipyridyl radical monoanion present either in the crystal structure, occupying a dianion site, or alternatively introduced as a result of manipulations of this highly air- and moisture-sensitive compound.

### 2.4.3 Electronic Structure and Bond Metrics

A comparison of the crystal structures of neutral 2,4´-bipy, **3** and **4** / **5** shows clear trends in bond metrics due to the varying oxidation state of the bipyridine moiety. DFT calculations show that the non-degenerate LUMO of the neutral species is very similar to that of the SOMO of the radical species and the HOMO of the doubly reduced species. It is this orbital that is populated upon reduction. This orbital has net π-antibonding character and is shown, together with a bond numbering scheme, in Figure 2.13.

During the step-wise reduction of 2,4´-bipyridine the neutral species LUMO is half and then fully populated. Any areas with local bonding character cause an

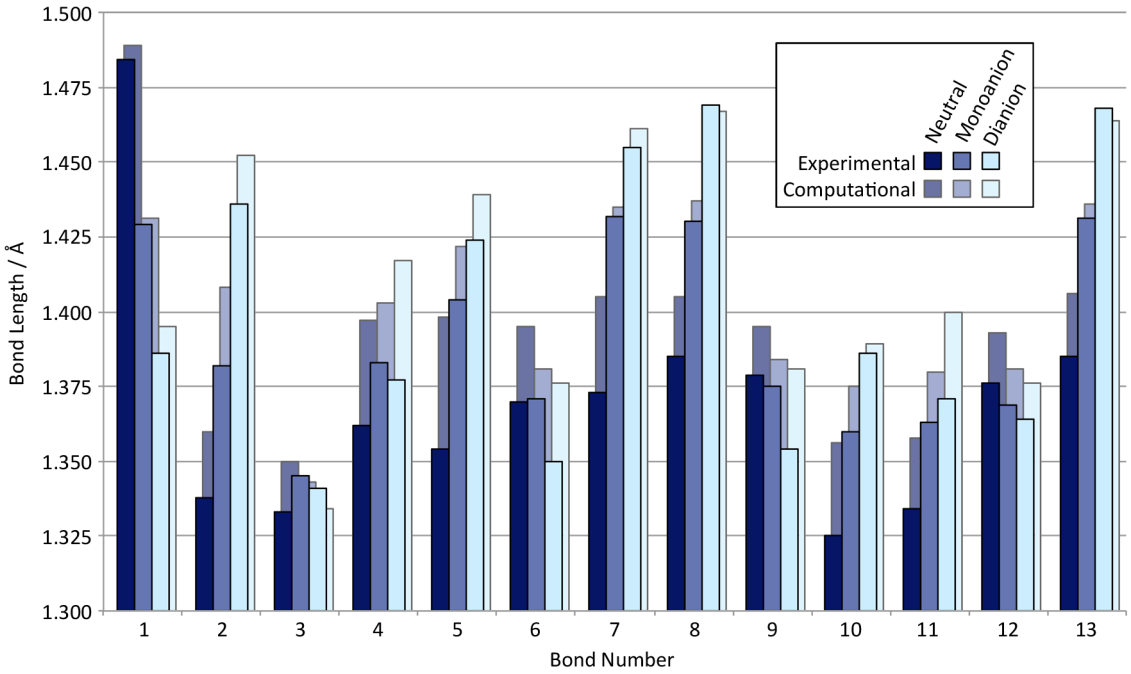



Figure 2.14: Graphical comparison of experimental and calculated bond lengths in 2,4´-bipyridine and its reduced forms in **3**, **4** and **5**.

increase in bond order and shortening of bond lengths, while conversely any areas of local antibonding character cause a decrease in bond order and an elongation of bonds. Thus upon reduction bonds 1, 6, 9 and 12 would be expected to shorten while bonds 2, 5, 7, 8, 10, 11 and 13 would be expected to become longer. This is observed experimentally and data are provided in Figure 2.14 and Table 2.8. The most substantial changes are to the lengths of bonds 1, 2, 7, 8 and 13. Bonds 3 and 4 show small, often statistically meaningless changes. The greatest variation in bond length is observed for bond 1, the inter-ring bond which contracts from 1.484(av) Å in the neutral species, to 1.429(3) Å in **3** due to an increase in π character. A second reduction causes a further decrease in bonding distance to give an effective double-bond with lengths of 1.385(av) or 1.386(av) Å in **4** and **5**, respectively. Similar arguments can be made to rationalise the changes in other bond lengths. The trends observed and the bond lengths themselves are consistent with those computed from unrestricted geometry optimised DFT calculations.

| | 2,4´-bipy | | 2,4´-bipy$^{\bullet-}$ | | 2,4´-bipy$^{2-}$ | | |
|---|---|---|---|---|---|---|---|
| Bond: | literature[59–61] | [DFT] | **3** | [DFT] | **4** | **5** | [DFT] |
| 1 | 1.484(av) | [1.489] | 1.429(3) | [1.431] | 1.385(av) | 1.386(av) | [1.395] |
| 2 | 1.338(av) | [1.360] | 1.382(3) | [1.408] | 1.434(av) | 1.436(av) | [1.452] |
| 3 | 1.333(av) | [1.350] | 1.345(3) | [1.343] | 1.344(av) | 1.341(av) | [1.334] |
| 4 | 1.362(av) | [1.397] | 1.383(3) | [1.403] | 1.375(av) | 1.377(av) | [1.417] |
| 5 | 1.354(av) | [1.398] | 1.404(3) | [1.422] | 1.428(av) | 1.424(av) | [1.439] |
| 6 | 1.370(av) | [1.395] | 1.371(3) | [1.381] | 1.353(av) | 1.350(av) | [1.376] |
| 7 | 1.373(av) | [1.405] | 1.432(3) | [1.435] | 1.457(av) | 1.455(av) | [1.461] |
| 8 | 1.385(av) | [1.405] | 1.430(3) | [1.437] | 1.464(av) | 1.469(av) | [1.467] |
| 9 | 1.379(av) | [1.395] | 1.375(3) | [1.384] | 1.357(av) | 1.354(av) | [1.381] |
| 10 | 1.325(av) | [1.356] | 1.360(3) | [1.375] | 1.386(av) | 1.386(av) | [1.389] |
| 11 | 1.334(av) | [1.358] | 1.363(3) | [1.380] | 1.377(av) | 1.371(av) | [1.400] |
| 12 | 1.376(av) | [1.393] | 1.369(3) | [1.381] | 1.359(av) | 1.359(av) | [1.376] |
| 13 | 1.385(av) | [1.406] | 1.431(3) | [1.436] | 1.465(av) | 1.468(av) | [1.464] |

Table 2.8: Bond lengths for neutral 2,4´-bipyridine and its reduced forms in **3**, **4** and **5**. When multiple crystallographically unique bonds are present in a structure, mean lengths are given. Values in square brackets come from geometry optimised structures using DFT calculations. All bond lengths are in Å.

Unlike the case of 2,2´-bipyridine, the positions of the nitrogen atoms in 2,4´-bipyridine and its reduced forms do not allow chelation to take place, allowing examination and discussion of the inter-ring torsional angle. As 2,4´-bipyridine is sequentially reduced there is an increasing preference for ring co-planarity due to the increasing double bond character of bond 1. However, for the four examples of the neutral species crystallographically characterised and published in the CSD this angle ranges between 0.16° and 32.31°. As a result it appears that the ring torsion angle is strongly affected by crystal packing effects. Mean torsional angles of 4.27° in **3** and 0.77° and 1.31° in **4** and **5**, respectively, show quite clearly that this is an unsuitable diagnostic metric for determination of the oxidation state of 2,4´-bipyridine.

## 2.5 4,4´-Bipyridine

The literature contains a vast amount of information on 4,4´-bipyridine, detailing both its spectroscopic characteristics as well as reporting its inclusion in a wealth of structures. In particular, 4,4´-bipy has seen considerable use in the fields of coordination polymers and metal–organic frameworks, where it is routinely employed as a rigid, linear linker.[62–67] At the time of writing, the CSD structural database lists 5115 structures incorporating the ligand, however prior to this research only the neutral species had been crystallographically characterised.

### 2.5.1 4,4´-Bipyridyl Radical Anion

The earliest documentation of the 4,4´-bipyridyl radical anion (4,4´-bipy$^{\bullet-}$) comes from solution EPR studies of organic radicals which were generated *in situ* from the reduction of pyridine by alkali metals.[1] Further spectroscopic and electrochemical investigations corroborated the existence of the radical species and provided considerable information about the redox behaviour of the solvated molecule.[18,21–23] More recently the use of *ab initio* methods and Raman spectroscopic measurements have been used to further investigate the structure of the monoanion,[8,24–26] however outside of this computed model, no structural information existed for the 4,4´-bipyridyl radical anion prior to this research.

#### 2.5.1.1 Synthesis

Na(4,4´-bipy)(en) (**6**) was prepared by the reaction of 4,4´-bipy with one equivalent of sodium metal in ethylenediamine. This yielded an intensely coloured purple solution from which dark-purple air- and moisture-sensitive crystals containing the 4,4´-bipyridyl radical anion (4,4´-bipy$^{\bullet-}$) were isolated four days after layering with benzene.

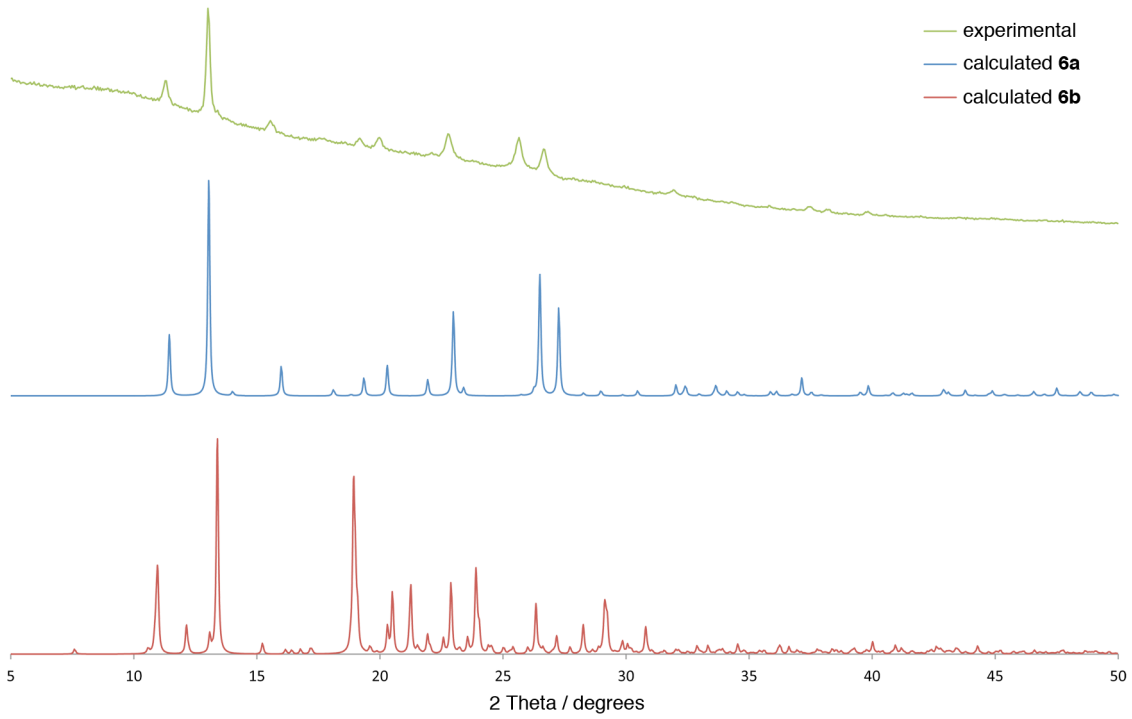



Figure 2.15: Comparison of calculated and experimental powder X-ray diffraction patterns for **6a** and **6b**.

#### 2.5.1.2 Structural Characterisation

Two compositionally identical polymorphs of **6** were found to crystallise, Na(4,4´-bipy)(en) (**6a**) and $Na_2$(4,4´-bipy)$_2$(en)$_2$ (**6b**), both of which display similar bond metric parameters in the bipyridyl moiety. Powder X-ray diffraction measurements indicate that **6a** is the major product with contributions from **6b** frequently not observable in the resultant patterns (Figure 2.15). Bulk composition has additionally been confirmed by elemental microanalysis however this technique cannot be used to verify product ratios in this instance.

The structure of **6a** consists of one-dimensional zig-zag chains that lie in a plane perpendicular to the mid-plane of the *ab* and *bc* crystallographic planes (Figure 2.16a and b). Each sodium atom is in a distorted square planar environment, interacting with one bidentate ethylenediamine with a Na1 to N1E distance of 2.504(3) Å, and two symmetry related bipyridyl anions at N1 at a distance of 2.427(4) Å. Adjacent

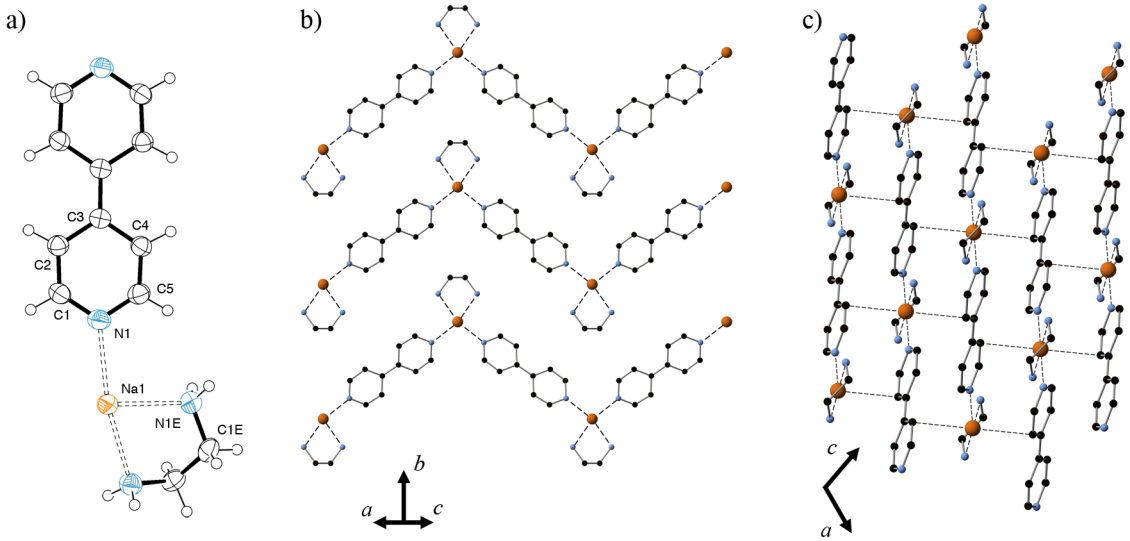



Figure 2.16: (**a**) Thermal ellipsoid representation of the atoms in the asymmetric unit of **6a**. Symmetry generated atoms are not labelled. Anisotropic displacement ellipsoids pictured at the 50% probability level. (**b**) Interactions forming the one-dimensional chain-like structure highlighting packing to form a sheet. (**c**) Packing diagram illustrating the electrostatic interactions between adjacent sheets. Note that in (b) and (c), hydrogen atoms have been omitted for clarity.

sheets are then held together by electrostatic interactions between the sodium cations of one sheet and the π manifolds of bipyridyl anions in neighbouring sheets, with a closest contact point of 3.042(2) Å between Na1 and C4 (Figure 2.16c).

The minor product polymorph, **6b**, has a slightly more complex structure. Na1 is coordinated to four bipyridyl anion linkers in a distorted tetrahedral environment, giving rise to a negatively charged pseudo diamondoid network with Na–N interaction distances in the range of 2.359(2) to 2.392(2) Å (Figure 2.17a). Networks of this topology, incorporating 4,4´-bipyridine linkers and a range of metal centres are well known, but ordinarily carry a positive charge with anions situated in lattice cavities.[65] An charge-inverted situation is present in **6b** where the negatively charged network must incorporate $[Na(en)_2]^+$ charge balancing cations in the lattice cavities. Both ethylenediamine molecules are coordinated to Na2 in a bidentate manner with N–Na distances between 2.421(2) and 2.518(4) Å. An open face allows a further interaction

with C21, C22 and C23 of a nearby bipyridyl anion with the closest contact being 3.026(2) Å to C22 as depicted in Figure 2.17a. The crystal structure is made up of three such interpenetrating networks, illustrated in Figure 2.17b and c.

#### 2.5.1.3 Spectroscopic Characterisation

EPR studies on bipyridyl radicals generated *in situ* by the use of alkali metals provided some of the first evidence of the reduced form of 4,4´-bipyridine.[1] Both solid and solution EPR measurements were run on samples of **6** and prove the existence of the 4,4´-bipyridyl radical species. Solution studies reveal a resonance, centred at a $g$ value of 2.0046. The relatively high symmetry of 4,4´-bipyridine compared to the 2,2´- and 2,4´- isomers results in less hyperfine coupling. Coupling to two magnetically identical $^{14}$N nuclei ($I = 1$), and two sets of four magnetically identical $^{1}$H nuclei ($I = 1/2$), should give rise to a splitting pattern with 125 peaks: a quintet of quintets of quintets. However, these splittings overlap, making the quintets less obvious (Figure 2.18a). The simulated spectrum was calculated using coupling constants reported by Carrington and compares well with the solution resonance observed.[1,55] A solid sample of **6** gave rise to a single, symmetric resonance with a $g$ factor of 2.0025 (Figure 2.18b). This is a close match to the value for a free electron ($g = 2.002319$) and is consistent with the presence of an unpaired electron in a π-orbital.

Raman measurements reveal an intense band at 1345 cm$^{-1}$ associated with an inter-ring stretching mode, which though present in spectra of the neutral 4,4´-bipyridine species, occurs at 1300 cm$^{-1}$. This value compares well with literature reported peak positions of 1350 cm$^{-1}$.[24,26] A second intense, diagnostically useful band occurs in the C=C and C=N stretching region at 1510 cm$^{-1}$ (reported in the literature at 1509 cm$^{-1}$) in a region containing no intense bands in the neutral species.

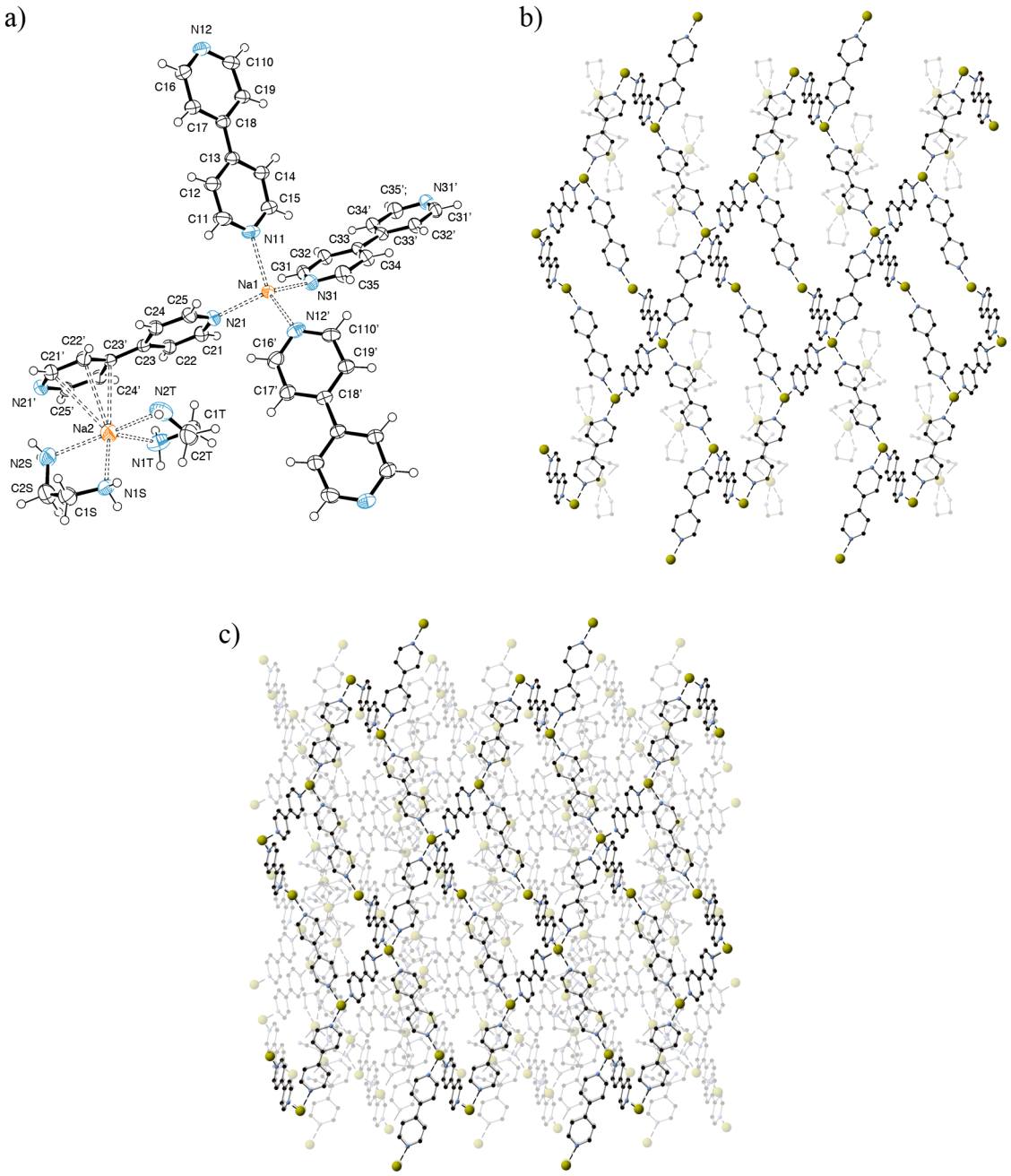



Figure 2.17: (**a**) Thermal ellipsoid representation of the atoms in the asymmetric unit of **6b**. Atom positions are labelled with primes to denote symmetry generated equivalents, included to illustrate coordination environment. Anisotropic displacement ellipsoids pictured at the 50% probability level. (**b**) One of the three interpenetrated distorted diamondoid networks depicted with translucent charge balancing cation complexes. (**c**) Packing diagram showing all three interpenetrated networks with the network in b) highlighted to guide the eye. Note that in (b) and (c), hydrogen atoms have been omitted for clarity.

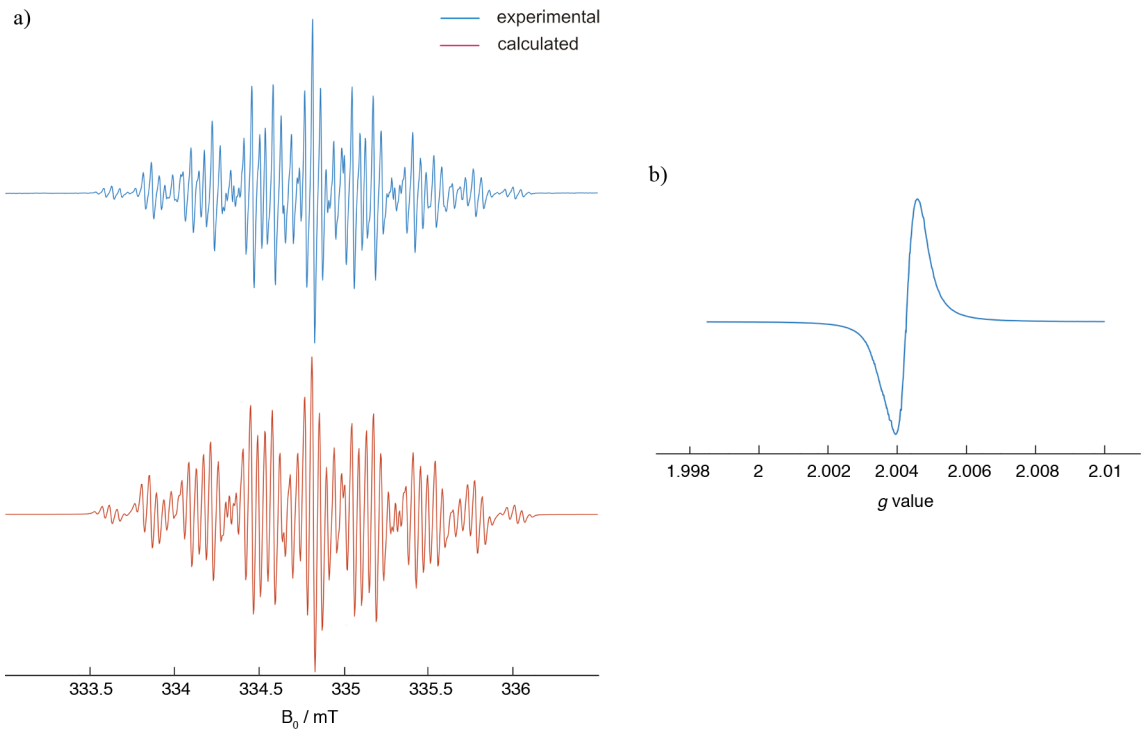



Figure 2.18: (**a**) Comparison of experimental and calculated solution EPR spectra for **6**. (**b**) Solid state EPR spectrum for **6**.

### 2.5.2 4,4´-Bipyridyl Dianion

While there has been a considerable amount of research published concerning the singly reduced radical species 4,4´-bipy$^{\bullet-}$, there is much less information on the doubly reduced species, 4,4´-bipy$^{2-}$, despite electrochemical studies that show that the dianion should be chemically accessible using alkali metals.[18,22,23]

#### 2.5.2.1 Synthesis

$Na_2$(4,4´-bipy)(en)$_2$ (**7**) was prepared by the reaction of 4,4´-bipy with slightly greater than two equivalents of sodium metal in ethylenediamine. This yielded an intensely coloured dark purple solution from which dark-purple air- and moisture-sensitive plate-like crystals containing the 4,4´-bipyridyl dianion (4,4´-bipy$^{2-}$) were isolated several days after layering with benzene.

#### 2.5.2.2 Structural Characterisation

The 4,4´-bipyridyl dianion, **7**, was found to undergo a phase transition between 200 and 250 K, changing from the *Pnma* space group (**7a**) at low temperatures to the closely related but non-isomorphic supergroup *Cmca* (**7b)** at higher temperatures. The structure of **7a** initially appears complex, but a closer examination reveals a layered, interpenetrated structure. Each 4,4´-bipyridyl dianion acts as a bridge between two crystallographically distinct sodium atoms Na1 and Na2 with nitrogen to sodium interaction distances of 2.360(2) and 2.372(2) Å, respectively. These units are in turn linked by terminally bonded ethylenediamine molecules, forming undulating two-dimensional sheets (Figure 2.19a and b) with interaction distances of 2.462(2) and 2.472(2) Å for Na1–N1A and Na2–N2A, respectively. Three such sheets are interpenetrated to form layers, running parallel to the crystallographic *bc* plane. Aside from the mechanical weave holding sheets together, each bipyridyl dianion interacts with sodium cations of the neighbouring sheets via the π manifold, as indicated in Figure 2.19a. In this way Na2 interacts with the C2, C3 and C2´ positions of a bipyridyl moiety in an adjacent sheet with contact distances of 2.873(2), 2.801(2) and 2.873(2)Å, respectively. On the opposite side of the anion C5, C4 and C5´ interact with Na1 with bond distances of 2.879(2), 2.828(2) and 2.879(2) Å, respectively. Sheets stack along the crystallographic *a* axis with no obvious inter-layer interactions (Figure 2.19c).

The structure of the higher temperature phase, **7b** is closely related to that of the lower temperature phase with the most significant change being the converging of the previously crystallographically distinct Na1 and Na2 atoms in **7a** to form a single crystallographically unique cation in **7b**. This causes minor changes in the interaction distances of coordinated nitrogen atoms with new distances of 2.363(4) and 2.471(3) Å for Na1–N1 and Na1–N1A, respectively. Coordination distances to the π manifold of the bipyridyl dianion are also affected, changing to 2.886(4) and 2.826(4) Å for

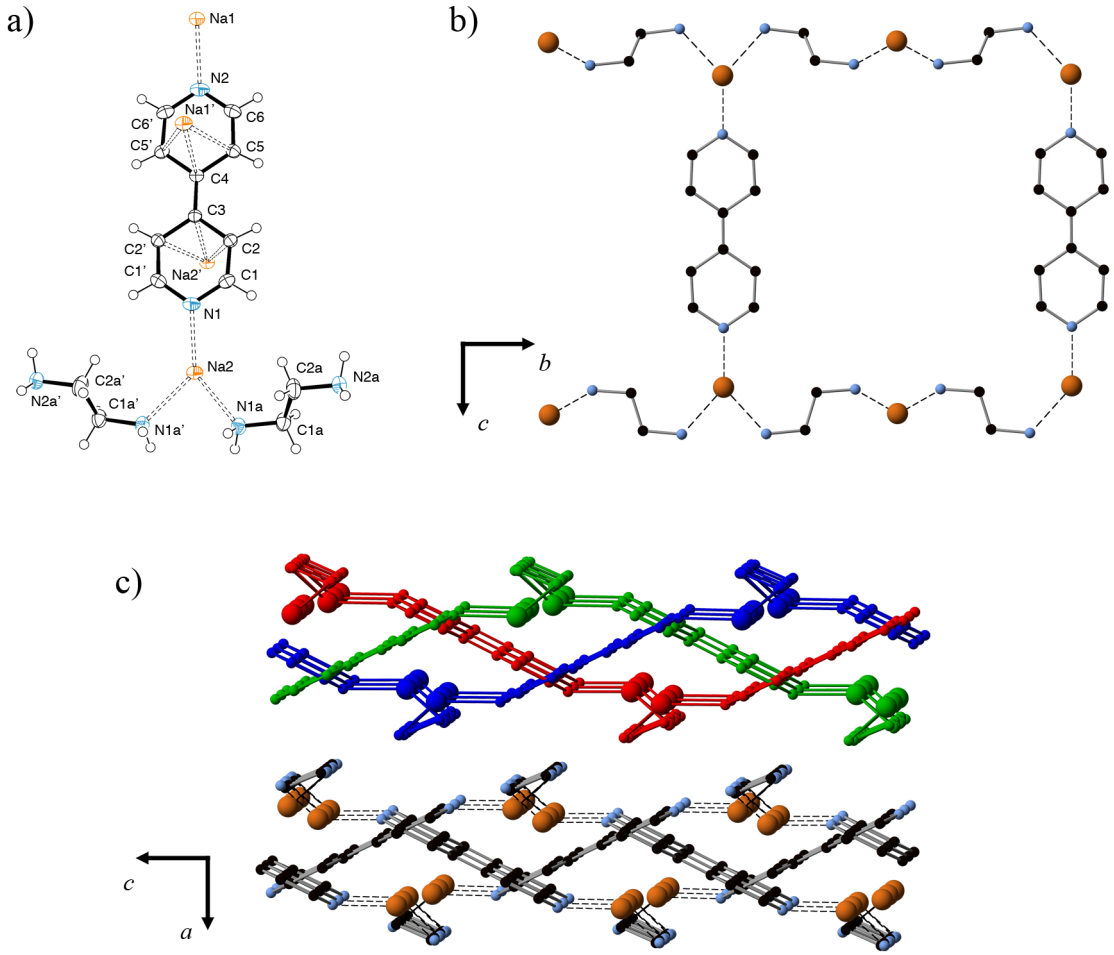



Figure 2.19: (**a**) Thermal ellipsoid representation of the atoms in the asymmetric unit of **7a**. Atom positions are labelled with primes to denote symmetry generated equivalents included to illustrate coordination environment. Anisotropic displacement ellipsoids pictured at the 50% probability level. (**b**) One of the three interpenetrated sheets present in a layer viewed along the crystallographic *a* axis. (**c**) Packing diagram showing two adjacent layers. The three interpenetrated sheets are shown in different colours on the top layer. This view along the crystallographic *b* axis also highlights the lack of inter-layer interactions. Note that in (b) and (c), hydrogen atoms have been omitted for clarity.

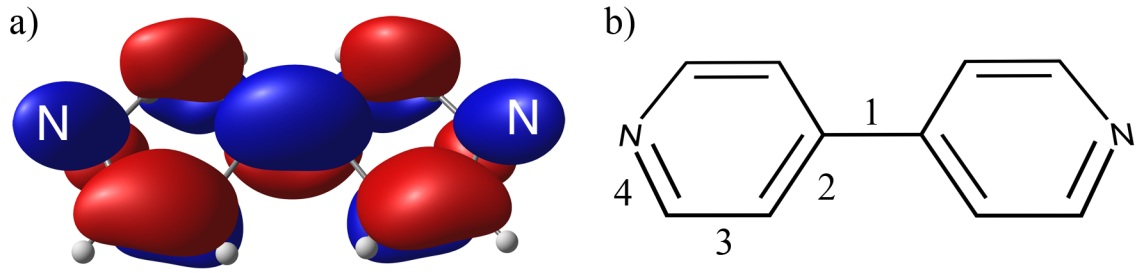



Figure 2.20: (**a**) DFT calculated 4,4´-bipy LUMO showing the alternating bonding and antibonding interactions in the π manifold. (**b**) Numbering scheme used in describing bond metric changes.

Na1–C2 and Na1–C3, respectively. Bulk sample composition was corroborated by elemental microanalysis.

#### 2.5.2.3 Spectroscopic Characterisation

As with the other bipyridyl dianion isomers already discussed in this chapter, EPR measurements on solid samples of **7** reveal a very weak resonance of the same shape and position as that of the 4,4´-bipyridyl radical anion. This indicates that a small amount of the singly reduced species remains, despite the excess of sodium used in the synthesis of the dianion. Alternatively, a small amount of decomposition may occur in the course of sample manipulations, causing partial oxidation to form trace amounts of the radical.

The Raman spectra of multiple samples of **7** look very similar to that of the singly reduced species **6** and as such no useful diagnostic bands may be identified in this instance.

### 2.5.3 Electronic Structure and Bond Metrics

When comparing bond metric data from the crystal structures of neutral 4,4´-bipyridine and its reduced forms in **6a**, **6b**, **7a** and **7b**, a strong correlation between bond lengths and bipyridine oxidation state emerges. Analogous DFT calculations to those used

| | 4,4´-bipy | | 4,4´-bipy$^{\bullet-}$ | | | 4,4´-bipy$^{2-}$ | | |
|---|---|---|---|---|---|---|---|---|
| Bond: | CSD[35] | [DFT] | **6a** | **6b** | [DFT] | **7a** | **7b** | [DFT] |
| 1 | 1.484(av) | [1.494] | 1.424(3) | 1.425(av) | [1.435] | 1.383(3) | 1.384(8) | [1.392] |
| 2 | 1.390(av) | [1.407] | 1.427(av) | 1.424(av) | [1.440] | 1.465(av) | 1.460(4) | [1.472] |
| 3 | 1.383(av) | [1.394] | 1.368(av) | 1.368(av) | [1.382] | 1.364(av) | 1.359(4) | [1.378] |
| 4 | 1.336(av) | [1.356] | 1.357(av) | 1.354(av) | [1.377] | 1.378(av) | 1.369(4) | [1.395] |

Table 2.9: Bond lengths for neutral 4,4´-bipyridine and its reduced forms in **6a**, **6b**, **7a** and **7b**. When multiple crystallographically unique bonds are present in a structure, mean lengths are given. Values in square brackets come from geometry optimised structures using DFT calculations. All bond lengths are in Å.

for the 2,2´- and 2,4´-bipy isomers again show that the neutral species LUMO is very similar to the radical species SOMO and to the dianionic species HOMO, and that it is this orbital that becomes incrementally populated upon ligand reduction. The orbital has overall π-antibonding character but contains localised bonding and antibonding regions on alternate bonds. This is shown in Figure 4.18 along with a bond numbering scheme. Areas with a local bonding interaction are expected to incrementally shorten upon orbital occupation as the bond order increases, whilst those areas with a local antibonding interaction are expected to elongate due to a decreased bond order. As such, bonds 1 and 3 are expected to shorten whilst bonds 2 and 4 are expected to lengthen with successive reductions. Again, experimental results follow the predicted trends with the inter-ring bond, bond 1, showing the greatest changes: 1.484(av) Å in the neutral species, reducing to 1.424(av) Å in the radical anion and further contracting to 1.384(av) Å in the dianion. These bond lengths and trends are mirrored by the unrestricted geometry optimised structures from DFT calculations as can be seen in Figure 2.21 and Table 4.2.

Torsion angles between the pyridyl rings of 4,4´-bipyridine are perhaps the most likely of all the bipyridine isomers to provide a diagnostic means to determine oxidation state as the linker is free to rotate about this axis without the changes to bonding that would typically accompany such a motion in the 2,2´ or 4,4´-bipyridine isomers. Theoretical studies have show that the preferred torsion angle for the neutral species

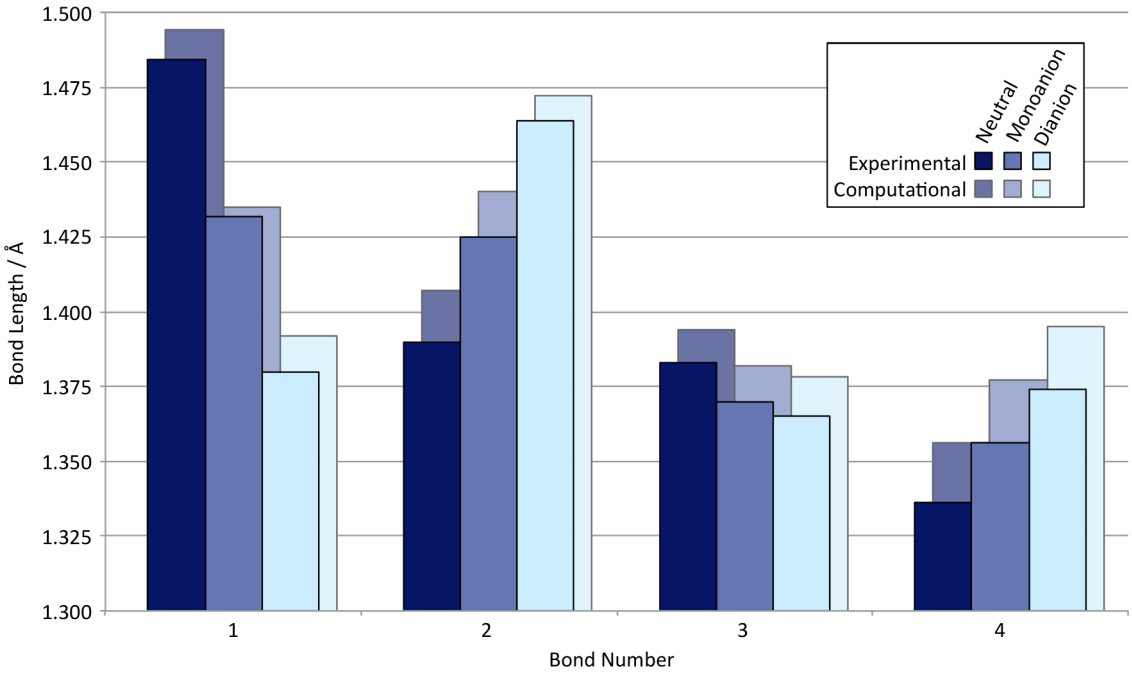



Figure 2.21: Graphical comparison of experimental and calculated bond lengths in 4,4´-bipyridine and its reduced forms in **6** and **7**.

of 4,4´-bipyridine is 40.8°,[68] with the rings expected to become increasingly coplanar as successive reductions add increasing double-bond character to bond 1. The mean torsional angle of structures in the CSD is 18°,[35] however many near planar examples do exist and so lattice effects appear dominant. The mean torsion angles for the singly and doubly reduced species are 0.815° and 1.93°, respectively, meaning that this remains unusable as a diagnostic metric, even in the case of 4,4´-bipyridine.

## 2.6 Summary of Chapter 2

This chapter details the synthesis and structural characterisation of the single and double reduction products of the 2,2´, 2,4´ and 4,4´-bipyridine isomers. In all cases results are compared to literature values (where available) and explained by reference to DFT calculated models. The following chapters build upon this work by examining the incorporation of reduced bipyridine ligands in a range of transition metal

complexes.

The study of 4,4´-bipyridine reduction products was carried out in the course of the final year of my undergraduate degree.

The research in this chapter has been published in peer reviewed journals.[69,70]

## 2.7 References


[1] Carrington, A.; dos Santosveiga, J. *Mol. Phys.* **1962**, *5*, 21.

[2] Saito, Y.; Takemoto, J.; B, H.; Nakamoto, K. *Inorg. Chem.* **1972**, *11*, 2003.

[3] Kawashima, H.; Kato, T.; Shida, T. *J. Raman Spectrosc.* **1991**, *22*, 187.

[4] Castella-Ventura, M.; Kassab, E.; Buntinx, G.; Poizat, O. *PCCP* **2000**, *2*, 4682.

[5] Danzer, G. D.; Golus, J. A.; Strommen, D. P.; Kincaid, J. R. *J. Raman Spectrosc.* **1990**, *21*, 3.

[6] Bradley, P. G.; Kress, N.; Hornberger, B. A.; Dallinger, R. F.; Woodruff, W. H. *J. Am. Chem. Soc.* **1981**, *103*, 7441.

[7] Oe, S.; Fukushima, K. *J. Mol. Struct.* **1990**, *223*, 337.

[8] Kihara, H.; Gondo, Y. *J. Raman Spectrosc.* **1986**, *17*, 263.

[9] Konig, E.; Herzog, S. *J. Inorg. Nucl. Chem.* **1970**, *32*, 585.

[10] Mahon, C.; Reynolds, W. L. *Inorg. Chem.* **1967**, *6*, 1927.

[11] Konig, E.; Kremer, S. *Chem. Phys. Lett.* **1970**, *5*, 87.

[12] Zahlan, A.; Heineken, F. W.; Bruin, M.; Bruin, F. *J. Chem. Phys.* **1962**, *37*, 683.

[13] Veiga, J. D. S.; Reynolds, W. L.; Bolton, J. R. *J. Chem. Phys.* **1966**, *44*, 2214.

[14] Henning, J. C. M. *J. Chem. Phys.* **1966**, *44*, 2139.

[15] Van Voorst, J. D. W.; Zijlstra, W. G.; Sitters, R. *Chem. Phys. Lett.* **1967**, *1*, 321.

[16] Konig, E.; Fischer, H. *Z. Naturforsch. A.* **1962**, *A 17*, 1063.

[17] Kaim, W. *Ber.* **1981**, *114*, 3789.

[18] Brown, O. R.; Butterfield, R. J. *Electrochim. Acta* **1982**, *27*, 321.

[19] Ne, T.; Re, H.; Bard, A. J. *J. Am. Chem. Soc.* **1973**, *95*, 6582.

[20] Yang, L.; Wimmer, F. L.; Wimmer, S.; Zhao, J. X.; Braterman, P. S. *J. Organomet. Chem.* **1996**, *525*, 1.

[21] Braterman, P. S.; Song, J. I. *J. Org. Chem.* **1991**, *56*, 4678.

[22] Kalyanaraman, V.; Rao, C. N. R.; George, M. V. *J. Chem. Soc. B* **1971**, 2406.

[23] Roullier, L.; Laviron, E. *Electrochim. Acta* **1978**, *23*, 773.

[24] Ould-Moussa, L.; Poizat, O.; Castella-Ventura, M.; Buntinx, G.; Kassab, E. *J. Phys. Chem.* **1996**, *100*, 2072.

[25] Castella-Ventura, M.; Kassab, E. *J. Raman Spectrosc.* **1998**, *29*, 511.

[26] Diez, R. P.; Jubert, A. H.; Ottavianelli, E. *J. Mol. Struct.* **1993**, *106*, 241.

[27] Bock, H.; Lehn, J. M.; Pauls, J.; Holl, S.; Krenzel, V. *Angew. Chem. Int. Ed.* **1999**, *38*, 952.

[28] Evans, W. J.; Gonzales, S. L.; Ziller, J. W. *J. Am. Chem. Soc.* **1994**, *116*, 2600.

[29] Zi, G. F.; Jia, L.; Werkema, E. L.; Walter, M. D.; Gottfriedsen, J. P.; Andersen, R. A. *Organometallics* **2005**, *24*, 4251.

[30] Mansell, S. M.; Adams, C. J.; Bramham, G.; Haddow, M. F.; Kaim, W.; Norman, N. C.; McGrady, J. E.; Russell, C. A.; Udeen, S. J. *Chem. Commun.* **2010**, *46*, 5070.

[31] Ruoff, R. S.; Kadish, K. M.; Boulas, P.; Chen, E. C. M. *J. Phys. Chem.* **1995**, *99*, 8843.

[32] Bratsch, S. G. *J. Phys. Chem. Ref. Data* **1989**, *18*, 1.

[33] Bratsch, S. G.; Lagowski, J. J. *J. Solution Chem.* **1987**, *16*, 583.

[34] Wilkinson, G.; Gillard, R. D.; McCleverty, J. A.; Reedijk, J. *Heterocyclic Nitrogen-donor Ligands in Comprehensive Coordination Chemistry: The Synthesis, Reactions, Properties and Applications of Coordination Compounds*; Pergamon Press: Oxford, U.K., 1987; Vol. 2.

[35] *Numbers taken from the Cambridge Structural Database (CSD) Version 5.33 Update 2*; Feb 2012.

[36] Kaim, W. *Coord. Chem. Rev.* **1987**, *76*, 187.

[37] Creutz, C. *Comment. Inorg. Chem.* **1982**, *1*, 293.

[38] Schultz, M.; Boncella, J. M.; Berg, D. J.; Tilley, T. D.; Andersen, R. A. *Organometallics* **2002**, *21*, 460.

[39] Walter, M. D.; Berg, D. J.; Andersen, R. A. *Organometallics* **2006**, *25*, 3228.

[40] Booth, C. H.; Walter, M. D.; Kazhdan, D.; Hu, Y. J.; Lukens, W. W.; Bauer, E. D.; Maron, L.; Eisenstein, O.; Andersen, R. A. *J. Am. Chem. Soc.* **2009**, *131*, 6480.

[41] Chisholm, M. H.; Huffman, J. C.; Rothwell, I. P.; Bradley, P. G.; Kress, N.; Woodruff, W. H. *J. Am. Chem. Soc.* **1981**, *103*, 4945.

[42] Mork, B. V.; McMillan, A.; Yuen, H.; Tilley, T. D. *Organometallics* **2004**, *23*, 2855.

[43] Lenges, C. P.; White, P. S.; Marshall, W. J.; Brookhart, M. *Organometallics* **2000**, *19*, 1247.

[44] Radonovich, L. J.; Eyring, M. W.; Groshens, T. J.; Klabunde, K. J. *J. Am. Chem. Soc.* **1982**, *104*, 2816.

[45] Echegoyen, L.; DeCian, A.; Fischer, J.; Lehn, J.-M. *Angew. Chem. Int. Ed. Engl.* **1991**, *30*, 838.

[46] McGarrity, J. F.; Ogle, C. A. *J. Am. Chem. Soc.* **1985**, *107*, 1805.

[47] Ogle, C. A.; Bates, R. B. *Carbanion chemistry*; Springer-Verlag: Berlin ;, 1983.

[48] Jackman, L. M.; Lange, B. C. *Tetrahedron* **1977**, *33*, 2737.

[49] Wilkinson, G.; Stone, F.; Abel, E.; Wardell, J. *Alkali Metals in Comprehensive Organometallic Chemistry*; Pergamon Press: Oxford, U.K., 1982; Vol. 1.

[50] Buchholz, S.; Harms, K.; Marsch, M.; Massa, W.; Boche, G. *Angew. Chem. Int. Ed. Engl.* **1989**, *28*, 72.

[51] Giese, H. H.; Habereder, T.; Knizek, J.; Noth, H.; Warchhold, M. *Eur. J. Inorg. Chem.* **2001**, 1195.

[52] Wang, G. C.; Haushalter, R. C. *Inorg. Chem.* **1997**, *36*, 3806.

[53] Jones, C. D. W.; DiSalvo, F. J.; Haushalter, R. C. *Inorg. Chem.* **1998**, *37*, 821.

[54] Rabe, G. W.; Heise, H.; Yap, G. P. A.; Liable-Sands, L. M.; Guzei, I. A.; Rheingold, A. L. *Inorg. Chem.* **1998**, *37*, 4235.

[55] Stoll, S.; Schweiger, A. *J. Magn. Reson.* **2006**, *178*, 42.

[56] Fedushkin, I. L.; Petrovskaya, T. V.; Girgsdies, F.; Kohn, R. D.; Bochkarev, M. N.; Schumann, H. *Angew. Chem. Int. Ed.* **1999**, *38*, 2262.

[57] Weil, J.; Bolton, J. *Electron Paramagnetic Resonance: Elementary Theory and Practical Applications*; Wiley, 2007.

[58] Frisch, M. J.; Trucks, G. W.; Schlegel, H. B.; Scuseria, G. E.; Robb, M. A.; Cheeseman, J. R.; Montgomery, J. A., Jr.; Vreven, T.; Kudin, K. N.; Burant, J. C.; Millam, J. M.; Iyengar, S. S.; Tomasi, J.; Barone, V.; Mennucci, B.; Cossi, M.; Scalmani, G.; Rega, N.; Petersson, G. A.; Nakatsuji, H.; Hada, M.; Ehara, M.; Toyota, K.; Fukuda, R.; Hasegawa, J.; Ishida, M.; Nakajima, T.; Honda, Y.; Kitao, O.; Nakai, H.; Klene, M.; Li, X.; Knox, J. E.; Hratchian, H. P.; Cross, J. B.; Bakken, V.; Adamo, C.; Jaramillo, J.; Gomperts, R.; Stratmann, R. E.; Yazyev, O.; Austin, A. J.; Cammi, R.; Pomelli, C.; Ochterski, J. W.; Ayala, P. Y.; Morokuma, K.; Voth, G. A.; Salvador, P.; Dannenberg, J. J.; Zakrzewski, V. G.; Dapprich, S.; Daniels, A. D.; Strain, M. C.; Farkas, O.; Malick, D. K.; Rabuck, A. D.; Raghavachari, K.; Foresman, J. B.; Ortiz, J. V.; Cui, Q.; Baboul, A. G.; Clifford, S.; Cioslowski, J.; Stefanov, B. B.; Liu, G.; Liashenko, A.; Piskorz, P.; Komaromi, I.; Martin, R. L.; Fox, D. J.; Keith, T.; Al-Laham, M. A.; Peng, C. Y.; Nanayakkara, A.; Challacombe, M.; Gill, P. M. W.; Johnson, B.; Chen, W.; Wong, M. W.; Gonzalez, C.; Pople, J. A. *Gaussian03, Revision D.01*; Gaussian Inc: Wallingford, CT, 2004.

[59] Syssa-Magale, J. L.; Boubekeur, K.; Palvadeau, P.; Meerschaut, A.; Schollhorn, B. *CrystEngComm* **2005**, *7*, 302.

[60] Morimoto, M.; Irie, M. *Chem. Eur. J.* **2006**, *12*, 4275.

[61] Tong, M.; Ye, B.; Cai, J.; Chen, X.; Ng, S. *Inorg. Chem.* **1998**, *37*, 2645.

[62] Stang, P. *Chem. Eur. J.* **1998**, *4*, 19.

[63] Olenyuk, B.; Fechtenkotter, A.; Stang, P. *J. Chem. Soc., Dalton Trans.* **1998**, 1707.

[64] Jones, C. *Chem. Soc. Rev.* **1998**, *27*, 289.

[65] Yaghi, O.; Li, H.; Davis, C.; Richardson, D.; Groy, T. *Acc. Chem. Res.* **1998**, *31*, 474.

[66] Kitagawa, S.; Kitaura, R.; Noro, S. *Angew. Chem. Int. Ed.* **2004**, *43*, 2334.

[67] James, S. L. *Chem. Soc. Rev.* **2003**, *32*, 276.

[68] Barone, V.; Lelj, F.; Cauletti, C.; Piancastelli, M. N.; Russo, N. *Mol. Phys.* **1983**, *49*, 599.

[69] Denning, M. S.; Irwin, M.; Goicoechea, J. M. *Inorg. Chem.* **2008**, *47*, 6118.

[70] Gore-Randall, E.; Irwin, M.; Denning, M. S.; Goicoechea, J. M. *Inorg. Chem.* **2009**, *48*, 8304.

# Chapter 3

# Reduction of Transition Metal Complexes of 2,2´-Bipyridine

## 3.1 Introduction

The ability of 2,2´-bipyridine to act as a bidentate ligand to elements from all areas of the periodic table has resulted in its incorporation into a vast number of complexes making it a ubiquitous ligand in the field of coordination chemistry.[1–3] One result of this extensive use is that there exists a large volume of data reported in the chemical literature documenting the properties of both bipyridine itself and of the complexes it forms.

The reduction of 2,2´-bipyridine to yield its radical anionic and dianionic forms has been well established, as discussed in Chapter 2. DFT calculations were used to rationalise changes in bond metrics, determined experimentally from single crystal X-ray diffraction studies. These show that chemical reduction involves the stepwise population of an energetically low-lying bipyridine π orbital with overall antibonding character (Figure 3.1a). Nodes between bonds and the resulting opposing phases of the orbital around adjacent bonds causes alternating bond elongation and contrac-

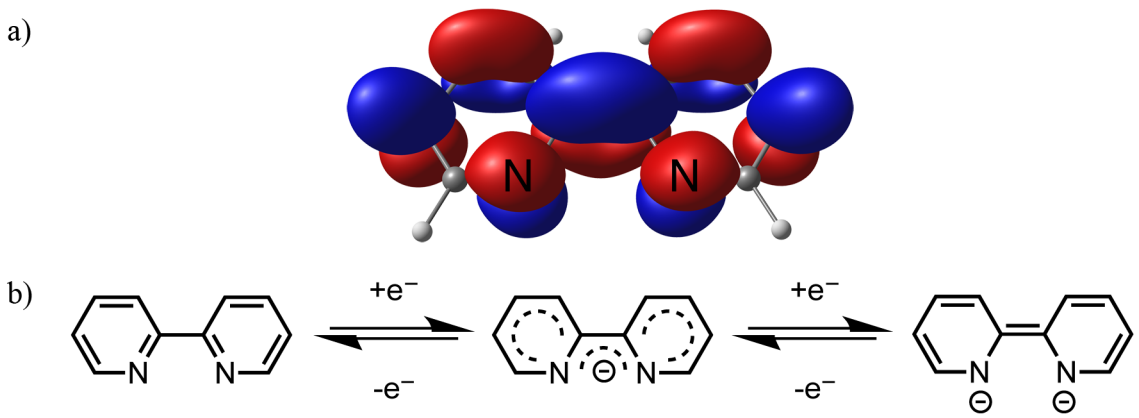



Figure 3.1: (**a**) The LUMO of neutral 2,2´-bipyridine. (**b**) Lewis structure representations of the neutral, radical anionic and dianionic forms of 2,2´-bipyridine, rationalising the decrease in inter-ring bond length.

tion as the orbital is populated, with the largest change occuring at the previously identified inter-ring bond which was found to contract in statistically significant steps from approximately 1.49 Å in the neutral species, to 1.43 Å in the singly reduced radical anion and to 1.39 Å in the dianion (Figure 3.1b).[4]

### 3.1.1 Structurally Characterised Compounds Containing Reduced 2,2´-Bipyridyl Ligands

Several main group, lanthanide and actinide complexes incorporating reduced forms of bipyridine have been synthesised and structurally characterised. These findings are briefly summarised here, with reference to the diagnostic bond metric data determined from the alkali metal salts detailed in the previous chapter.

#### 3.1.1.1 Main Group Compounds

Structures containing reduced forms of 2,2´-bipyridine have been reported for five main group compounds. The crystal structure of the earliest reported example, Si(2,2´-bipy)$_2$ from 1979, was determined using considerably poorer instrumentation than is available today (Figure 3.2).[5] Large esd values and anisotropic refinement

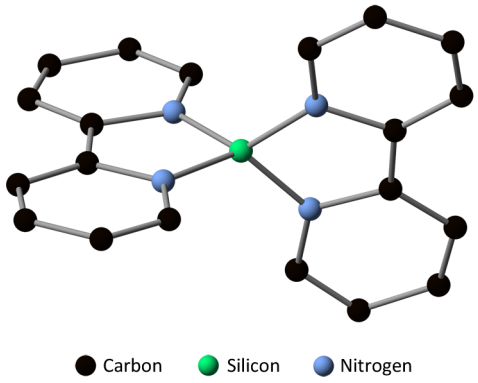



Figure 3.2: Crystal structure of Si(2,2´-bipy)$_2$. Hydrogen atoms have been omitted for clarity.[5]

of the silicon atom alone prevent a rigorous interpretation of the X-ray data, but inter-pyridyl bond lengths of 1.34(1) and 1.35(1) Å are certainly consistent with the authors interpretation of the compound's electronic configuration, namely an Si(IV) cation and two doubly reduced bipyridyl ligands.

The remaining four structures were published far more recently and benefit from extensive improvements in single crystal X-ray diffraction experiment techniques. In 2003 the anion [Al(2,2´-bipy)$_2$]$^-$ was characterised in [Li(THF)$_4$][Al(2,2´-bipy)$_2$], displaying bipyridyl inter-ring bonds of 1.365 and 1.371 Å (no esd values given, Figure 3.3).[6] Though the bond metrics and intuitive charge assignments suggest the complex should contain two dianionic ligands, NMR and computational studies indicate that the charge on aluminium is non-integer, lying between 2+ and 3+, requiring some radical anionic ligand character.

Most recently, three related boron complexes were reported by Russell, Norman and co-workers.[7,8] BCl$_2$(2,2´-bipy), BCl(2,2´-bipy) and BPh(2,2´-bipy) (Figure 3.4) crystallise with inter-ring bond lengths of 1.413(3), 1.379(2) and 1.380(av) Å, respectively. This corroborates EPR or NMR (as appropriate) spectroscopic results and DFT calculations supporting the assignment of the first compound as containing a radial monoanionic bipyridyl ligand and the latter two as containing dianionic ligands.

A summary of these findings is presented in Table 3.1.

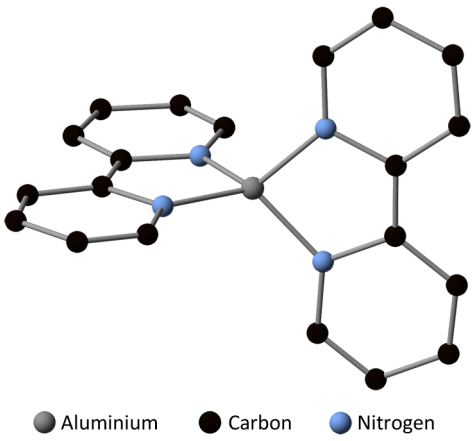



Figure 3.3: Crystal structure of the $[Al(2,2´\text{-bipy})_2]^-$ anion structurally characterised in $[Li(THF)_4][Al(2,2´\text{-bipy})_2]$. Hydrogen atoms have been omitted for clarity.[6]

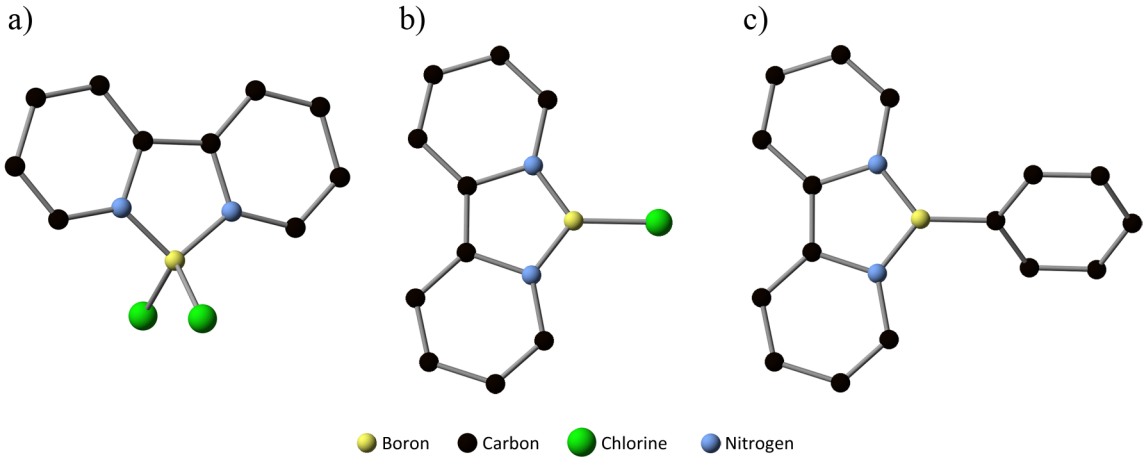



Figure 3.4: Crystal structures of (**a**) $BCl_2(2,2´\text{-bipy})$ (**b**) $BCl(2,2´\text{-bipy})$ and (**c**) $BPh(2,2´\text{-bipy})$. Hydrogen atoms have been omitted for clarity.[7,8]

| Compound: | Inter-pyridyl bond length (Å): | Proposed electronic configuration: |
|---|---|---|
| $Si(2,2´\text{-bipy})_2$ | 1.34(1), 1.35(1) | $Si(IV)[(2,2´\text{-bipy})^{2-}]_2$ |
| $[Li(THF)_4][Al(2,2´\text{-bipy})_2]$ | 1.365, 1.371 | $[Al(III)[(2,2´\text{-bipy})^{2-}]_2]^-$ |
| $[BCl_2(2,2´\text{-bipy})]$ | 1.413(3) | $BCl_2[(2,2´\text{-bipy})^{\bullet-}]$ |
| $[BCl(2,2´\text{-bipy})]$ | 1.379(2) | $BCl[(2,2´\text{-bipy})^{2-}]$ |
| $[BPh(2,2´\text{-bipy})]$ | 1.380(av) | $BPh[(2,2´\text{-bipy})^{2-}]$ |

Table 3.1: Summary of inter-pyridyl bond distances and proposed electronic configurations for the main group compounds discussed in this section.

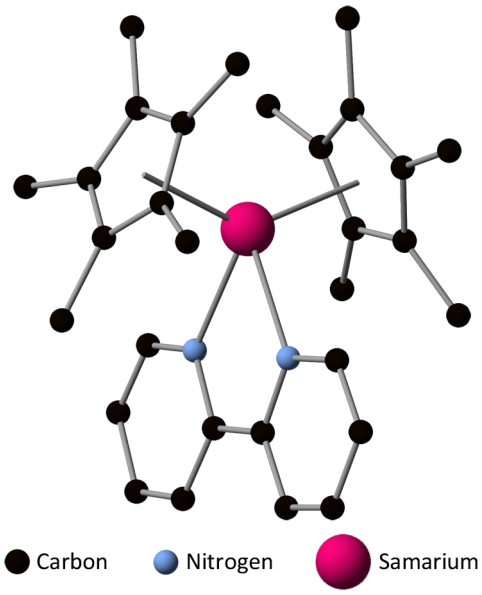



Figure 3.5: Crystal structure of $Cp^*_2Sm(2,2´\text{-bipy})$ ($Cp^* = C_5Me_5$). Hydrogen atoms have been omitted for clarity.[9]

#### 3.1.1.2 Lanthanide Compounds

While ligand bonding within lanthanide compounds is often interpreted as being highly ionic in character, there is potential for multiple cation oxidation states in the presence of redox active ligands such as 2,2´-bipyridine. This phenomenon has made the study of these species far from trivial. For example, in 1989 Evans and co-workers structurally characterised $Cp^*_2Sm(2,2´\text{-bipy})$ ($Cp^* = C_5Me_5$, Figure 3.5).[9] This compound may be rationalised within two competing formulations; either as a Sm(II) site coordinated by a neutral bipyridine ligand, or as a Sm(III) site coordinated by a radical anionic bipyridyl ligand. The structural data reveal an inter-ring bond length of 1.429(4) Å, making a case for the Sm(III) assignment, which was corroborated by NMR and IR studies.

The ytterbium analogue of this structure, $Cp^*_2Yb(2,2´\text{-bipy})$, was structurally characterised in 2002 by Tilley, Andersen and co-workers (Figure 3.6a).[10] The authors report a bipyridyl inter-ring bond length of 1.383(av) Å which suggested the presence of a reduced bipyridyl ligand. Subsequent EPR, SQUID and DFT measurements were

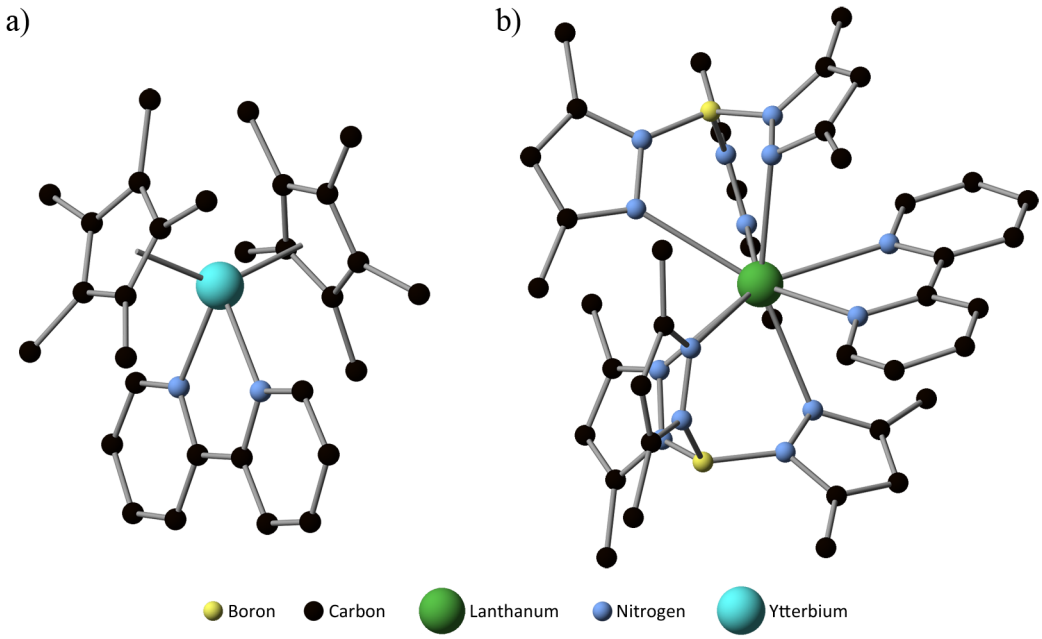



Figure 3.6: Crystal structures of (**a**) La($Tp^{Me_2}$)$_2$(2,2´-bipy) ($Tp^{Me_2}$ = hydrotris(3,5-dimethylpyrazolyl)borate and (**b**) Cp*$_2$Yb(2,2´-bipy). Hydrogen atoms have been omitted for clarity.[10,13]

used to investigate the electronic structure of this system which was found to have a significant temperature dependance, varying between $(Me_5C_5)_2$Yb(II)(2,2´-bipy) and $(Me_5C_5)_2$Yb(III)[(2,2´-bipy)$^{\bullet-}$].[11,12]

NMR spectroscopy and SQUID magnetometry were used by Roitershtein and co-workers in 2003 to demonstrate the presence of a singly reduced bipyridyl radical anion in La($Tp^{Me_2}$)$_2$(2,2´-bipy) ($Tp^{Me_2}$ = hydrotris(3,5-dimethylpyrazolyl)borate which was crystallographically characterised and exhibited a bipyridyl inter-ring bond distance of 1.44(2) Å (Figure 3.6b).[13] NMR studies revealed a spectrum containing no resonances associated with the bipyridyl ligand while the magnetic response recorded was consistent with a single unpaired electron.

A summary of these findings is presented in Table 3.2.

| Compound: | Inter-pyridyl bond length (Å): | Proposed electronic configuration: |
|---|---|---|
| $Cp^*_2Sm(2,2´\text{-bipy})$ | 1.429(4) | $Cp^*_2Sm(III)[(2,2´\text{-bipy})^{\bullet-}]$ |
| $Cp^*_2Yb(2,2´\text{-bipy})$ | 1.383(av) | $Cp^*_2Yb(III)[(2,2´\text{-bipy})^{\bullet-}]$ |
| $La(Tp^{Me_2})_2(2,2´\text{-bipy})$ | 1.44(2) | $La(III)(Tp^{Me_2})_2[(2,2´\text{-bipy})^{\bullet-}]$ |

Table 3.2: Summary of inter-pyridyl bond distances and proposed electronic configurations for the lanthanide compounds discussed in this section.

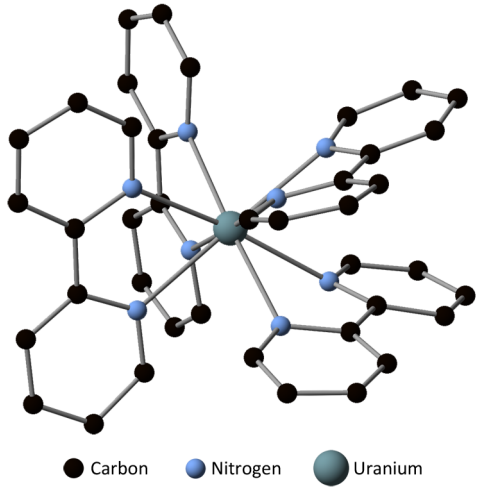



Figure 3.7: Crystal structure of $U(2,2´\text{-bipy})_4$. Hydrogen atoms were not modelled in the literature structure.[14]

#### 3.1.1.3 Actinide Compounds

The earliest structurally characterised actinide complex containing a 2,2´-bipyridine ligand with a short inter-pyridyl bond distance was published in 1975. Despite a reported short inter-pyridyl ring bond length of 1.416(av) Å, $U(2,2´\text{-bipy})_4$ (Figure 3.7) was initially regarded as a U(0) compound.[14] Although esd values for this structure are large, it has been more recently discussed as a U(II) complex with two electrons delocalised across all four bipyridyl ligands. However without further characterisation no definitive analysis is possible.[15,16]

The oxidation state ambiguity in the previous complex is partially addressed by two related species, $Cp^*(C_8H_8)U(2,2´\text{-bipy})$ (Figure 3.8a) and $(Tp^{Me_2})_2U(2,2´\text{-bipy})$ ($Tp^{Me_2}$ = hydrotris(3,5-dimethylpyrazolyl)borate, Figure 3.8b). Both systems have

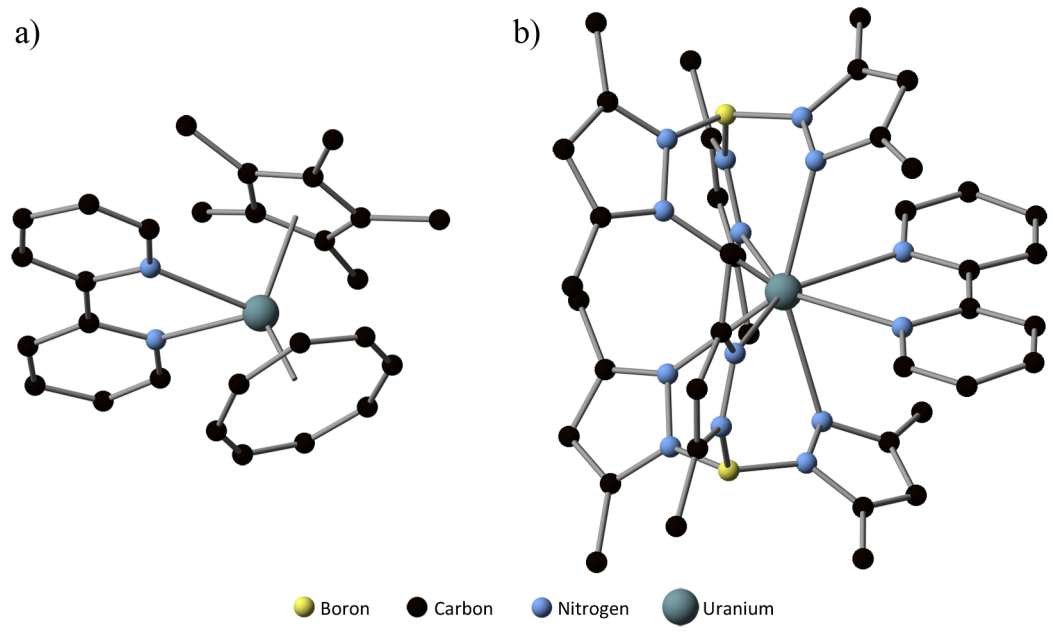



Figure 3.8: Crystal structures of (**a**) Cp*($C_8H_8$)U(2,2´-bipy) and (**b**) ($Tp^{Me_2}$)$_2$U(2,2´-bipy) ($Tp^{Me_2}$ = hydrotris(3,5-dimethylpyrazolyl)borate. Hydrogen atoms have been omitted for clarity.[17,18]

been discussed as U(II) complexes incorporating reduced bipyridyl ligands. Single crystal X-ray diffraction measurements reveal inter-ring bond lengths of 1.427(3) and 1.409(13) Å, respectively, which in conjunction with spectroscopic and theoretical investigations, strongly suggest the existence of singly reduced bipyridyl radical ligands in each complex.[17,18]

Most recently, the thorium complex ($\eta^5$-1,2,4($t$-Bu)$_3$C$_5$H$_2$)$_2$Th(2,2´-bipy) was crystallographically characterised (Figure 3.9) by Walter and co-workers.[19] The reported inter-pyridyl bond length of 1.382(8) Å is considerably shorter than those of the uranium complexes above. The potential presence of a 2,2´-bipyridyl dianion was confirmed by NMR studies: the $^1$H spectrum was consistent with a diamagnetic Th(IV) compound but showed unusual bipyridyl resonance shifts of between 7.08 and 5.29 ppm, attributed to reduced deshielding around the bipyridyl aromatic rings.

A summary of these findings is presented in Table 3.3.

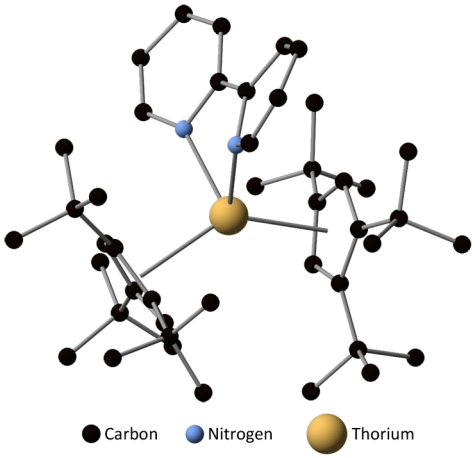



Figure 3.9: Crystal structure of ($\eta^5$-1,2,4($t$-Bu)$_3$C$_5$H$_2$)$_2$Th(2,2´-bipy). Hydrogen atoms have been omitted for clarity.[19]

| Compound: | Inter-pyridyl bond length (Å): | Proposed electronic configuration: |
|---|---|---|
| U(2,2´-bipy)$_4$ | 1.416(av) | U(II)(2,2´-bipy)$_2$[(2,2´-bipy)$^{\cdot-}$]$_2$ |
| Cp*(C$_8$H$_8$)U(2,2´-bipy) | 1.427(3) | Cp*(C$_8$H$_8$)U(II)[(2,2´-bipy)$^{\cdot-}$] |
| (Tp$^{Me_2}$)$_2$U(2,2´-bipy) | 1.409(13) | (Tp$^{Me_2}$)$_2$U(II)[(2,2´-bipy)$^{\cdot-}$] |
| (Cp$^{t\text{-}Bu_3}$)$_2$Th(2,2´-bipy) | 1.382(8) | (Cp$^{t\text{-}Bu_3}$)$_2$Th(IV)[(2,2´-bipy)$^{2-}$] |

Table 3.3: Summary of inter-pyridyl bond distances and proposed electronic configurations for the actinide compounds discussed in this section. Cp$^{t\text{-}Bu_3}$ = ($\eta^5$-1,2,4($t$-Bu)$_3$C$_5$H$_2$)

### 3.1.2 Transition Metal Compounds

There are far fewer transition metal complexes unequivocally shown to incorporate a reduced bipyridine ligand, none of which have been structurally characterised. The first example of such a complex was Na[$Cr(CO)_4$(2,2´-bipy)], synthesised via the alkali metal reduction of $Cr(CO)_4$(2,2´-bipy). Several independent studies have been carried out on this species and EPR, electronic absorption, IR spectroelectrochemistry and UV/Vis spectroscopy as well as DFT calculations indicate the presence of radical monoanionic character on the bipyridine ligand.[20,21] Small increases in electron density were calculated for all carbonyl groups in the reduced species. This increase in electron density was observed experimentally by IR spectroscopy, with the two equatorial CO ligands in particular found to be considerably weakened. This is explained as a consequence of significant π-backbonding from the electron rich bipyridyl radical anion to the metal d orbitals which can then donate electron density to the antibonding π*(CO) orbital.[22,23]

However, although no publications specifically report coordination complexes containing an anionic bipyridyl ligand, three structures exist in which bond metric data is consistent with the presence of a reduced bipyridyl moiety. These were discussed in detail in Chapter 1 and so only a brief summary is provided here.

The crystal structures of Mo(*i*-PrO)$_2$(2,2´-bipy)$_2$, Co($C_5Me_5$)(2,2´-bipy) and the anionic complex in [K(dibenzo-18-crown-6)][Ru($C_5Me_5$)(2,2´-bipy)] are shown in Figure 3.10.[24–26] The inter-pyridyl bond lengths in these ligands are 1.425(4), 1.419(3) and 1.401(9) Å, respectively, suggesting that the first two compounds may contain a bipyridyl radical monoanion while the latter system may contain a dianion. In the first two examples, unusual bonding is rationalised by reference to resonance canonicals and not by consideration of ligand reduction. The shorter bipyridyl inter-ring bond in the ruthenium complex was not discussed by the authors, but time resolved NMR measurements reveal a diamagnetic system that decomposes to give a param-

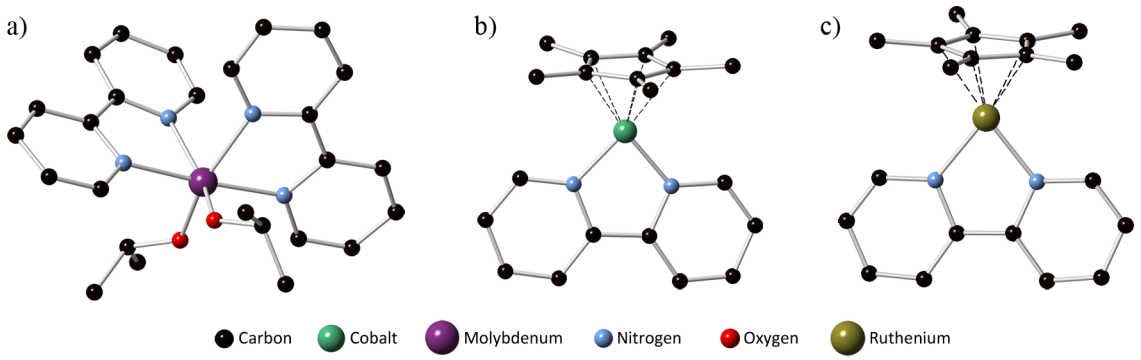



Figure 3.10: Crystal structures of (**a**) Mo(*i*-PrO)$_2$(2,2´-bipy)$_2$, (**b**) Co($C_5Me_5$)(2,2´-bipy) and (**c**) the anionic complex in [K(dibenzo-18-crown-6)][Ru($C_5Me_5$)(2,2´-bipy)]. Hydrogen atoms have been omitted for clarity.

agnetic response. Of particular note are two bipyridyl hydrogen resonances occuring at 5.87 and 5.57 ppm. These are considerably more shielded than might be ordinarily expected for an aromatic system and are very similar to the 5.29 ppm shift observed for the thorium complex discussed in the previous section. This provides some support for the existence of a doubly reduced bipyridyl ligand (which would be diamagnetic) that is slowly oxidised to the singly reduced (and paramagnetic) radical monoanion. The authors note that the high air- and moisture-sensitivity of the compound prevented a more rigorous analysis.

### 3.1.3 Non-Innocent Behaviour

When a ligand capable of existing in multiple oxidation states is coordinated to a central atom that may also be found in one of several oxidation states there can be ambiguities in assignment of electronic structure and the potential for non-innocent behaviour. For the alkali metal salts detailed in the previous chapter this uncertainty was not possible, but for a transition metal complex containing 2,2´-bipyridine there are up to three potential electronic structure assignments. Consider the hypothetical complex [$ML_n$(2,2´-bipy)]$^{m+}$; this could exist as [$ML_n$]$^{m+}$(2,2´-bipy), [$ML_n$]$^{(m+1)+}$(2,2´-bipy)$^{\bullet-}$ or [$ML_n$]$^{(m+2)+}$(2,2´-bipy)$^{2-}$. Distinguishing between such

species without EPR spectroscopy and magnetic data is highly challenging.

An additional subtlety is that reduction of the metal could conceivably lead to increased π-backbonding from an electron rich metal centre to the same bipyridine orbital that would be occupied by direct reduction of the ligand. Were this to happen there would be considerable difficulty associated with distinguishing the two effects. This problem has been identified and discussed in the literature with recent theoretical calculations suggesting that 2,2´-bipyridine is a poor π-acceptor and thus that if this donation does take place, its effect will not be great.[27–31]

The aim of the work reported in this chapter is the synthesis and characterisation of a homologous series of complexes where neutral and reduced forms of 2,2´-bipyridine are coordinated to dimesityl metal centres. Subsequently, trends in the magnetic and electronic properties of these compounds may be analysed to determine the extent to which X-ray structure bond metrics may be used as a tool in the identification of 2,2´-bipyridine ligand oxidation states in transition metal compounds. Furthermore, comparison of results across the series will be used to probe the level of π-backbonding that takes place.

## 3.2 Neutral Compounds: $[M(2,2´\text{-bipy})(mes)_2]^0$

The structures discussed here and in the next section (the reduced analogues) are subsequently analysed together allowing for trends and their potential causes to be discussed.

### 3.2.1 General Synthesis

The neutral species $M(2,2´\text{-bipy})(mes)_2$ (M = Cr, Mn, Fe, Co, Ni) discussed in this section were (with the exception of Ni) synthesised by the reaction of a $M(mes)_2$ containing precursor with 2,2´-bipyridine. Crystalline samples were obtained by the

slow diffusion of hexanes into a concentrated THF solution of the reaction products.

## 3.2.2 Synthesis and Structural Characterisation

### 3.2.2.1 Cr(2,2´-bipy)(mes)$_2$·THF

This compound was prepared following an adapted literature preparation.[32] Reaction of $CrCl_2$ with two equivalents of (mes)MgBr at –78 °C in THF and addition of an excess of 2,2´-bipyridine formed a purple solution and light purple precipitate. The purple solution was filtered and combined with multiple THF washings of the purple solid. Slow diffusion of hexanes into a concentrated THF solution yielded crystals of Cr(2,2´-bipy)(mes)$_2$·THF (**8**), while diffusion of benzene yielded Cr(2,2´-bipy)(mes)$_2$·1.5$C_6H_6$ (Figure 3.11). Solvent elimination from samples exposed to vacuum and subsequent loss of crystallinity prevented collection of powder X-ray data. An elemental microanalysis measurement was consistent with a solvent free composition.

### 3.2.2.2 Mn(2,2´-bipy)(mes)$_2$

Reaction of Mn(mes)$_2$ with 2,2´-bipyridine in THF caused the formation of a blue solution, which yielded small crystals of Mn(2,2´-bipy)(mes)$_2$ (**9**, Figure 3.12) upon slow diffusion of hexanes. Bulk purity of the solid was confirmed by both a powder X-ray diffraction pattern which was found to match that calculated from the single crystal X-ray diffraction data (Figure 3.13), and by elemental microanalysis.

### 3.2.2.3 Fe(2,2´-bipy)(mes)$_2$

As with the synthesis of **9**, reaction of $Fe_2(mes)_4$ with half an equivalent of 2,2´-bipyridine in THF, generated a deep red solution. Crystals from this solution were determined to be Fe(2,2´-bipy)(mes)$_2$ (**10**, Figure 3.14), with bulk sample purity

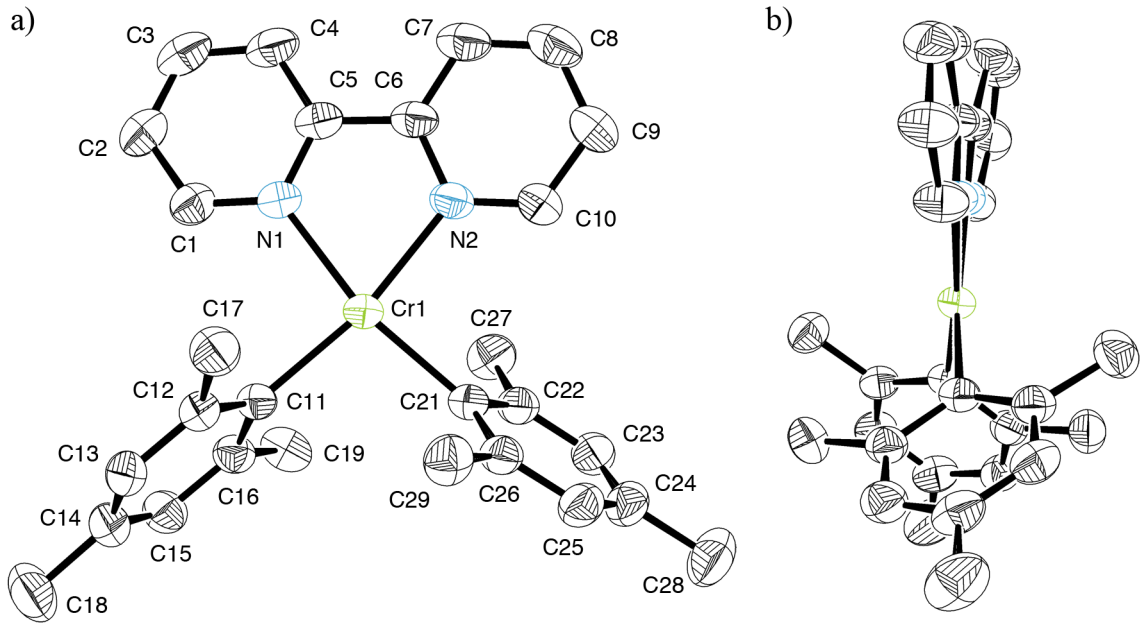



Figure 3.11: (**a**) Thermal ellipsoid representation of the asymmetric unit in **8**. (**b**) Orientation highlighting the pseudo square planar coordination environment, $\phi_{(Cr1,N1,N2)\text{-}(Cr1,C11,C12)} = 8.1^{\circ}$. Anisotropic displacement ellipsoids pictured at the 50% probability level. Hydrogen atoms and solvent molecules have been omitted for clarity.

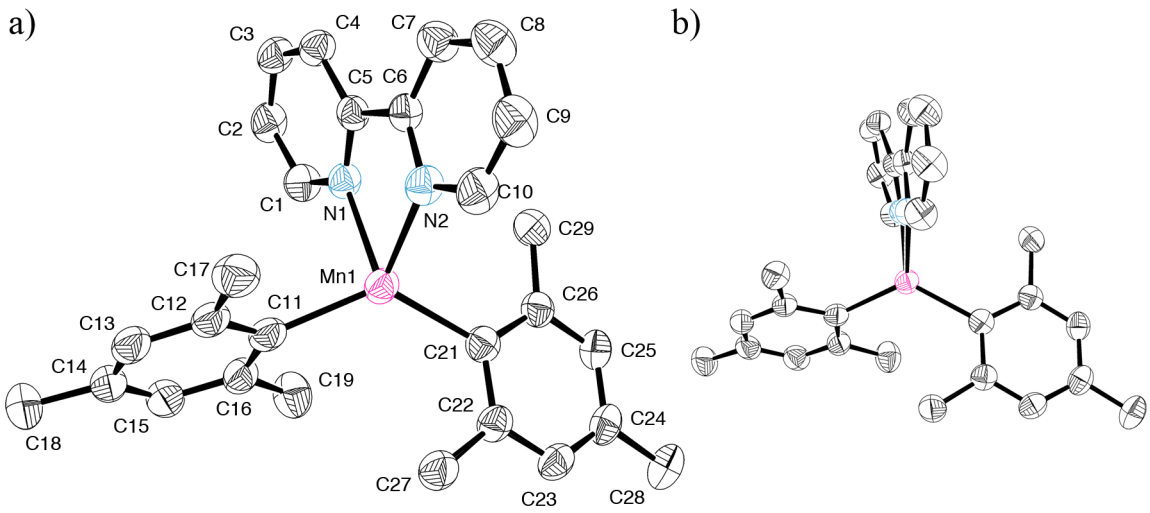



Figure 3.12: (**a**) Thermal ellipsoid representation of the asymmetric unit of **9**. (**b**) Orientation highlighting the pseudo tetrahedral coordination environment, $\phi_{(Mn1,N1,N2)\text{-}(Mn1,C11,C12)} = 70.6^{\circ}$. Anisotropic displacement ellipsoids pictured at the 50% probability level. Hydrogen atoms have been omitted for clarity.

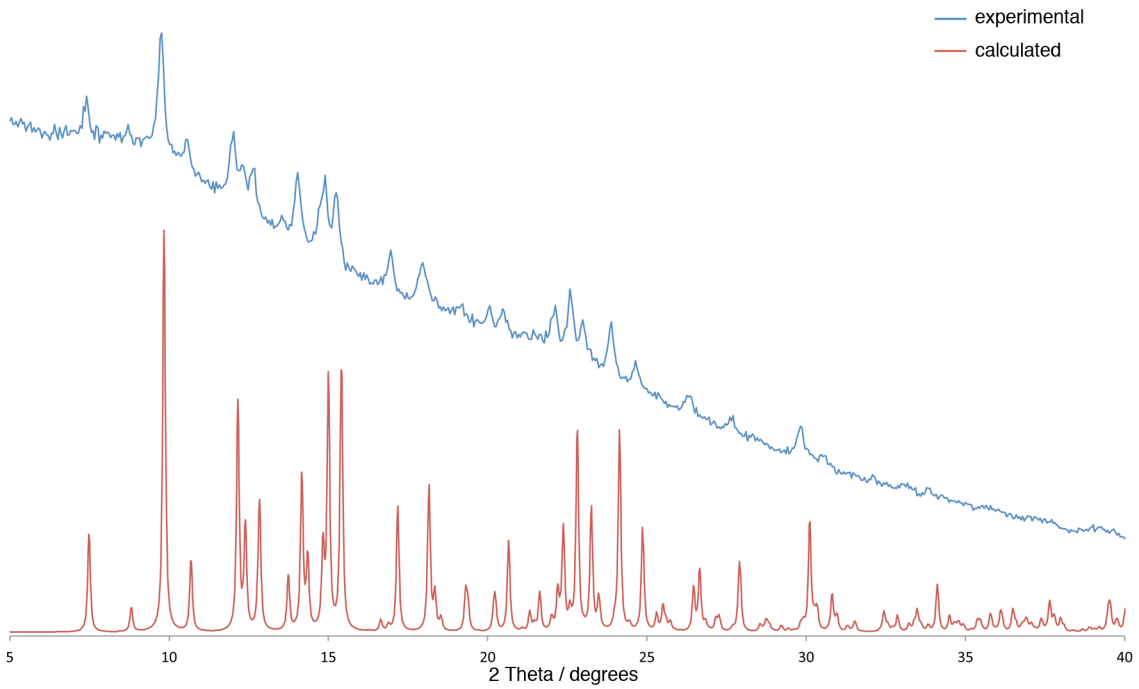



Figure 3.13: Comparison of calculated and experimental powder X-ray diffraction patterns for **9**.

confirmed by a powder X-ray diffraction pattern (Figure 3.15) and elemental microanalysis.

#### 3.2.2.4 Co(2,2´-bipy)(mes)$_2$·THF

Co(mes)$_2$(PPhEt$_2$)$_2$ and 2,2´-bipyridine were reacted together in THF to form a dark red solution, from which black crystals of Co(2,2´-bipy)(mes)$_2$·THF were isolated (**11**, Figure 3.16). A powder X-ray diffraction pattern was found to match that calculated from a separate room-temperature single crystal X-ray data collection (Figure 3.17) due to anisotropy in the unit cell expansion with temperature (no change of space group was observed). Table 3.4 lists the unit cell parameters at 150 and 293 K. Elemental microanalysis demonstrated compositional sample purity.

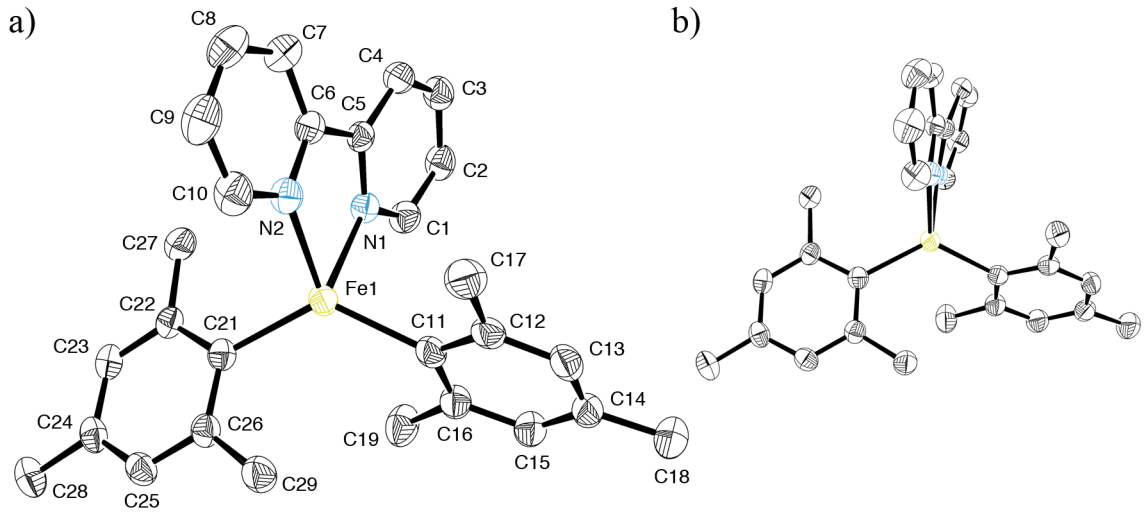



Figure 3.14: (**a**) Thermal ellipsoid representation of the asymmetric unit of **10**. (**b**) Orientation highlighting the pseudo tetrahedral coordination environment, $\phi_{(Fe1,N1,N2)\text{-}(Fe1,C11,C12)} = 70.2°$. Anisotropic displacement ellipsoids pictured at the 50% probability level. Hydrogen atoms have been omitted for clarity.

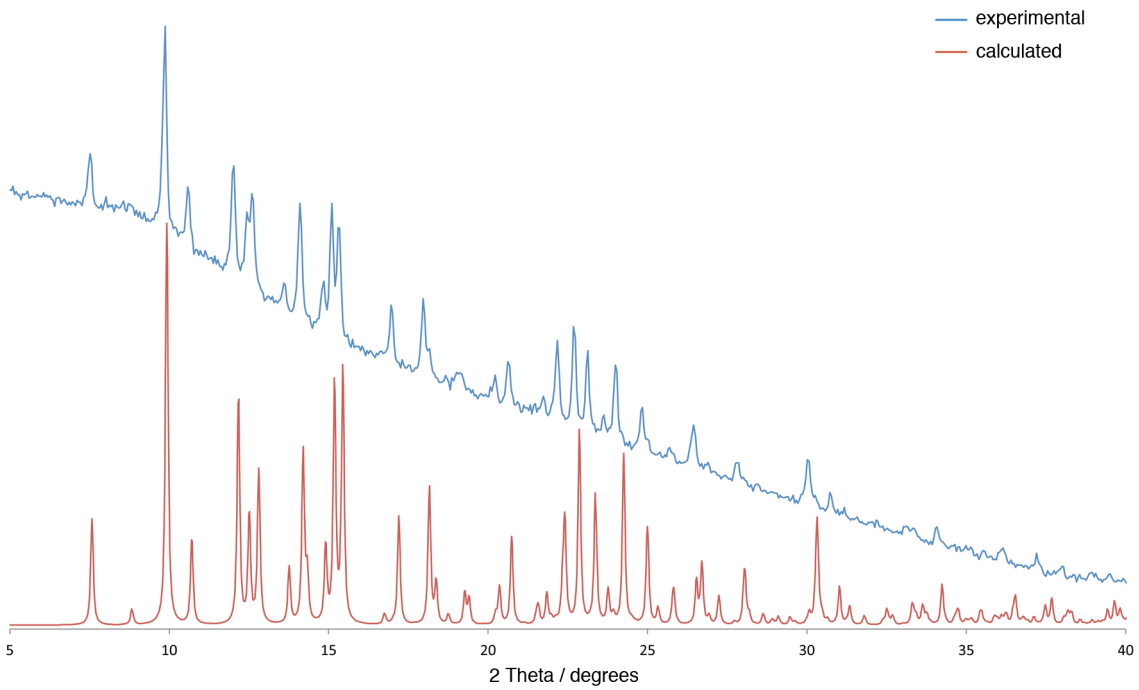



Figure 3.15: Comparison of calculated and experimental powder X-ray diffraction patterns for **10**.

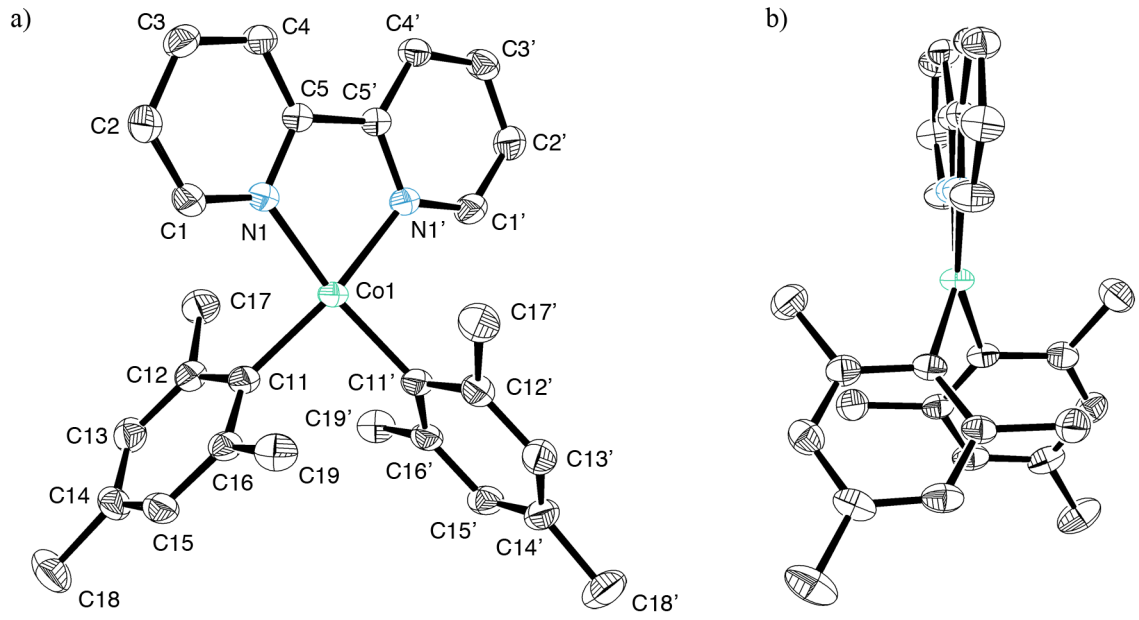



Figure 3.16: (**a**) Thermal ellipsoid representation of the asymmetric unit of **11**. (**b**) Orientation highlighting the pseudo square planar coordination environment, $\phi_{(Co1,N1,N2)\text{-}(Co1,C11,C12)} = 22.0°$. Anisotropic displacement ellipsoids pictured at the 50% probability level. Atom positions labelled with primes denote symmetry generated equivalents related by $0.5 - x$, $0.5 - y$, $z$. Hydrogen atoms and solvent molecules have been omitted for clarity.

| | 150(2) K | 293(2) K |
|---|---|---|
| space group | *Pccn* | *Pccn* |
| crystal system | orthorhombic | orthorhombic |
| $a$ / Å | 10.7358(1) | 11.4458(2) |
| $b$ / Å | 14.5102(1) | 14.2281(2) |
| $c$ / Å | 17.9942(1) | 18.1595(4) |
| $V$ / Å$^3$ | 2803.11(4) | 2957.31(10) |
| $\rho_{calc}$ / g cm$^{-3}$ | 1.245 | 1.180 |

Table 3.4: Selected X-ray data parameters from a crystal of **11** at 150 and 293 K. Note the difference in unit cell parameters arising due to the effects of anisotropic thermal expansion.

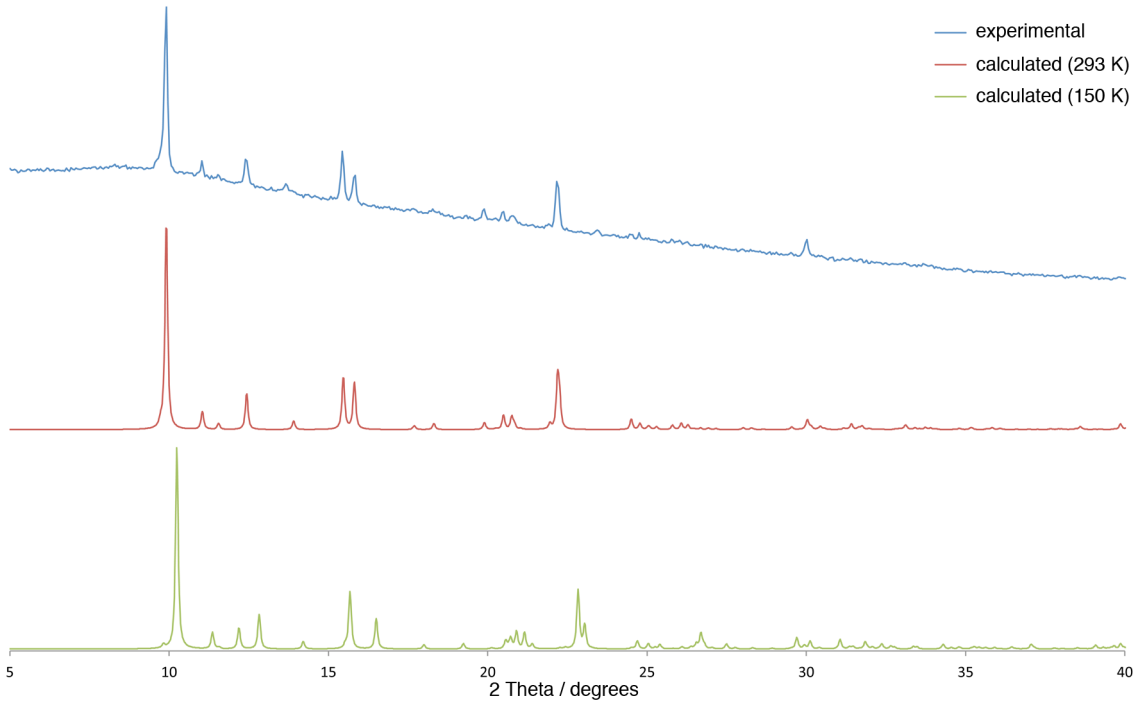



Figure 3.17: Comparison of temperature resolved (red, 293 K and green, 150 K) calculated powder patterns with experimental (blue, 293 K) powder X-ray diffraction data for sample **11**, illustrating the effects of anisotropy in the temperature dependent crystal lattice expansion of this sample.

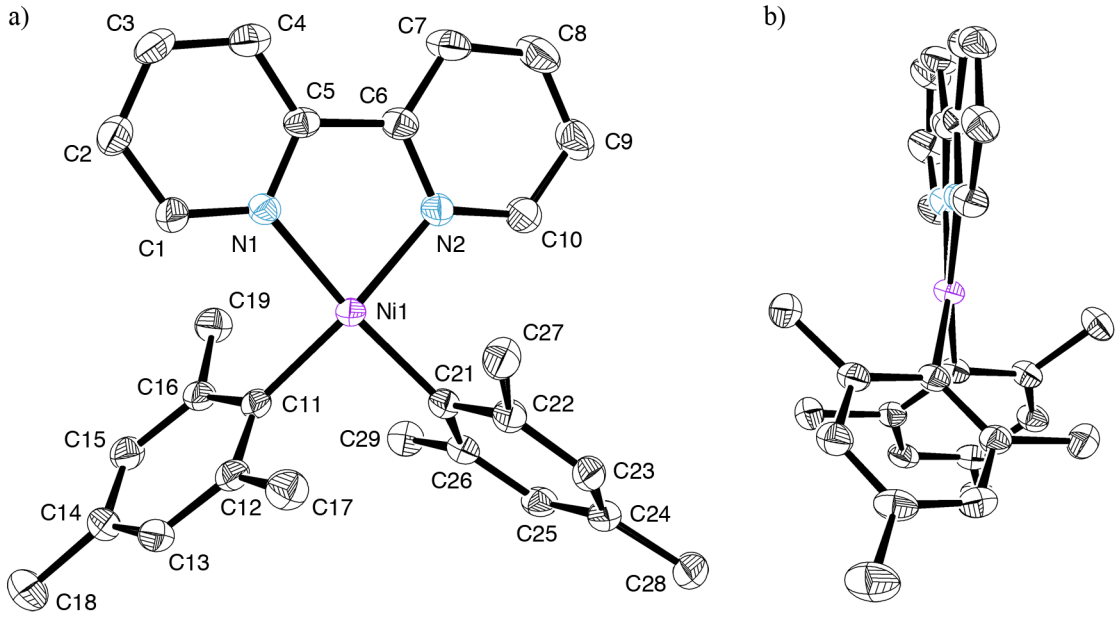



Figure 3.18: (**a**) Thermal ellipsoid representation of the asymmetric unit of **12**. (**b**) Orientation highlighting the pseudo square planar coordination environment, $\phi_{(Ni1,N1,N2)\text{-}(Ni1,C11,C12)} = 12.4°$. Anisotropic displacement ellipsoids pictured at the 50% probability level. Hydrogen atoms have been omitted for clarity.

#### 3.2.2.5 Ni(2,2´-bipy)(mes)$_2$

This was prepared following a literature procedure.[33,34] Crystals were isolated from a purple THF solution and were confirmed to be Ni(2,2´-bipy)(mes)$_2$ (**12**, Figure 3.18). Phase purity was determined by comparison of a powder X-ray diffraction pattern with that calculated from the single crystal X-ray diffraction (Figure 3.19). Bulk purity was confirmed by elemental microanalysis.

## 3.3 Reduced Compounds: [M(2,2´-bipy)(mes)$_2$]$^-$

### 3.3.1 General Synthesis

The compounds detailed in this section were all formed by the reduction of the relevant neutral species precursor, using either potassium metal or potassium graphite (Figure 3.20). The variety of sequestering agents used is a result of the requirement

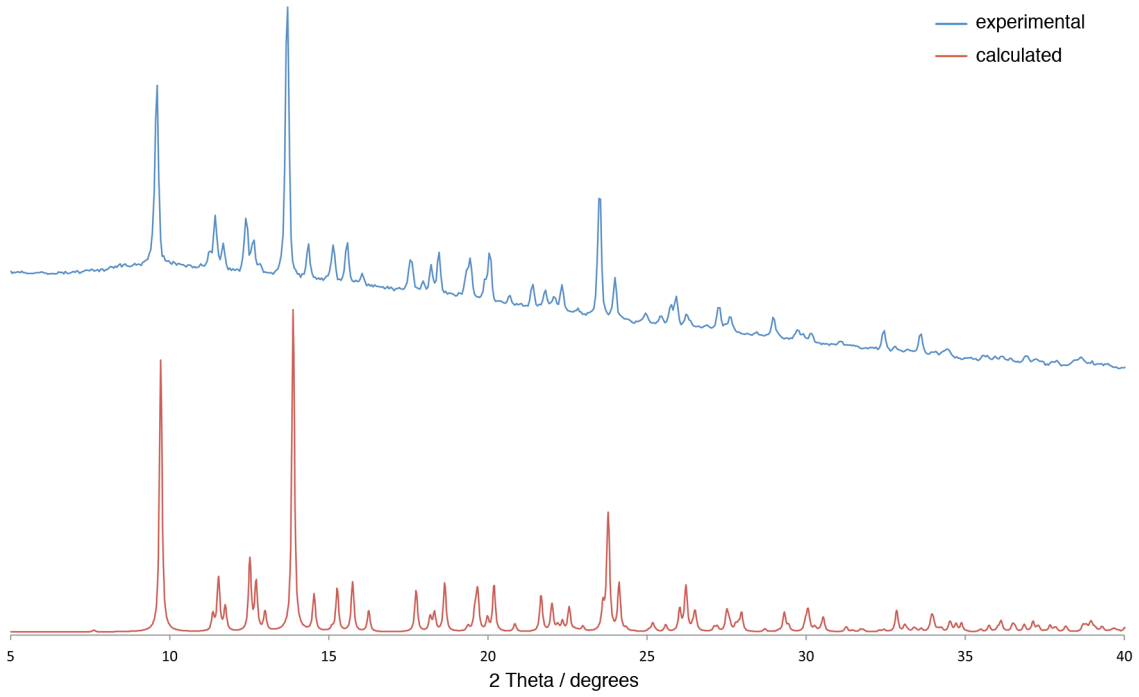



Figure 3.19: Comparison of calculated and experimental powder X-ray diffraction patterns for **12**.

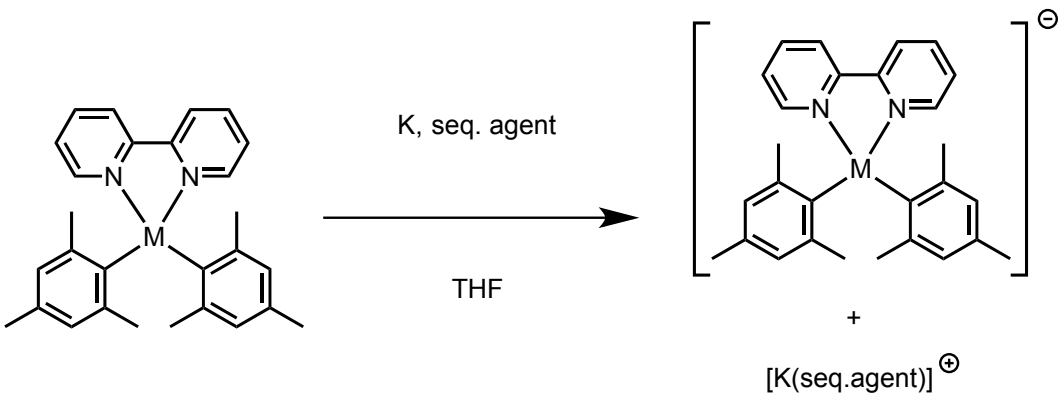



Figure 3.20: General scheme for the synthesis of the $[M(2,2´\text{-bipy})(mes)_2]^-$ products described in this chapter.

for highly accurate X-ray structural information. Formation of sufficiently large, high quality crystals of these very air- and moisture-sensitive samples proved challenging and frequently a specific sequestering agent was needed to ensure optimal crystal growth. Crystals were typically grown by the slow diffusion of hexanes into a concentrated THF solution of the product.

## 3.3.2 Synthesis and Structural Characterisation

### 3.3.2.1 [K(dibenzo-18-crown-6)·THF][Cr(2,2´-bipy)(mes)$_2$]·2THF

The reaction of **8** with $KC_8$ in the presence of dibenzo-18-crown-6 yielded a brown solution, from which dark brown crystals of [K(dibenzo-18-crown-6)·THF][Cr(2,2´-bipy)(mes)$_2$]·2THF were isolated (**13**, Figure 3.21). A loss of crystallinity upon grinding prevented collection of a powder X-ray diffraction pattern, while the high air- and moisture-sensitivity of the sample appeared to lead to at least partial decomposition and incomplete combustion (likely due to carbide formation) of samples submitted for elemental microanalysis.

### 3.3.2.2 [K(18-crown-6)][Mn(2,2´-bipy)(mes)$_2$]

The reduction of **9** was effected using potassium metal in THF in the presence of 18-crown-6, resulting in a dark brown solution from which small crystals of [K(18-crown-6)][Mn(2,2´-bipy)(mes)$_2$]·2THF were isolated in low yield (**14a**, Figure 3.22). Due to the size of crystals produced, data were collected using synchrotron radiation at Beam Station I19 of the Diamond Light Source. Larger crystals could be grown from pyridine/toluene solutions, characterised as [K(18-crown-6)][Mn(2,2´-bipy)(mes)$_2$]·0.67py·0.67tol (**14b**, Figure 3.23, py = pyridine, tol = toluene). Attempts to synthesise a pure microcrystalline sample of this compound were unsuccessful for two reasons: very low yields were obtained of this highly reactive species making product manipulation challenging; and the tendency of mixtures containing

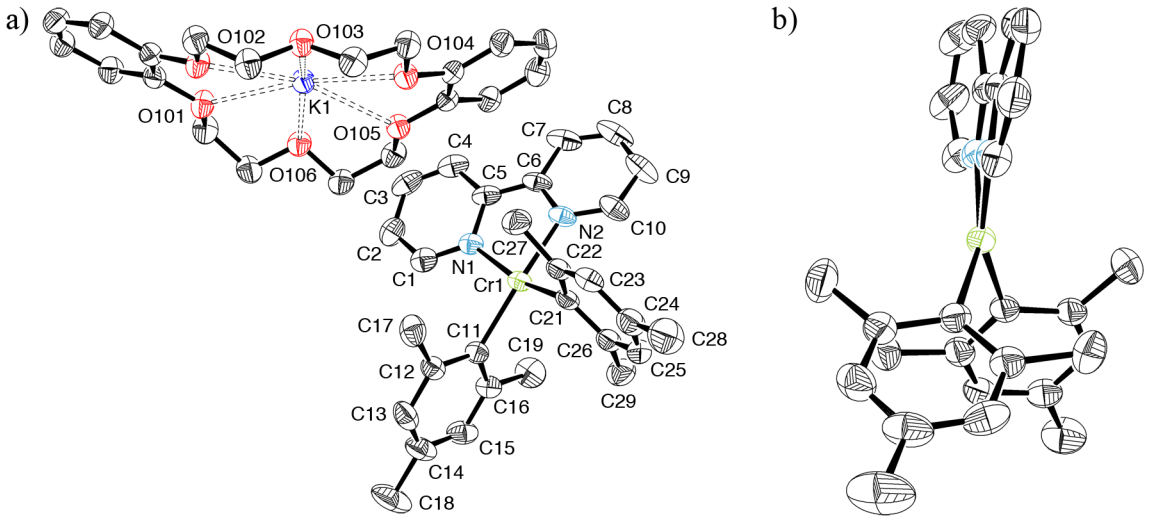



Figure 3.21: (**a**) Thermal ellipsoid representation of the asymmetric unit of **13**. (**b**) View highlighting the pseudo square planar coordination environment, $\phi_{(Cr1,N1,N2)\text{-}(Cr1,C11,C12)} = 22.7°$. Anisotropic displacement ellipsoids pictured at the 50% probability level. Hydrogen atoms and solvent molecules have been omitted for clarity.

even a slight excess of reducing agent to yield oils rather than crystals.

#### 3.3.2.3 [K(2,2,2-crypt][Fe(2,2´-bipy)(mes)$_2$]

Compound **10** was reduced by potassium metal in the presence of 2,2,2-crypt in THF. The resulting dark brown solution yielded dark purple and pale green crystals. The dark purple product was crystallographically characterised as [K(2,2,2-crypt)][Fe(2,2´-bipy)(mes)$_2$] (**15**, Figure 3.24), while the pale green crystals were determined to be [K(2,2,2-crypt)][Fe(mes)$_3$]·$C_6H_{12}$(**18**, Figure 3.25). A pure sample of **15** was obtained by the slow diffusion of toluene into a mixture of **15** and **18** in pyridine. The success of this technique was confirmed by elemental microanalysis and a powder X-ray diffractogram which matched the pattern calculated from the crystal structure of **15** (Figure 3.26). Despite repeated attempts, the synthesis or isolation of a pure sample of **18** was unsuccessful. Selected structural parameters from the crystal structure of **18** are given Table 3.5.

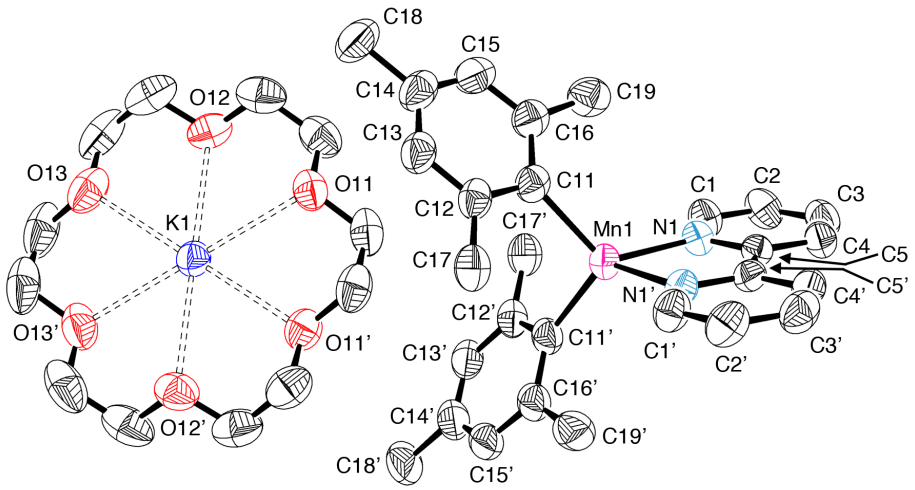



Figure 3.22: Thermal ellipsoid representation of the asymmetric unit of **14a**. $\phi_{(Mn1,N1,N2)\text{-}(Mn1,C11,C12)} = 81.9°$. Anisotropic displacement ellipsoids pictured at the 50% probability level. Atom positions labelled with primes denote symmetry generated equivalents related by $x$, $-y$, $z$. Hydrogen atoms and solvent molecules have been omitted for clarity.

| | |
|---|---|
| Distance: Fe1–C11 | 2.074(3) |
| Distance: Fe1–C21 | 2.085(3) |
| Distance: Fe1–C31 | 2.083(3) |
| Angle: C11–Fe1–C21 | 116.1(1) |
| Angle: C21–Fe1–C31 | 121.1(1) |
| Angle: C31–Fe1–C11 | 122.7(1) |
| 'Blade angle' mes(C11) | 64.7 |
| 'Blade angle' mes(C21) | 60.9 |
| 'Blade angle' mes(C31) | 70.6 |
| Distance Fe1–plane(C11, C21, C31) | 0.044 |

Table 3.5: Selected structural parameters from the crystal structure of **18**. 'Blade angle' refers to the rotation of the associated mesityl group relative to the C11, C21, C31 plane. Distances are given in Ångström and angles in degrees.

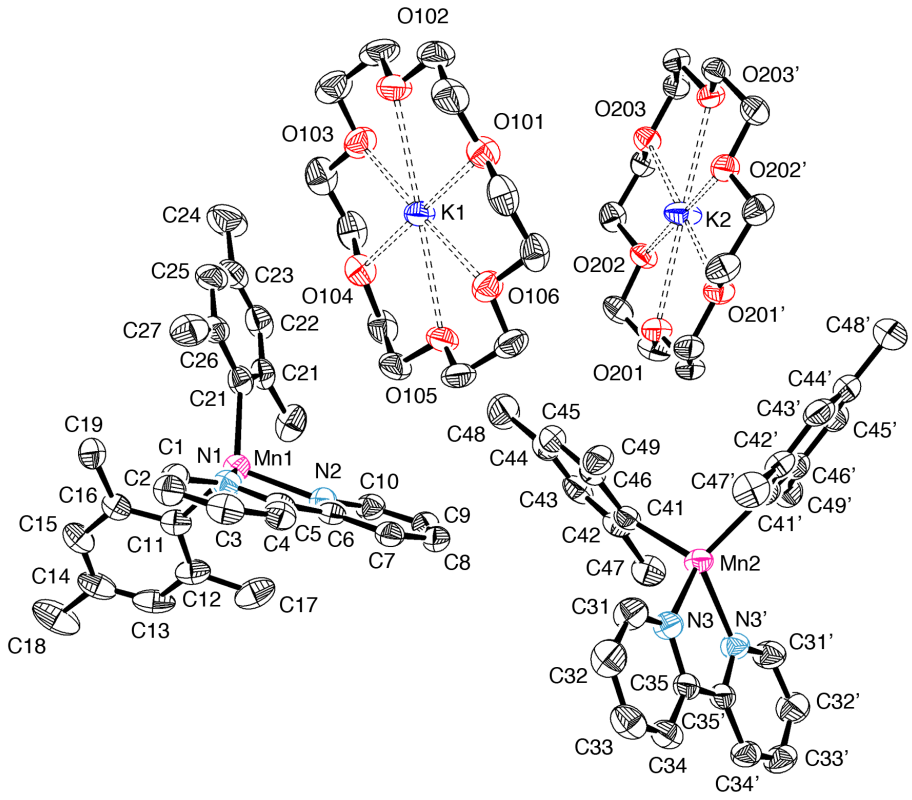



Figure 3.23: Thermal ellipsoid representation of the asymmetric unit of **14b**. $\phi_{(Mn1,N1,N2)\text{-}(Mn1,C11,C12)}$ = 82.3(av)°. Anisotropic displacement ellipsoids pictured at the 50% probability level. Atom positions labelled with primes denote symmetry generated equivalents related by $-x$, $y$, $-z+1/2$. Hydrogen atoms and solvent molecules have been omitted for clarity.

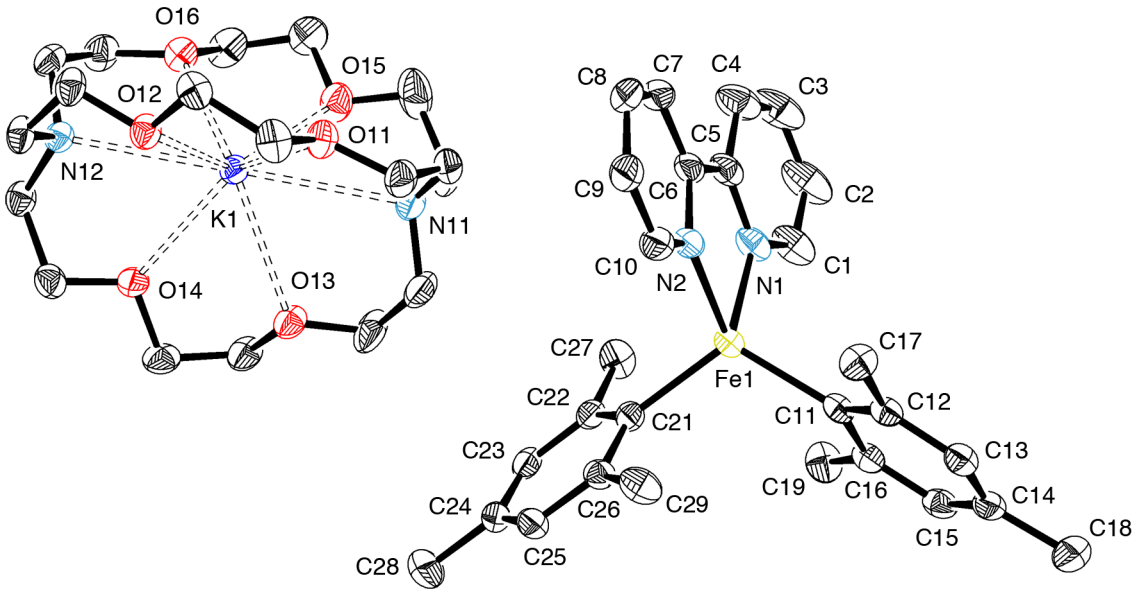



Figure 3.24: Thermal ellipsoid representation of the asymmetric unit of **15**. $\phi_{(Fe1,N1,N2)\text{-}(Fe1,C11,C12)} = 78.6°$. Anisotropic displacement ellipsoids pictured at the 50% probability level. Hydrogen atoms have been omitted for clarity.

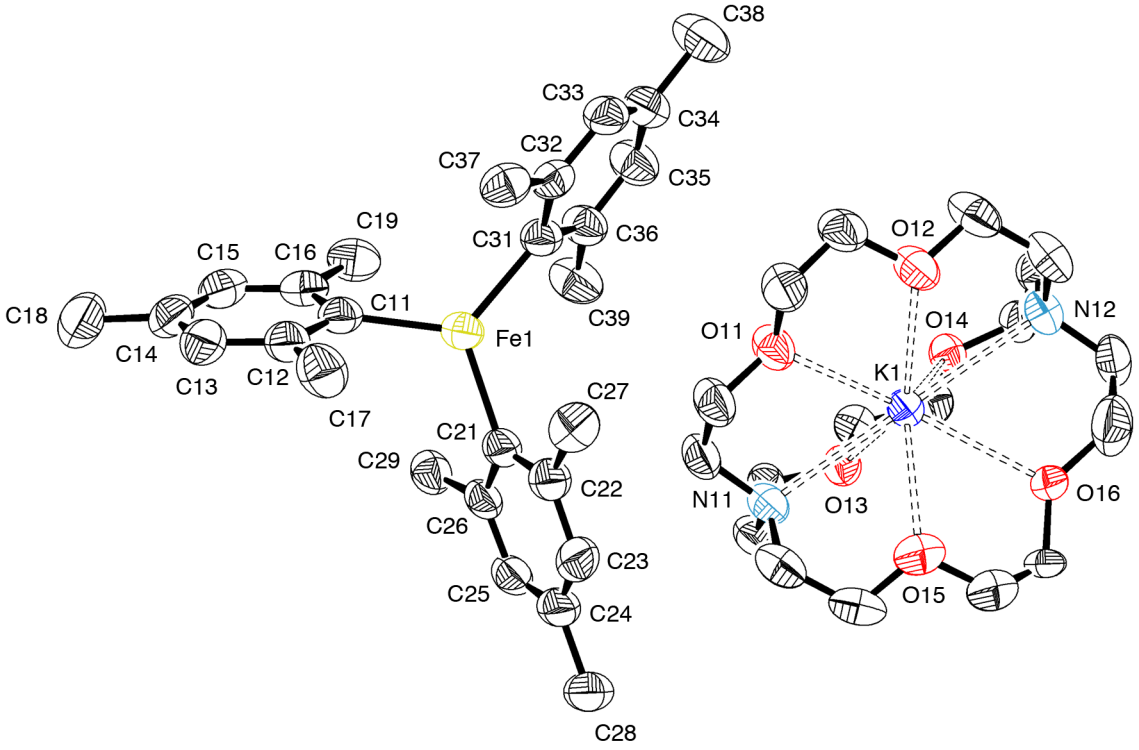



Figure 3.25: Thermal ellipsoid representation of the asymmetric unit of **18**. Anisotropic displacement ellipsoids pictured at the 50% probability level. Hydrogen atoms and a hexane molecule have been omitted for clarity.

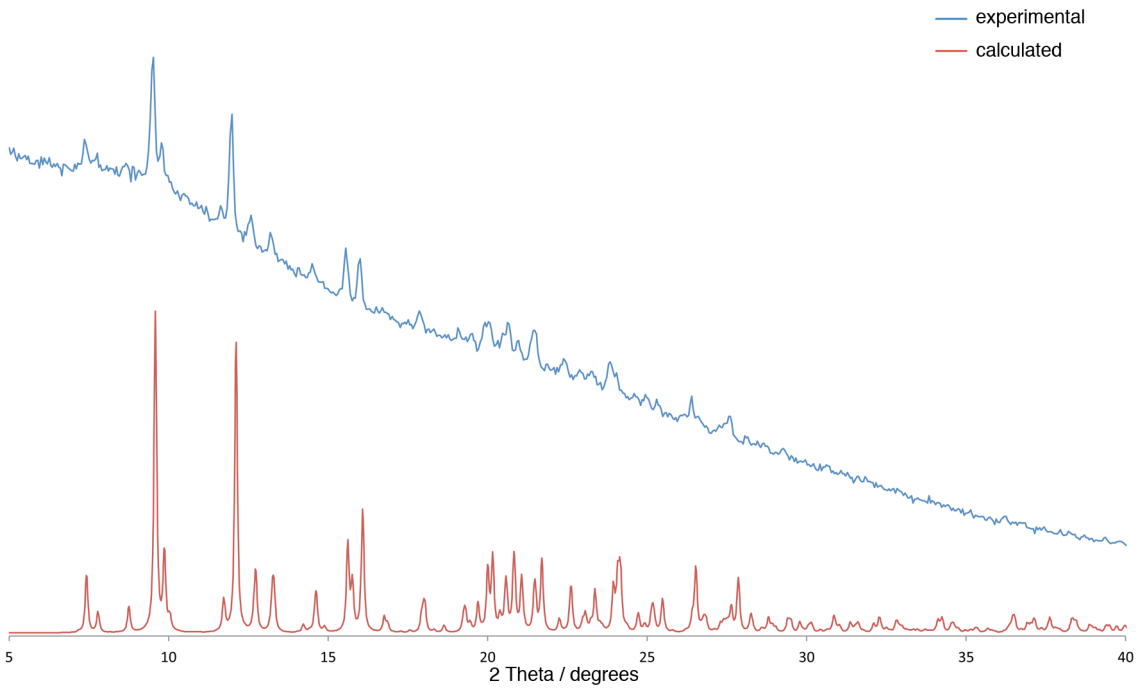



Figure 3.26: Comparison of calculated and experimental powder X-ray diffraction patterns for **15**.

#### 3.3.2.4 [K(2,2,2-crypt)][Co(2,2´-bipy)(mes)$_2$]

Potassium metal in the presence of 2,2,2-crypt was used to reduce a solution of **11** in THF, forming a dark brown solution which yielded crystals of [K(2,2,2-crypt)][Co(2,2´-bipy)(mes)$_2$] (**16**, Figure 3.27). A powder X-ray diffraction pattern was found to match that calculated from the single crystal structure (Figure 3.28) while bulk composition was proved by elemental microanalysis.

#### 3.3.2.5 [K(2,2,2-crypt)][Ni(2,2´-bipy)(mes)$_2$]

The reduction of **12** was achieved using $KC_8$ in the presence of 2,2,2-crypt in THF. The resulting solution yielded dark purple crystals of [K(2,2,2-crypt)][Ni(2,2´-bipy)-(mes)$_2$] (**17**, Figure 3.29). Phase and compositional purity were determined using powder X-ray diffraction (Figure 3.30) and elemental microanalysis.

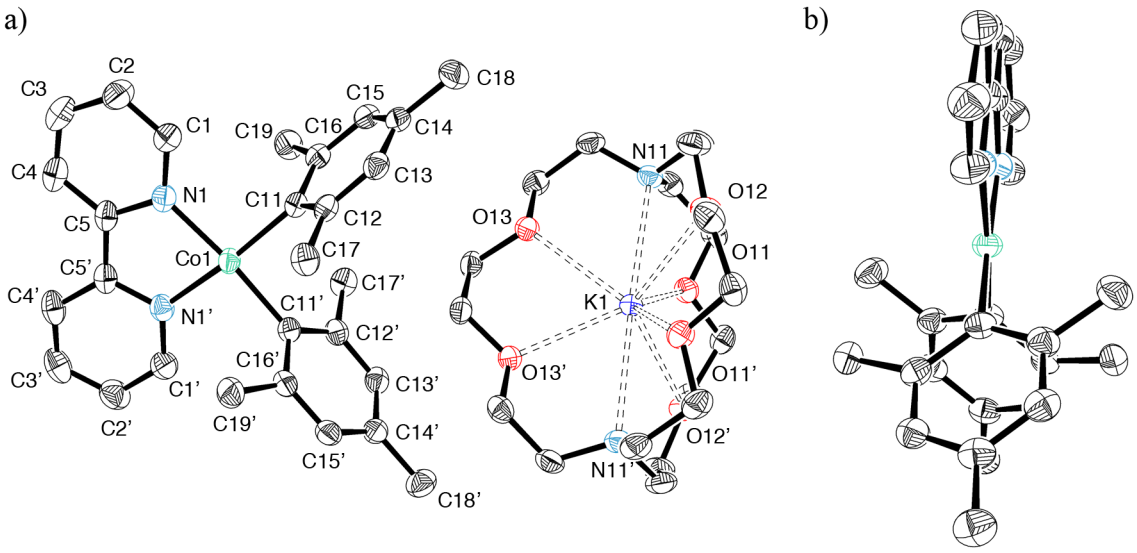



Figure 3.27: (**a**) Thermal ellipsoid representation of the asymmetric unit of **16**. (**b**) View highlighting the pseudo square planar coordination environment, $\phi_{(Co1,N1,N2)\text{-}(Co1,C11,C12)} = 4.2°$. Anisotropic displacement ellipsoids pictured at the 50% probability level. Atom positions labelled with primes denote symmetry generated equivalents related by $y$, $x$, $-z$. Hydrogen atoms have been omitted for clarity.

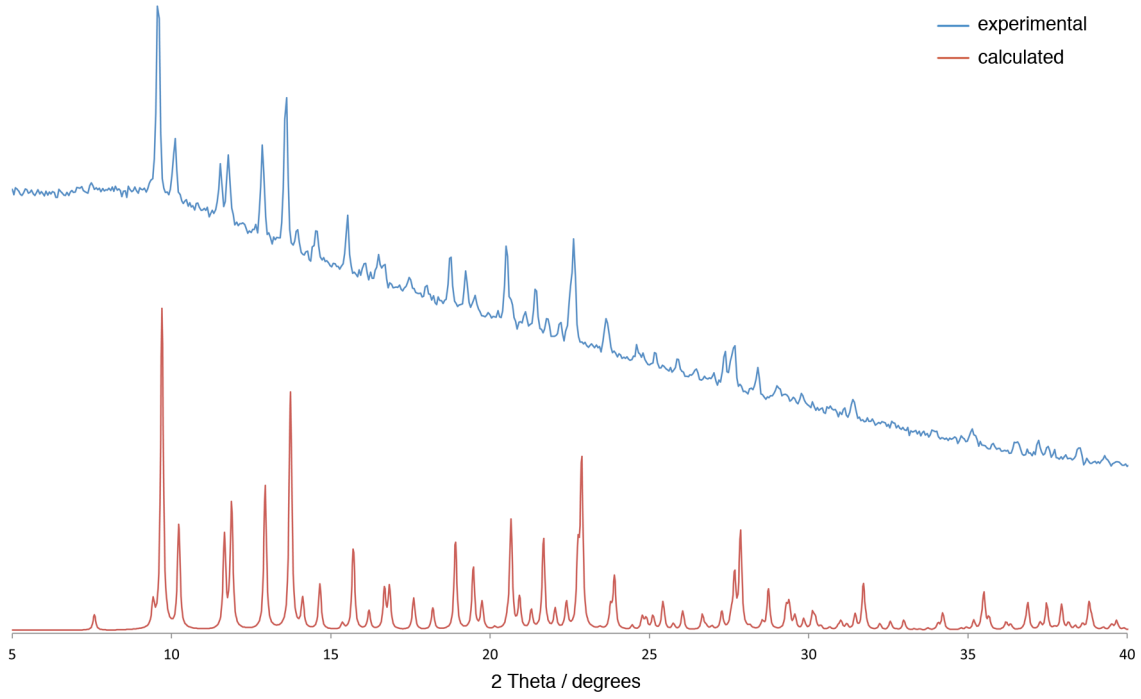



Figure 3.28: Comparison of calculated and experimental powder X-ray diffraction patterns for **16**.

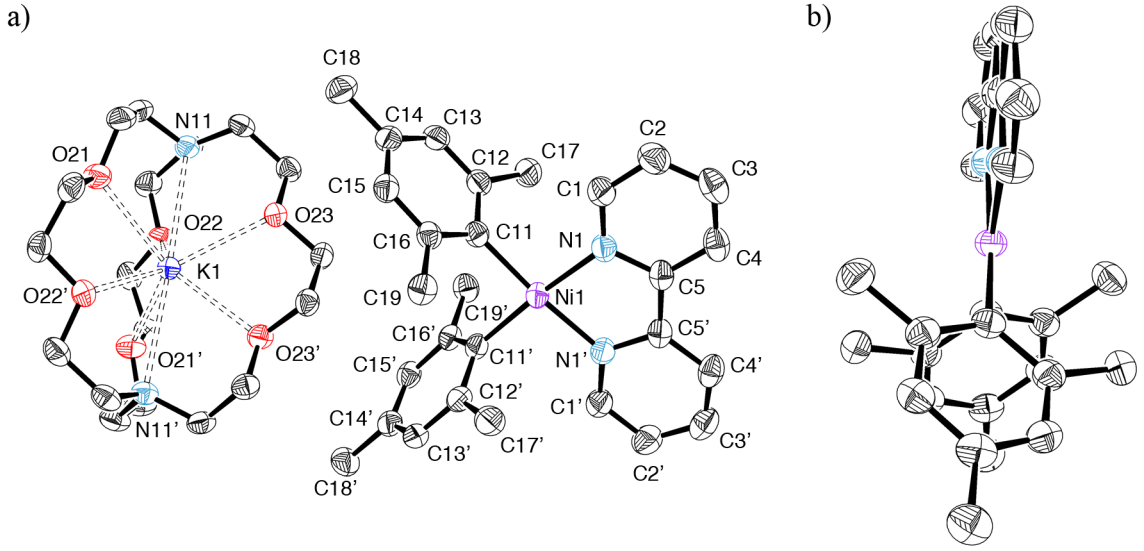



Figure 3.29: (**a**) Thermal ellipsoid representation of the asymmetric unit of **17**. (**b**) View highlighting the pseudo square planar coordination environment, $\phi_{(Ni1,N1,N2)\text{-}(Ni1,C11,C12)} = 5.3°$. Anisotropic displacement ellipsoids pictured at the 50% probability level. Atom positions labelled with primes denote symmetry generated equivalents related by $y$, $x$, $-z$. Hydrogen atoms have been omitted for clarity.

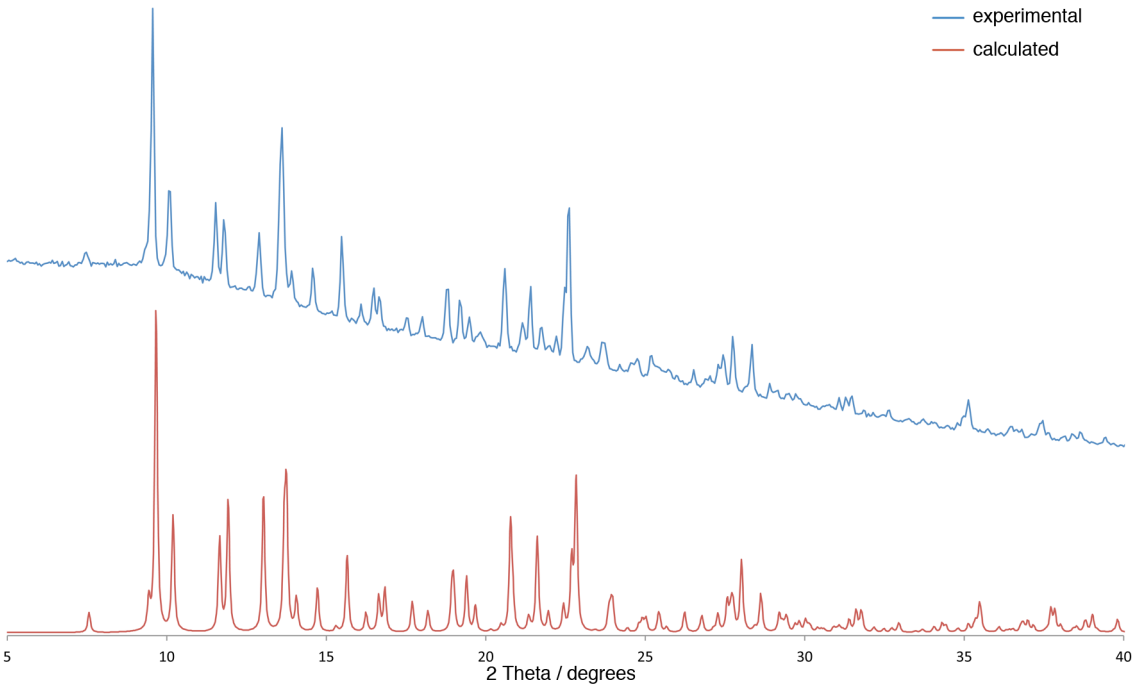



Figure 3.30: Comparison of calculated and experimental powder X-ray diffraction patterns for **17**.

## 3.4 Results and Discussion

### 3.4.1 Trends in Bond Metrics

The crystal structures given in the previous section show both tetrahedral and square planar coordination modes. By considering the atoms immediately surrounding the transition metal a torsion angle ($\phi$) may be defined between the plane containing M, C11 and C12, and the plane containing M, N1 and N2. For a pseudo square planar species this value should fall between 0 to 20° while in pseudo tetrahedral compounds a much larger angle of 70 to 90° is found. Within the neutral species, the chromium, cobalt and nickel containing structures (**8**, **11** and **12**) fall into the former category ($\phi$ = 8.1, 22.0 and 12.4°, respectively), while the manganese and iron complexes (**9** and **10**) are in the latter category ($\phi$ = 70.6 and 70.2°, respectively). Ligand field theory explains the preference for the pseudo square planar orientation of the $d^4$ chromium (**8**) and $d^8$ nickel (**12**) complexes as well as the pseudo tetrahedral coordination around the $d^5$ manganese (**9**) and $d^6$ iron (**10**) sites.[35] However, cobalt complexes may exhibit either tetrahedral or square planar geometry and for this system DFT calculations reveal only a small energy difference between the two, with the observed square planar species having the lower energy, potentially a result of the relatively strong ligand field generated by the mesityl ligands.

Moving across the series, there is substantial variation in M–C and M–N bond distances (Figure 3.32a). Initially considering only the pseudo square planar complexes (chromium, cobalt and nickel), there is a systematic decrease in both sets of bond distances. This is due to increased effective nuclear charge on traversing the first row transition metal series from left to right. The two pseudo tetrahedral complexes (manganese and iron) show a similar trend though bond distances are longer owing to the population of orbitals with M–C and M–N antibonding character in this geometry (relative to the square planar complexes). This effect is shown diagramatically in

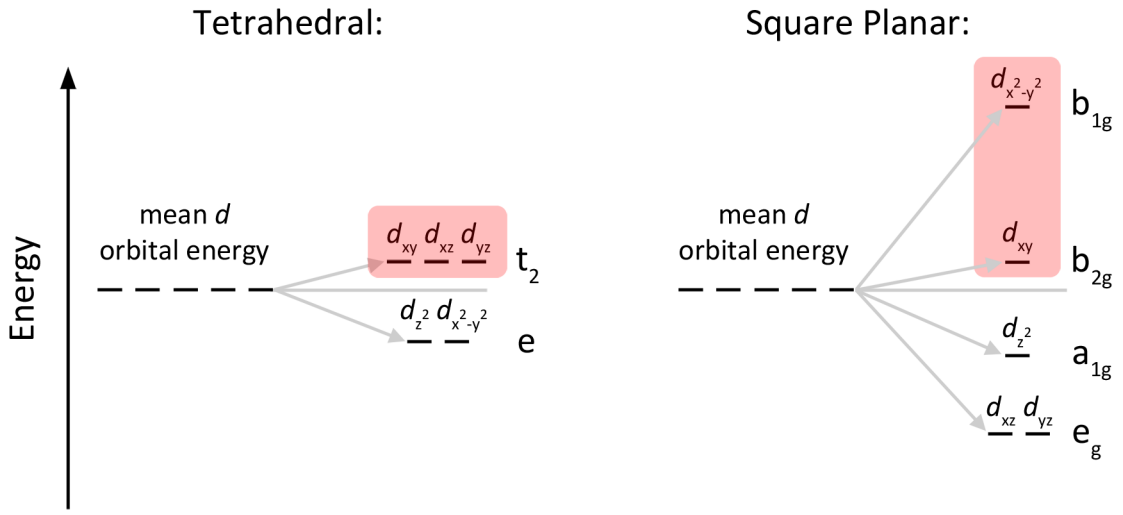



Figure 3.31: Diagramatic representation of the relative energies of the *d* orbitals in idealised tetrahedral and square planar geometries.

Figure 3.31 where the highlighted orbitals have antibonding character. The high-spin tetrahedral $d^5$ manganese (**9**) and $d^6$ iron (**10**) complexes populate the $t_2$ antibonding orbitals while the other (square planar) systems populate primarily bonding orbitals. The occupied antibonding orbitals in the tetrahedral geometry are responsible for the observed elongation of M–C and M–N bonds. Interestingly, bond metrics within the bipyridine ligand remains virtually unchanged across the series, suggesting no significant backbonding from the metal takes place. This is consistent with the calculations of 2,2´-bipyridine having low π-acceptor ability reported by Dieck and co-workers.[27]

The anionic complexes maintain the same general structures adopted by their neutral congeners. Pseudo square planar coordination was observed about the chromium (**13**), cobalt (**16**) and nickel (**17**) metal centres, with torsion angles of 22.7, 4.2, and 5.3°, respectively while the manganese (**14a** and **b**) and iron (**15**) anionic complexes retain tetrahedral geometry, exhibiting torsion angles of 81.9, 82.3 and 78.6°, respectively).

Trends in M–C and M–N bond lengths are similar to those observed for the neutral species (Figure 3.32b), and show the same decrease in bond lengths due to increase

in effective nuclear charge, superimposed over the bond lengthening effects of the tetrahedral geometry of the manganese and iron complexes.

Comparison of the datasets in Figure 3.32 (numerical values given in Table 3.6) shows that M–C bond lengths are not substantially affected by complex reduction; the largest change being 0.032 Å between the cobalt systems. The M–N bond lengths show more dependance on complex charge around the early nuclei (chromium, manganese and iron) with contractions of around 0.07 Å; the effect is far less pronounced for the later nuclei in the series. As with the neutral species, the bipyridyl inter-ring bond lengths are almost invariant with metal cation. A mean contraction of 0.06 Å relative to the metrics from the neutral species provides an early indication of ligand reduction in all cases.

For compounds containing either oxidation state of bipyridine, the almost invariant inter-pyridyl bond lengths observed would be highly unanticipated in the presence of metal to ligand π-backbonding, which might well be expected to vary with transition metal and thus to change this bond length substantially across the series.

### 3.4.2 Magnetism and Spectroscopy

SQUID magnetometry was used to examine the magnetic properties of all complexes described in this chapter with the aim of clarifying oxidation states of metals and determining whether the bipyridine ligands of the reduced species exhibit non-innocent behaviour. Due to the high air- and moisture-sensitivity of these compounds (in particular the reduced species) it proved challenging to synthesise samples without formation of trace amounts of ferromagnetic decomposition products. Though difficult to detect by other methods, such small levels of impurity were revealed by magnetometry studies because they give rise to a response several orders of magnitude larger than a paramagnetic species would generate.[36] In such situations high field measurements were made, saturating the ferromagnetic impurity and allowing magnetic

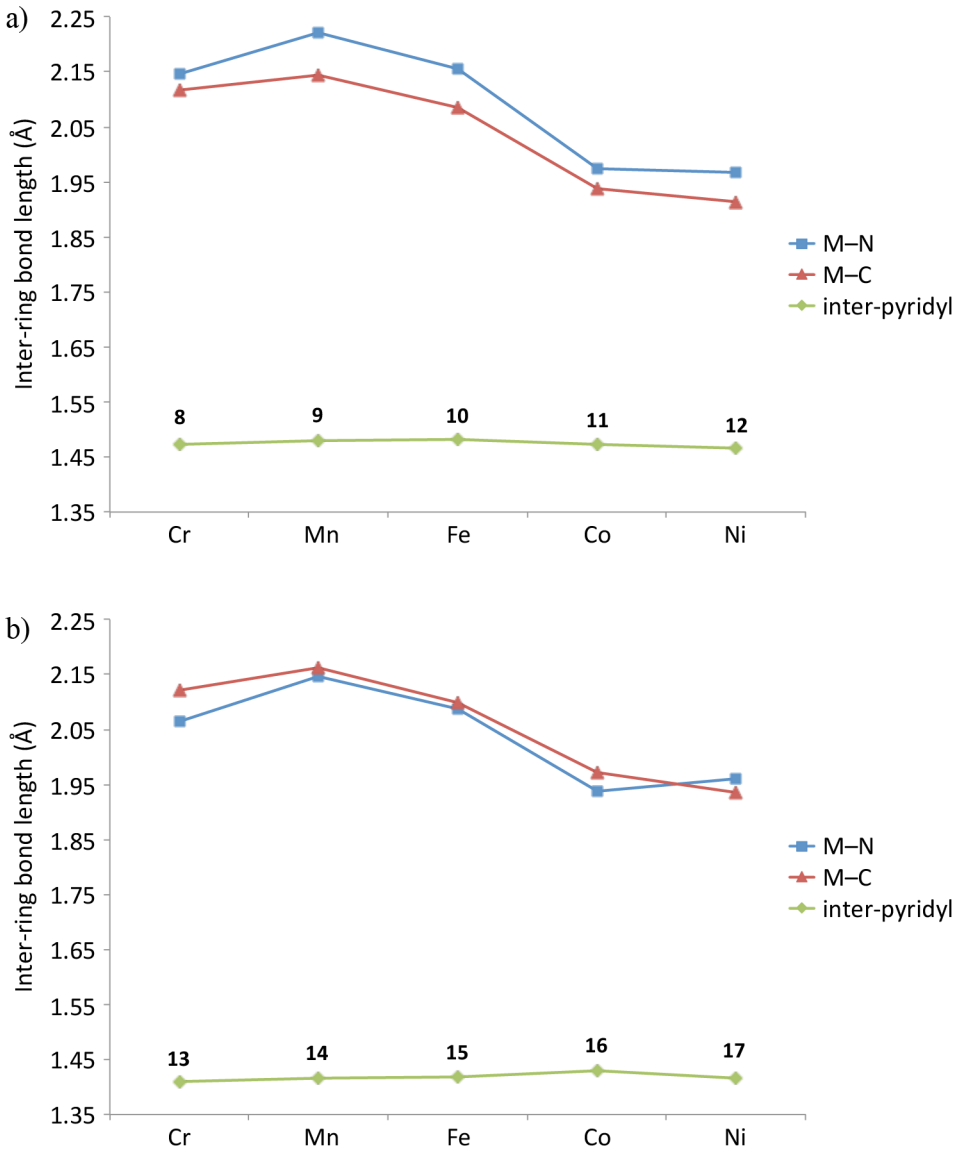



Figure 3.32: Trends in bond bond metrics for **a**) neutral species **8** to **12** and **b**) reduced species **13** to **17**.

| | M = Cr | | M = Mn | | M = Fe | | M = Co | | M = Ni | |
|---|---|---|---|---|---|---|---|---|---|---|
| | **8** | **13** | **9** | **14a**, **14b** | **10** | **15** | **11** | **16** | **12** | **17** |
| C5–C6 | 1.473(3) | 1.410(4) | 1.480(4) | 1.422(6), 1.409(av) | 1.479(3) | 1.418(3) | 1.473(4) | 1.429(4) | 1.465(4) | 1.416(4) |
| N1–C1, N2–C10 | 1.342(av) | 1.361(av) | 1.344(av) | 1.337(4), 1.352(av) | 1.343(av) | 1.356(av) | 1.345(3) | 1.364(2) | 1.343(av) | 1.354(3) |
| N1–C5, N2–C6 | 1.359(av) | 1.390(av) | 1.349(av) | 1.381(4), 1.390(av) | 1.351(av) | 1.386(av) | 1.363(2) | 1.382(2) | 1.359(av) | 1.390(2) |
| C1–C2, C9–C10 | 1.384(av) | 1.361(av) | 1.383(av) | 1.374(5), 1.362(av) | 1.380(av) | 1.372(av) | 1.382(3) | 1.369(3) | 1.382(av) | 1.378(3) |
| C2–C3, C8–C9 | 1.379(av) | 1.403(av) | 1.378(av) | 1.396(5), 1.409(av) | 1.381(av) | 1.400(av) | 1.382(3) | 1.401(3) | 1.372(av) | 1.400(4) |
| C3–C4, C7–C8 | 1.380(av) | 1.357(av) | 1.379(av) | 1.349(5), 1.354(av) | 1.380(av) | 1.359(av) | 1.382(3) | 1.364(3) | 1.380(av) | 1.360(3) |
| C4–C5, C6–C7 | 1.388(av) | 1.414(av) | 1.390(av) | 1.416(4), 1.422(av) | 1.393(av) | 1.419(av) | 1.382(2) | 1.408(2) | 1.386(av) | 1.419(3) |
| M–N1, M–N2 | 2.147(av) | 2.065(av) | 2.222(av) | 2.141(2), 2.150(av) | 2.155(av) | 2.087(av) | 1.975(2) | 1.937(1) | 1.967(av) | 1.961(2) |
| M–C11, M–C21 | 2.118(av) | 2.122(av) | 2.144(av) | 2.151(3), 2.173(av) | 2.085(av) | 2.099(av) | 1.939(2) | 1.971(2) | 1.914(av) | 1.935(2) |
| torsion angle *a* | 11.3 | 12.7 | 15.2 | 3.2, 1.2(av) | 13.8 | 9.2 | 5.8 | 4.4 | 3.2 | 4.7 |
| torsion angle *b* | 8.1 | 22.7 | 70.6 | 81.9, 82.3(av) | 70.2 | 78.6 | 22.0 | 4.2 | 12.4 | 5.3 |

Table 3.6: Selected interatomic distances and angles from the crystal structures of **8** to **15**, **17** and **18**. Defining *a*: bipyridine inter-pyridyl bond torsion angle; *b*: (M, N1, N2)/(M, C11, C12) torsional angle. Bond lengths are in Ångström and angles are in degrees.

susceptibility to be determined from the gradients of linear sections of magnetisation versus field plots. All samples were found to exhibit paramagnetic responses with the exception of **12**, the neutral Ni species, which is diamagnetic.

The neutral species **8** to **11** show approximately linear responses, as is expected for paramagnetic species with little to no spin-orbit coupling (Figure 3.33a). Such data may be modelled using the Curie-Weiss law:

$$\chi_{\mathrm{mol}} = \frac{N_{\mathrm{A}}\mu_0\mu_{\mathrm{B}}^2 S(S+1)}{3k}\frac{g^2}{T-\Theta} + \chi_{\mathrm{TIM}}$$

where $\chi_{\mathrm{TIM}}$ is the temperature-independent magnetism. Values of $g$, $\Theta$ and $\chi_{\mathrm{TIM}}$ were determined using the simplex algorithm to locate the global minimum in the error functional defined as $F = \sum \mid \mu_i^{\mathrm{o}} - \mu_i^{\mathrm{c}} \mid$, where $\mu_i^{\mathrm{o}}$ and $\mu_i^{\mathrm{c}}$ are the observed and calculated magnetic moments, respectively. The temperature-independent parameter is likely to receive contributions from several possible effects:

1. Any contribution from population of excited states (i.e. the real temperature-independent paramagnetism).

2. Approximations made in estimating diamagnetic contributions using Pascal's constants.

3. The contribution from the sample container.

4. Contributions from any trace ferromagnetic impurities.

Despite these potential sources of error, the fitted results are sufficiently accurate to determine numbers of unpaired electrons in each complex and, for the reduced species, the coupling occurring between metal and ligand-based spin densities. These results are given in Table 3.7.

The $g$ values for the first three compounds (**8**, **9** and **10**) are close to that of a free electron, suggesting minimal spin-orbit coupling takes place. A slight increase in $\mu_{\mathrm{eff}}$

| Complex (metal) | Diamagnetic correction/ $10^{-4}$ emu mol$^{-1}$ | $\mu_{\text{eff}}/\mu_{\text{B}}$ at 300 K | spin state $S$ | $g$ | $\Theta$/K | $\chi_{\text{TIM}}$/ $10^{-4}$ emu mol$^{-1}$ |
|---|---|---|---|---|---|---|
| **8** (Cr) | –2.95 | 4.55 | 2 | 1.84 | –0.4 | 2.3 |
| **9** (Mn) | –2.94 | 5.74 | $^5/_2$ | 1.91 | –0.3 | 4.7 |
| **10** (Fe) | –2.93 | 5.12 | 2 | 2.09 | –0.9 | 0.0 |
| **11** (Co) | –2.92 | 2.62 | $^1/_2$ | 2.67 | –0.4 | 6.4 |
| **13** (Cr) | –5.35 | 3.87 | $\mid 2 - {}^1/_2 \mid = {}^3/_2$ | 1.88 | –1.0 | 7.4 |
| **14** (Mn) | –4.79 | 4.84 | $\mid {}^5/_2 - {}^1/_2 \mid = 2$ | 1.81 | –5.4 | 19.6 |
| **15** (Fe) | –5.60 | 4.98 | $\mid 2 - {}^1/_2 \mid = {}^3/_2$ | | | |
| **16** (Co) | –5.59 | 1.88 | $\mid {}^1/_2 + {}^1/_2 \mid = 1$ | | | |
| **17** (Ni) | –5.59 | 1.27 | $\mid 0 - {}^1/_2 \mid = {}^1/_2$ | 1.83 | –1.5 | –3.7 |

Table 3.7: Parameters obtained by fitting Curie-Weiss Law behaviour to magnetic responses of paramagnetic compounds **8** to **17**.

at around 150 K shown by the iron species (**10**) is attributed to a partial reorientation of the unanchored polycrystalline sample upon warming and has prevented more complete modeling of the data.

In contrast, the large $g$ value of 2.67 found for complex **11** is consistent with a significant mixing of orbital angular momentum. A potential complication in this case is the significant change in lattice parameters observed when measuring crystals at different temperatures (Table 3.4). Although distortions of the cobalt centre are small, changes to intermolecular distances may affect exchange interactions with neighbouring molecules. Any such interactions are likely to be small however, as evidenced by the small and negative value of the Weiss constant.

The magnetic responses of reduced compounds **13** to **17** are shown in Figure 3.33b. The chromium and manganese species (**13** and **14**) are consistent with structures containing M(II) metal centres (having $S_{\text{metal}} = 2$ and $^5/_2$, respectively), that are antiferromagnetically coupled to a $S_{\text{bipy}} = {}^1/_2$ radical ligand. In such a system the ground spin state is given by $S_{\text{min}} = |S_{\text{metal}} - S_{\text{bipy}}|$ and an excited state $S_{\text{max}} = |S_{\text{metal}} + S_{\text{bipy}}|$. The energy difference between these states is then given by: $\Delta = -J/2[S_{\text{max}}(S_{\text{max}} + 1) - S_{\text{min}}(S_{\text{min}} + 1)]$.[37] This leads to the values of $\Delta$ shown in Table

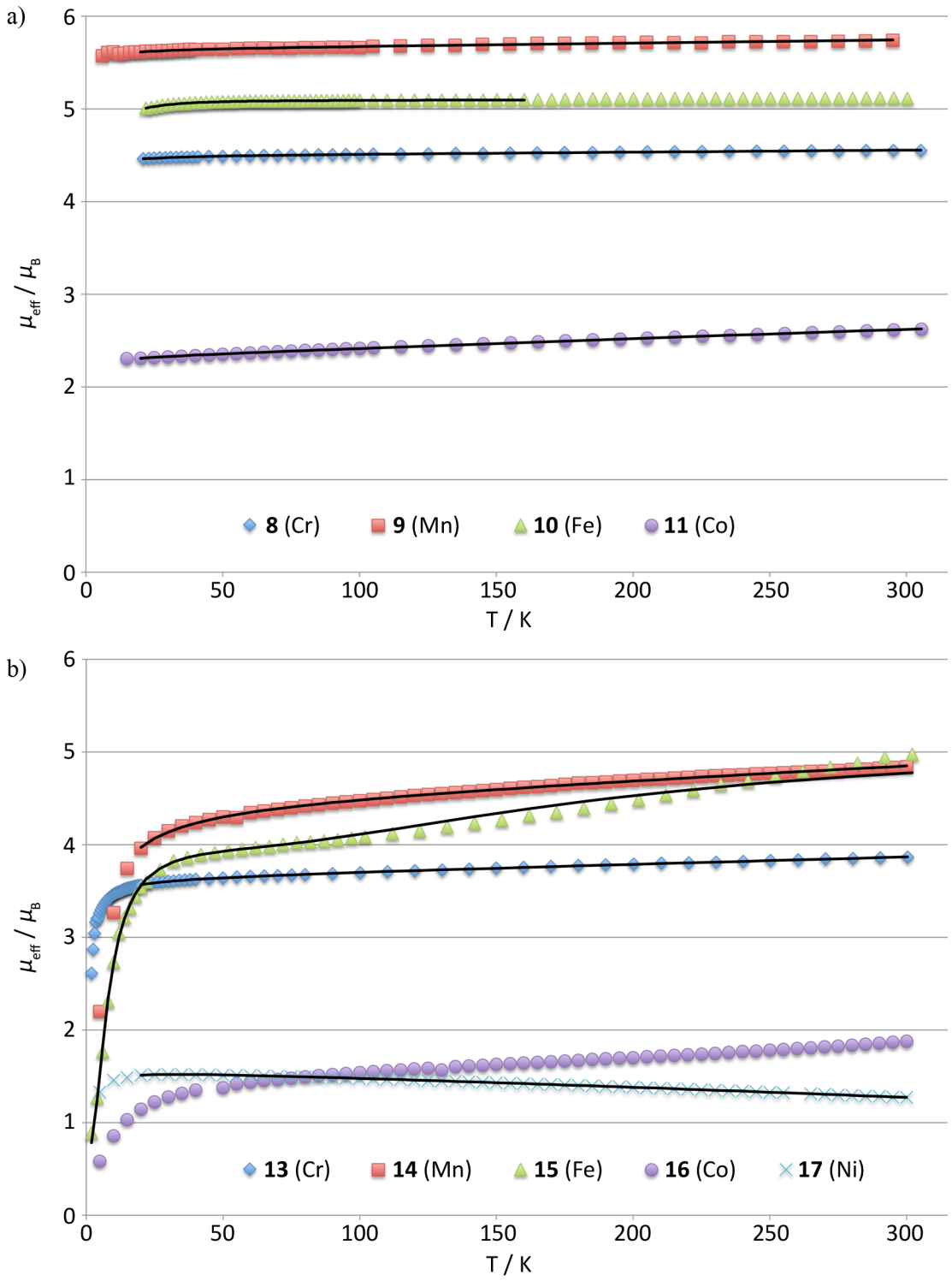



Figure 3.33: Effective magnetic moments of (**a**) neutral species **8** to **11** and (**b**) reduced species **13** to **17**. Shapes represent observed data points observed for each compound while calculated fits are represented by continuous lines.

| Complex (metal) | $\Delta$ | $J$ / cm$^{-1}$ (DFT) |
|---|---|---|
| **13** (Cr) | $-5/2J$ | –508 |
| **14** (Mn) | $-3J$ | –492 |
| **15** (Fe) | $-5/2J$ | –656 |
| **16** (Co) | $-2J$ | +396 |
| **17** (Ni) | - | - |

Table 3.8: Values of $\Delta$ and DFT computed values of $J$.

3.8. For these first two examples (**13** and **14**) the antiferromagnetic interaction is sufficiently strong ($J <$ –350 cm$^{-1}$) that the $S_{\text{min}}$ ground state is exclusively populated at all temperatures measured. Thus the effective magnetic moment remains constant and results may be modelled using the Curie-Weiss law.

The magnetic behaviour of the reduced iron complex **15** is less straightforward to interpret. There are three distinct limiting cases for a system with $S_{\text{Fe}} = 2$ and $S_{\text{bipy}} = 1/2$. If the spins are ferromagnetically coupled then $S_{\text{total}} = 5/2$ and the effective magnetic moment is given by $\mu_{\text{eff}} = g[(S_{\text{total}})(S_{\text{total}} + 1)]^{1/2} = 5.92\ \mu_{\text{B}}$, while completely antiferromagnetic coupling would give $S_{\text{total}} = 3/2$ and $\mu_{\text{eff}} = 3.87\ \mu_{\text{B}}$. If both spin systems were present but non-interacting then $\mu_{\text{eff}} = ({\mu_1}^2 + {\mu_2}^2)^{1/2} = 5.20\ \mu_{\text{B}}$. At low temperatures the observed magnetic moment is 3.8 $\mu_{\text{B}}$, consistent with a $S = 3/2$ ground state. However at temperatures above 100 K this model breaks down. By fitting the data with a Heisenberg-Dirac Hamiltonian function, the temperature dependent behaviour of $\mu_{\text{eff}}$ is explained by the accessibility and partial occupancy of the higher energy S = 5/2 state at elevated temperatures.

The reduced cobalt species **16** displays a similar temperature dependent magnetic response, varying from 1.2 $\mu_{\text{B}}$ at 20 K to 1.9 $\mu_{\text{B}}$ at 300 K. These values lie between the spin-only values calculated for a $S_{\text{total}} = 0$ and a $S_{\text{total}} = 1$ system, which are 0 and 2.83 $\mu_{\text{B}}$, respectively. This may reflect either an analogous behaviour as discussed above for the iron analogue, a substantial orbital angular momentum contribution as was found for the neutral species **10**, or a combination of both effects.

No magnetic exchange is expected between the diamagnetic Ni(II) complex **17**

and the bipyridyl radical. At 20 K the observed magnetic susceptibility of 1.51 $\mu_B$ is close to the predicted 1.73 $\mu_B$ of a $S = 1/2$ system. The decrease in $\mu_{eff}$ at higher temperatures is attributed to unsaturated trace impurities.

The interpretation of the magnetic data presented here was done in collaboration with Radovan Herchel of Palacký University, Olomouc, Czech Republic.

### 3.4.3 Mössbauer Spectroscopy

The iron containing compounds in this chapter can uniquely be examined using $^{57}$Fe Mössbauer spectroscopy to accurately determine the oxidation state of the central iron atoms in **10** and **15**. This permits distinction between two potential reduction products:

1. The bipyridine ligand is reduced to form a bipyridyl radical anion.

2. The iron(II) atom is reduced to iron(I) with the bipyridyl ligand unaffected.

Temperature resolved measurements of spectra between 85 and 295 K show that the neutral species **10** is a paramagnetic high-spin iron(II) complex in a pseudo tetrahedral coordination environment. The 85 K spectrum is shown in Figure 3.34a. The observed quadrupole doublet is asymmetric because of anisotropic absorption effects, in turn a result of the needle-like crystal morphology of the sample. The data were fitted with a single quadrupole doublet having uniform line width but differing component areas to reflect this. The isomer shifts ($\delta$) observed fall between 0.511 and 0.406 mm s$^{-1}$ over the 85 to 295 K range (Table 3.9). These values are slightly lower than would be expected for a tetrahedral complex, and possibly result from the strong $\sigma$-donor properties of the mesityl ligands.[38] The quadrupolar splitting ($\Delta E_Q$) of approximately 0.65 mm cm$^{-1}$ is consistent with a distorted tetrahedral coordination environment.

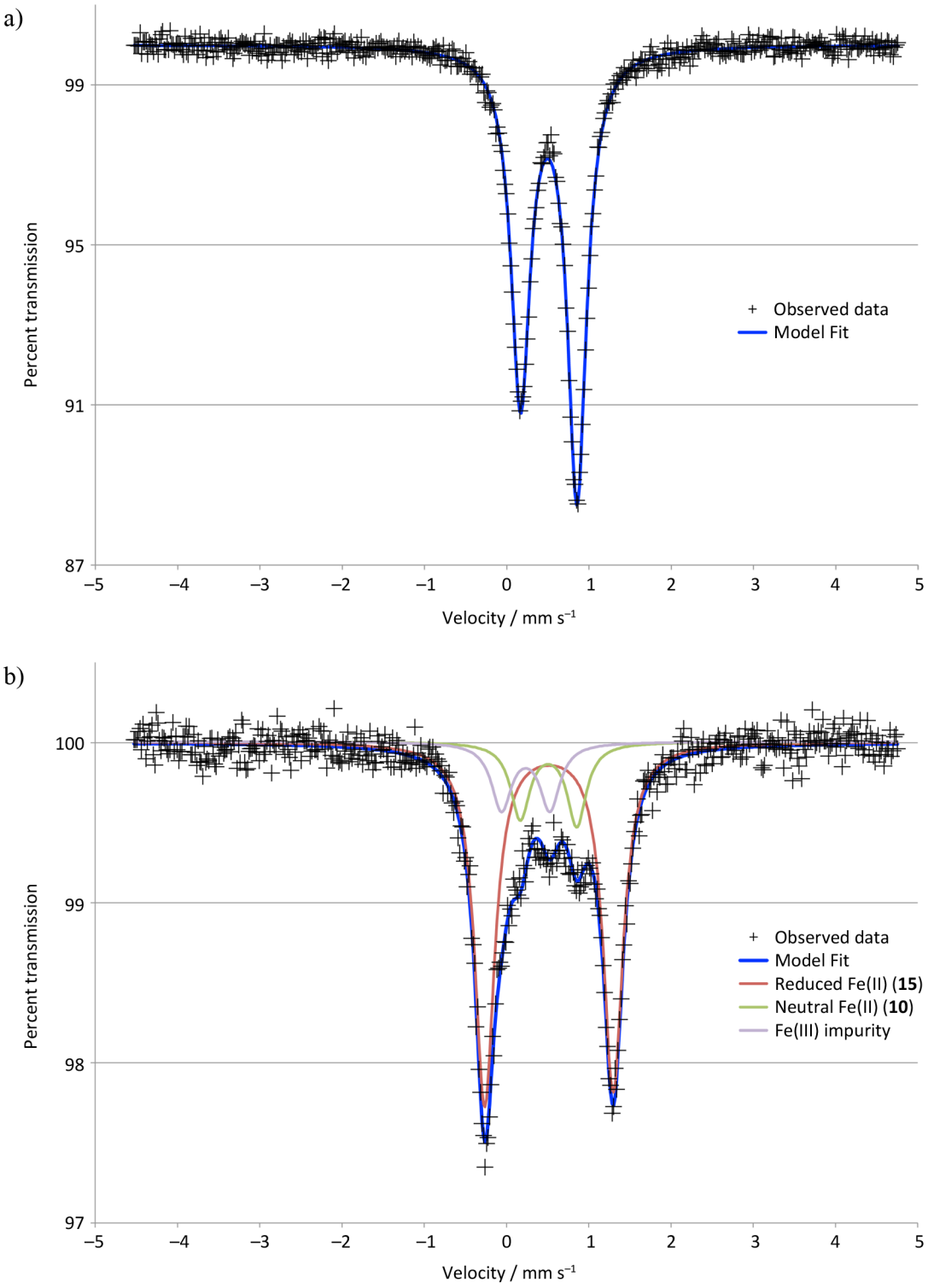



Figure 3.34: Mössbauer spectra of (**a**) compound **10** and (**b**) compound **15**, both obtained at 85 K. The lower spectrum shows the fitted components that generate the observed plot.

| Complex | T / K | $\delta$ / mm s$^{-1}$ | $\Delta E_Q$ / mm s$^{-1}$ | $\Gamma$ / mm s$^{-1}$ | area / % | assignment |
|---|---|---|---|---|---|---|
| **10** | 295 | 0.406 | 0.62 | 0.28 | 100 | **10** |
| | 255 | 0.425 | 0.63 | 0.25 | 100 | **10** |
| | 225 | 0.441 | 0.64 | 0.26 | 100 | **10** |
| | 155 | 0.481 | 0.67 | 0.25 | 100 | **10** |
| | 85 | 0.511 | 0.69 | 0.28 | 100 | **10** |
| **15** | 295 | 0.408 | 1.36 | 0.34 | 30.9 | **15** |
| | | 0.406 | 0.62 | 0.28 | 21.4 | **10** |
| | | 0.156 | 0.62 | 0.37 | 47.6 | Fe(III) |
| | 225 | 0.455 | 1.49 | 0.30 | 52.1 | **15** |
| | | 0.441 | 0.64 | 0.26 | 19.0 | **10** |
| | | 0.182 | 0.74 | 0.40 | 28.9 | Fe(III) |
| | 155 | 0.497 | 1.56 | 0.29 | 59.0 | **15** |
| | | 0.481 | 0.67 | 0.25 | 13.6 | **10** |
| | | 0.206 | 0.62 | 0.46 | 27.4 | Fe(III) |
| | 85 | 0.516 | 1.56 | 0.29 | 71.2 | **15** |
| | | 0.511 | 0.69 | 0.28 | 15.3 | **10** |
| | | 0.235 | 0.59 | 0.29 | 13.5 | Fe(III) |

Table 3.9: Mössbauer spectral parameters of **10** and **15** relative to 295K $\alpha$-iron powder.

The reduced species, **15**, proved to be significantly more air- and moisture-sensitive than its neutral precursor, with spectra revealing the presence of three iron environments. The major component is consistent with a tetrahedral iron(II) compound while two minor components are also present. One minor component has identical parameters to the neutral species **10** while the other is consistent with a high-spin iron(III) compound (presumably a decomposition product (Figure 3.34b)). It is not known if this final component is a result of the synthetic route employed, or arises as a result of sample manipulations in preparing the Mössbauer spectral absorber, but the latter seems more likely as samples are unavoidably necessarily briefly exposed to air before mounting them in the spectrometer. Isomer shifts ($\delta$) for the major component range between 0.516 and 0.408 mm s$^{-1}$ between 85 and 295 K (Table 3.9). These values are close to those reported by Wieghardt for two related bis($\alpha$-diamine)iron(II) complexes (0.50 and 0.65 mm s$^{-1}$ at 80 K).[39,40] Despite having similar isomer shifts, the quadrupolar splittings for **10** and **15** are significantly different with the latter be-

ing more than double the former at all temperature points measured. This change is unexpected as the coordination environment around the iron site is not substantially changed between **10** and **15**. However, DFT calculations indicate that this variable is highly dependent upon immediate ligand positions. Furthermore, to distinguish between the effects of ligand movement and any influence of a negatively charged radical anionic ligand, DFT computations were performed to calculate the parameters for **10** with the geometry of **15** and vice versa. In both cases the quadrupolar splitting was found to be heavily influenced by ligand geometry with virtually no contribution from the presence of an electron in the bipyridine LUMO.

In conclusion, the Mössbauer data indicate that in both **10** and **15** the oxidation state of the central iron atom can be assigned as II.

The collection and interpretation of Mössbauer data presented here was done in collaboration with Gary Long of The University of Missouri, Rolla, Missouri.

### 3.4.4 EPR Spectroscopy

All paramagnetic samples were additionally studied by EPR spectroscopy. The requirement for highly diluted solution samples (on the order of millimolar), coupled with the highly air- and moisture-sensitive nature of the compounds involved frequently meant that it was not possible to obtain solution measurements. Despite rigorous drying of solvents, glassware and other apparatus, sample decomposition in solution remained a challenging problem.

The neutral species **8** (chromium) and **10** (iron) are $S$ = integer systems and as such exhibit non-Kramers ion behaviour and remained virtually EPR silent, with very weak resonances observed being of similar size to the response of the microwave cavity. Samples **9** (manganese) and **11** (cobalt) gave rise to extremely broad signals around $g$ factors of 2.009 and 2.428, respectively (Figure 3.35 a and b). These values are consistent with those obtained from a fit of the magnetic data for each

| Nucleus: | 2× $^{14}$N | 2× $^{1}$H | 2× $^{1}$H | 2× $^{1}$H | 2× $^{1}$H |
|---|---|---|---|---|---|
| Model / Hz | 9.501 | 11.126 | 4.288 | 1.989 | 2.017 |
| Model / mT | 0.339 | 0.397 | 0.153 | 0.071 | 0.072 |
| Literature / mT | 0.335 | 0.408 | 0.150 | 0.081 | 0.065 |

Table 3.10: Comparison of coupling constants obtained from fitted data of the EPR spectrum of **17** (Ni) with previously published literature values.[34]

compound: 1.91 and 2.67, respectively). This substantial broadening may occur due to the close proximity of spin-active nuclei in the crystal lattice introducing inter-spin dipole-dipole and exchange interactions and allowing rapid relaxation. Attempts to magnetically dilute samples by the co-precipitation of **9** with $[NBu_4][PF_6]$ were found to only slightly reduce this effect.

The reduced species **13** to **17** are all EPR active. The solid state spectra of **13** (chromium) was collected at 10 K and room temperature (Figure 3.35c) and reveals a sharp resonance with a $g$ factor of 1.986. Similarly, room-temperature solid- and THF solution-state measurements of **14** (manganese) revealed a sharp resonance with a $g$ factor of 2.003 (Figure 3.35d). Room temperature measurements of solid samples of both **15** (iron) and **16** (cobalt) exhibit large, broad responses around $g$ factors of 2.086 and 2.189, respectively. This broadening is likely the result of significant spin-orbit coupling of the radical ligand electron with the metal centre. Interestingly, both spectra also exhibit sharp, far smaller and similarly positioned resonances at $g$ = 1.994 and 2.016, respectively (Figure 3.35 e and f). Both solid- and solution-state room temperature measurements of **17** (nickel) reveal a resonance at around $g$ = 2.010. The latter measurement demonstrates a hyperfine splitting pattern that was modelled using MATLAB and the EasySpin toolkit (Figure 3.36).[41,42] Parameters from the model compare well with previously published data and are given in Table 3.10.[34] The MATLAB code used to refine these parameters is provided electronically on the Supporting Information disk.

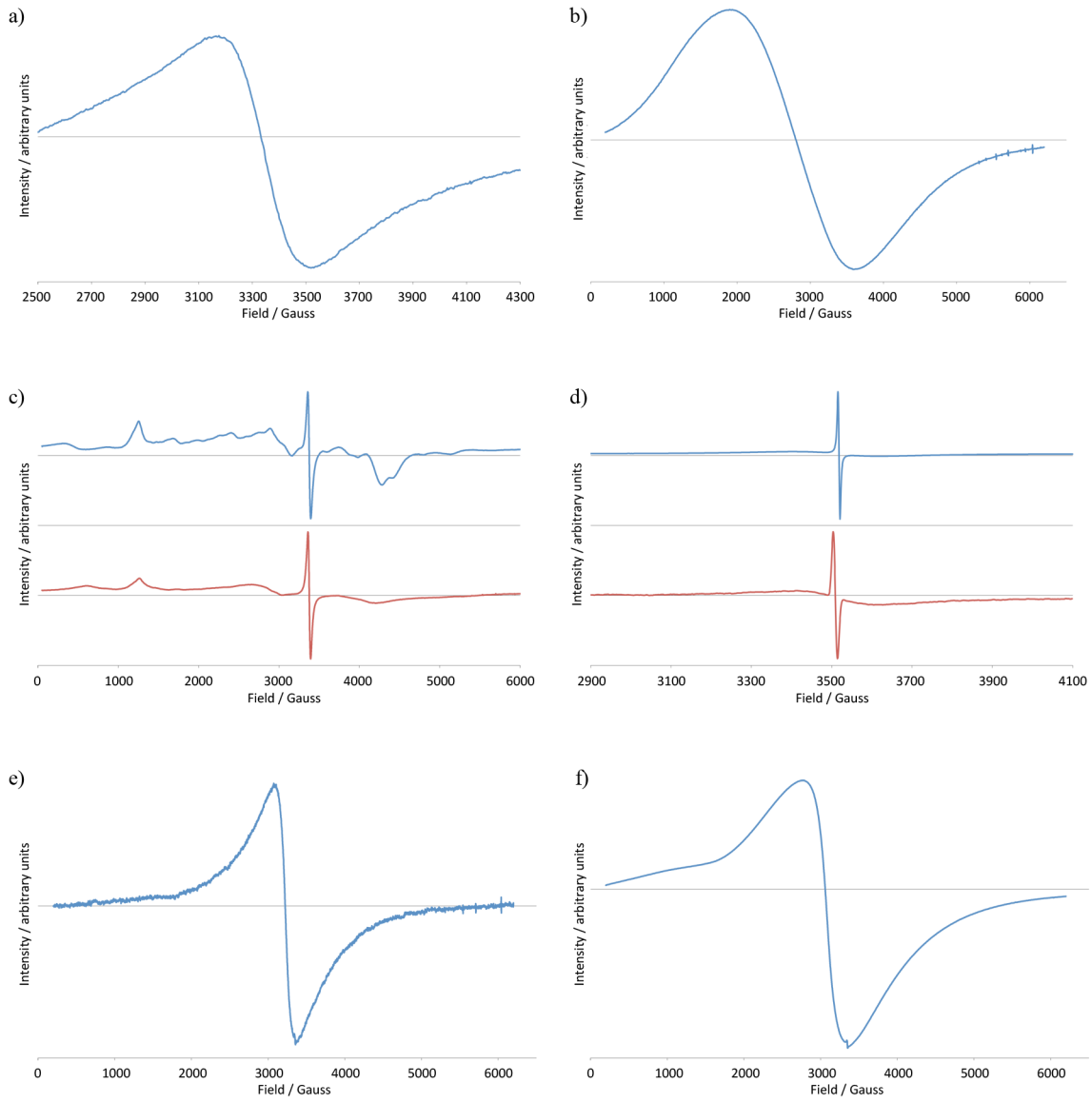



Figure 3.35: EPR responses of: **a**) solid-state spectrum of **9** (Mn) at 298 K; **b**) solid-state spectrum of **11** (Co) at 298 K; **c**) solid state spectra of **13** (Cr) at 10 K (top) and 298 K (bottom); **d**) Solid state (top) and solution-state (bottom) spectra of **14** (Mn) at 298 K; **e**) solid-state spectrum of **15** (Fe) at 298 K; **f**) solid-state spectrum of **16** (Co) at 298 K.

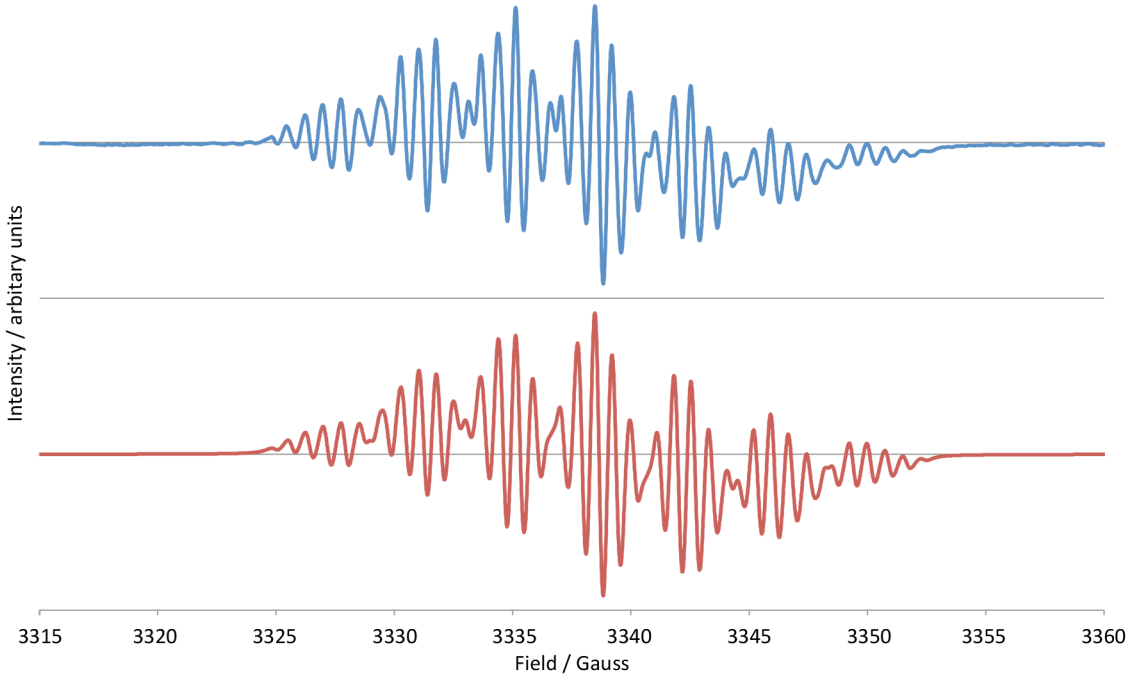



Figure 3.36: Solution-state EPR spectrum of **17** (Ni) at 298 K (top) and modelled spectrum (bottom).

### 3.4.5 Infrared and Raman Spectroscopy

Previous work by Nakamoto and co-workers provided a series of diagnostic IR bands to aid determination of of the oxidation state of 2,2´-bipyridine ligands.[43] Table 3.11 provides a summary of these values and of additional Raman values identified by the study of the alkali metal salts detailed in Chapter 2. The IR and Raman spectra of each of the compounds detailed in this chapter have been recorded and are shown in Figures 3.37 to 3.40, with the relevant diagnostic bands highlighted. Although not conclusive by itself, it is clear that there is evidence for the presence of a neutral bipyridine ligand in each of compounds **8** to **12** and of a reduced bipyridyl ligand in compounds **13** to **17** that corroborates the interpretation of the other measurements described in this chapter.

| | Range: | Neutral Species | Radical Monoanion |
|---|---|---|---|
| IR | 900 – 1000 $cm^{-1}$ | No bands | strong: 950 $cm^{-1}$ |
| | 1500 – 1650 $cm^{-1}$ | strong: 1600 $cm^{-1}$ | multiple strong: 1525 $cm^{-1}$ |
| Raman | 630 – 670 $cm^{-1}$ | medium band: 650 $cm^{-1}$ | no bands |
| | 950 – 1050 $cm^{-1}$ | medium band: 1020 $cm^{-1}$ | medium band: 990 $cm^{-1}$ |
| | 1200 – 1250 $cm^{-1}$ | no bands | strong band: 1220 $cm^{-1}$ |

Table 3.11: Diagnostic IR and Raman bands for determining the oxidation state of 2,2´-bipyridine.[43]

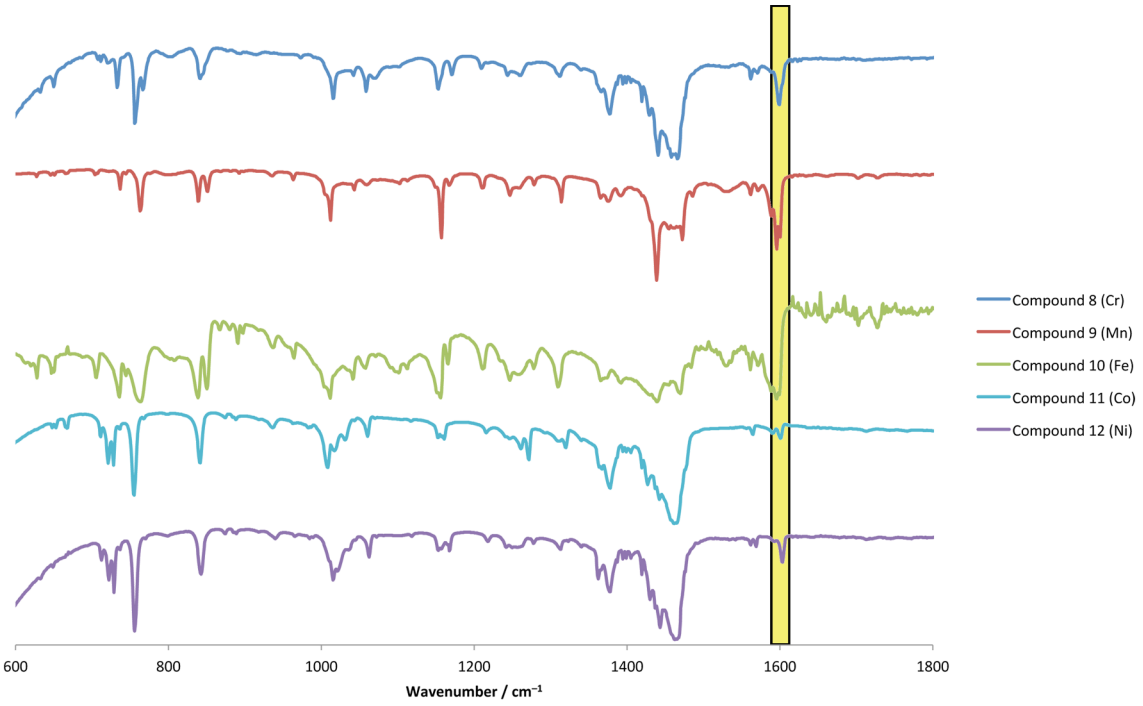



Figure 3.37: IR spectra of the neutral compounds **8** to **12**. The diagnostic region at 1600 $cm^{-1}$ is highlighted.

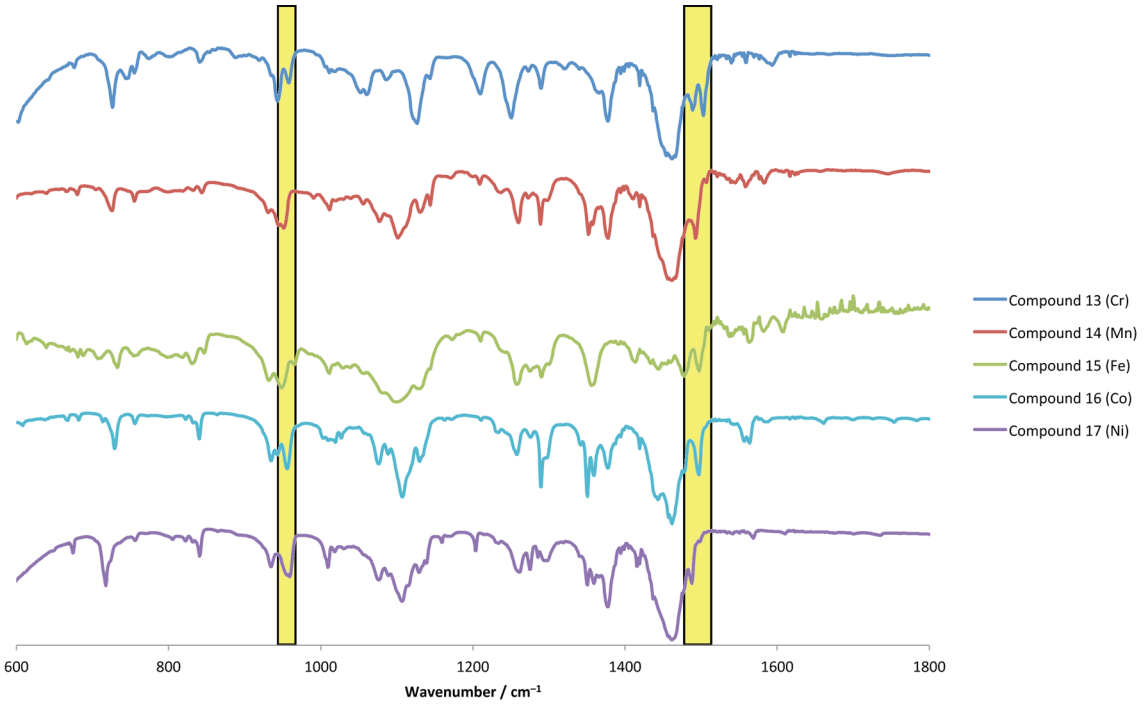



Figure 3.38: IR spectra of the reduced compounds **13** to **17**. The diagnostic regions at 950 and 1525 $cm^{-1}$ are highlighted.

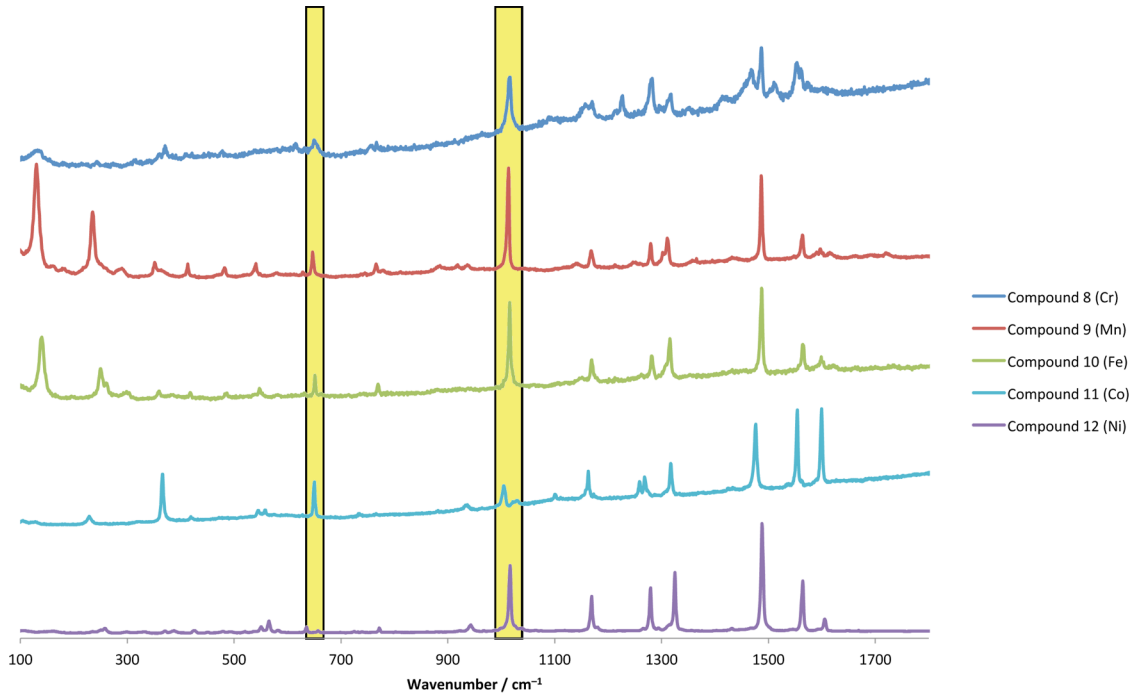



Figure 3.39: Raman spectra of the neutral compounds **8** to **12**. The diagnostic regions at 650 and 1010 $cm^{-1}$ are highlighted.

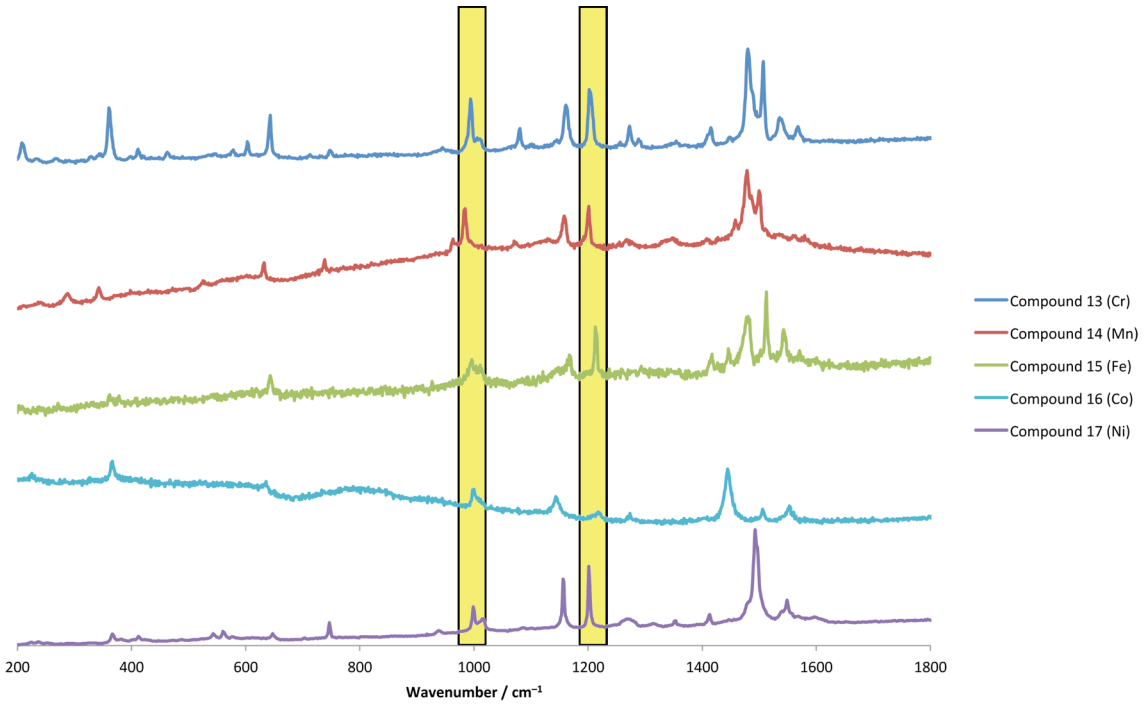



Figure 3.40: Raman spectra of the reduced compounds **13** to **17**. The diagnostic regions at 990 and 1220 $cm^{-1}$ are highlighted.

### 3.4.6 Trends in Electronic Structure

Using the coordinates determined from the single crystal X-ray diffraction structures as a starting point, computations at the DFT level were used to refine geometry optimisations and predict electronic density distributions for the neutral and reduced complexes discussed in this chapter. Metal–ligand bond lengths were found to be systematically slightly longer than those observed experimentally; however the trends observed experimentally are accurately reproduced. The observed ligand geometries were likewise identified as energy minima with the calculations for the chromium, cobalt and nickel complexes calculations yielding square planar structures and the manganese and iron systems calculations showing tetrahedral coordination around the metal. As mentioned earlier, close energy minima were found for square planar and tetrahedral geometries of both cobalt species. As a consequence both sets of data have been analysed. Comparison of inter-pyridyl bond lengths between neu-

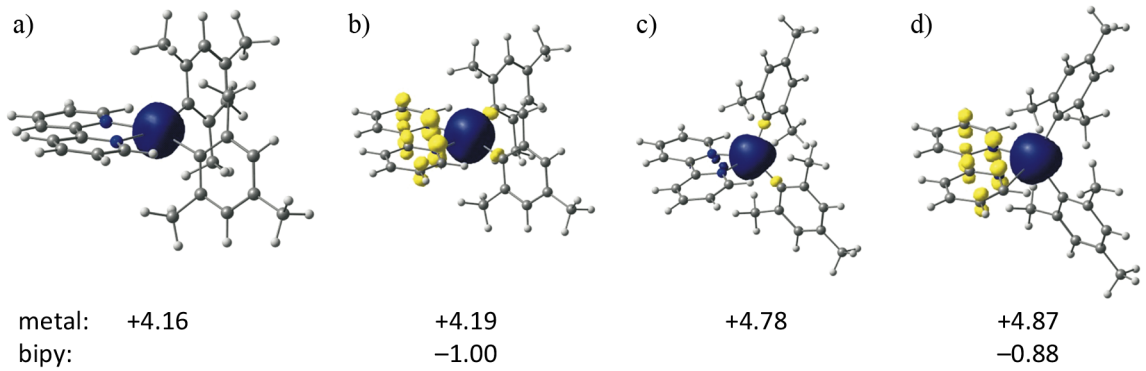



Figure 3.41: Mulliken spin densities for the transition metal complexes in **a**) **8** (Cr neutral), **b**) **13** (Cr reduced), **c**) **9** (Mn neutral) and **d**) **14** (Mn reduced).

tral and reduced computed structures reveals a contraction in going to the reduced forms. M–N bonds are found to shorten by less than is observed experimentally while M–C bond lengths are found to slightly elongate which was not observed crystallographically. Although this suggests that M–N and M–C bonding is not perfectly described by the calculations the overall trends in electronic structure appear to be well reproduced. Relevant bond metrics and electronic parameters are listed in Table 3.12.

Net Mulliken spin densities on the bipyridyl ligands of the reduced compounds show that the ligands possess radical anionic character in all cases. Figure 3.41 shows the spin density plots for the chromium and manganese complexes.

The magnetic behaviours of the reduced complexes **13** to **17** are best explained by considering the pseudo tetrahedral and pseudo square-planar ligand geometries separately. The examples of the former geometry, **14** (Mn) and **15** (Fe), exhibit very strong antiferromagnetic coupling, arising as a result of overlap of the bipyridyl π* orbital with the transition metal $d_{xz}$ orbital, which additionally contains a M–C antibonding component. Calculated exchange coupling constants, $J$, are large and negative, which compares favourably with experimental measurements that suggest $J < -350$ cm$^{-1}$. Thus in both cases anti-ferromagnetic coupling ($S = 2$ and $S = 3/2$, respectively) are significantly more stable than the $S = 3$ and $S = 5/2$ alteratives.

| | Cr | | Mn | | Fe | | Co | | | | Ni | |
|---|---|---|---|---|---|---|---|---|---|---|---|---|
| | **8** | **13** | **9** | **14** | **10** | **15** | $\mathbf{11_{sp}}$ | $\mathbf{16_{sp}}$ | $\mathbf{11_{td}}$ | $\mathbf{16_{td}}$ | **12** | **17** |
| $M_s$ | 2 | $^3/_2$ | $^5/_2$ | 2 | 2 | $^3/_2$ | $^1/_2$ | 1 | $^3/_2$ | 1 | 0 | $^1/_2$ |
| $S_M$; $S_{bipy}$ [a] | 2; 0 | 2; $^1/_2$ | $^5/_2$; 0 | $^5/_2$; $^1/_2$ | 2; 0 | 2; $^1/_2$ | 1/2; 0 | $^1/_2$; $^1/_2$ | $^3/_2$; 0 | $^3/_2$; $^1/_2$ | 0; 0 | 0; $^1/_2$ |
| M–N | 2.19 | 2.14 | 2.22 | 2.19 | 2.20 | 2.13 | 2.04 | 2.02 | 2.12 | 2.07 | 2.01 | 1.99 |
| M–C | 2.12 | 2.17 | 2.13 | 2.20 | 2.09 | 2.14 | 1.96 | 1.98 | 2.04 | 2.09 | 1.93 | 1.95 |
| C(5)–C(6) | 1.48 | 1.43 | 1.48 | 1.43 | 1.48 | 1.43 | 1.48 | 1.43 | 1.48 | 1.43 | 1.48 | 1.43 |
| $\Phi$ [b] | 18.9 | 20.1 | 63.9 | 75.9 | 67.5 | 73.8 | 17.1 | 17.3 | 69.5 | 74.8 | 17.0 | 16.8 |
| $J$ [c] | | –508 | | –492 | | –656 | | +396 | | –1050 | | |
| $\langle S^2 \rangle$ | 6.05 | 4.69 | 8.84 | 6.89 | 6.05 | 4.62 | 0.78 | 2.03 | 3.80 | 2.80 | 0.00 | 0.76 |
| $\rho_M$ | 4.16 | 4.19 | 4.78 | 4.87 | 3.73 | 3.74 | 1.25 | 1.21 | 2.63 | 2.66 | 0.00 | 0.03 |
| $\rho_{bipy}$ | | –1.00 | | –0.88 | | –0.86 | | 0.92 | | –0.80 | | 0.98 |

Table 3.12: Optimised geometric and electronic parameters for compounds **8** to **17**. Bond lengths are given in Ångström. [a]Local spin on metal and ligand centres. [b]Angle between the planes containing (M, N1, N2) and (M, C11, C12), given in degrees. [c]Coupling constant $J$, given in $cm^{-1}$, calculated using Yamaguchi's formula.[44]

In the square planar geometry of **13** (Cr), the four low-lying metal d orbitals are all singly occupied and the bipyridyl-based radical electron is antiferromagnetically coupled through the essentially non-bonding $d_{xz}$ orbital. By contrast, in **17** (Ni) the same four low lying orbitals are fully occupied and no exchange coupling is possible. As was mentioned earlier, optimised geometry calculations identified tetrahedral and square-planar conformations for both the neutral (**11**) and reduced (**16**) cobalt complexes with near identical energy. In the neutral species the square-planar complex ($\mathbf{11_{sp}}$) is favoured ($S = 1/2$) by 4 kcal mol$^{-1}$ and while this is the same geometry as is observed crystallographically, it may be argued that so small a calculated energy difference is not statistically meaningful. Analysis of the reduced analogue (**16**) is challenging owing to the potential for ferromagnetic or antiferromagnetic coupling between the metal centre and the bipyridyl ligand radical. In a tetrahedral orientation ($\mathbf{16_{td}}$), coupling is largely analogous to the manganese and iron cases discussed above, resulting in strong antiferromagnetic couplings and a $S = 1$ ground state. The hypothetical alternative square planar case ($\mathbf{16_{sp}}$) has the lowest energy electron vacancy in the $d_{z^2}$ orbital, which is approximately orthogonal to the bipyridyl $\pi^*$ orbital. A result of this orthogonality is the requirement for ferromagnetic coupling, creating another triplet ($S = 1$) state, but with a substantially different electronic structure to that of $\mathbf{16_{td}}$. The energy separation of these two states is calculated to be 2 kcal mol$^{-1}$, with the pseudo tetrahedral structure slightly favoured (in contrast to the crystallographically determined geometry). Although the reasons for the magnetic properties observed for **16** remain unclear, this very small energy difference makes assignment of the ground state highly ambiguous and the number of accessible electronic configurations at very similar energies would certainly be expected to show unusual behaviour.

It is interesting to compare trends between X-ray and DFT generated structural parameters where the effects of coordination of neutral and reduced forms of bipyri-

dine may be examined (Tables 3.6 and 3.12). The most obvious change upon reduction is the inter-pyridyl bond length of the bipyridyl ligand. It is clear that this is almost exclusively influenced by ligand oxidation state (as postulated by Wieghardt and co-workers),[29–31] and that the metric may be compartmentalised into two non-overlapping (and hence diagnostic) regions: 1.48 Å for neutral species and 1.41 Å for monoanionic forms. M–N bond lengths also appear to vary substantially with bipyridine oxidation state, but the trend is less clear due to the variance in transition metal radius across the chromium to nickel series and changes between pseudo square planar and pseudo tetrahedral geometries. For complexes of the latter conformation (**9** and **14,** Mn; **10** and **15**, Fe) a M–N bond length contraction of approximately 0.07 Å is observed upon moving from manganese to iron. This is mirrored in the M–C bond lengths and is the result of increased effective nuclear charge. However, reduction of **9** or **10** is accompanied by a further 0.07 Å decrease in M–N bond lengths while M–C bond lengths are significantly less affected, exhibiting a 0.01 Å elongation. The theoretically calculated tetrahedral cobalt species displays a similar response, though there is obviously no corroborating X-ray data in this case. This shortening arises because there is strong antiferromagnetic coupling of the predominantly bipyridyl π* based orbital which also incorporates a component of M–N bonding character (Figure 3.42).

The square planar chromium complexes exhibit a similar 0.08 Å contraction of the M–N bond lengths upon reduction (relative to an almost invariant M–C bond length). This is again the result of antiferromagnetic coupling and the presence of some M–N bonding character within the bipyridyl π* based orbital (Figure 3.43a).

The ferromagnetic interaction observed in the cobalt species arises because the bipyridyl π* based orbital does not have the correct symmetry to overlap with the metal $d_{z^2}$ orbital. The π* bipyridine orbital contains M–N antibonding character, causing a smaller magnitude 0.04 Å elongation upon reduction (Figure 3.43b). Finally,

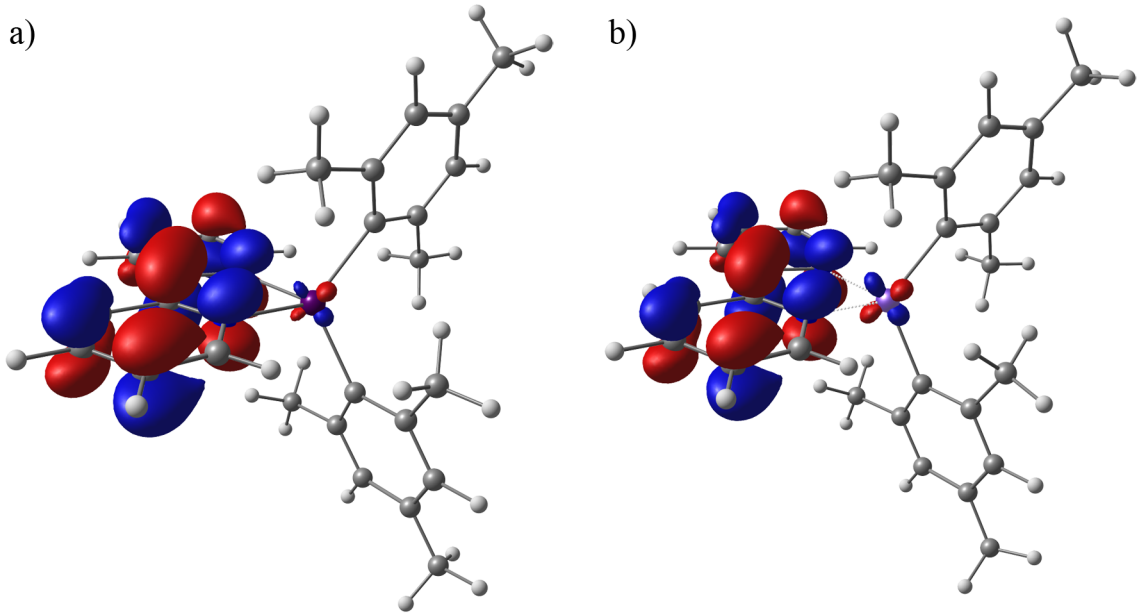



Figure 3.42: The singly occupied bipyridyl π* based orbitals of **a**) **14** (Mn) and **b**) **15** (Fe), both of which incorporate M–N bonding character.

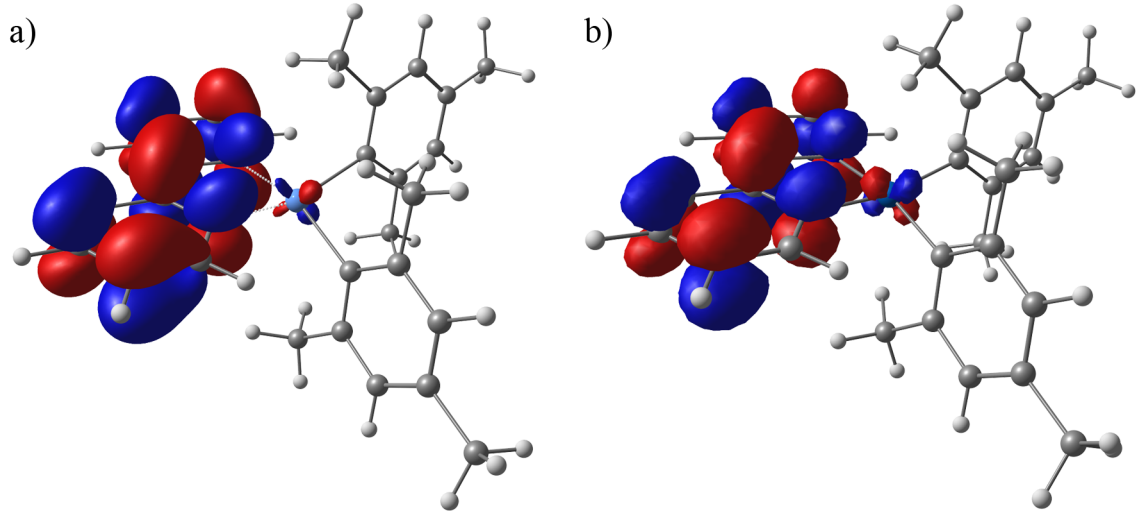



Figure 3.43: The singly occupied bipyridyl π* based orbitals of **a**) **13** (Cr) and **b**) **16** (Co), incorporating M–N bonding and antibonding character, respectively.

in the nickel complexes, no spin-orbit coupling is possible and so M–N bond lengths show only statistically insignificant change upon reduction.

The data presented here strongly imply that the magnitude of any π-backbonding (in both the neutral and reduced cases) is not sufficient to influence bond metrics. Variation in both M–C and particularly M–N bond lengths may be rationalised by considerations of geometry, transition metal radius trends and orbital symmetries alone. One final interesting observation is the serendipitous computation of a closed shell Co(I) system, isoelectronic with the neutral nickel complex (**12**). The nature of the calculation makes its description as a diamagnetic $d^8$ complex with a neutral bipyridine ligand unambiguous. This theoretical complex is around 20 kcal $mol^{-1}$ higher in energy than the two potential ground state structures (and so has no bearing on interpretation of magnetic data) but does feature a bipyridine inter-ring bond length of 1.44 Å. This is considerably shorter than the equivalent 1.48 Å distance in **12**, and demonstrates that for a sufficiently electron rich metal it is possible to observe structural effects due to π-backbonding. Though this species can be examined theoretically, its phyiscal isolation seems far less plausible: the requirement of a sufficiently electron rich site to permit π-backbonding will not be attainable without encouraging metal to ligand electron transfer to a far greater degree to create a system analogous to the reduced cobalt species detailed here.

The theoretical computations presented here were carried out at the DFT level by Tobias Krämer and Professor John McGrady of the University of Oxford.

### 3.4.7 Attempts to Synthesise Complexes of the Bipyridyl Dianion

The alkali metal salts of bipyridine described in Chapter 2 include both singly reduced radical bipyridyl species as well as doubly reduced dianionic species. Despite significant effort, it has not proved possible to characterise a transition metal complex

containing a dianionic bipyridyl ligand. Reaction products were typically either oils, amorphous powders or mixtures of decomposition products when reducing agents were used at ratios exceeding that required for a single reduction with, in some cases, 1.1 equivalents sufficient to prevent sample crystallisation.

## 3.5 Summary of Chapter 3

This chapter has detailed the synthesis and characterisation of a homologous series of transition metal complexes of the form $M(mes)_2(2,2´\text{-bipy})$ (M = Cr to Ni) together with their reduction products. Subsequent analysis has shown that bond metric data may be used as a diagnostic tool in the determination of the charge on the bipyridine ligand. The research described in this chapter has been published in peer-reviewed journals.[45,46]

## 3.6 References

[1] Sykes, A.; Constable, E. C. *Homoleptic Complexes of 2,2'-Bipyridine*; Academic Press Limited: London, 1989; Vol. 34.

[2] Kaes, C.; Katz, A.; Hosseini, M. W. *Chem. Rev.* **2000**, *100*, 3553.

[3] Tunney, J.; McMaster, J.; Garner, C. *Comprehensive Coordination Chemistry II*; McCleverty, J.; Meyer, T., Eds.; Elsevier-Pergamon, Oxford, 2004; Vol. 8, p 459.

[4] Gore-Randall, E.; Irwin, M.; Denning, M. S.; Goicoechea, J. M. *Inorg. Chem.* **2009**, *48*, 8304.

[5] Morancho, R.; Pouvreau, P.; Constant, G.; Jaud, J.; Galy, J. *J. Organomet. Chem.* **1979**, *166*, 329.

[6] Nikiforov, G. B.; Roesky, H. W.; Noltemeyer, M.; Schmidt, H. G. *Polyhedron* **2004**, *23*, 561.

[7] Mansell, S. M.; Adams, C. J.; Bramham, G.; Haddow, M. F.; Kaim, W.; Norman, N. C.; McGrady, J. E.; Russell, C. A.; Udeen, S. J. *Chem. Commun.* **2010**, *46*, 5070.

[8] Mansell, S. M.; Norman, N. C.; Russell, C. A. *Dalton Trans.* **2010**, *39*, 5084.

[9] Evans, W.; Drummond, D. *J. Am. Chem. Soc.* **1989**, *111*, 3329.

[10] Schultz, M.; Boncella, J. M.; Berg, D. J.; Tilley, T. D.; Andersen, R. A. *Organometallics* **2002**, *21*, 460.

[11] Walter, M. D.; Berg, D. J.; Andersen, R. A. *Organometallics* **2006**, *25*, 3228.

[12] Booth, C. H.; Walter, M. D.; Kazhdan, D.; Hu, Y. J.; Lukens, W. W.; Bauer, E. D.; Maron, L.; Eisenstein, O.; Andersen, R. A. *J. Am. Chem. Soc.* **2009**, *131*, 6480.

[13] Roitershtein, D.; Domingos, A.; Pereira, L. C. J.; Ascenso, J. R.; Marques, N. *Inorg. Chem.* **2003**, *42*, 7666.

[14] Del Piero, G. Z. A. B. G., G.; Perego *Cryst. Struct. Commun.* **1975**, *4*, 521.

[15] Mehdoui, T.; Berthet, J.-C.; Thuéry, P.; Salmon, L.; Rivière, E.; Ephritikhine, M. *Chem. Eur. J.* **2005**, *11*, 6994.

[16] Bart, S. C.; Heinemann, F. W.; Anthon, C.; Hauser, C.; Meyer, K. *Inorg. Chem.* **2009**, *48*, 9419.

[17] Takase, M. K.; Fang, M.; Ziller, J. W.; Furche, F.; Evans, W. J. *Inorg. Chim. Acta* **2010**, *364*, 167.

[18] Kraft, S. J.; Fanwick, P. E.; Bart, S. C. *Inorg. Chem.* **2010**, *49*, 1103.

[19] Ren, W.; Zi, G.; Walter, M. D. *Organometallics* **2012**, *31*, 672.

[20] Kaizu, Y.; Kobayashi, H. *Bull. Chem. Soc. Jpn.* **1970**, *43*, 2492.

[21] Kaizu, Y.; Kobayashi, H. *Bull. Chem. Soc. Jpn.* **1972**, *45*, 470.

[22] Vlcek, A.; Baumann, F.; Kaim, W.; Grevels, F.; Hartl, F. *J. Chem. Soc., Dalton Trans.* **1998**, 215.

[23] Zalis, S.; Daniel, C.; Vlcek, A. *J. Chem. Soc., Dalton Trans.* **1999**, 3081.

[24] Chisholm, M. H.; Huffman, J. C.; Rothwell, I. P.; Bradley, P. G.; Kress, N.; Woodruff, W. H. *J. Am. Chem. Soc.* **1981**, *103*, 4945.

[25] Lenges, C. P.; White, P. S.; Marshall, W. J.; Brookhart, M. *Organometallics* **2000**, *19*, 1247.

[26] Mork, B. V.; McMillan, A.; Yuen, H.; Tilley, T. D. *Organometallics* **2004**, *23*, 2855.

[27] Dieck, H. T.; Franz, K.-D.; Hohmann, F. *Ber.* **1975**, *108*, 163.

[28] Leyssens, T.; Peeters, D.; Orpen, A. G.; Harvey, J. N. *Organometallics* **2007**, *26*, 2637.

[29] Scarborough, C. C.; Wieghardt, K. *Inorg. Chem.* **2011**, *50*, 9773.

[30] Scarborough, C. C.; Sproules, S.; Weyhermuller, T.; DeBeer, S.; Wieghardt, K. *Inorg. Chem.* **2011**, *50*, 12446.

[31] Bowman, A. C.; Sproules, S.; Wieghardt, K. *Inorg. Chem.* **2012**, *51*, 3707.

[32] Edema, J. J. H.; Gambarotta, S.; Vanbolhuis, F.; Smeets, W. J. J.; Spek, A. L.; Chiang, M. Y. *J. Organomet. Chem.* **1990**, *389*, 47–59.

[33] Seidel, W. *Z. Chem.* **1985**, *25*, 411.

[34] Klein, A. *Z. Anorg. Allg. Chem.* **2001**, *627*, 645.

[35] Janes, R.; Moore, E. *Metal–Ligand Bonding*; Royal Society of Chemistry, 2004.

[36] Davies, S. G.; Orchard, A. F. *Magnetochemistry*; Oxford University Press, 2003.

[37] Atkins, P. W.; Friedman, R. S. *Molecular Quantum Mechanics*; Oxford University Press, 1996.

[38] Long, G. J. *Mössbauer Spectroscopy Applied to Inorganic Chemistry*; Springer-Verlag New York, LCC, 1984.

[39] Bart, S. C.; Chłopek, K.; Bill, E.; Bouwkamp, M. W.; Lobkovsky, E.; Neese, F.; Wieghardt, K.; Chirik, P. J. *J. Am. Chem. Soc.* **2006**, *128*, 13901.

[40] Muresan, N.; Lu, C. C.; Ghosh, M.; Peters, J. C.; Abe, M.; Henling, L. M.; Weyhermöller, T.; Bill, E.; Wieghardt, K. *Inorg. Chem.* **2008**, *47*, 4579.

[41] MATLAB *version 7.12.0 (R2011a)*; The MathWorks Inc.: Natick, Massachusetts, 2011.

[42] Stoll, S.; Schweiger, A. *J. Magn. Reson.* **2006**, *178*, 42.

[43] Saito, Y.; Takemoto, J.; B, H.; Nakamoto, K. *Inorg. Chem.* **1972**, *11*, 2003.

[44] Yamaguchi, K.; Takahara, Y.; Fueno, T. *Applied Quantum Chemistry*; Vedene, H. S.; Schaefer, H. F.; Morokuma, K., Eds.; Springer-Verlag New York, LLC, 1986; p 155.

[45] Irwin, M.; Jenkins, R. K.; Denning, M. S.; Kramer, T.; Grandjean, F.; Long, G. J.; Herchel, R.; McGrady, J. E.; Goicoechea, J. M. *Inorg. Chem.* **2010**, *49*, 6160.

[46] Irwin, M.; Doyle, L. R.; Krämer, T.; Herchel, R.; McGrady, J. E.; Goicoechea, J. M. *Inorg. Chem.* **2012**, *51*, 12301.

# Chapter 4

# Reduction of Zinc Complexes of 4,4´-Bipyridine

## 4.1 Introduction

While 2,2´-bipyridine features extensively as a chelating ligand in coordination chemistry, the 4,4´-isomer is similarly ubiquitous in the fields of metal organic frameworks (MOFs) and coordination polymer chemistry.[1–3] The ability of 4,4´-bipyridine to act as a rigid linear linker, coupled with transition metal preferences for specific ligand orientations, gives rise to three-dimensional systems. Figure 4.1 shows a recent example of such a structure that incorporates 4,4´-bipyridine, bridging tetrahedrally coordinated copper(I) sites.[4] The structure is built from metal cations and neutral linkers that form two interpenetrating diamondoid structures. Due to the overall positive charge of the framework there is a requirement for charge balancing camphorate anions in the lattice cavities.

While 4,4´-bipyridine is still frequently encountered in these type of structures, recent work, in particular by Yaghi and co-workers, has led to alternative design considerations for the synthesis of MOFs. Rather than depending upon ligand field

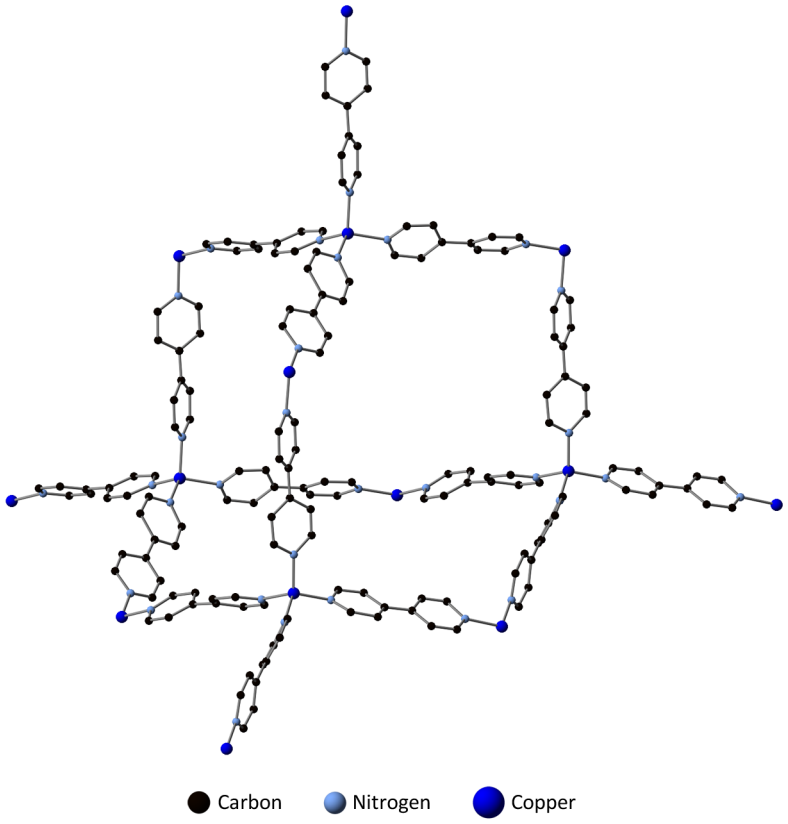



Figure 4.1: The diamondoid network formed by 4,4´-bipyridine linkers and Cu(I) cations in $[Cu_2(4,4´\text{-bipy})_4]\cdot(\text{d-Hcam})_2\cdot(4,4´\text{-bipy})_2\cdot 12(H_2O)$.[4] Hydrogen atoms, a second interpenetrated network, bipyridine guest molecules and charge balancing camphorate anions have been omitted for clarity.

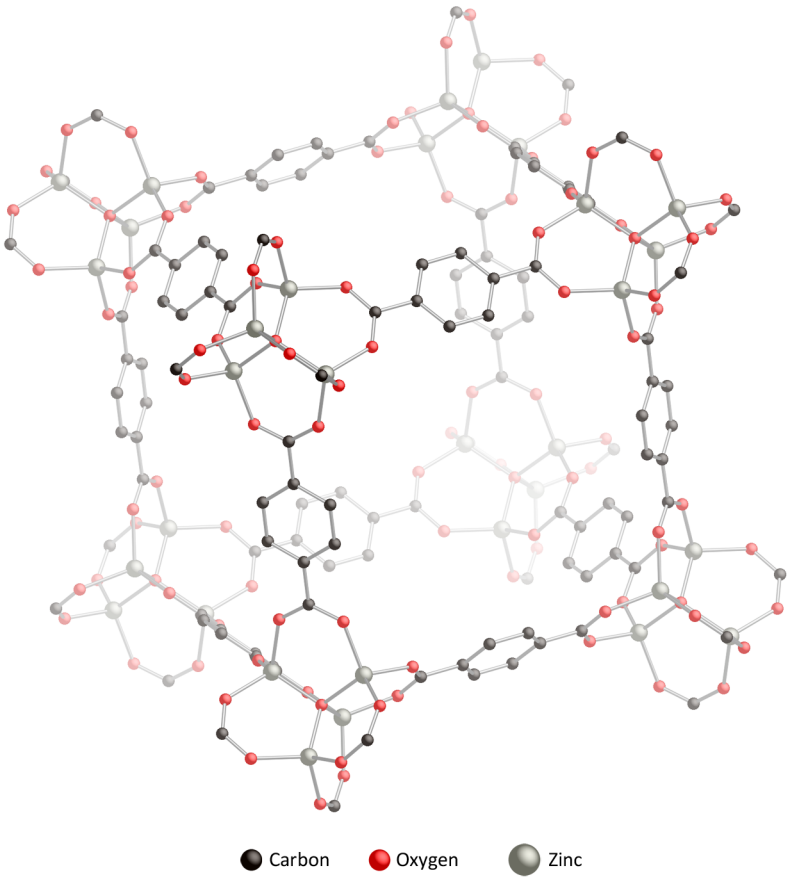



Figure 4.2: The structure of one of two interpenetrated networks in MOF-5.[7] Hydrogen atoms have been omitted for clarity.

effects to influence coordination geometry about metal atoms, the use of polyatomic cationic secondary building units (SBUs) such as zinc oxides, together with dicarboxylate anionic ligands has led to the synthesis of a series of isoreticular structures with more predictable geometries and high rigidity.[5,6] One of the most well known of these is MOF-5, shown in Figure 4.2.[7] Very recently, the Yaghi group published a series of similar systems incorporating increasingly long linkers to generate structures with large, cylindrical shaped pore sizes, up to 98 Å in diameter.[8]

Molecular squares incorporating 4,4´-bipyridine have been shown to undergo ligand centred mixed valency (LCMV) whereby electrochemical reduction of a complex causes additional electrons to be localised on the bipyridine linkers (rather than on

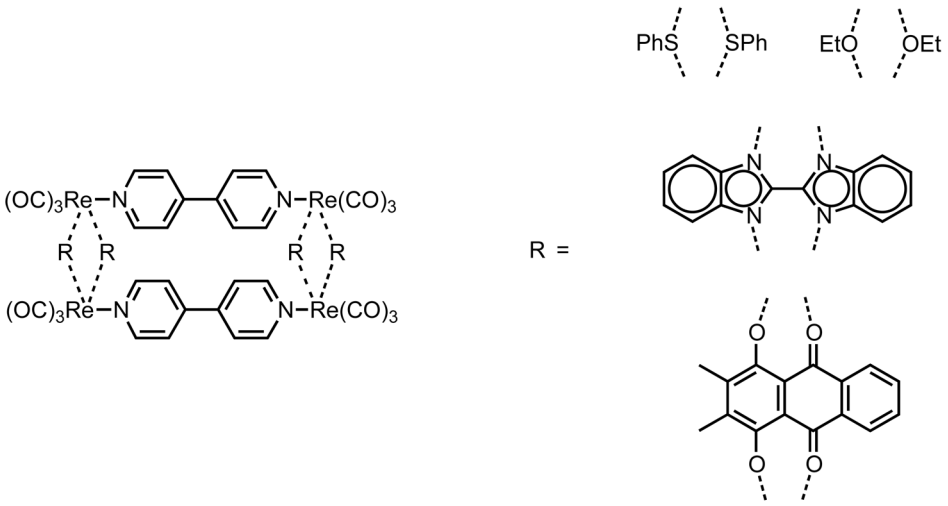



Figure 4.3: Structures of 4,4´-bipyridine containing molecular squares.

the metal cations) without causing change to the square structure itself (Figure 4.3). Both electrode and alkali metal reductions have been employed in the addition of one or three electrons to the systems, generating asymmetry in the bipyridine linker oxidation states. These oxidation states were found to easily interconvert, with IR measurements and DFT calculations revealing inter-valence transitions between the two linkers.

As mentioned in Chapter 1, while the redox chemistry of this ligand is well known, there exists no structural data of its reduction products outside of the alkali metal salts already published as part of this research project. The aim of the research presented in this chapter was to synthesise a complex containing a 4,4´-bipyridine ligand bridging two metal centres and to examine the effects of its reduction. The reaction scheme in Figure 4.4 shows the synthetic route to the compounds discussed.

## 4.2 $Zn_2$(4,4´-bipyridine)$(mes)_4$

Reactions analogous to those detailed in Chapter 3 were performed using $Zn(mes)_2$ and 4,4´-bipyridine, resulting in the synthesis of a crystalline sample of $Zn_2$(4,4´-bipyridine)$(mes)_4$(**19**). Though examples of 4,4´-bipyridine bridging two metallic

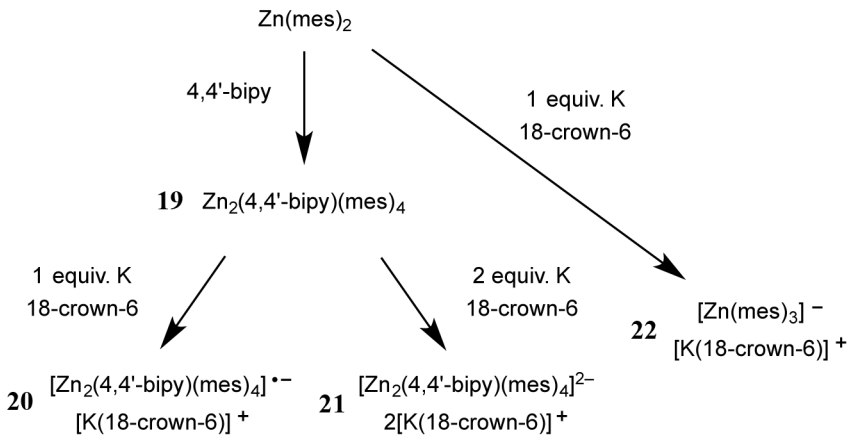



Figure 4.4: Schematic of reactions described in Chapter 4.

sites are quite abundant in the chemical literature,[12–14] examples of 4,4´-bipyridine bridged dimers of otherwise homoleptic metal sites are extremely rare,[15–28] with only three structurally characterised examples.[29–31]

### 4.2.1 Synthesis

$Zn_2$(4,4´-bipyridine)$(mes)_4$ (**19**) was prepared by the direct reaction of 4,4´-bipyridine with two equivalents of $Zn(mes)_2$ in tetrahydrofuran (THF). This yielded a pale yellow coloured solution from which colourless air- and moisture-sensitive needle-like crystals of the product were isolated following the slow diffusion of hexanes into a concentrated solution.

### 4.2.2 Structural Characterisation

Figure 4.5 shows one of the two crystallographically distinct $Zn_2$(4,4´-bipy)$(mes)_4$ complexes in **19**, each consisting of a bipyridine linker bridging two dimesityl zinc sites. Both $Zn_2$(4,4´-bipy)$(mes)_4$ units exhibit very similar structural and bond metric parameters and hence only one complex is depicted for clarity. Bond metrics are discussed in detail in Section 4.5 with reference to the other structures detailed in this chapter. Bulk purity of the solid has been confirmed by powder X-ray diffraction

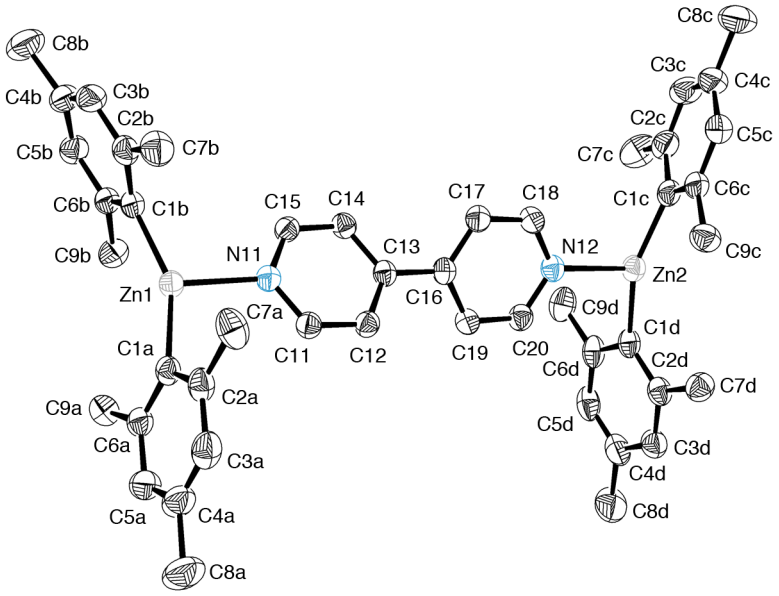



Figure 4.5: Thermal ellipsoid representation of one of the two crystallographically unique $Zn_2$(4,4´-bipy)$(mes)_4$ complexes in **19**. Anisotropic displacement ellipsoids pictured at the 50% probability level. Hydrogen atoms have been omitted for clarity.

(Figure 4.6) and elemental microanalysis.

### 4.2.3 Spectroscopic Characterisation

Both $^1$H and $^{13}$C{$^1$H} NMR studies of a $d_8$-THF solution of **19** were carried out, with assignment of the former aided by a two-dimensional COSY spectrum. Carbon atom resonances were subsequently fully assigned by reference to two-dimensional HSQC and HMBC spectra. These results are discussed in Section 4.5.

Additional solution NMR studies were carried out to determine if the crystallographically identified complex above was representative of the sample in solution or whether some degree of dissociation takes place, as indicated in Figure 4.7. The $^1$H resonances of the 4,4´-bipyridine moiety in **19** (at $\delta$ = 8.57 and 7.71 ppm for the *ortho*- and *meta*- positions, respectively) are slightly shifted, relative to those of free 4,4´-bipyridine (at $\delta$ = 8.69 and 7.67 ppm, respectively), consistent with the existence

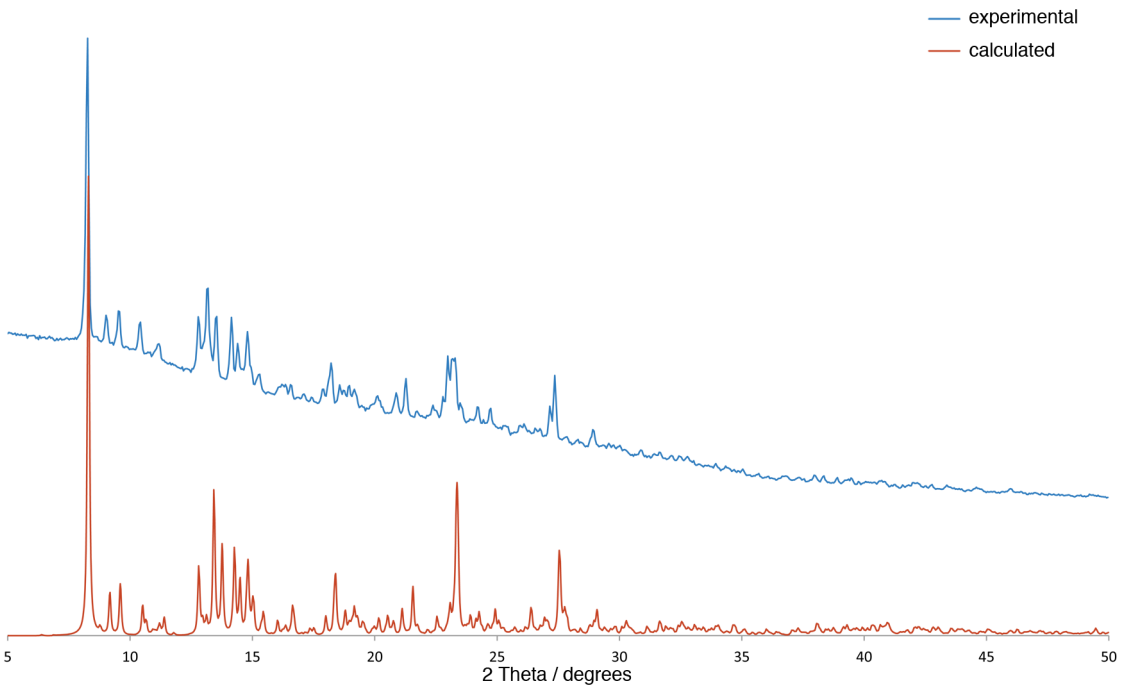



Figure 4.6: Comparison of calculated and experimental powder X-ray diffraction patterns for **19**.




Figure 4.7: Dissociation equilibrium for **19**.

of the coordinated species in solution. However, additional NMR studies can be used to further support this hypothesis. A one-dimensional NOESY experiment involving the selective inversion of the mesityl *ortho*-methyl group resonance (2.42 ppm) resulted in enhanced signal intensities of the mesityl *meta*-protons and also the 4,4´-bipy *ortho*-protons (Figure 4.8). A smaller signal intensity increase was also observed for the theoretically more distant 4,4´-bipyridine *meta*-protons. This through-space interaction requires physical close proximity of the mesityl *ortho*-methyl groups to the 4,4´-bipyridine hydrogen atoms and as such is consistent with $Zn(mes)_2$ and 4,4´-bipyridine being bonded together in solution.

Additionally, room-temperature diffusion experiments were conducted on $d_8$-THF

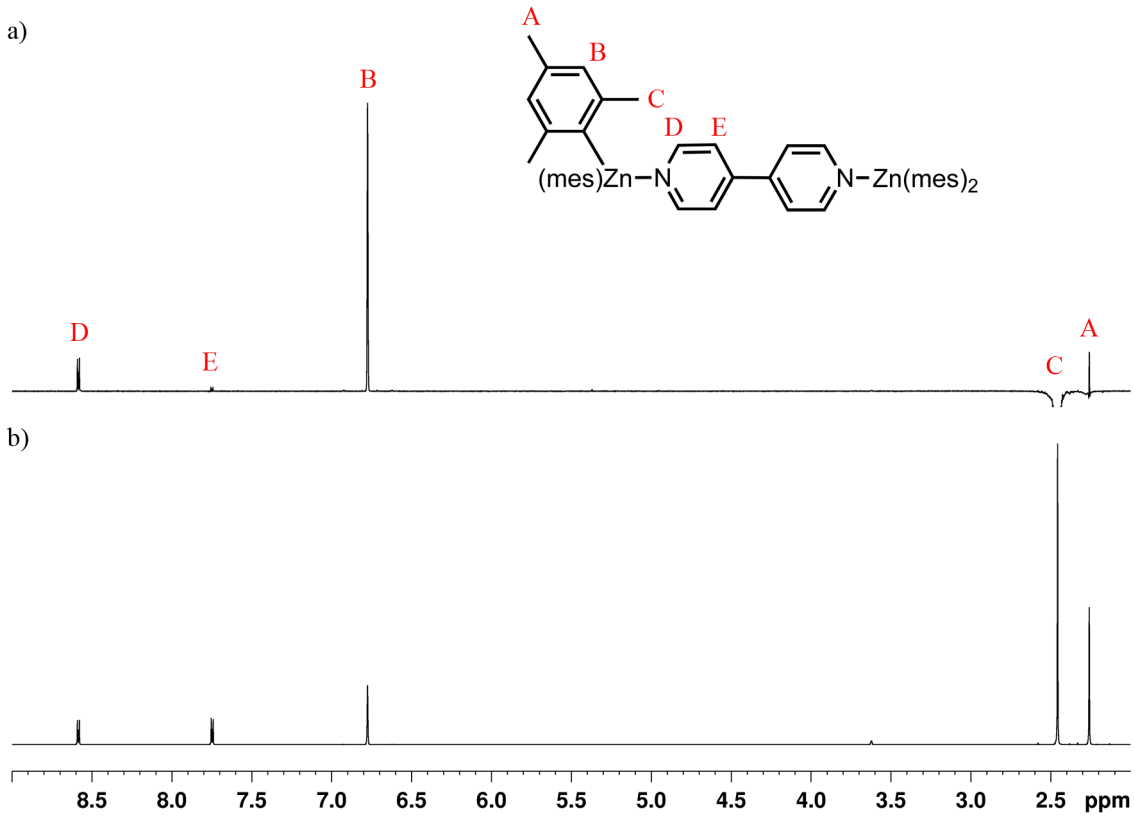



Figure 4.8: (**a**) One-dimensional NOESY spectrum of **19**, arising as a result of saturating resonance C. (**b**) $^{1}$H NMR spectrum of **19** in the absence of irradiation at resonance C, provided for comparison of resonance intensities.

| | A | B | C | D | E |
|---|---|---|---|---|---|
| 4,4´-bipy | - | - | - | $1.913 \times 10^{-9}$ | $1.911 \times 10^{-9}$ |
| $\delta$ | - | - | - | (8.71 ppm) | (7.70 ppm) |
| $Zn(mes)_2$ | $1.185 \times 10^{-9}$ | $1.171 \times 10^{-9}$ | $1.181 \times 10^{-9}$ | - | - |
| $\delta$ | (2.24 ppm) | (6.75 ppm) | (2.49 ppm) | - | - |
| **19** | $1.031 \times 10^{-9}$ | $1.027 \times 10^{-9}$ | $1.021 \times 10^{-9}$ | $1.132 \times 10^{-9}$ | $1.133 \times 10^{-9}$ |
| $\delta$ | (2.26 ppm) | (6.76 ppm) | (2.46 ppm) | (8.58 ppm) | (7.75 ppm) |

Table 4.1: Resonance shifts ($\delta$) and diffusion coefficient ($D$) values for 4,4´-bipyridine, $Zn(mes)_2$ and **19**. Proton positions follow the notation shown in Figure 4.8 on the previous page. All diffusion coefficient values are reported in $m^2/s$, and associated shifts are shown in brackets beneath.

solutions of $Zn(mes)_2$, 4,4´-bipyridine and **19** to determine the degree of any dissociation present. The diffusion coefficients ($D$) observed for **19** show that the values arising due to the 4,4´-bipyridine resonances ($1.132 \times 10^{-9}$ and $1.133 \times 10^{-9}$ $m^2/s$ for *ortho-* and *meta-* positions, respectively) are very close to those of the $Zn(mes)_2$ moieties ($1.027 \times 10^{-9}$, $1.021 \times 10^{-9}$, and $1.031 \times 10^{-9}$ $m^2/s$, for the *meta*-protons, the *ortho*-methyl, and *para*-methyl substituents, respectively). Small deviations in the values obtained suggest that if there is a dissociation equilibrium it lies strongly towards the complexed form. Table 4.1 summarises the results of these measurements and also shows the significantly different $D$ values obtained from solutions of 4,4´-bipyridine and $Zn(mes)_2$, corroborating this conclusion.

IR and Raman studies were carried out to evaluate the success of potential diagnostic bands identified in Chapter 2 for the determination of the oxidation state of 4,4´-bipyridine. For a neutral ligand, a medium to strong peak should be observed at around 1300 $cm^{-1}$ and there should be an absence of intense peaks in the region around 1500 $cm^{-1}$. Both of these predictions are observed with the proposed diagnostic band appearing at 1290 $cm^{-1}$ in the Raman spectrum.

## 4.3 $Zn_2$(4,4´-bipyridine)$(mes)_4$ Radical Monoanion

Whilst bimetallic complexes comprising of metal centres bridged by a 4,4´-bipyridyl radical anion have been proposed in the chemical literature,[32–34] prior to this compound no examples were known for which X-ray structural data are available.

### 4.3.1 Synthesis

Reaction of **19** with one equivalent of potassium metal in THF in the presence of 18-crown-6 (1,4,7,10,13,16-hexaoxacyclooctadecane) formed a dark blue solution. Subsequent slow diffusion of hexanes into a concentrated solution yielded dark blue air- and moisture-sensitive block-like crystals of [K(18-crown-6)$(THF)_2$][$Zn_2$(4,4´-bipyridine)$(mes)_4$] (**20**) after several days.

### 4.3.2 Structural Characterisation

Two compositionally identical polymorphs of **20** were found to crystallise: [K(18-crown-6)$(THF)_2$]$_2$[$Zn_2$(4,4´-bipyridine)$(mes)_4$]$_2$ in **20a** and [K(18-crown-6)$(THF)_2$]$_3$ [$Zn_2$(4,4´-bipyridine)$(mes)_4$]$_3$ in **20b**. In both **20a** and **20b**, the structures of all $Zn_2$(4,4´-bipyridine)$(mes)_4$ anions are very similar and share the same connectivity as that of the neutral parent in **19**. Figure 4.9 shows one radical anion moiety in **20a**. Bulk purity of the solid has been confirmed by powder X-ray diffraction, however, due to high similarity between the two calculated powder patterns for **20a** and **20b**, and poor crystallinity of the ground sample, it is not possible to distinguish which polymorph represents the major product (Figure 4.10).

### 4.3.3 Spectroscopic Characterisation

Solid and solution EPR spectra were recorded for **20**, with the former revealing a strong resonance with a $g$ factor of 2.0039 (Figure 4.11a). This value is typical for

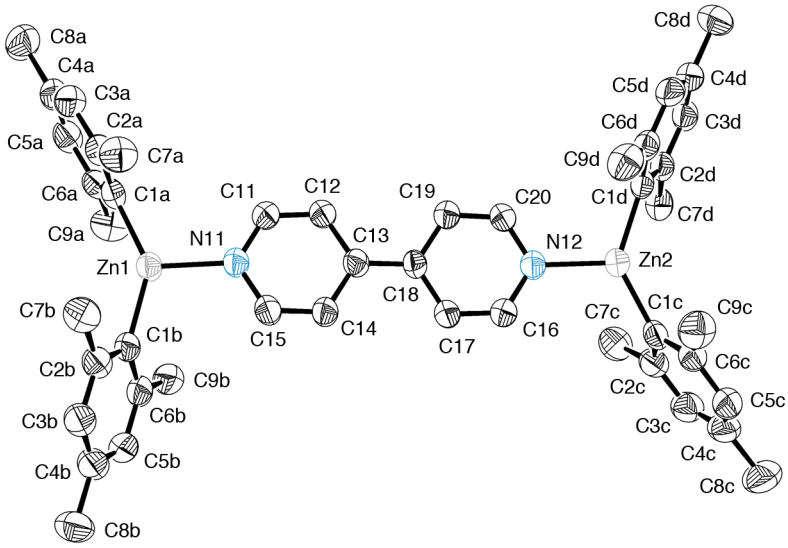



Figure 4.9: Thermal ellipsoid representation of one of the two crystallographically unique $[Zn_2(4,4´\text{-bipy})(mes)_4]^-$ complexes in **20a**. Anisotropic displacement ellipsoids pictured at the 50% probability level. Hydrogen atoms have been omitted for clarity.

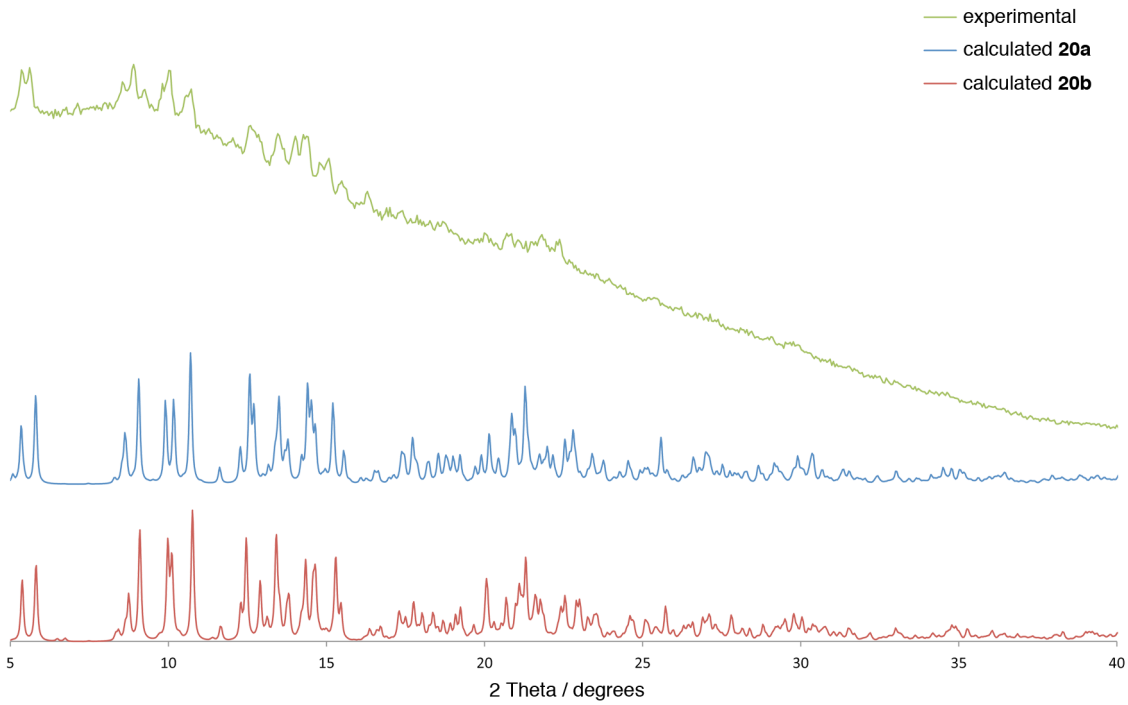



Figure 4.10: Comparison of calculated and experimental powder X-ray diffraction patterns for **20a** and **20b**.

an electron delocalised in an aromatic orbital and is very similar to the value of $g$ = 2.0043 recorded for solid samples of alkali metal salts of the 4,4´-bipyridyl radical such as Na(4,4´-bipy) in **6**.

The solution EPR spectrum of **20** exhibits a highly complex asymmetric resonance with extensive hyperfine coupling (Figure 4.11b). All attempts to model this splitting pattern have proven unsuccessful. It is probable that the asymmetry arises due to the superposition of two different paramagnetic species. NMR diffusion measurements of the neutral parent, **19**, indicate a small level of dissociation may be present in solution. At the high dilution levels required for EPR measurements the degree of dissociation of $[Zn_2(4,4´\text{-bipyridine})(mes)_4]^-$ to $Zn(mes)_2$ and the 4,4´-bipyridyl monoanion is potentially greater due to the higher effective THF concentration favouring heavily solvated $Zn(mes)_2$. Thus while the dominant EPR signal is due to **20**, the observed signal is the algebraic sum of both **20** and a unknown contribution from a dissociated 4,4´-bipyridyl radical. Both resonances would be expected to exhibit a high number of hyperfine interactions and to have considerable overlap (the 4,4´-bipyridyl radical signal is known to have a $g$ factor of 2.0044).[35] As a result of this, deconvolution of the two signals is extremely challenging and ultimately proved impossible to achieve. It is worth noting that the asymmetric response was found to be reproducible on each occasion that a solution EPR recording of **20** was attempted.

Raman studies carried out on alkali metal salts of the 4,4´-bipyridyl radical, detailed in Chapter 2, suggest two diagnostic peaks should be present: an inter-ring stretching mode at around 1350 $cm^{-1}$ and a C=C and C=N stretch at around 1510 $cm^{-1}$. These are found in the Raman spectrum of **20** at 1352 and 1515 $cm^{-1}$, respectively.

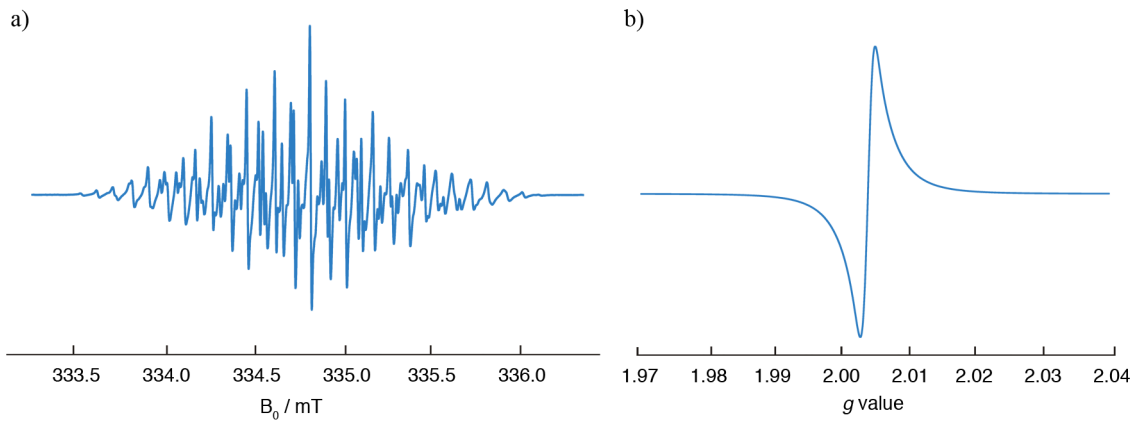



Figure 4.11: (**a**) Solution-phase and (**b**) Solid-state EPR spectra for **20**.

## 4.4 $Zn_2$(4,4´-bipyridine)$(mes)_4$ Dianion

Unlike the transition metal structures containing 2,2´-bipyridine detailed in Chapter 3, reaction of the $Zn_2$(4,4´-bipyridine)$(mes)_4$ neutral parent compound and two equivalents of alkali metal yielded crystalline products containing a doubly reduced bipyridyl moiety. The dianionic species discussed in this section represents the first structurally characterised coordination compound containing a dianionic 4,4´-bipyridyl linker.

### 4.4.1 Synthesis

Reaction of **19** with two equivalents of potassium metal in THF in the presence of 18-crown-6 formed a dark brown solution. Subsequent slow diffusion of hexanes into this solution yielded dark brown air- and moisture-sensitive plate-like crystals of [K(18-crown-6)]$_2$[$Zn_2$(4,4´-bipyridine)$(mes)_4$] (**21**).

### 4.4.2 Structural Characterisation

The asymmetric unit of **21** contains half a $[Zn_2(4,4´\text{-bipyridine})(mes)_4]^{2-}$ dianion and a full $[K(18\text{-crown-6})]^+$ cation. Unlike both polymorphs of the singly reduced species

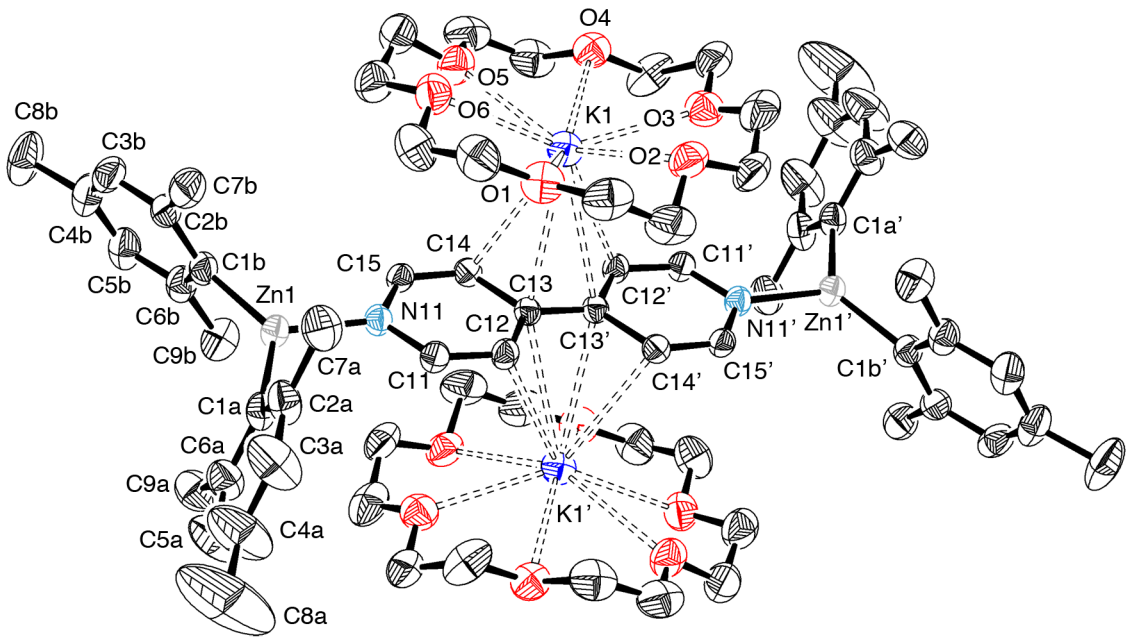



Figure 4.12: Thermal ellipsoid representation of the atoms in the asymmetric unit of **21**. Atom positions are labelled with primes to denote symmetry generated equivalents, included to illustrate coordination environment. Hydrogen atoms have been omitted for clarity. Anisotropic displacement ellipsoids pictured at the 50% probability level.

(**20a** and **20b**), in **21** a $[K(18\text{-crown-6})]^+$ cation is coordinated to each side of the bipyridyl dianion, rather than to THF solvent molecules, possibly due to the increased electrostatic attraction afforded by the double negative charge. K1 interacts with C12´, C13´, C13 and C14 with distances of 3.318(2), 3.225(2), 3.115(2) and 3.146(2) Å, respectively, shown in Figure 4.12. A full discussion of anion bond metrics in **21** and their variation with complex oxidation state is given in Section 4.5. Bulk sample purity was confirmed by elemental microanalysis and powder X-ray diffraction (Figure 4.13).

Whilst preparing samples of **21**, occasionally a side product of the previously reported trimesitylzinc(II) anion was encountered in [K(18-crown-6)] $[Zn(mes)_3]$ (**22**).[36] It was subsequently found possible to exclusively synthesise this by the direct reduction of $Zn(mes)_2$ in THF using potassium metal and 18-crown-6 to generate a pale

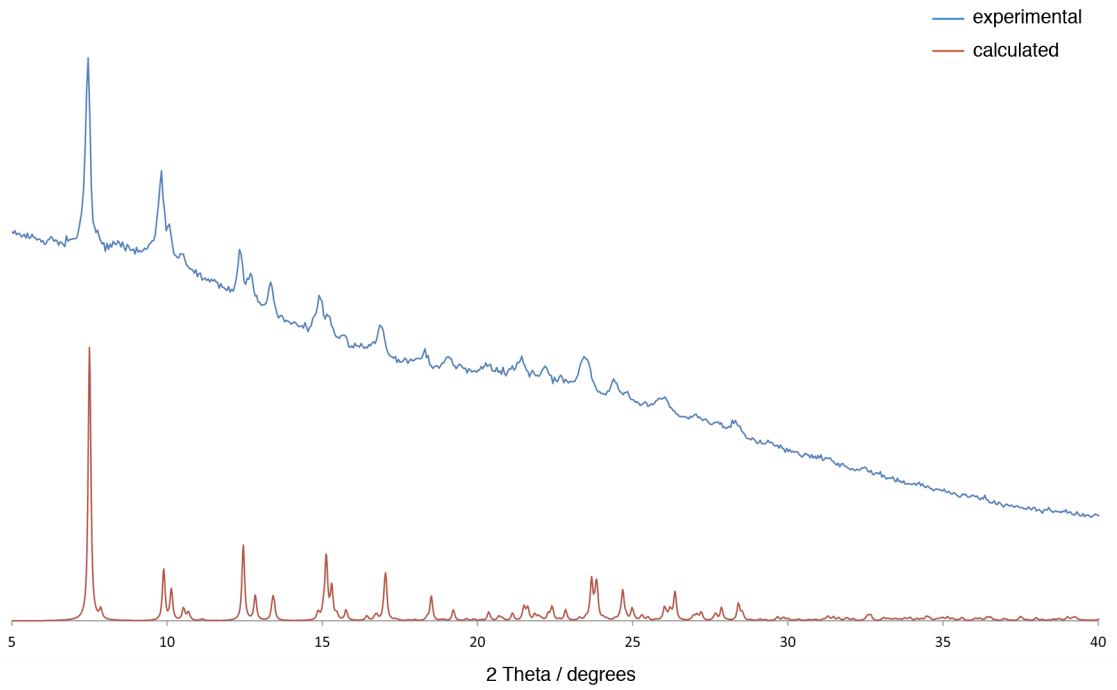



Figure 4.13: Comparison of calculated and experimental powder X-ray diffraction patterns for **21**.

brown solution. Slow diffusion of hexanes into a concentrated solution yielded colourless air- and moisture-sensitive block-like crystals of **22**. The asymmetric unit of **22** is shown in Figure 4.14. Bulk sample purity has been confirmed by elemental microanalysis and powder X-ray diffraction (Figure 4.15).

### 4.4.3 Spectroscopic Characterisation

DFT calculations on the doubly reduced 4,4´-bipyridyl species indicate that it should be diamagnetic. The EPR spectrum of a solid sample of **21** shows a very weak resonance, similar to that of **20**. This is attributed to trace amounts of the singly reduced species present, unavoidably introduced during the EPR sample preparation due to the high air- and moisture-sensitivity of **21**. Confirmation of bulk sample diamagnetism was obtained from $d_8$-THF solution $^{1}$H and $^{13}$C{$^{1}$H} NMR spectra. Complete assignment of the former (including identification of a small amount of **22**

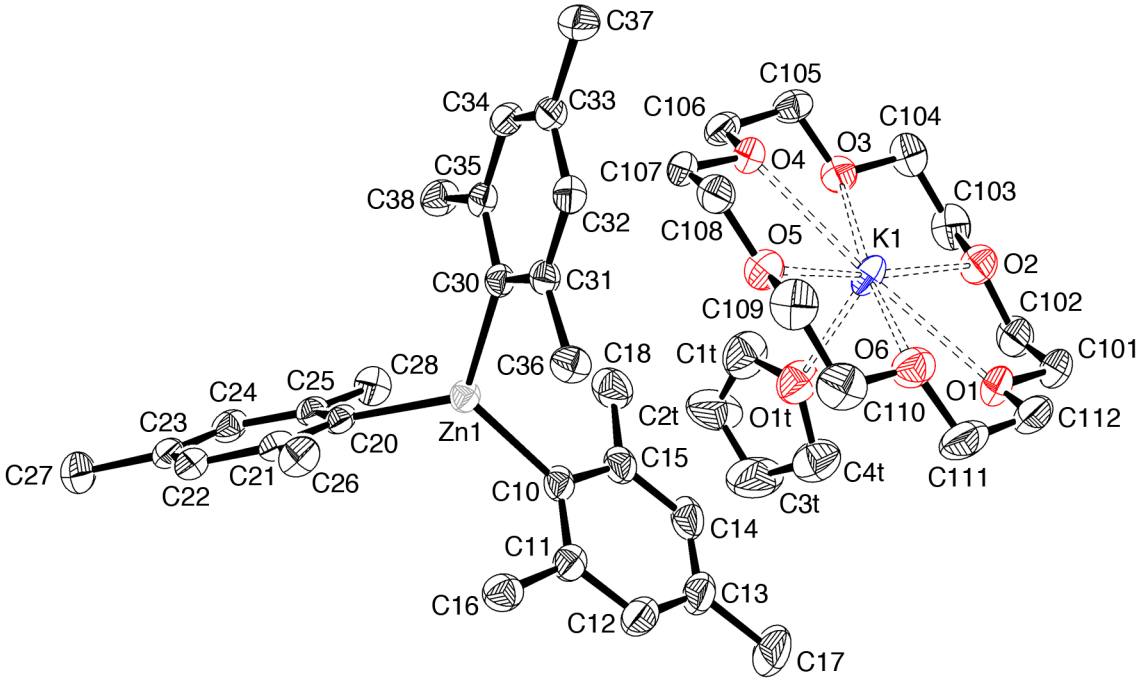



Figure 4.14: Thermal ellipsoid representation of the atoms in the asymmetric unit of **22**. Hydrogen atoms have been omitted for clarity. Anisotropic displacement ellipsoids pictured at the 50% probability level.

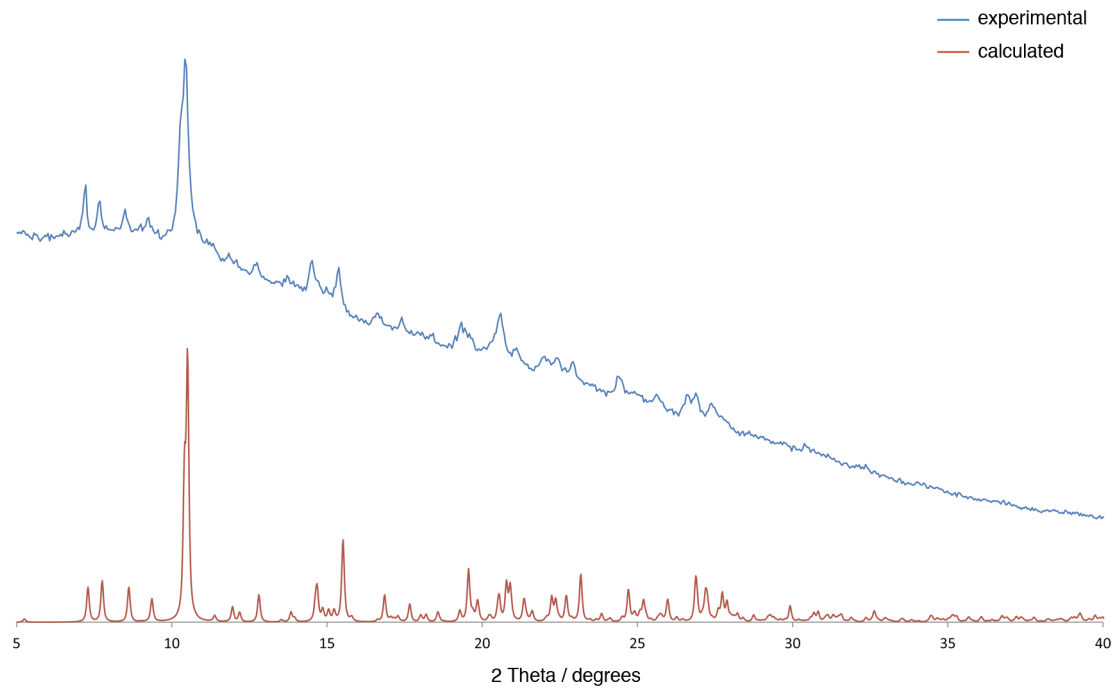



Figure 4.15: Comparison of calculated and experimental powder X-ray diffraction patterns for **22**.

present in samples) was aided by a two-dimensional COSY spectrum while HSQC and HMBC spectra were employed to tentatively assign carbon resonances. The bipyridyl dianion hydrogen resonances occur at $\delta = 5.92$ and 4.51 ppm for the *ortho*- and *meta*-positions, respectively. These chemical shifts are consistent with values previously reported for the only documented example of a 2,2´-bipyridyl dianion, $(Yb(2,2´\text{-bipy})(THF)_2)_3$, which were observed at $\delta = 6.54$, 5.28, 5.02, and 4.01 ppm.[37] Differences in $^1$H resonance positions are discussed with reference to those of the neutral parent complex in Section 4.5.

The IR and Raman spectra of **21** are very similar to those of **20** and a lack of substantially different bands prevents further analysis.

Comparison of the $^1$H NMR spectra of **19** and **21** provides information about differences in bonding within the 4,4´-bipyridyl moiety in the solution state. Figure 4.16 shows the changes in resonance positions between the neutral species and the dianion. The bipyridine hydrogen resonances exhibit an immediately obvious difference, changing from $\delta = 8.57$ and 7.71 ppm in the neutral species to $\delta = 5.92$ and 4.51 ppm in the dianion. This may be rationalised using the resonance canonical pictured in Figure 4.17. Here the two electrons are as far apart as possible, while being situated on the most electronegative atoms. The cost for this stabilisation of negative charge is loss of aromaticity around the ring system and the resultant formation of alternating single and double bonds. This explains the 2 – 3 ppm shift change observed, from the aromatic region in the neutral species to a more alkene-like region in the dianion.

## 4.5 Electronic Structure and Bond Metrics

Compounds **19**, **20** and **21** all contain $[Zn_2(4,4´\text{-bipy})(mes)_4]^{n-}$ (n = 0, 1, 2) units, in which a 4,4´-bipyridyl moiety bridges two $Zn(mes)_2$ centres. The greatest structural change observed upon the reduction of this complex is contraction of the Zn–N

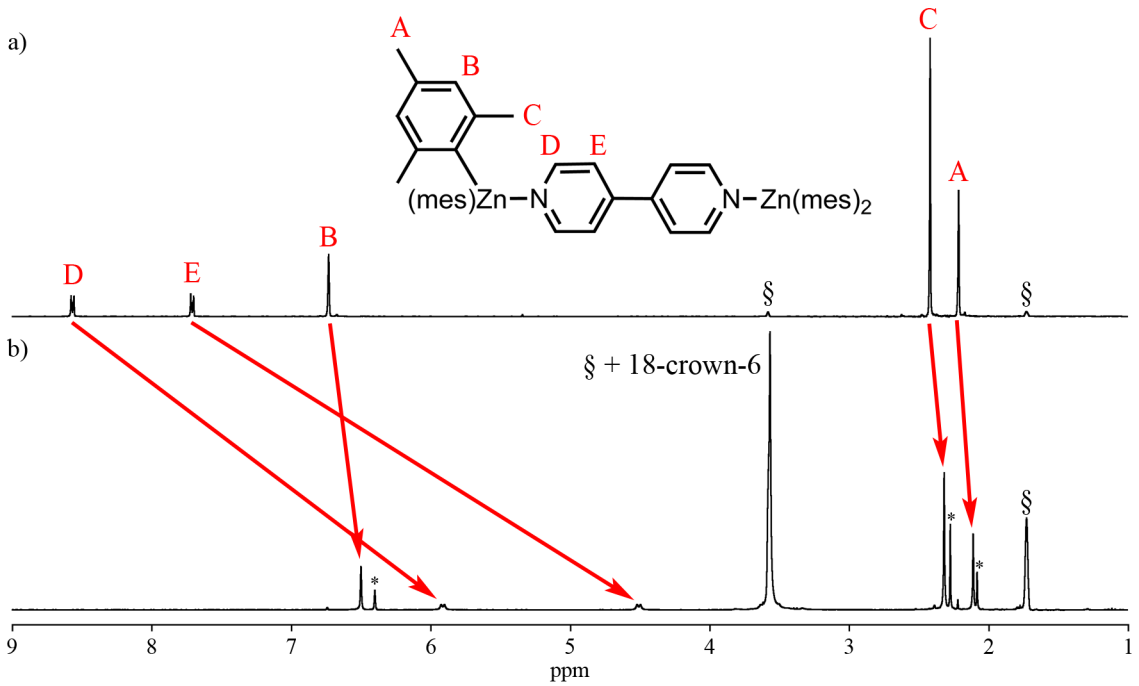



Figure 4.16: (**a**) $^{1}$H NMR spectrum of **19**. (**b**) $^{1}$H NMR spectrum of **21**. Resonances marked § correspond to the THF solvent, while those marked * are due to the presence of a small amount of **22**.

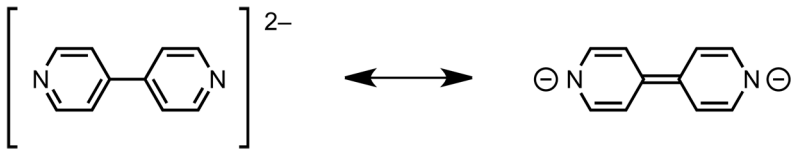



Figure 4.17: Resonance canonicals of the 4,4´-bipyridyl dianion in **21**.

distances. These shorten from 2.183(av) Å in the neutral species, **19**, to 2.043(av) Å in **20** and to 1.977(2) Å in **21**. This is due to an increasing electrostatic contribution to the Zn–N bond with the result that there is slight weakening of the Zn–C bonds to the strongly $\sigma$-donating mesityl groups, which elongate from 1.975(av) Å in **19** to 1.989(av) Å in **20** and to 2.004(av) Å in **21**. It is interesting to note this trend is also exhibited by the 2,2´-bipyridine complexes reported in Chapter 3, albeit to a lesser extent.

The second largest structural deviation is found for the 4,4´-bipyridyl moiety inter-ring bond. This shortens significantly, from 1.482(av) Å in the neutral complex, to 1.420(av) Å in the radical species and to 1.373(4) Å in the dianionic species. These values are in excellent agreement with those determined for the alkali metal salts of 4,4´-bipyridine anions detailed in Chapter 2. This contraction may be explained by reference to the population of the same orbital. The image is reproduced here for convenience, together with a bond numbering scheme in Figure 4.18. Though π*-antibonding overall, the lobe covering bond 1 has local π-bonding character, with the result that its incremental population causes increasing double bond character in the reduced species and hence a shortening of the inter-ring bond. A similar argument would explain the contraction of bond 3, while converse reasoning rationalises the elongation of bonds 2 and 4. An interesting result of the population of this orbital is the increasing preference for planar bipyridyl geometry which is evidenced by a decrease in the torsion angle between the bipyridyl rings.

DFT calculations were employed to help analyse the structure and bonding in all three oxidation states of the $Zn_2$(4,4´-bipy)$(mes)_4$ complex. These were found to be in good agreement with those obtained from single crystal X-ray diffraction structures. Table 4.2 shows the variation in selected bond metrics with oxidation state, and also includes values obtained from geometry optimised calculations.

Many examples of metal organic frameworks employ 4,4´-bipyridine as a rigid

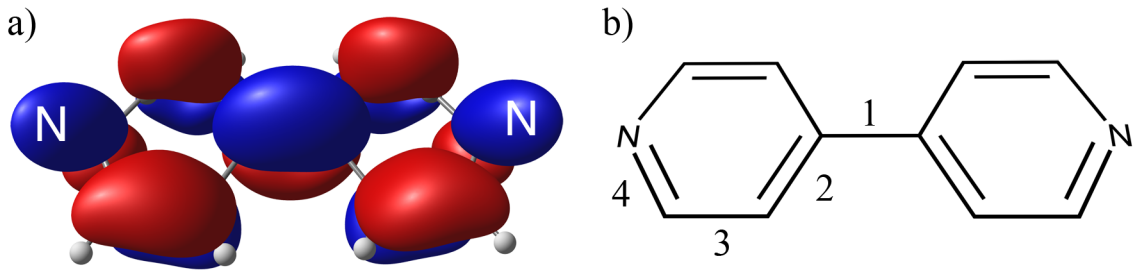



Figure 4.18: (**a**) DFT calculated 4,4´-bipyridine LUMO showing the alternating bonding and antibonding interactions in the π manifold. (**b**) Numbering scheme used in describing bond metric changes.

| | 4,4´-bipy | | 4,4´-bipy$^{\bullet-}$ | | | 4,4´-bipy$^{2-}$ | |
|---|---|---|---|---|---|---|---|
| Bond: | **19** | [DFT] | **20a** | **20b** | [DFT] | **21** | [DFT] |
| 1 | 1.482(av) | [1.48] | 1.417(av) | 1.423(av) | [1.43] | 1.373(4) | [1.38] |
| 2 | 1.394(av) | [1.40] | 1.426(av) | 1.425(av) | [1.43] | 1.465(av) | [1.47] |
| 3 | 1.383(av) | [1.39] | 1.363(av) | 1.366(av) | [1.37] | 1.354(av) | [1.36] |
| 4 | 1.342(av) | [1.33] | 1.361(av) | 1.359(av) | [1.36] | 1.379(av) | [1.38] |
| Zn–N | 2.183(av) | [2.24] | 2.043(av) | 2.043(av) | [2.07] | 1.977(2) | [1.97] |
| Zn–mes | 1.975(av) | [2.01] | 1.987(av) | 1.992(av) | [2.03] | 2.004(av) | [2.06] |
| Torsion | 35.25(av) | [38.2] | 2.83(av) | 2.40(av) | [0.0] | 0.00 | [0.0] |

Table 4.2: Selected bond metrics for **19**, **20** and **21**. When multiple crystallographically unique bonds are present in a structure, mean lengths are given. Values in square brackets were obtained from geometry optimised structures using DFT calculations. All bond lengths are in Å and torsion angles are in degrees.

| | Neutral species | | Dianion species | |
|---|---|---|---|---|
| Resonance: | **19** | [DFT] | **21** | [DFT] |
| A | 2.21, s | 2.28 | 2.11, s | 1.96 |
| B | 6.73, s | 6.93 | 6.50, s | 6.38 |
| C | 2.42, s | 2.42 | 2.32, s | 2.32 |
| D | 8.57, d | 8.51 | 5.92, d | 6.20 |
| E | 7.71, d | 7.40 | 4.51, d | 4.66 |

Table 4.3: Comparison of experimentally determined and DFT calculated $^1$H NMR chemical shift values for **19** and **21**. Position notation is as depicted in Figure 4.16. All shifts are given in ppm.

linker and as a result it is worth highlighting the combined effect of reducing Zn–N, bond 1 and bond 3 distances. The Zn–Zn´ distance is observed to reduce from 11.435(av) Å in **19**, to 11.232(av) Å in **20** and to 11.187(1) Å in **21**. This represents an overall reduction of 2.2% which may allow the formation of switchable host/guest solids as a result of tunable pore or cavity sizes.

To verify the hypothesised relationship between aromaticity and changes in $^1$H NMR resonance positions mentioned earlier, shifts were computed using DFT calculations and Nuclear Independent Chemical Shifts (NICS) were employed to probe the aromaticity of the ring system. The DFT calculations for **19** and **21** duplicate the same change in bipyridyl hydrogen resonance positions, with $\delta_{\text{calc}} = 8.51$ and 7.40 ppm determined for the neutral species and $\delta_{\text{calc}} = 6.20$ and 4.66 ppm for the dianion. Table 4.3 lists the experimentally and theoretically determined shifts for hydrogen atoms in these species.

The NICS analysis is able to measure the degree of aromaticity in a ring by calculating the electronic environment around a dummy atom placed 1 Å above a suspected aromatic site (in this instance the centre of a pyridyl ring). In the neutral species, a strongly negative value of –9.78 ppm is indicative of substantial aromatic character and is virtually the same as the value of –9.82 ppm calculated for a free, neutral 4,4´-bipyridine molecule. Subsequent incremental reduction causes an increase in NICS values, with the radical species calculated to be –1.88 ppm and the dianion

to be +4.08 ppm. The latter value is very close to that calculated for a free 4,4´-bipyridyl dianion (+4.94 ppm) and suggests the presence of an anti-aromatic ring, corroborating the results of the previously mentioned NMR studies.

Further computations were carried out using the Atoms In Molecules (AIM) methodology which examines the shape of electron density at central C–C bond critical points. The calculated ellipticity ($\epsilon$) is a measure of the symmetry of electronic density in a cross-section of a bond at this position. A value of $\epsilon$ close to zero represents a cylindrically symmetrical, σ-type bond. In the transition to a formal double bond, the values of $\epsilon$ increase, reflecting increasing asymmetry in electron distribution as a consequence of increasing π-character in the bond. Aromatic systems typically have $\epsilon$ values close to 0.23, while double bonds have values nearer 0.45. The calculated $\epsilon$ values for bond 1 in **19**, **20** and **21** increase with the level of reduction, from 0.04 for the neutral species, to 0.18 for the radical anion and to 0.34 for the dianion, showing increasing double bond character. The changes in resonance positions observed in the $^1$H NMR spectra of **19** and **21** are explained by the $\epsilon$ values calculated for bond 3: 0.22 in the neutral species and 0.37 in the dianion.

Despite multiple attempts, cyclic voltammetric measurements to determine the standard potentials for the electrochemical reduction of the $Zn_2$(4,4´-bipy)$(mes)_4$ complex proved unattainable. Extensive sparging of dried solvents with dinitrogen and transfer of solutions under inert atmospheres proved inadequate in preventing decomposition of samples of **19**. The 0.1 mM concentrations required for such measurements are assumed to be too low to allow manipulation of solutions of the complex on a bench top, even under inert atmospheres.

## 4.6 Summary of Chapter 4

This chapter details the synthesis of three compounds, each containing an isostructural $[Zn_2(4,4'\text{-bipy})(mes)_4]^{n-}$ moiety in a different oxidation state (n = 0, 1, 2). Experimental structural and electronic investigations are supported by theoretical calculations and show the effects of incremental reduction arising from the stepwise population of the neutral species LUMO.

The work discussed in this chapter has been published in a peer reviewed journal.[38]

## 4.7 References


[1] Wilkinson, G.; Gillard, R. D.; McCleverty, J. A.; Reedijk, J. *Heterocyclic Nitrogen-donor Ligands in Comprehensive Coordination Chemistry: The Synthesis, Reactions, Properties and Applications of Coordination Compounds*; Pergamon Press: Oxford, U.K., 1987; Vol. 2.

[2] James, S. L. *Chem. Soc. Rev.* **2003**, *32*, 276.

[3] Thanasekaran, P.; Luo, T.-T.; Wu, J.-Y.; Lu, K.-L. *Dalton Trans.* **2012**, *41*, 5437.

[4] Zhang, J.; Liu, R.; Feng, P.; Bu, X. *Angew. Chem. Int. Ed.* **2007**, *46*, 8388.

[5] O'Keeffe, M.; Yaghi, O. M. *Chem. Rev.* **2012**, *112*, 675.

[6] Rosi, N. L.; Eddaoudi, M.; Kim, J.; O'Keeffe, M.; Yaghi, O. M. *CrystEngComm* **2002**, 401.

[7] Rosi, N. L.; Kim, J.; Eddaoudi, M.; Chen, B.; O'Keeffe, M.; Yaghi, O. M. *J. Am. Chem. Soc.* **2005**, *127*, 1504.

[8] Deng, H.; Grunder, S.; Cordova, K. E.; Valente, C.; Furukawa, H.; Hmadeh, M.; Gándara, F.; Whalley, A. C.; Liu, Z.; Asahina, S.; Kazumori, H.; O'Keeffe, M.; Terasaki, O.; Stoddart, J. F.; Yaghi, O. M. *Science* **2012**, *336*, 1018.

[9] Dinolfo, P. H.; Williams, M. E.; Stern, C. L.; Hupp, J. T. *J. Am. Chem. Soc.* **2004**, *126*, 12989.

[10] Dinolfo, P. H.; Hupp, J. T. *J. Am. Chem. Soc.* **2004**, *126*, 16814.

[11] Bhattacharya, D.; Sathiyendiran, M.; Luo, T. T.; Chang, C. H.; Cheng, Y. H.; Lin, C. Y.; Lee, G. H.; Peng, S. M.; Lu, K. L. *Inorg. Chem.* **2009**, *48*, 3731.

[12] Yaghi, O.; Li, H.; Davis, C.; Richardson, D.; Groy, T. *Acc. Chem. Res.* **1998**, *31*, 474.

[13] Kitagawa, S.; Kitaura, R.; Noro, S. *Angew. Chem. Int. Ed.* **2004**, *43*, 2334.

[14] Biradha, K.; Sarkar, M.; Rajput, L. *Chem. Commun.* **2006**, 4169.

[15] Soldatov, D. V.; Tinnemans, P.; Enright, G. D.; Ratcliffe, C. I.; Diamente, P. R.; Ripmeester, J. A. *Chem. Mater.* **2003**, *15*, 3826.

[16] Liu, S.-H.; Chen, X.-F.; Zhu, X.-H.; Duan, C.-Y.; You, X.-Z. *J. Coord. Chem.* **2001**, *53*, 223.

[17] Lai, C. S.; Liu, S.; Tiekink, E. R. T. *CrystEngComm* **2004**, *6*, 221.

[18] Chen, X.-F.; Liu, S.-H.; Zhu, X.-H.; Vittal, J. J.; Tan, G.-K.; You, X.-Z. *Acta Crystallogr. Sect. A* **2000**, *56*, 42.

[19] Diskin-Posner, Y.; Patra, G. K.; Goldberg, I. *Chem. Commun.* **2002**, 1420.

[20] Pascu, S. I.; Waghorn, P. A.; Conry, T. D.; Lin, B.; Betts, H. M.; Dilworth, J. R.; Sim, R. B.; Churchill, G. C.; Aigbirhio, F. I.; Warren, J. E. *Dalton Trans.* **2008**, 2107.

[21] Konarev, D. V.; Khasanov, S. S.; Slovokhotov, Y. L.; Saito, G.; Lyubovskaya, R. N. *CrystEngComm* **2008**, *10*, 48.

[22] Shukla, A. D.; Dave, P. C.; Suresh, E.; Das, A.; Dastidar, P. *J. Chem. Soc., Dalton Trans.* **2000**, 4459.

[23] Kleij, A. W.; Kuil, M.; Tooke, D. M.; Lutz, M.; Spek, A. L.; Reek, J. N. H. *Chem. Eur. J.* **2005**, *11*, 4743.

[24] Litvinov, A. L.; Konarev, D. V.; Kovalevsky, A. Y.; Neretin, I. S.; Coppens, P.; Lyubovskaya, R. N. *Cryst. Growth Des.* **2005**, *5*, 1807.

[25] Manohar, A.; Ramalingam, K.; Bocelli, G.; Righi, L. *Inorg. Chim. Acta* **2001**, *314*, 177.

[26] Benson, R. E.; Ellis, C. A.; Lewis, C. E.; Tiekink, E. R. *CrystEngComm* **2007**, *9*, 930.

[27] Tao, J.; Yin, X.; Zheng, L.; Ng, S. *Main Group Met. Chem.* **2002**, *25*, 321.

[28] Croitor, L.; Coropceanu, E. B.; Jeanneau, E.; Dementiev, I. V.; Goglidze, T. I.; Chumakov, Y. M.; Fonari, M. S. *Cryst. Growth Des.* **2009**, *9*, 5233.

[29] Ogrin, D.; van Poppel, L. H.; Bott, S. G.; Barron, A. R. *Dalton Trans.* **2004**, 3689.

[30] Batsanov, A. S.; Begley, M. J.; Hubberstey, P.; Stroud, J. *Dalton Trans.* **1996**, 1947.

[31] Coropceanu, E.; Croitor, L.; Gdaniec, M.; Wicher, B.; Fonari, M. *Inorg. Chim. Acta* **2009**, *362*, 2151.

[32] Kaim, W. *Inorg. Chim. Acta Lett.* **1981**, *53*, L151.

[33] Kaim, W. *J. Organomet. Chem.* **1984**, *262*, 171.

[34] Gross, R.; Kaim, W. *Angew. Chem. Int. Ed. Engl.* **1985**, *24*, 856.

[35] Denning, M. S.; Irwin, M.; Goicoechea, J. M. *Inorg. Chem.* **2008**, *47*, 6118.

[36] Krieger, M.; Geiseler, G.; Harms, K.; Merle, J.; Massa, W.; Dehnicke, K. *Z. Anorg. Allg. Chem.* **1998**, *624*, 1387.

[37] Fedushkin, I. L.; Petrovskaya, T. V.; Girgsdies, F.; Kohn, R. D.; Bochkarev, M. N.; Schumann, H. *Angew. Chem. Int. Ed.* **1999**, *38*, 2262.

[38] Irwin, M.; Kraemer, T.; McGrady, J. E.; Goicoechea, J. M. *Inorg. Chem.* **2011**, *50*, 5006.

# Chapter 5

# Experimental

## 5.1 Manipulation of Air- and Moisture-Sensitive Compounds

Due to the high air- and moisture-sensitivity of the majority of the compounds discussed in this thesis, all manipulations were performed under an inert atmosphere, either using standard Schlenk line or glovebox techniques.

A Schlenk line consists of two parallel manifolds, one connected to a cylinder of inert gas (argon in the case of this work) and the other to a continuously operating rotovane vacuum pump (shown as (**A**) and (**B**), respectively, in Figure 5.1). Typically there are four dual manifold connectors allowing several pieces of apparatus to be used at a time. Glassware is attached to the line by thick-walled tubing capable of holding a vacuum. The vacuum manifold is connected via a liquid nitrogen filled cold trap (**C**) which prevents volatiles entering the pump. Vacuum pressure is monitored by means of a Pirani pressure gauge (**D**) with a typical base pressure of $4 \times 10^{-3}$ mbar or lower. The inert gas manifold may be purged by means of an oil bubbler (**E**). The Young's taps (shown in yellow) allow vessels and tubing to be cycled alternately between vacuum and the inert gas. This is done three times prior to use, to remove

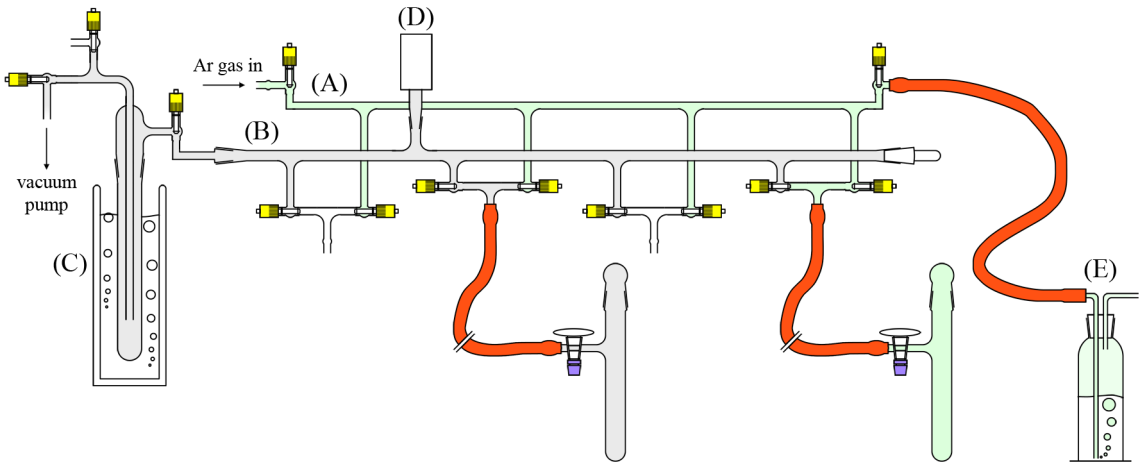



Figure 5.1: Schematic of a Schlenk line and two Schlenk tubes. Argon shown in pale green, vacuum shown in pale grey.

oxygen and moisture. Glassware is typically heated when under vacuum to facilitate the removal of any adsorbed moisture on the vessel walls. Schlenk line techniques are particularly suited to manipulations involving solutions: control of pressures between different vessels allows the transfer of liquids between flasks via cannulae, without exposure to the atmosphere.

An MBraun glovebox was used for the storage and weighing of solids, as well as for small scale reactions. This consists of a sealed stainless steel box with a clear Lexan polycarbonate front window, containing mounted butyl rubber gloves to allow manipulation of the glovebox contents. Samples are transferred into or out of the box by means of two chambers which may be cycled between vacuum and dinitrogen. The glovebox atmosphere was maintained by gas circulation through molecular sieves, copper catalyst and activated charcoal, removing water, oxygen and solvent vapour, respectively. This afforded oxygen and moisture levels below 0.1 ppm.

## 5.2 Physical Measurements

Multiple techniques have been used to characterise the compounds detailed in this thesis, with many of them requiring some degree of adaptation to allow the measurement of highly air- and moisture-sensitive materials. For each technique discussed in this section, the instruments used are described, followed by a brief summary of the theory and implementation methodologies.

### 5.2.1 Single Crystal X-ray Diffraction

Single crystal X-ray diffraction (SXRD) data were recorded using a Enraf-Nonius Kappa-CCD diffractometer and a 95 mm CCD area detector with a graphite-monochromated molybdenum $K_\alpha$ source. Crystals were selected under Paratone-N oil, mounted on fibres and positioned under a dinitrogen stream. Dinitrogen flow temperatures were controlled by an Oxford Cryosystems cryostream. Equivalent reflections were merged and diffraction patterns processed using the DENZO and SCALEPACK programs.[1] Structures were subsequently solved using direct methods, and refined on $F^2$ using the SHELXL 97–2 and WINGX packages.[2,3]

The technique involves examining the pattern of a beam of X-rays which have been diffracted by a crystal. X-rays are generated by the electrons from a heated element being accelerated through a potential field (in a cathode ray tube) and directed onto a target material (Mo for all of the structures described in this thesis). The incident electrons can remove core electrons from the metal and, upon relaxation, X-rays are produced as electrons in higher shells fall down into the vacated shell. Several characteristic wavelengths of X-rays are produced, corrolating to orbital energy diferences. These then pass through a monochromator to isolate the most intense $K_\alpha$ radiation (wavelength = 0.71073 Å for Mo) and a collimator (to parallelise the beam) before being directed towards the sample (Figure 5.2).

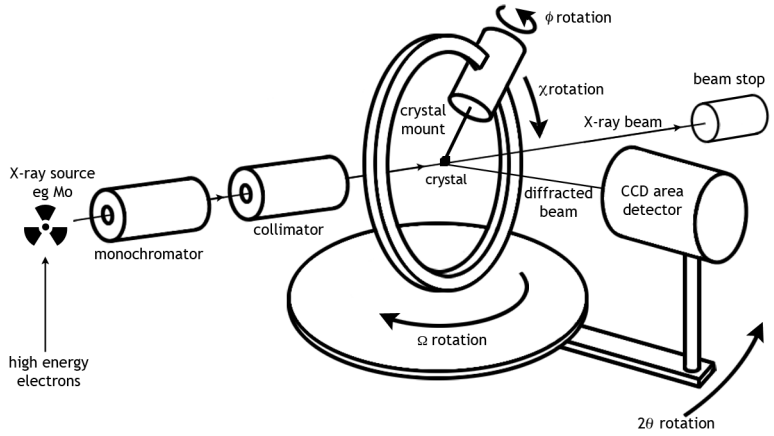



Figure 5.2: Schematic diagram of a four circle single crystal X-ray diffractometer.

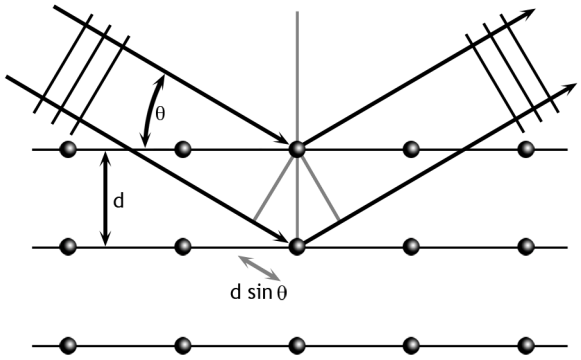



Figure 5.3: Diagrammatic explanation of Bragg's Law.

Bragg's law provides the condition for diffraction to occur: $2d\sin\vartheta = n\lambda$ where $d$ is the crystal lattice spacing, $\vartheta$ is the angle between the incident beam and lattice plane, $n$ is an integer and $\lambda$ is the wavelength of the X-ray radiation (Figure 5.3).[4] A detector (typically a CCD camera) records the diffraction pattern for multiple orientations of the crystal, source and detector. A computer is then able to determine the coordinates of diffracted beams. Once data has been collected, duplicated (or equivalent) reflections are used to make intensities of the data self-consistent. This provides empirical corrections for X-ray absorption effects, crystal movement in the beam and deviations in reflection intensity caused by data collection from non-spherical crystals. Electron density may be derived from structure factors (mathematical functions describing the amplitude and phase of a diffracted beam) using the formula: $\rho\left(xyz\right) = \frac{1}{V}\sum_{hkl} \mid F\left(hkl\right) \mid \exp\left[i\phi\left(hkl\right)\right]\exp\left[-2\pi i\left(hx + ky + lz\right)\right]$ where $\rho\left(xyz\right)$ is the electron density at coordinates (x,y,z), $V$ is the unit cell volume, $\mid F\left(hkl\right) \mid$ is the amplitude of the structure factor for a diffracted beam with Miller indices h,k,l and $\phi$ is the phase of this beam.[5] Two observations are immediately apparent:

1. Each reflection gives rise to information about electron density distribution throughout the unit cell and not (for example) about a specific atom or position in the unit cell.

2. Since X-ray detectors are able to measure the intensity of a diffracted beam (the square of the amplitude), but cannot determine its phase, there is a potential major problem as both pieces of data are required to generate a map of electron density. This has been termed the 'phase problem'.

With the advent of fast computers, the 'phase problem' has largely been overcome using a computational technique called 'direct methods'. This generates sufficiently accurate estimates of phases to allow Fourier transforms of reflection data to give useful information about electron density. In turn, this may be modelled to calcu-

late increasingly precise phase estimates. Iterations of this process and assignment of atomic positions based upon relative magnitudes of electron density permits the determination of a three-dimensional model of the crystal structure.

### 5.2.2 Powder X-ray Diffraction

Transmission powder X-ray patterns were recorded using a Siemens D5000 diffractometer in modified Debye-Scherrer geometry and equipped with an MBraun position sensitive detector. The instrument produced Cu $K_{\alpha 1}$ radiation (wavelength = 1.54056 Å) using a germanium monochromator and a standard Cu source. Data were recorded on samples in flame-sealed capillaries under dinitrogen. The capillaries were mounted on a goniometer head and aligned so that rotation occurred along the long central axis of the capillary. During a measurement the capillary was rotated at approximately 60 rpm to minimise any preferred orientation effects that might occur.

Powder X-ray diffraction (PXRD) provides less information than single crystal X-ray diffraction because the resultant pattern is compressed into a single spatial dimension.[6,7] However, once a crystal structure is known, its powder X-ray pattern can be calculated and the PXRD pattern can be used to test whether a large sample contains exclusively a single crystalline phase or a mixture. In the work presented in this thesis, this technique is used extensively to determine phase purity of bulk samples, which is immediately apparent upon comparison with a calculated pattern from SXRD data.

The X-rays are produced in the same manner as outlined above (though typically with a Cu source). The powder consists of a great number of single crystallites, in theory representing every possible orientation of a single crystal. At a given angle that satisfies Bragg's law, rather than a single diffracted beam being produced, a conical shaped diffraction geometry occurs instead. As the detector (typically an area or position sensitive detector) moves it intersects these cones to collect the diffracted

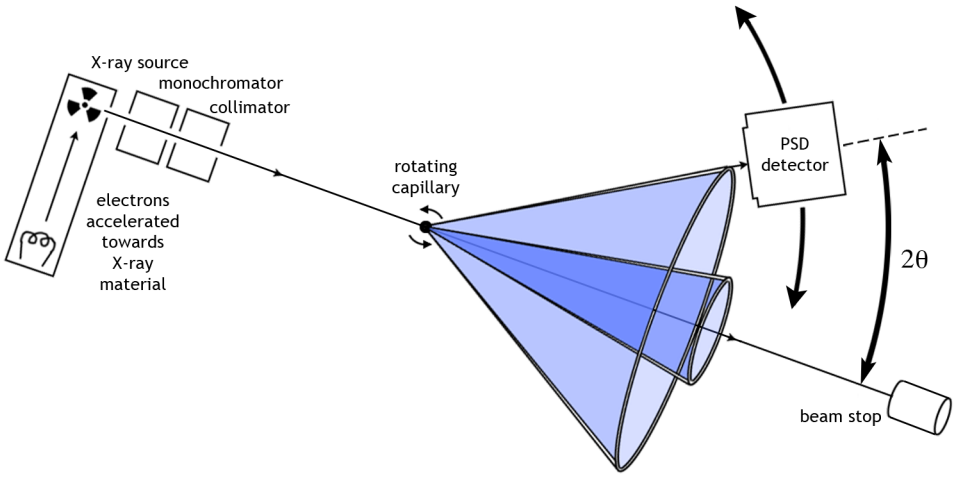



Figure 5.4: Schematic diagram of a transmission X-ray diffractometer.

pattern data (Figure 5.4).

### 5.2.3 Superconducting Quantum Interference Device Magnetometry (SQUID)

SQUID magnetometry measurements were measured on unanchored polycrystalline samples with a Quantum Design MPMS XL SQUID magnetometer. Due to the extreme air- and moisture-sensitivity of the complexes, samples were flame-sealed under vacuum in Suprasil tubes.

Samples are typically cooled to 5 K in zero applied field and the magnetic susceptibility is measured between 5 and 300 K in a 0.01 T applied field. The sample is subsequently field cooled to 5 K and the magnetic susceptibility is measured at temperatures up to 300 K. Where values observed for samples show virtually identical responses the two measurements are merged. Diamagnetic corrections have been calculated for all samples using Pascal's constants.[8]

Where ferromagnetic impurities in samples were encountered, magnetisation was measured at high fields, saturating the ferromagnetic response. Following an initial zero-field cooling to 5 K, the sample was warmed to 300 K and the magnetic suscepti-

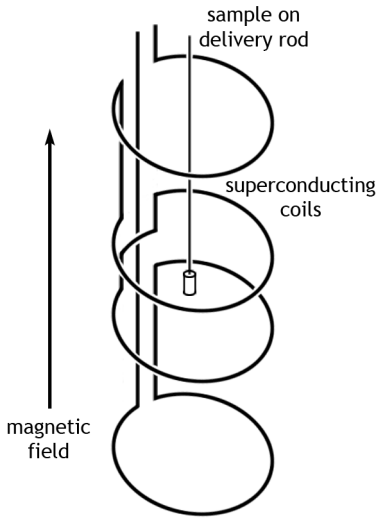



Figure 5.5: SQUID instrument superconducting coil configuration.

bility at each temperature was measured at five applied fields between 4 and 5 T. The slope of the resulting linear plot of the molar magnetization as a function of applied field was used to obtain the molar magnetic susceptibility at each temperature.

A SQUID magnetometer measures extremely small magnetic fields.[9] In the field of chemistry it can be used to determine the type and magnitude of magnetism a compound exhibits (for example diamagnetism, paramagnetism, ferromagnetism and antiferromagnetism). The sample is lowered, via a long rod, into the centre of a magnet and is surrounded by a superconducting wire that is coiled such that any drift in magnetic field will cause no current flow (Figure 5.5). As the rod is raised and lowered through the coils, the magnetic moment of the sample induces a current in the pickup wires. This is transferred to the SQUID which is situated below the magnet and isolated from the magnetic field by a superconducting shield. The SQUID uses Josephson junctions (two superconductors separated by an extremely thin insulator) to convert the extremely small induced current flows into readily recordable voltages.

### 5.2.4 Electron Paramagnetic Resonance

Continuous wave (CW) electron paramagnetic resonance (EPR) experiments were performed using an X-band Bruker BioSpin GmbH EMX spectrometer equipped with a high sensitivity Bruker probehead and a low-temperature Oxford Instruments CF935 helium-flow cryostat. Experiments were conducted using 2-10 mW microwave power, 0.1 mT modulation amplitude, and a modulation frequency of 100 kHz. The magnetic field was calibrated at room temperature with an external 2,2-diphenyl-1-picrylhydrazyl standard (g = 2.0036).

EPR may be used to probe the electronic structure of paramagnetic species.[10,11] Sample $g$ factor values may be calculated from the equation: $hv = g\mu_B B_0$ where $h$ is Planck's constant, $v$ is the microwave frequency, $\mu_B$ is the Bohr Magneton and $B_0$ is the applied field strength. Variation of $B_0$ while $v$ is held constant allows determination of $g$ factors for solid and solution state samples. Solution EPR spectra show the environment of any unpaired electron through hyperfine splitting patterns caused by coupling with non-zero nuclear spins of neighbouring atoms.

The technique works by placing the paramagnetic sample within a magnetic field and exposing it to microwave radiation (with a frequency of approximately 9.5 GHz in an X-Band spectrometer) produced by a Gunn diode.[12] The magnetic field gives rise to a Zeeman splitting, lifting the degeneracy of $m_s = \pm 1/2$ spin states (Figure 5.6).

The frequency of the source is initially tuned to produce a standing wave in the microwave cavity, such that no power is reflected from the cavity to the detector. Any excitation from $m_s = -1/2$ to $m_s = +1/2$ will absorb microwave power and thus change the amplitudes of the forwards and reverse wave contributions to the standing wave. This causes a change in the reflected power from the cavity. However, such changes are typically very small and comparable to the noise from the detector, source and cavity assembly. To allow detection of these weak signals, the Gunn diode output is divided,

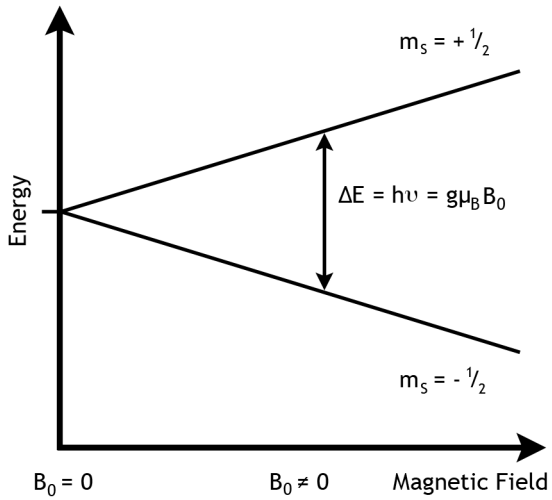



Figure 5.6: The Zeeman effect: electronic degeneracy is lifted in a magnetic field.

with a proportion of emitted microwaves travelling directly to the detector while the remainder travel via the sample cavity. The two beams are then recombined so that constructive interference occurs. Secondary coils allow modulation of the magnetic field applied to the sample ($B_0$), typically by 100 kHz, causing the signal reflected from the cavity to be similarly modulated (Figure 5.7). Since the detected intensity is proportional to the square of the total field, if the cavity microwave field energy is much smaller than the reference field, the following approximation may be used:

$$I \propto E_{\text{tot}}^2 = (E_{\text{ref}} + E_{\text{cav}})^2 = E_{\text{ref}}^2 + 2E_{\text{ref}}E_{\text{cav}} + E_{\text{cav}}^2 \approx E_{\text{ref}}^2 + 2E_{\text{ref}}E_{\text{cav}}$$

and, since only $E_{\text{cav}}$ is modulated, a 100 kHz phase sensitive detector is able to isolate the rightmost term of the above equation, with the signal greatly amplified by the $E_{\text{ref}}$ contribution.

### 5.2.5 Infrared Spectroscopy

Infrared (IR) data were recorded on solid samples in Nujol mulls. The mulls were made up inside an inert atmosphere glovebox and the KBr plates were placed in

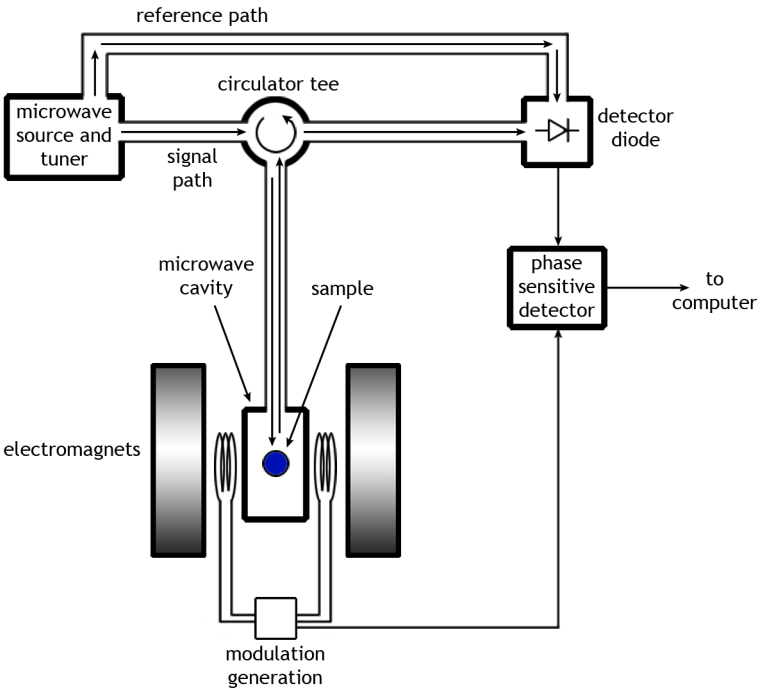



Figure 5.7: Simplified schematic of an EPR instrument.

an airtight container prior to data collection. Spectra were recorded on a Nicolet Magna-IR 560 spectrometer in absorbance mode (Happ-Genzel FT apodisation) with a Ge/CsI beam splitter and liquid nitrogen cooled Mercury Cadmium Telluride (MCT) detector.

At its most basic level, an IR spectrum shows the radiation energies that a sample is capable of absorbing, typically causing the excitation of molecular vibrational modes. Modern spectrometers are able to record IR spectra extremely rapidly due to a design incorporating a Michelson interferometer (Figure 5.8).[13] By moving one mirror in a stepwise manner, each position causes multiple discrete simultaneous frequencies of IR light to reach the sample, generating an interferogram. Recording data for multiple steps allows the use of a Fourier transform to convert between mirror distance data and wavenumber ($cm^{-1}$) data, forming the sample IR spectrum.

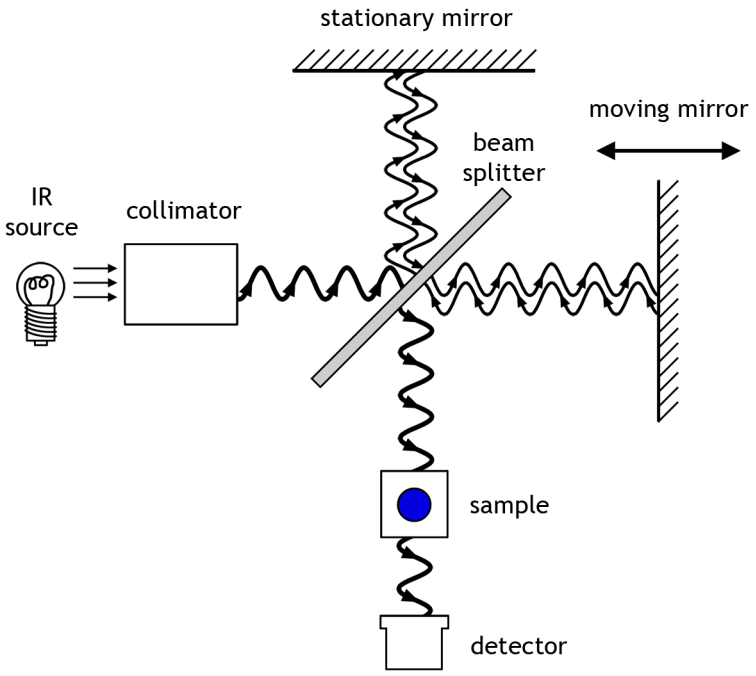



Figure 5.8: Simplified schematic of an IR spectrometer.

### 5.2.6 Raman Spectroscopy

Raman spectra were recorded from solid samples, in flame-sealed Pyrex capillaries under dinitrogen using a Dilor Labram 300 spectrometer. Excitation radiation was produced by a 20 mW helium-neon laser operating at a wavelength of 632.817 nm. Optical density filters could be inserted into the beam to reduce photon flux, decreasing the likelihood that photochemical reactions would take place during the measurement. Measurements were typically obtained at 0.1% of full intensity with a counting time of 100 s. Calibration of the spectrometer was performed before each measurement by referencing to the 520.7 nm line of a silicon wafer.

This technique is complementary to the IR measurements discussed above, but differs in that vibrational modes of a system are instead probed by the inelastic scattering of monochromatic light, typically from a laser source.[14] Incident photons interact with the polarisation tensor of a target molecule, causing an excitation to a virtual energy level (which is higher in energy than a real electronic transition) before

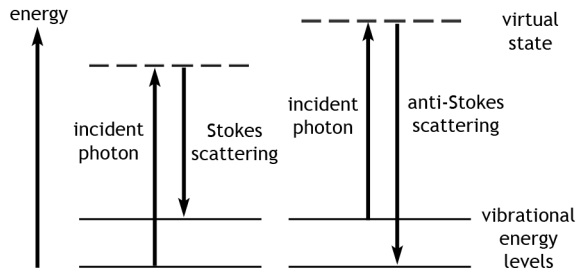



Figure 5.9: Raman transitions.

rapid thermal energy loss to a different vibrational energy level. The gross selection rule for Raman spectroscopy requires that there be a change in the polarizability of the molecule during the vibration. Excitations are usually from the ground vibrational energy level which always spans the totally symmetric representation of the group. This gives rise to Stokes lines. A small number of molecules will be excited from a higher starting energy level (due to the Boltzmann populations) and once excited, these molecules can relax to the ground state energy level creating the weaker anti-Stokes lines. Usually only the more intense Stokes lines are recorded (Figure 5.9).

### 5.2.7 Nuclear Magnetic Resonance

$^{1}$H and $^{13}$C Nuclear magnetic resonance (NMR) spectra of dilute samples were acquired at 299.9 and 75.4 MHz, respectively, on a Varian Mercury-vx 300 NMR spectrometer. $^{13}$C NMR spectra were run at 125.8 MHz on a Bruker AVII 500 spectrometer equipped with a $^{13}$C cryoprobe. $^{13}$C and $^{1}$H spectra were referenced to $d_8$-THF ($\delta_{\mathrm{C}} = 25.37$ ppm) and to the most shielded residual protic solvent resonance (THF $\delta_{\mathrm{H}} = 1.73$ ppm), respectively. Diffusion and NOE experiments were performed on a Bruker AVII 500 spectrometer equipped with a TXI inverse probe regulated at 298 K. Diffusion experiments utilised the BPP-LED stimulated echo sequence with diffusion times ($\Delta$) of 50 ms, bipolar diffusion-encoding field gradient pulses of total duration 4 ms ($\delta$) and longitudinal eddy current delays (LED) of 5 ms.[15] Additional 0.6 ms purging gradients were applied whenever magnetisation was longitudinal. All gradi-

ent pulses were of half-sine profiles with effective diffusion-encoding gradient strengths ranging from 0.5 to 20.5 G $cm^{-1}$ (corrected for half-sine profiles). Data analysis was performed using Bruker TOPSPIN software. 1D NOESY spectra were recorded using a single pulsed field gradient selective excitation scheme utilising a 40 ms selective Gaussian inversion pulse and with a NOE mixing time of 0.8 s.

While the majority of compounds discussed in this thesis are paramagnetic, comprehensive solution phase NMR studies have been carried out on two diamagnetic complexes detailed in Chapter 4. Like EPR, NMR arises as a result of Zeeman splitting of the $m_s = \pm 1/2$ (for an $I = 1/2$ nucleus) in an external magnetic field. The energy difference for a transition is given by $\triangle E = \hbar\gamma B_0$, where $\hbar$ is (Planck constant / $2\pi$), $\gamma$ is the nuclear gyromagnetic ratio and $B_0$ is the applied field strength.[16] However, unlike EPR, the effect is nucleus based, rather than electron based. Energy differences are extremely small making the technique intrinsically insensitive in the absence of strong fields, large gyromagnetic ratios and high active isotope abundances.

In an NMR experiment a pulse of radiation induces transitions from the ground state to the higher energy states and a free induction decay is recorded as the sample returns to a Boltzmann distribution. A Fourier transform then allows conversion from this time-domain data to a frequency-domain. A given atomic site experiences a magnetic field that is the sum of an externally applied field and a local field caused by electron density of other nearby nuclei that can partially shield the atom from the external field. Excitation energies between nuclear spin levels are therefore close, but crucially different for magnetically inequivalent nuclei, allowing different environments to be detected. These differences are termed 'chemical shifts' and are reported as a fraction (ppm) relative to the shift of a reference compound in the same field.

Sophisticated irradiation pulses may be used to carry out more advanced studies, such as two-dimensional COSY, HSQC, and HMBC measurements or diffusion and nuclear Overhauser effect (NOE) experiments. The latter is used to detect the through

space proximity of two or more sites and operates by the saturation of a specific resonance. This causes a change in resonance intensity of physically close nuclei and may be used to determine the coordination environment of a sample, or distinguish between different stereoisomers in an enantiomerically pure compound.

### 5.2.8 Mössbauer Spectroscopy

Mössbauer spectra were measured between 85 and 295 K in a Janis SuperVariTemp cryostat with a constant-acceleration spectrometer which utilised a rhodium matrix $^{57}$Co source and was calibrated at 295 K with α-iron powder. The Mössbauer spectral absorbers contained about 50 mg/cm$^2$ of powder mixed with boron nitride; the absorbers were prepared in an argon atmosphere and mounted in the cryostat under an atmosphere of dinitrogen. The relative statistical errors are ±0.005 mm/s for the isomer shifts, $\delta$, ±0.01 mm/s for the quadrupole splittings, $\triangle E_{\mathrm{Q}}$, and line widths, $\Gamma$, and ±0.3% for the relative component areas; the absolute errors are approximately twice the statistical errors.

Mössbauer spectroscopy is used to investigate extremely small changes in the energy levels of an atomic nucleus that arise as a result of oxidation state, coordination environment and local magnetic field.[17] A solid sample is able to absorb gamma rays of energy equal to nuclear excitation energies. These are typically produced by an excited state of the same isomer. The most common route to this is via a radioactive nucleus that decays via such an excited system. For example, $^{57}$Fe Mössbauer spectroscopy uses a radioactive $^{57}$Co source which decays via electron capture to an excited form of $^{57}$Fe, that then releases a gamma ray as it relaxes to the $^{57}$Fe ground state. The energy of this emitted gamma ray is extremely precise and almost perfectly monochromatic, making the technique extraordinarily sensitive, capable of detecting energy changes of the order of parts per $10^{11}$. Physical movement of the $^{57}$Co source using a constant acceleration linear motor (sinusoidal velocity)

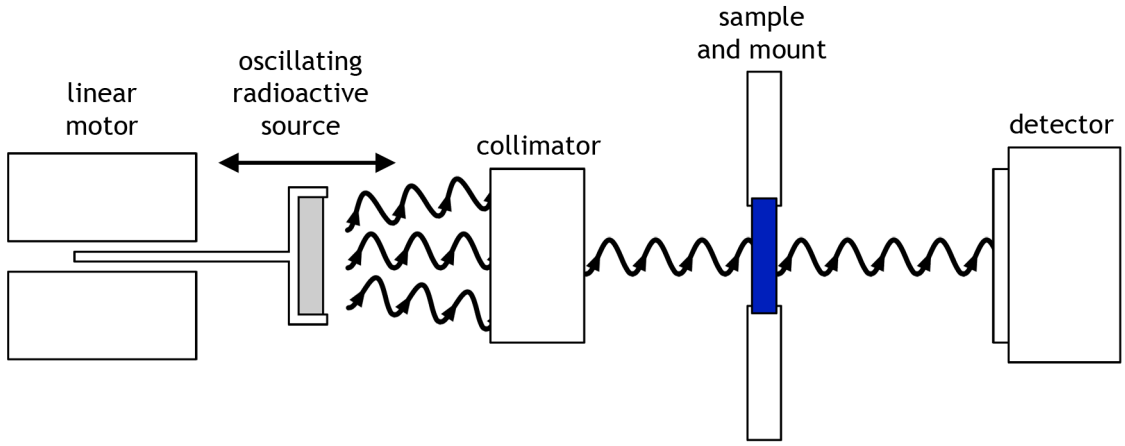



Figure 5.10: Simplified schematic of a Mössbauer spectrometer.

causes a Doppler effect allowing precise sweeping of a narrow range of gamma energies (typically of the order of tens of nanoelectronvolts) as shown in Figure 5.10. For samples containing nuclei with $I = 3/2$, such as $^{57}$Fe, the resulting plot of gamma ray absorption against source velocity shows two peaks. The peak separation is termed the 'quadrupole splitting' while the mean position of the two peaks relative to 0 m/s is called the 'isomer shift'. These parameters can be used to probe the oxidation state and coordination environment of a complex.

### 5.2.9 Elemental Microanalysis

CHN elemental analyses were performed on 5 mg samples, submitted under vacuum in flame-sealed Pyrex ampules, to either Stephen Boyer of the London Metropolitan University or to Elemental Microanalysis Ltd. (Devon, U.K.).

The technique examines the products from instantaneous sample oxidation to determine percentages of carbon, hydrogen and nitrogen in the submitted sample. A known mass of sample (approximately 1 mg) is loaded into a thin-walled tin container which is dropped into a continuously helium purged quartz combustion tube at 1000 °C. At the same time the helium flow is briefly replaced by pure oxygen causing flash combustion. Passage of the resulting gasses over copper removes any remaining

elemental oxygen and reduces nitrogen oxides to nitrogen. The combustion products are then separated as helium carries them through a chromatographic column before a thermal conductivity detector determines the concentrations of carbon dioxide, water and nitrogen. The percentages of carbon, hydrogen and nitrogen in the sample may then be calculated.

## 5.3 Density Functional Theory Calculations

Density functional theory (DFT) calculations, including unrestricted geometry optimisations, have been carried out on all of the compounds described in this thesis.

Investigation of the neutral bipyridine isomers and alkali metal salts of their reduced forms discussed in Chapter 2 were performed using the Gaussian03 package, revision D.01, on the University of Oxford's "ORAC" cluster.[18] All DFT calculations were seeded with atomic coordinates derived from single-crystal X-ray diffraction experiments and employed the Becke three-parameter hybrid functional with the Lee-Yang-Parr correlation (B3LYP) in conjunction with the 3-21+G* basis set.[19–24] Isotropic Fermi contact coupling constants were calculated for the optimised geometries of the three radical species.

Calculations on the neutral and reduced transition metal complexes containing 2,2´-bipyridine discussed in Chapter 3 were performed using the ORCA and Gaussian09 (revision A.02) packages.[25,26] Unrestricted geometry optimisations, starting from crystal structure coordinates, were carried out using the B3LYP functional in conjunction with the TZVP basis set on the transition metal site and immediately coordinated atoms,[27] and the SVP basis set elsewhere.[28] Mössbauer parameters of the two Fe systems were determined with non-relativistic single point calculations on single-crystal X-ray structures using the B3LYP functional in combination with the CP(PPP) basis set for Fe and TZVP for nitrogen, carbon and hydrogen atoms.[29]

The Mössbauer isomer shifts referenced to α-iron at room temperature were calculated from the computed electron densities at the iron centre using the expression $\delta\,(\mathrm{mm/s}) = \alpha\,(\rho_0 - C) + \beta$, where $\alpha$ = –0.367 ± 0.015 (mm/s)/$a_0{}^3$, $\beta$ = 6.55 ± 0.25 mm/s and $C$ = 11800 electrons/$a_0{}^3$ (where $a_0$ is the Bohr radius) proposed by Neese and co-workers.[30]

The calculations on the zinc 4,4´-bipyridine complexes described in Chapter 4 were carried out using the Gaussian09 package, Revision A.02.[25] Unrestricted geometry optimisations were performed using the M05-2X functional (which provides better geometries than the previously mentioned B3LYP alternative).[31] The TZVP basis set was used on Zn and all coordinating atoms, while the SVP basis set was used on the remaining atoms. Atoms In Molecules (AIM) analysis was performed using the AIM2000 package.[32,33] $^1$H chemical shifts were calculated using the Gauge-Independent Atomic Orbital (GIAO) method,[34,35] using the optimised geometries determined above. However, the calculations were performed using the B3LYP functional,[19,20,36,37] with a basis set optimised for shielding constants, aug-pcS-2 (triple ζ quality) on the hydrogen atoms of the bipyridyl moiety and one mesityl group which acted as an internal standard.[38] For other atoms the same TZVP and SVP basis sets mentioned above were used. Relative chemical shifts ($\delta$) were obtained by referencing the nuclear magnetic shielding constants of the probe atoms against the arithmetic mean of the isotropic magnetic shielding constants of the ortho-methyl protons which appear as an intense singlet in the experimental NMR spectra. Nucleus-Independent Chemical Shift (NICS) values were calculated using the GIAO method.[39,40] The NICS probes (ghost atoms) were placed 1 Å above the centres of the bipyridyl moiety rings (defined as the average of the Cartesian coordinates of the ring atoms). The NICS(1) values largely reflect the influence of π-electrons and are therefore a better indicator of the ring current (aromaticity) than the values at the centre, where σ-bonding contributions are also of importance.

## 5.4 Preparation of Materials

### 5.4.1 Solvents

Solvents (benzene, 99.9%; diethyl ether, 99.9%; hexanes, 99.9%; toluene, 99.9%; Rathburn Chemicals Ltd.) were dried using an MBraun SPS-800 solvent purification system and stored in gas-tight ampoules under argon, with the exceptions of tetrahydrofuran (THF) and 1,4-dioxane (both 99.9%, Rathburn Chemicals Ltd.) which were distilled over sodium metal/benzophenone. Ethylenediamine (99%, Alfa Aesar) and pyridine (99.9%, Rathburn Chemicals Ltd.) were distilled over sodium metal and calcium hydride, respectively. Small scale purification of $d_8$-THF and $d_6$-benzene (Apollo Scientific Ltd.) was achieved by vacuum distillation of the solvent from calcium hydride. All solvents were stored in gas tight ampoules under argon. Additionally, benzene, 1,4-dioxane, diethyl ether, hexanes, THF and toluene were stored over activated 3 Å molecular sieves (Acros). Ethanol ($\geq$99.8%, Sigma-Aldrich) was used as supplied.

### 5.4.2 Reagents

Table 5.1 shows the reagents used in the preparation of the compounds detailed in this thesis (including those used for the synthesis of precursors) together with any additional purification steps undertaken. All compounds were stored in a glovebox unless indicated by an asterisk.

### 5.4.3 Synthesis of Precursors

Many of the transition metal complex synthesis routes detailed in this chapter use $M_n(mes)_{2n}$ (mes = 2,4,6-$Me_3C_6H_2$), (M = Mn, Fe, Co, Zn, with n = 3, 2, 2, 2, respectively). The synthesis of these compounds and other previously reported synthetic routes employed in the course of this research are detailed below.

| Compound | Purity | Source | Procedure |
|---|---|---|---|
| 2,2´-bipy | >99% | TCI Europe | Dried under vacuum |
| 2,4´-bipy | >99% | TCI Europe | Dried under vacuum |
| 4,4´-bipy | >99% | Acros Organics | Dried under vacuum |
| $CrCl_2$ | 99.9% | Strem Chemicals Inc. | Used as supplied |
| $CoBr_2$ | Co 26.6% min. | Alfa Aesar | Used as supplied |
| $Co(mes)_2(PEt_2Ph)_2$ | Synthesised by a literature procedure (see subsection 5.4.3) | | |
| 18-crown-6 | 99% | Alfa Aesar | Dried under vacuum |
| 2,2,2-crypt | ≥99% | Merck | Dried under vacuum |
| dibenzo-18-crown-6 | 98% | Sigma-Aldrich | Dried under vacuum |
| $KC_8$ | Synthesised by a literature procedure (see subsection 5.4.3) | | |
| $FeCl_2$ | 98% | Strem Chemicals Inc. | Used as supplied |
| $Fe_2Mes_4$ | Synthesised by a literature procedure (see subsection 5.4.3) | | |
| graphite powder* | < 20 micron | Sigma-Aldrich | Used as supplied |
| (mes)Br* | 99% | Alfa Aesar | Stored over 3Å sieves |
| (mes)Li | Synthesised by a literature procedure (see subsection 5.4.3) | | |
| Mg turnings* | not given | Fisher | Used as supplied |
| $MnCl_2$ | 97% | Strem Chemicals Inc. | Used as supplied |
| $Mn_3(mes)_6$·tol | Synthesised by a literature procedure (see subsection 5.4.3) | | |
| Ni(2,2´-bipy)$(mes)_2$ | Synthesised by a literature procedure (see subsection 5.4.3) | | |
| $NiBr_2$ | 99+% | Strem Chemicals Inc. | Used as supplied |
| $PEt_2Ph$ | 98% | Alfa Aesar | Used as supplied |
| $PMe_3$ | 99% | Strem Chemicals Inc. | Used as supplied |
| potassium | 99.95% | Sigma-Aldrich | Used as supplied |
| rubidium | 99.9+% | Strem Chemicals Inc. | Used as supplied |
| sodium in paraffin | not given | BDH Chemicals | Washed with hexanes |
| $ZnBr_2$ | 99.9%-Zn | Strem Chemicals Inc. | Used as supplied |
| $Zn(mes)_2$ | Synthesised by a literature procedure (see subsection 5.4.3) | | |

Table 5.1: List of reagents used and purification methods (where relevant). An asterisk indicates an item was not stored in the glovebox. All compounds are anhydrous.

#### 5.4.3.1 Synthesis of (mes)MgBr

Typically, mesityl bromide (8.84 g, 0.044 mol) was added to a Schlenk tube containing THF (50 mL) and Mg metal (1.537 g, 0.063 mol) which was immersed in an ice water bath at 0 °C. The reaction mixture was stirred and allowed to warm to room temperature overnight, forming a dark brown solution of the Grignard reagent (mes)MgBr. The solution was filtered via cannula into a second Schlenk tube, leaving 0.474 g, 0.019 mol of unreacted Mg (once dried). It should be noted that this procedure was used whenever (mes)MgBr is referenced below, with the scale adjusted to that of the referencing reaction.

#### 5.4.3.2 Synthesis of (mes)Li

Donor free (mes)Li was prepared following a modified literature procedure.[41] A hexane solution of *n*-BuLi (21.5 mL, 0.034 mol) was added to a solution of (mes)Br (6.15 ml, 0.040 mol) in $Et_2O$/hexane (10/20 mL) at 0 °C. The mixture was stirred overnight whilst warming to room temperature, during which time a white precipitate of (mes)Li formed. This was separated by filtration and washed with hexanes (2 × 20 mL) to leave a white powder (yield: 1.62 g, 38%).

#### 5.4.3.3 Synthesis of $KC_8$

Potassium graphite was synthesised via a modified literature preparation.[42] Graphite powder (5 g, 0.42 mol) was added to a Schlenk tube which was carefully evacuated and transferred into a glovebox. A magnetic follower and one eighth of an equivalent potassium metal was added (2.1g, 0.053 mol) before the vessel was returned to a Schlenk line. The Schlenk was heated under an argon atmosphere in a sand bath with vigorous stirring overnight, during which time the black powder changed to the bronze colour of $KC_8$.

#### 5.4.3.4 Synthesis of $Mn_3(mes)_6$·toluene

$Mn_3(mes)_6$·tol was prepared according to a modified literature procedure.[43] A THF solution of (mes)MgBr (100 mL, 0.084 mol) was added in a drop-wise manner to a THF solution (250 mL) of $MnCl_2$·1.5THF (9.3 g, 0.040 mol) at –30 °C. The brown suspension was warmed to room temperature and stirred overnight, before the solution was heated under refluxing conditions for a further 5 hours. Addition of 1,4-dioxane (62 mL) caused the formation of a very fine white suspension which was stirred overnight and left to stand for 2 hours prior to filtration. The resulting solution was evaporated to dryness to give a green solid that was redissolved in warm toluene (40 mL). A small amount of undissolved solid was removed by filtration, whilst the solution temperature was maintained. Cooling the solution in a –15 °C freezer caused formation of the product (crystalline yield: 4.52 g, 39%).

#### 5.4.3.5 Synthesis of $Fe_2(mes)_4$

The compound $Fe_2(mes)_4$ was prepared following a literature procedure.[44] A THF solution of (mes)MgBr (20 mL, 0.079 mol) was added drop-wise to a THF/dioxane (250/50 mL) suspension of $FeCl_2$·1.5THF (9.3 g, 0.039 mol) at –30 °C. The resulting suspension was stirred while slowly warming to room temperature. The mixture was stirred at room temperature for a further 2 hours. Magnesium halide salts were removed by filtration and the remaining dark coloured solution was exposed to vacuum until a dry dark brown solid remained. This was dissolved in $Et_2O$ (150 mL) and a small amount of undissolved solid was removed by filtration. The solution was then concentrated to 30 mL and placed in a –20 °C freezer overnight, forming dark red/brown crystals (crystalline yield: 7.7 g, 67%).

#### 5.4.3.6 Synthesis of $Co(mes)_2(PEt_2Ph)_2$

This compound was prepared using a literature procedure.[45] Diethylphenylphosphine (4.0 mL, 0.23 mol) was added to an ethanol solution (40 mL) of $CoBr_2$ (2.5 g, 0.011 mol). This immediately caused the precipitation of turquoise crystals of $CoBr_2(PEt_2Ph)_2$ which were isolated by filtration. Addition of benzene (50 mL) to $CoBr_2(PEt_2Ph)_2$ (6.0 g, 0.011 mol) generated a blue solution which was added drop-wise to a –30 °C THF solution of (mes)MgBr (26 mL, 0.039 mol). The mixture was warmed to 20 °C and stirred for 40 minutes. The mixture was cooled again to –30 °C before hydrolysis was effected by addition of dilute hydrochloric acid. Benzene (80 mL) was added and the organic layer separated, washed with distilled water (2 × 30 mL) and dried over $MgSO_4$. Filtration to remove the drying agent and vacuum removal of the solvent at room temperature yielded lemon-yellow crystals of the product (crystalline yield: 5.1 g, 74%).

#### 5.4.3.7 Synthesis of Ni(2,2´-bipy)$(mes)_2$

Ni(2,2´-bipy)$(mes)_2$ was prepared following a literature procedure.[46,47] Triphenylphosphine (11.5 g, 0.044 mol) was added to $NiBr_2$ (4.4 g, 0.020 mol) in THF (50 mL) and the suspension then stirred for 2 hours, to form a dark green solution. This was cooled to 0 °C before a THF solution of (mes)MgBr (20 mL, 0.020 mol) was added in a drop-wise manner. After a further 1 hour stirring, addition of aqueous saturated $NH_4Cl$ (ca. 20 mL) caused hydrolysis, yielding a bright yellow precipitate of NiBr(mes)$(PPh_3)_2$ that was isolated by filtration and dried under vacuum after washing with distilled water (3 × 20 mL) and hexanes (3 × 20 mL).

2,2´-bipyridine (2,2´-bipy) (1.46 g, 9.3 mmol) was then added to a portion of NiBr(mes)$(PPh_3)_2$ (4.5 g, 8.7 mmol) in $Et_2O$ (120 mL) and the resulting suspension was stirred for 2 hours before standing overnight in a –5 °C fridge. Dark red crystals of Ni(2,2´-bipy)Br(mes) were isolated by filtration and washed with cold $Et_2O$.

Li(mes) (0.60 g, 4.7 mmol) was added to a toluene solution (50 mL) containing a portion of Ni(2,2´-bipy)Br(mes) (1.8 g, 4.5 mmol). The mixture was stirred for 3 hours at 70 °C, during which time the dark red solution turned dark purple. Reduction of the solvent volume to 5 mL and addition of 5 mL of $Et_2O$ caused precipitation of Ni(2,2´-bipy)$(mes)_2$ which was isolated by filtration before washing with cold pentane ($3 \times 15$ mL) and dried under vacuum. Filtrates were combined and recrystallised from $Et_2O$. These products were then combined (crystalline yield: 1.62 g, 76%).

#### 5.4.3.8 Synthesis of $Zn(mes)_2$

This preparation is based on a modified synthesis of $Zn(^iPr)_2$.[48,49] A THF solution of (mes)MgBr (50 mL, 0.044 mol) was added drop-wise to a Schlenk tube containing $ZnBr_2$ (4.98 g, 0.022 mol) in THF (40 mL) at –78 °C and stirred whilst the reaction was slowly allowed to warm to room temperature overnight, yielding a white precipitate and a light brown solution. A slight excess of 1,4-dioxane (4.0 mL, 0.047 mol) was added and the solution then further stirred for 12 hours to aid precipitation of the magnesium salts. The white solid was removed by filtration before the remaining solution was placed in a freezer at –80 °C for 24 hours. This yielded white crystalline needles of $Zn(mes)_2$ (crystalline yield: 3.55g, 52.8%).

## 5.5 Synthesis of Compounds 1 to 22

### 5.5.1 Compound 1: K(2,2´-bipy)(en)

2,2´-bipy (0.144 g, 0.92 mmol) and potassium metal (0.038 g, 0.97 mmol) were dissolved in approximately 4 mL of ethylenediamine, instantly yielding a deep-purple solution. The reaction mixture was stirred for approximately 24 hours in a capped sample vial in a nitrogen-filled glovebox. The solution was filtered into a crystallisation ampoule while in the glovebox by passing it through a Pasteur pipette containing

packed glass wool at the constriction. Prior to use, an ampoule containing the glass-wool-packed pipette was heated under vacuum to drive off all traces of moisture and air. After filtration, the sealed ampoule was transferred to a Schlenk line, where it was layered with toluene (approximately 20 mL). During layering, the ampoule was cooled in a water bath (8 °C) and then transferred to a fridge (8 – 10 °C) to aid the crystallisation of the product. Two polymorphic crystalline products formed after 4 days: K(2,2´-bipy)(en) (**1a**) and $K_4$(2,2´-bipy)$_4$(en)$_4$ (**1b**). Both crystallised as large purple/black block-like crystals and were found to be suitable for single crystal X-ray diffraction. Crystalline yield: 93.7 mg, 39.8%. Anal. Calcd for $C_{12}H_{16}KN_4$: C, 56.42; H, 6.32; N, 21.95. Found: C, 56.62; H, 6.40; N, 21.86. Solid-state EPR measurements recorded a $g$ value of 2.0033. Solution-phase EPR measurements recorded a $g$ value of 2.0035. IR ($cm^{-1}$): 626 (m), 683 (s), 709 (s), 738 (w), 817 (w) 939 (s), 974 (s), 1005 (s), 1139 (m), 1155 (m), 1260 (s), 1282 (w), 1404 (m), 1495 (m), 1561 (w). Raman ($cm^{-1}$): 343 (m), 626 (w), 972 (m), 1020 (w), 1029 (w), 1142 (w), 1157 (s), 1208 (w), 1259 (w), 1347 (m), 1461 (s), 1471 (m), 1495 (m), 1560 (w).

### 5.5.2 Compound 2: $Rb_2$(2,2´-bipy)$(en)_2$

Sample **2** was prepared by the same method as that employed for the synthesis of **1** using 2,2´-bipy (0.192 g, 1.2 mmol) and rubidium metal (0.221 g, 2.6 mmol). Purple/black rod-like crystals of **2** suitable for single crystal X-ray diffraction were isolated from an ethylenediamine/toluene mixture (crystalline yield: 192 mg, 35.0%). Powder X-ray diffraction studies found that the bulk sample matched the calculated diffraction pattern, as predicted from single crystal data. Anal. Calcd for $C_{14}H_{24}N_6Rb_2$: C, 37.57; H, 5.41; N, 18.79. Found: C, 37.56; H, 5.51; N, 18.70. Solid-state EPR measurements recorded a weak resonance with a $g$ value of 2.0033. IR ($cm^{-1}$): 612 (vs), 639 (m), 668 (s), 675 (s), 708 (w), 755 (m), 801 (s), 830 (m), 867 (m), 887 (s), 902 (m), 928 (w), 980 (s), 1018 (m), 1039 (vs), 1090 (s), 1099 (s), 1149

(w), 1260 (s), 1290 (m), 1322 (w), 1363 (m), 1399 (s), 1560 (m), 1590 (m). Raman ($cm^{-1}$): 327 (w), 433 (m), 464 (w), 589 (w), 607 (w), 642 (w), 709 (m), 916 (m), 957 (s), 989 (s), 1083 (s), 1108 (w), 1137 (m), 1154 (w), 1233 (s), 1303 (m), 1345 (w), 1434 (s), 1469 (m), 1493 (s), 1578 (s).

### 5.5.3 Compound 3: K(2,4´-bipy)(en)

K(2,4´-bipy)(en) was prepared using a method analogous to that described for the synthesis of **1**. 2,4´-bipy (0.152 g, 0.97 mmol) and potassium metal (0.040 g, 1.0 mmol) were reacted in ethylenediamine and subsequently layered with toluene. Dark-purple/black plate-like crystals of **3** suitable for single crystal X-ray diffraction were isolated from an the solvent mixture after 4 days (crystalline yield: 25.7 mg, 11.7%). Powder X-ray diffraction studies found that the bulk sample matched the calculated diffraction pattern, as predicted from single crystal data. Anal. Calcd for $C_{12}H_{16}KN_4$: C, 56.42; H, 6.32; N, 21.95. Found: C, 56.36; H, 6.27; N, 21.86. Solid-state and solution-phase EPR measurements recorded a $g$ value of 2.0037. IR ($cm^{-1}$): 625 (w), 668 (w), 689 (m), 739 (m), 745 (m), 772 (w), 793 (m), 932 (m), 944 (s), 960 (w), 978 (m), 1016 (m), 1144 (s), 1202 (s), 1252 (m), 1267 (w), 1303 (w), 1426 (s), 1559 (s), 1586 (s), 1597 (s). Raman ($cm^{-1}$): 335 (m), 429 (w), 590 (w), 598 (w), 741 (w), 982 (m), 1012 (s), 1028 (w), 1040 (m), 1087 (w), 1149 (m), 1204 (m), 1226 (m), 1260 (w), 1304 (w), 1348 (s), 1406 (w), 1427 (s), 1476 (s), 1504 (s), 1572 (m), 1597 (s).

### 5.5.4 Compound 4: $K_4$(2,4´-bipy)$_2$(en)$_{3.5}$

$K_4$(2,4´-bipy)$_2$(en)$_{3.5}$ was prepared using similar methodology to that described for the synthesis of **1**, using 2,4´-bipy (0.149 g, 0.95 mmol) and potassium metal (0.078 g, 2.0 mmol). Dark-purple/black needle-like crystals formed from an ethylenediamine/toluene mixture after 4 days. Crystalline yield: 263.7 mg, 81.4%. Anal. Calcd for $C_{27}H_{44}K_4N_{11}$: C, 47.73; H, 6.53; N, 22.69. Found: C, 47.62; H, 6.51; N, 22.66.

Solid-state EPR measurements recorded a weak resonance with a $g$ value of 2.0035. IR ($cm^{-1}$): 620 (w), 636 (s), 671 (w), 700 (w), 710 (m), 733 (m), 748 (m), 799 (s), 819 (w), 875 (m), 900 (s), 950 (vs), 981 (m), 1018 (m), 1050 (w), 1072 (m), 1114 (s), 1171 (s), 1208 (s), 1257 (vs, sh), 1290 (vs), 1366 (m), 1410 (w), 1433 (s), 1483 (m), 1502 (m), 1574 (s), 1607 (m). Raman ($cm^{-1}$): 331 (m), 407 (w), 566 (w), 712 (w), 953 (w), 981 (s), 1012 (w), 1025 (w), 1038 (w), 1072 (m), 1127 (m), 1169 (w), 1210 (m), 1226 (w), 1261 (m), 1344 (m), 1372 (w), 1384 (w), 1431 (m), 1446 (w), 1474 (m), 1504 (s), 1576 (w), 1605 (s).

### 5.5.5 Compound 5: $Rb_4(2,4´\text{-bipy})_2(en)_{3.5}$

$Rb_4(2,4´\text{-bipy})_2(en)_{3.5}$ was prepared using a method analogous to that described for the synthesis of **1**. 2,4´-bipy (0.155 g, 0.99 mmol) and rubidium metal (0.178 g, 2.1 mmol) were reacted in ethylenediamine and subsequently layered with diethyl ether. Purple rod-like crystals suitable for X-ray diffraction formed after 6 days from the solvent mixture (crystalline yield: 349 mg, 58.2%). Powder X-ray diffraction studies found that the bulk sample matched the calculated diffraction pattern, as predicted from single crystal data. Anal. Calcd for $C_{27}H_{44}N_{11}Rb_4$: C, 37.49; H, 5.13; N, 17.82. Found: C, 37.39; H, 5.07; N, 17.83. Solid-state EPR measurements recorded a weak resonance with a $g$ value of 2.0038. IR and Raman data for sample **5** were found to be closely related with those recorded for sample **4**: IR ($cm^{-1}$): 620 (w), 634 (s), 668 (s), 700 (w), 710 (m), 732 (m), 748 (m), 771 (m), 802 (m), 819 (w), 902 (s), 951 (vs), 979 (s), 987 (m), 1017 (m), 1023 (m), 1038 (w), 1050 (w), 1070 (m), 1112 (s), 1170 (s), 1205 (s), 1255 (vs), 1263 (vs), 1291 (vs), 1371 (m), 1408 (m), 1433 (s), 1497 (m), 1560 (w), 1576 (s), 1595 (m), 1604 (m). Raman ($cm^{-1}$): 331 (m), 426 (w), 574 (w), 591 (w), 634 (w), 710 (w), 905 (w). 952 (m), 981 (s), 1011 (m), 1025 (w), 1067 (m), 1110 (w), 1118 (m), 1146 (w), 1166 (m), 1210 (m), 1254 (m), 1263 (w), 1346 (m), 1360 (w), 1381 (w), 1425 (s), 1434 (s), 1474 (s), 1501 (s), 1574 (m), 1602 (s).

### 5.5.6 Compound 6: Na(4,4´-bipy)(en)

Sample **6** was prepared by the same method as that employed for the synthesis of **1** using 4,4´-bipy (0.150 g, 0.96 mmol) and sodium metal (0.024 g, 1.0 mmol). After layering with benzene this yielded two polymorphic crystalline products after 1 day: Na(4,4´-bipy)(en) (**6a**) and $Na_2$(4,4´-bipy)$_2$(en)$_2$ (**6b**). Both crystallised as purple/black block-like crystals and were found to be suitable for single crystal X-ray diffraction. Crystalline yield: 168 mg, 73.0%. Anal. Calcd for $C_{12}H_{16}N_4Na$: C, 60.24; H, 6.74; N, 23.41. Found: C, 60.12; H, 6.71; N, 23.36. Solid-state EPR measurements recorded a a $g$ value of 2.0025 while solution-phase experiments revealed a $g$ value of 2.0046. Raman ($cm^{-1}$): 343 (w), 698 (w), 744 (m), 1001 (m), 1040 (s), 1074 (w), 1227 (w), 1348 (s), 1368 (vs), 1431 (w), 1509 (vs), 1614 (vs), 1677 (w).

### 5.5.7 Compound 7: $Na_2$(4,4´-bipy)(en)$_2$

$Na_2$(4,4´-bipy)(en)$_2$ was prepared using similar methodology to that described for the synthesis of **1**, using 4,4´-bipy (0.150 g, 0.96 mmol) and sodium metal (0.055 g, 2.4 mmol). Dark-purple plate-like crystals formed from an ethylenediamine/benzene mixture after 2 days. Crystalline yield: 163 mg, 51.0%. Anal. Calcd for $C_7H_{12}N_3Na$: C, 52.16; H, 7.50; N, 26.07. Found: C, 52.07; H, 7.53; N, 26.03. Solid-state EPR measurements recorded a weak resonance with a $g$ value of 2.0043. Raman ($cm^{-1}$): 342 (w), 742 (w), 837 (w), 970 (w), 1004 (m), 1041 (w), 1231 (w), 1347 (s), 1396 (w), 1506 (vs) 1613 (vs), 1699 (w), 1793 (w), 1860 (w).

### 5.5.8 Compound 8: Cr(2,2´-bipy)(mes)$_2$

A suspension of $CrCl_2$ (1.00 g, 8.1 mmol) was stirred in THF (40 mL) in a Schlenk tube at –78 °C before the dropwise addition of a 0.41 M solution of (mes)MgBr in THF (40 mL, 16.3 mmol). The resulting brown solution was slowly warmed to –20 °C

to form a purple solution which was stirred for 10 hours. After re-cooling to –78 °C, 2,2´-bipy (3.81 g, 24.4 mmol) in THF (20 mL) was added in a dropwise manner and the system then allowed to warm to room temperature overnight, yielding an intensely coloured purple solution and a light purple precipitate, assumed to be composed of additional undissolved product and Mg(2,2´-bipy)ClBr. Filtration and subsequent drying *in vacuo* yielded 0.45 g of a dark purple solid. Further washings of the reaction precipitates with THF allowed the isolation of an additional 2.07 g of product (60% total yield). Slow diffusion of hexanes into a saturated THF solution yielded small crystals with the literature unit cell of Cr(2,2´-bipy)$(mes)_2$·THF,[50] while similar diffusion into a benzene solution yielded crystals of Cr(2,2´-bipy)$(mes)_2$·1.5$C_6H_6$. The solvent of crystallisation was found to be removed when samples were sealed under vacuum. Anal. Calcd for $C_{28}CrH_{30}N_2$: C, 75.31; H, 6.77; N, 6.27. Found: C, 74.95; H, 6.60; N, 6.06. A diamagnetic correction of –0.00034738 $cm^3$ $mol^{-1}$ was applied to SQUID magnetometry measurements. The corrected data exhibit a magnetic moment of 4.82 $\mu_B$ relative to a calculated spin-only value of 4.90 $\mu_B$ for a high spin chromium(II) complex. A solid state EPR spectrum was recorded at room temperature and exhibited a very weak resonance with a $g$ value of 1.986. IR ($cm^{-1}$): 650 (w), 733 (m), 756 (s), 767 (m), 800 (w), 842 (m), 1015 (m), 1059 (w), 1153 (m), 1171 (w), 1244 (w), 1260 (w), 1311 (w), 1377 (s), 1429 (w), 1441 (s), 1458 (s), 1562 (w), 1571 (w), 1600 (s). Raman ($cm^{-1}$): 132 (w), 371 (w), 650 (w), 1016 (s), 1159 (m), 1170 (m), 1227 (m), 1282 (s), 1318 (m), 1414 (w), 1468 (m), 1487 (s), 1510 (w), 1554 (m), 1561 (w), 1572 (w).

### 5.5.9 Compound 9: Mn(2,2´-bipy)$(mes)_2$

$Mn_3(mes)_6$ (150.0 mg, 0.17 mmol) and 2,2´-bipy (80.0 mg, 0.51 mmol) were weighed out into a sample vial and dissolved in THF (5 mL) inside an inert atmosphere glovebox and stirred for 6 hours. The resulting dark blue solution was filtered

and layered with hexanes. After three days, very small, flat, needle-like crystals of Mn(2,2´-bipy)$(mes)_2$ had formed which were found to be suitable for single crystal X-ray diffraction (121 mg, 52% crystalline yield). A powder X-ray diffraction pattern matched that calculated from the single crystal structure. Anal. Calcd for $C_{28}H_{30}MnN_2$: C, 74.82; H, 6.73; N, 6.23. Found: C, 74.62; H, 6.70; N, 6.15. A diamagnetic correction of –0.00029434 $cm^3$ $mol^{-1}$ was applied to SQUID magnetometry measurements. The sample displays a Curie-Weiss paramagnetic response with a molar magnetic moment of 5.62 $\mu_B$ compared to a calculated spin-only value of 5.92 $\mu_B$ for a high spin, Mn(II) complex. The close proximity of spin 5/2 nuclei in the crystal lattice is responsible for highly unusual solid-state EPR spectra due to extensive spin coupling of adjacent sites. Attempts to reduce this by co-precipitating **9** with $t$-$Bu_4NPF_6$ were partially successful, as exhibited by the increased intensity of a resonance with a $g$ value of approximately 2.0017, though the presence of the same complex background indicates the presence of significant amounts of the original neat sample. IR ($cm^{-1}$): 627 (w), 645 (w), 665 (w), 704 (w), 707 (w), 737 (m), 743 (w), 763 (m), 799 (w), 839 (m), 850 (m), 892 (w), 934 (w), 963 (w), 1012 (s), 1043 (w), 1058 (w), 1102 (w), 1112 (w), 1157 (s), 1167 (w), 1210 (m), 1246 (m), 1257 (w), 1279 (w), 1314 (m), 1365 (w), 1374 (m), 1390 (w), 1485 (w), 1528 (w), 1562 (w), 1571 (w), 1588 (m), 1596 (s), 1600 (s), 1701 (w), 1726 (w). Raman ($cm^{-1}$): 127 (w), 237 (w), 287 (w), 343 (w), 524 (w), 632 (w), 738 (w), 963 (w), 984 (m), 1070 (w), 1159 (m), 1201 (m), 1268 (w), 1348 (w), 1458 (w), 1478 (s), 1500 (m), 1534 (w), 1559 (w), 1579 (w).

### 5.5.10 Compound 10: Fe(2,2´-bipy)$(mes)_2$

$Fe_2(mes)_4$ (200 mg, 0.35 mmol) and 2,2´-bipy (110 mg, 0.70 mmol) were dissolved in THF (5 mL) in a glovebox and stirred for an hour. A deep reddish-purple solution was immediately observable. The resulting solution was filtered and layered with

approximately 20 mL of hexanes. The mixture was left to crystallise over several days affording 195 mg of red crystalline Fe(2,2´-bipy)(mes)$_2$ (yield 62%). A powder X-ray diffraction pattern was obtained which matched the simulated diffraction pattern based on the single crystal X-ray diffraction data. Anal. Calcd for $C_{28}FeH_{30}N_2$: C, 74.65; H, 6.72; N, 6.22. Found: C, 74.52; H, 6.60; N, 6.23. SQUID magnetometry measurements were diamagnetically corrected (by –0.000286 cm$^3$ mol$^{-1}$) and show a Curie-Weiss paramagnetic response of 5.12 $\mu_B$ which differs from the spin-only formula calculated value of 4.90 $\mu_B$ due to a small amount of spin-orbit coupling. Sample **10** is EPR silent because the Fe(II) nucleus is an example of a non-Kramers ion ($S = 2$). IR (cm$^{-1}$): 628 (w), 647 (w), 705 (w), 735 (s), 744 (w), 763 (vs), 839 (s), 850 (m), 1012 (s), 1042 (w), 1057 (w), 1101 (w), 1112 (w), 1156 (s), 1166 (w), 1211 (w), 1247 (m), 1278 (w), 1310 (m), 1366 (m), 1392 (m), 1439 (vs), 1470 (m), 1530 (w), 1561 (w), 1571 (w), 1589 (m), 1596 (s), 1599 (s). Raman (cm$^{-1}$): 96 (w), 140(s), 250 (m), 293 (w), 359 (w), 419 (w), 483 (w), 548 (w), 651 (m), 770 (w), 1016 (s), 1170 (m), 1282 (m), 1315 (s), 1487 (s), 1565 (m), 1599 (w).

### 5.5.11 Compound 11: Co(2,2´-bipy)(mes)$_2$

Co(mes)$_2$(PPhEt$_2$)$_2$ (301.1 mg, 0.48 mmol) and 2,2´-bipy (74.9 mg, 0.48 mmol) were weighed out into a Schlenk tube in a glovebox. The reaction vessel was transferred to a Schlenk line and THF added (∼5 mL). The mixture was then stirred for 16 hours. During this time the brown/yellow solution turned a dark red colour. The reaction mixture was filtered and layered with hexanes. After three days black block-like crystals of Co(2,2´-bipy)(mes)$_2$·THF had formed and were found to be suitable for single crystal X-ray diffraction (101.1 mg, 40% crystalline yield). A powder X-ray diffraction pattern was found to match that calculated from a separate room temperature single crystal X-ray data collection. Anal. Calcd for $C_{28}CoH_{30}N_2$: C, 63.78; H, 7.69; N, 6.47. Found: C, 63.66; H, 7.54; N, 6.52. SQUID measurements

have been diamagnetically corrected by –0.00034438 $cm^3$ $mol^{-1}$. **11** does not display Curie-Weiss paramagnetism but instead exhibits a temperature dependant magnetic susceptibility, varying linearly from 2.31 $\mu_B$ at 20 K to 2.62 $\mu_B$ at 300K. The solid-state EPR spectrum of Co(2,2´-bipy)$(mes)_2$ reveals a single, extremely broad resonance (> 6000 Gauss), centred around a $g$ value of 2.45. IR ($cm^{-1}$): 648 (w), 652 (w), 667 (w), 712 (w), 721 (m), 728 (m), 736 (w), 755 (s), 768 (w), 841 (m), 874 (w), 888 (w), 935 (w), 963 (w), 983 (w), 1008 (m), 1016 (w), 1031 (w), 1061 (w), 1156 (w), 1216 (w), 1245 (w), 1261 (w), 1272 (m), 1308 (w), 1320 (w), 1363 (w), 1377 (m), 1394 (w), 1399 (w), 1405 (w), 1419 (w), 1427 (w), 1564 (w), 1590 (w), 1601 (w), 1709 (w), 1758 (w). Raman ($cm^{-1}$): 104 (w), 126 (w), 229 (w), 365 (m), 419 (w), 544 (w), 558 (w), 650 (m), 733 (w), 934 (w), 1004 (m), 1029 (w), 1001 (w), 1163 (m), 1259 (m), 1268 (m), 1317 (m), 1477 (s), 1554 (s), 1600 (s).

### 5.5.12 Compound 12: Ni(2,2´-bipy)$(mes)_2$

This was synthesised as detailed in section 5.4.3.7. Layering a THF solution with pentane yielded dark purple crystals of Ni(2,2´-bipy)$(mes)_2$. A powder X-ray diffraction pattern was found to match that calculated from the single crystal structure. Anal. Calcd for $C_{28}H_{30}N_2Ni$: C, 74.20; H, 6.67; N, 6.18. Found: C, 74.42; H, 6.56; N, 6.05. $^1$H NMR ($d_6$-benzene): $\delta$ (ppm) = 8.05 (d, 2H, bipyH$_{3,3´}$, $^3J_{H–H}$ = 6 Hz), 6.92 (s, 4H, HMes), 6.75 (t, 2H, bipyH$_{5,5´}$, $^3J_{H–H}$ = 6 Hz), 6.65 (d, 2H, bipyH$_{6,6´}$, $^3J_{H–H}$ = 6 Hz), 6.14 (t, 2H, bipyH$_{4,4´}$, $^3J_{H–H}$ = 6 Hz), 3.04 (s, 12H, $o$-$CH_3$), 2.41 (s, 6H, $p$-$CH_3$). IR ($cm^{-1}$): 713 (w), 722 (m), 729 (m), 737 (w), 756 (s), 843 (m), 874 (w), 889 (w), 940 (w), 1015 (m), 1021 (m), 1063 (w), 1153 (w), 1168 (w), 1218 (w), 1242 (w), 1250 (w), 1256 (w), 1278 (w), 1313 (w), 1340 (w), 1362 (m), 1377 (m), 1394 (w), 1405 (w), 1419 (w), 1430 (m), 1443 (s), 1562 (w), 1569 (w), 1604 (w). Raman ($cm^{-1}$): 258 (w), 550 (w) 566 (m), 635 (w), 772 (w), 943 (w), 1016 (s), 1170 (s), 1279 (s), 1325 (s), 1488 (s), 1564 (s), 1606 (m).

### 5.5.13 Compound 13: [K(dibenzo-18-crown-6)][Cr(2,2´-bipy)-(mes)$_2$]

THF (5 mL) was added to a sample vial containing **8** (75.0 mg, 0.15 mmol), $KC_8$ (22.7 mg, 0.17 mmol) and dibenzo-18-crown-6 (60.5 mg, 0.17 mmol) in a glovebox and stirred for 4 hours. Subsequent filtration and layering with hexanes yielded dark brown crystals of [K(dibenzo-18-crown-6)][Cr(2,2´-bipy)(mes)$_2$]·2THF suitable for single crystal X-ray diffraction (40 mg, 26% crystalline yield). IR ($cm^{-1}$): 726 (s), 744 (w), 841 (w), 943 (s), 958 (m), 1061 (m), 1087 (w), 1126 (s), 1209 (m), 1251 (s), 1290 (m), 1377 (s), 1419 (w), 1489 (m), 1503 (m), 1593 (w). Raman ($cm^{-1}$): 209 (m), 269 (w), 360 (s), 411 (w), 462 (w), 578 (w), 603 (m), 643 (s), 748 (w), 945 (w), 995 (s), 1011 (w), 1080 (m), 1161 (s), 1203 (s), 1273 (m), 1288 (w), 1354 (w), 1416 (m), 1480 (s), 1507 (s), 1536 (m), 1568 (m). SQUID magnetometry measurements were diamagnetically corrected (by –0.00069116 $cm^3$ $mol^{-1}$) and reveal a magnetic moment of 3.85 $\mu_B$ (compared to a spin-only value of 3.87 $\mu_B$). Solid state EPR spectra were recorded at room temperature and at 10 K and reveal complex anisotropic resonances centred about a $g$ value of 1.986.

### 5.5.14 Compound 14: [K(18-crown-6)][Mn(2,2´-bipy)(mes)$_2$]

THF (5 mL) was added to a sample vial containing **9** (66.0 mg, 0.15 mmol), K metal (6.1 mg, 0.16 mmol), and 18-crown-6 (39.0 mg, 0.15 mmol) in a glovebox and stirred for 24 hours. Filtration yielded a dark brown solution which, when layered with hexanes, produced very small crystals of [K(18-crown-6)][Mn(2,2´-bipy)(mes)$_2$]·2THF (**14a**) (ca. 5 mg, 4% crystalline yield). Due to the small size and weakly diffracting nature of the crystalline samples, single crystal X-ray diffraction data were collected at Beam Station I19 at the Diamond Light Source Synchrotron. Better quality crystalline samples suitable for single crystal X-ray diffraction on in-house in-

strumentation could be obtained from pyridine solutions which were allowed to diffuse into a toluene layer. These crystals were solved as [K(18-crown-6)][Mn(2,2´-bipy)(mes)2]·0.67py·0.67tol (**14b**) (py = pyridine, tol = toluene). Attempts to synthesise a pure microcrystalline compound were unsuccessful due to the very low yields of highly reactive species or the tendancy towards oil formation if even slight excesses of reducing agents were present. A diamagnetic correction was applied to SQUID magnetometry measurements of –0.00055946 $cm^3$ $mol^{-1}$. **14** deviates from Curie-Weiss paramagnetic behaviour with molar magnetic moments changing almost linearly between 4.15 $\mu_B$ and 4.85 $\mu_B$, at 35 K and 295 K, respectively. Solid-state and solution phase EPR spectra show intense resonances with $g$ values of 2.0035 and 2.0033, respectively. IR ($cm^{-1}$): 600 (w), 619 (w), 639 (w), 665 (w), 680 (w), 725 (m), 755 (w), 797 (w), 832 (w), 843 (w), 930 (w), 945 (w), 951 (s), 990 (w), 1011 (m), 1055 (w), 1077 (w), 1101 (s), 1130 (m), 1144 (m), 1172 (w), 1209 (w), 1235 (w), 1260 (s), 1273 (w), 1289 (s), 1294 (w), 1352 (s), 1358 (w), 1410 (w), 1419 (m), 1493 (m), 1506 (w), 1540 (w), 1558 (w), 1583 (w), 1617 (w), 1655 (w), 1695 (w), 1744 (w), 1807 (w), 1866 (w). Raman ($cm^{-1}$): 127 (w), 237 (w), 287 (w), 343 (w), 524 (w), 632 (w), 738 (w), 963 (w), 984 (m), 1070 (w), 1159 (m), 1201 (m), 1268 (w), 1348 (w), 1458 (w), 1478 (s), 1500 (m), 1534 (w), 1559 (w), 1579 (w).

### 5.5.15 Compound 15: [K(2,2,2-crypt)][Fe(2,2´-bipy)(mes)$_2$]

A portion of **10** (250 mg, 0.56 mmol) was reacted with K (22 mg, 0.56 mmol) and 2,2,2-crypt (212 mg, 0.56 mmol) in THF (5 mL) in a glovebox and left to stir overnight. The solution was filtered, layered with hexanes, and allowed to crystallise over several days yielding dark purple and pale green crystals. The crystalline products were identified as [K(2,2,2-crypt)][Fe(2,2´-bipy)(mes)$_2$] (**15**, dark purple) and [K(2,2,2-crypt)][Fe(mes)$_3$]·$C_6H_{12}$ (**18**, pale green). Species **15** was purified by redissolving the mixture of solids in pyridine, filtering, and layering the solution with

toluene. This yielded 148 mg of compositionally pure dark purple crystalline [K(2,2,2-crypt)][Fe(2,2´-bipy)(mes)$_2$] (yield 30%). A powder X-ray diffraction pattern was obtained which matched the simulated diffraction pattern based on the single crystal X-ray diffraction data. Anal. Calcd for $C_{46}FeH_{66}KN_4O_6$: C, 63.78; H, 7.69; N, 6.47. Found: C, 63.66; H, 7.54; N, 6.52. SQUID magnetometry measurements were diamagnetically corrected (by –0.000551 cm$^3$ mol$^{-1}$) and show a strong deviation from paramagnetic behaviour as a result of the mixing of different spin states. A room temperature solid-state EPR measurement exhibits a resonance with a $g$ factor of 2.086. IR (cm$^{-1}$): 613 (w) 639 (w), 681 (w), 688 (w), 708 (w), 733 (m), 754 (w), 799 (w), 831 (m), 847 (w), 932 (s), 949 (s), 965 (w), 1011 (m), 1029 (w), 1105 (vs), 1130 (s), 1210 (w), 1258 (s), 1275 (w), 1290 (m), 1356 (s), 1413 (w), 1434 (w), 1444 (m), 1478 (m), 1497 (m), 1537 (w), 1556 (w), 1563 (w), 1582 (w), 1608 (w). Raman (cm$^{-1}$): 242 (w), 366 (w), 377 (w), 414 (w), 431 (w), 478 (w), 539 (w), 573 (m), 607 (m), 617 (m), 670 (w), 742 (w), 984 (s), 1093 (m), 1141 (m), 1213 (s), 1349 (w), 1412 (m), 1477 (s), 1512 (s), 1521 (m), 1586 (m).

### 5.5.16 Compound 16: [K(2,2,2-crypt)][Co(2,2´-bipy)(mes)$_2$]

THF (4 mL) was added to a sample vial containing **11** (50.0 mg, 0.11 mmol), K metal (5.2 mg, 0.13 mmol) and 2,2,2-crypt (41.5 mg, 0.11 mmol) and stirred for 16 hours in a glovebox to yield a dark brown solution. Filtration and layering with hexanes yielded crystals of [K(2,2,2-crypt)][Co(2,2´-bipy)(mes)$_2$] after 10 days (25.4 mg, 26% crystalline yield). A powder X-ray diffraction pattern was found to match that calculated from the single crystal structure. Anal. Calcd for $C_{46}CoH_{66}KN_4O_6$: C, 63.57; H, 7.65; N, 6.45. Found: C, 63.26; H, 7.49; N, 6.45. A diamagnetic correction of –0.00055946 cm$^3$ mol$^{-1}$was made to SQUID measurements of **16**, which show more complex magnetic properties than Curie-Weiss paramagnetic behaviour alone. Magnetic moment varies between 1.27 $\mu_B$ and 1.88 $\mu_B$ at 30 K and 300 K,

respectively. EPR measurements on a solid sample of **16** show a very broad resonance ($>$ 6000 Gauss) centred on a $g$ value around 2.19. IR ($cm^{-1}$): 608 (w), 638 (w), 667 (w), 682 (w), 714 (w), 729 (s), 756 (w), 822 (w), 832 (w), 841 (m), 864 (w), 934 (s), 943 (w), 956 (s), 1003 (w), 1019 (w), 1027 (w), 1076 (m), 1088 (w), 1107 (s), 1130 (m), 1162 (w), 1173 (w), 1211 (w), 1231 (w), 1258 (m), 1276 (w), 1289 (s), 1295 (m), 1341 (w), 1351 (s), 1359 (m), 1419 (w), 1496 (s), 1556 (m), 1564 (m), 1661 (w), 1699 (w), 1726 (w), 1754 (w), 1783 (w). Raman ($cm^{-1}$): 72 (m), 80 (m), 88 (m), 96 (m), 103 (m), 112 (m), 120 (m), 126 (w), 136 (m), 225 (w), 365 (m), 635 (w), 803 (m, broad), 998 (m), 1143 (m), 1207 (w), 1271 (w), 1445 (s), 1506 (m), 1552 (m), 1809 (w), 2328 (s), 2440 (w, broad), 2587 (w, broad), 2885 (w, broad).

### 5.5.17 Compound 17: [K(2,2,2-crypt)][Ni(2,2´-bipy)(mes)$_2$]

THF (5 mL) was added to a sample vial containing **12** (50.0 mg, 0.11 mmol), $KC_8$ (14.9 mg, 0.11 mmol) and 2,2,2-crypt (41.5 mg, 0.11 mmol) and stirred in a glove-box for 4 hours. Filtration and layering with hexanes yielded dark purple crystals of [K(2,2,2-crypt)][Ni(mes)$_2$(2,2´-bipy)], suitable for single crystal X-ray diffraction. A powder X-ray diffraction pattern matched that calculated from the single crystal structure. A diamagnetic correction of –0.00055946 $cm^3$ $mol^{-1}$ was made to SQUID data of **17**, which show more complex magnetic properties than Curie-Weiss paramagnetic behaviour alone, with response varying between 1.52 $\mu_B$ and 1.27 $\mu_B$ at 30 K and 300 K, respectively. Solution-phase EPR measurements show a resonance centred on a $g$ value of 2.0045 that displays considerable hyperfine splitting. Solid-state EPR spectra were recorded at room temperature and at 10 K and reveal a strong resonance with a $g$ value of 2.0084. IR ($cm^{-1}$): 674 (w), 717 (m), 756 (w), 805 (w), 822 (w), 841 (w), 935 (m), 959 (m), 1010 (m), 1018 (w), 1077 (m), 1107 (s), 1129 (m), 1159 (w), 1203 (w), 1261 (m), 1275 (m), 1285 (w), 1294 (w), 1351 (m), 1360 (m), 1378 (s), 1416 (w), 1488 (m), 1569 (w). Raman ($cm^{-1}$): 155 (w), 366 (w), 413 (w), 544 (w),

561 (w), 647 (w), 746 (m), 940 (w), 999 (s), 1016 (m), 1086 (w), 1156 (s), 1201 (s), 1272 (m), 1314 (w), 1353 (m), 1413 (m), 1493 (s), 1549 (s), 1597 (w).

### 5.5.18 Compound 18: [K(2,2,2-crypt)][Fe(mes)$_3$]

Despite efforts to target the synthesis of this compound including the direct reduction of $Fe_2(mes)_4$ by K metal in the presence of 2,2,2-crypt, it was not possible to isolate a pure sample of **18**. Its synthesis as a side-product is detailed in subsection 5.5.15.

### 5.5.19 Compound 19: Zn$_2$(4,4´-bipy)(mes)$_4$

$Zn(mes)_2$ (300 mg, 0.99 mmol) and 4,4´-bipyridine (77 mg, 0.49 mmol) were dissolved in THF (approximately 4 mL) under an inert atmosphere and stirred for 5 hours, forming a pale yellow solution. The resulting solution was filtered and layered with hexanes. Large colourless needle-like crystals of $Zn_2$(4,4´-bipyridine)$(mes)_4$ formed overnight in good yield (240 mg, 63.6% crystalline yield). A powder X-ray diffraction pattern was obtained which matched the simulated diffraction pattern based on the single crystal X-ray diffraction data. Anal. Calcd for $C_{46}H_{52}N_2Zn_2$: C 72.34, H 6.86, N 3.67. Found: C 72.25, H 6.77, N 3.58. $^1$H NMR (299.9 MHz, $d_8$-THF): $\delta$ (ppm) 8.57 (d, 4H, *ortho*-4,4´-bipyridyl, $^3J_{\text{H–H}}$ = 6 Hz), 7.71 (d, 4H, *meta*-4,4´-bipyridyl, $^3J_{\text{H–H}}$ = 6 Hz), 6.73 (s, 8H, $C_6H_2(CH_3)_3$), 2.42 (s, 24H, *ortho*-$CH_3$), 2.21 (s, 12H, *para*-$CH_3$). The $^1$H NMR spectrum of **19** was assigned with the help of a COSY 2-D experiment. $^{13}$C NMR (75.4 MHz, $d_8$-THF): $\delta$ (ppm) 152.59 (s, *ipso*-$C_6H_2(CH_3)_3$), 151.45 (s, *ortho*-4,4´-bipyridyl), 147.05 (s, *para*-4,4´-bipyridyl), 145.48 (s, *ortho*-$C_6H_2(CH_3)_3$), 136.52 (s, *para*-$C_6H_2(CH_3)_3$), 126.48 (s, *meta*-$C_6H_2(CH_3)_3$), 122.88 (s, *meta*-4,4´-bipyridyl), 27.42 (s, *ortho*-$CH_3$), 21.58 (s, *para*-$CH_3$). $^{13}$C{$^1$H} NMR resonances were assigned with the help of HSQC and HMBC 2-D spectra. IR ($cm^{-1}$): 515 (w), 540 (m), 580 (w), 629 (s), 668 (w), 710 (w), 721 (w), 809 (s), 818 (s), 845 (s), 965 (w), 971 (w), 984 (w), 1005 (s), 1042 (m), 1070 (m), 1099 (w), 1215

(s), 1262 (w), 1285 (w), 1317 (w), 1412 (m), 1506 (w), 1525 (w), 1531 (w), 1539 (w), 1558 (w), 1570 (w), 1578 (w), 1602 (s). Raman ($cm^{-1}$): 298 (w), 332 (w), 397 (w), 552 (m), 580 (m), 658 (w), 770 (w), 944 (w), 1015 (m), 1019 (m), 1176 (w), 1233 (w), 1290 (m), 1298 (w), 1350 (w), 1381 (w), 1513 (w), 1605 (w), 1613 (m), 1637 (w).

### 5.5.20 Compound 20: [K(18-crown-6)(THF)$_2$][Zn$_2$(4,4´-bipy)-(mes)$_4$]

A portion of **19** (100 mg, 0.13 mmol), potassium metal (5 mg, 0.13 mmol), and 18-crown-6 (35 mg, 0.13 mmol) were dissolved in THF (5 mL) under an inert atmosphere giving rise to a deep blue solution. The reaction mixture was stirred overnight, filtered, and layered with hexanes. The mixture was allowed to slowly diffuse at a temperature between 8 and 10 °C over the course of several days, ultimately affording dark blue block-like crystals of [K(18-crown-6)(THF)$_2$][Zn$_2$(4,4´-bipyridine)(mes)$_4$] in good yield (115 mg, 72% crystalline yield). The crystals obtained from the THF/hexane solvent mixture proved to be suitable for single crystal X-ray diffraction and were found to contain two crystalline phases of identical composition (**20a** and **20b**). A powder X-ray diffraction pattern collected on the solid isolated from this reaction was found to only contain **20a** and **20b**. Anal. Calcd for $C_{66}H_{92}KN_2O_8Zn_2$: C 65.42, H 7.66, N 2.31. Found: C 61.60, H 6.94, N 2.73. CHN elemental analysis results consistently showed low concentrations of carbon and hydrogen. The room temperature EPR spectrum of a solid sample of **20** revealed a strong resonance with a $g$ value of 2.0039. IR ($cm^{-1}$): 539 (w), 578 (w), 618 (m), 668 (w), 687 (w), 772 (m), 775(m), 780 (w), 834 (w), 841 (m), 963 (s), 1020, (s), 1038 (w), 1103 (s), 1131 (w), 1171 (w), 1198 (s), 1220 (w), 1235 (w), 1248 (w), 1283 (m), 1350 (m) 1547 (w), 1592 (s). Raman ($cm^{-1}$): 387 (w), 427 (w), 688 (w), 712 (w), 751 (m), 1015 (m), 1047 (s), 1236 (s), 1352 (s), 1514 (s), 1630 (s).

### 5.5.21 Compound 21: $[K(18\text{-crown-}6)]_2[Zn_2(4,4´\text{-bipy})(mes)_4]$

A mixture of **19** (100 mg, 0.13 mmol), potassium metal (10 mg, 0.26 mmol), and 18-crown-6 (69.8 mg, 0.26 mmol) was dissolved in anhydrous THF (5 mL) under an inert atmosphere. The reaction mixture initially takes on a deep blue colour which, when stirred overnight, gives rise to a dark yellow/brown solution. The reaction mixture was filtered and layered with hexanes. After several days dark brown plate-like crystals of $[K(18\text{-crown-}6)]_2[Zn_2(4,4´\text{-bipyridine})(mes)_4]$ were obtained in high yields (141 mg, 81.9% crystalline yield). Anal. Calcd for $C_{70}H_{100}K_2N_2O_{12}Zn_2$: C 61.34, H 7.35, N 2.04. Found: C 61.28, H 7.20, N 1.87. $^1$H NMR (299.9 MHz, $d_8$-THF): $\delta$ (ppm) 6.50 (s, 8H, $C_6H_2(CH_3)_3$), 5.92 (d, 4H, *ortho*-4,4´-bipyridyl, $^3J_{H–H}$ = 6 Hz), 4.51 (d, 4H, *meta*-4,4´-bipyridyl, $^3J_{H–H}$ = 6 Hz), 3.57 (s, 48H, 18-crown-6), 2.32 (s, 24H, *ortho*-$CH_3$), 2.21 (s, 12H, *para*-$CH_3$). The $^1$H NMR spectrum of **21** exhibits some resonances arising from a $[Zn(mes)_3]^-$ impurity at 6.40 (s, 6H), 2.28 (s, 18H, *ortho*-$CH_3$), 2.08 (s, 9H, *para*-$CH_3$). $^{13}$C NMR (125.8 MHz, $d_8$-THF) $\delta$ (ppm): 161.48 (s, *para*-$C_6H_2(CH_3)_3$), 145.20 (s, *ortho*-$C_6H_2(CH_3)_3$), 139.78 (s, *ortho*-4,4´-bipyridyl), 132.88 (s, *ipso*-$C_6H_2(CH_3)_3$), 124.92 (s, *meta*-$C_6H_2(CH_3)_3$), 105.45 (*para*-4,4´-bipyridyl), 104.42 (s, *meta*-4,4´-bipyridyl), 72.01 (broad, s, 18-crown-6), 27.56 (s, *ortho*-$CH_3$), 21.56 (s, *para*-$CH_3$). The $^{13}$C NMR spectrum of **21** also exhibits some resonances arising from a $[Zn(mes)_3]^-$ impurity at 170.05 (s, *para*-$C_6H_2(CH_3)_3$), 145.31 (s, *ortho*-$C_6H_2(CH_3)_3$), 131.14 (s, *ipso*-$C_6H_2(CH_3)_3$), 124.55 (s, *meta*-$C_6H_2(CH_3)_3$), 72.01 (broad, s, 18-crown-6), 26.73 (s, *ortho*-$CH_3$), 21.75 (s, *para*-$CH_3$). $^{13}C\{^1H\}$ NMR resonances were tentatively assigned with the help of HSQC and HMBC 2-D spectra. IR ($cm^{-1}$): 668 (w), 722 (m), 801 (s), 841 (m), 934 (w), 949 (w), 962 (w), 983 (m), 1031 (w), 1109 (s), 1170 (w), 1197 (m), 1216 (w), 1252 (w), 1260 (w), 1284 (w), 1351 (m), 1506 (w), 1539 (w), 1559 (w), 1577 (w), 1608 (w). Raman ($cm^{-1}$): 742 (w), 989 (w), 1007 (w), 1046 (s), 1077 (w), 1233 (w), 1349 (s), 1507 (s), 1612 (s).

### 5.5.22 Compound 22: [K(18-crown-6)(THF)][Zn(mes)$_3$]

THF (approximately 5 mL) was added to a sample vial containing Zn(mes)$_2$ (100.1 mg, 0.33 mmol), potassium metal (approximately 13.0 mg, 0.33 mmol), and 18-crown-6 (90.4 mg, 0.34 mmol) in a glovebox. This initially formed a colourless solution, which became pale brown after about 5 min. This was stirred overnight before filtering off a dark precipitate (assumed to be elemental Zn), and the remaining light brown solution was layered with hexanes. After several days colourless block-like crystals of [K(18-crown-6)(THF)][Zn(mes)$_3$] formed, suitable for single crystal X-ray diffraction (111.1 mg, 42.3% crystalline yield). A powder X-ray diffraction pattern was obtained which matched the simulated diffraction pattern for **22** based on the single crystal X-ray diffraction data. Anal. Calcd for $C_{39}H_{57}KO_6Zn$: C 64.47, H 7.91. Found: C 64.08, H 7.67. (Note: There is a THF molecule present in the crystal structure which is removed when sealing the solid sample under vacuum). $^1$H NMR (299.86 MHz, $d_8$-THF): $\delta$ (ppm) 6.41 (s, 6H, $C_6H_2(CH_3)_3$), 3.57 (s, 24H, 18-crown-6), 2.28 (s, 18H, *ortho*-$CH_3$), 2.09 (s, 9H, *para*-$CH_3$). $^{13}$C NMR (125.80 MHz, $d_8$-THF) $\delta$ (ppm): 170.05 (s, *para*-$C_6H_2(CH_3)_3$), 145.31 (s, *ortho*-$C_6H_2(CH_3)_3$), 131.14 (s, *ipso*-$C_6H_2(CH_3)_3$), 124.55 (s, *meta*-$C_6H_2(CH_3)_3$), 72.01 (broad, s, 18-crown-6), 26.73 (s, *ortho*-$CH_3$), 21.75 (s, *para*-$CH_3$).

## 5.6 References


[1] Otwinowski, Z.; Minor, W. *Processing of X-ray diffraction data collected in oscillation mode*; Academic Press: New York, 1997.

[2] Sheldrick, G. M. *Acta Crystallogr. Sect. A* **2008**, *64*, 112.

[3] Farrugia, L. J. *J. Appl. Crystallogr.* **1999**, *32*, 837.

[4] Davies, S. G.; Clegg, W. *Crystal Structure Determination*; Oxford University Press, 1998.

[5] Clegg, W.; Blake, A. J.; Cole, J. M.; Evans, J.; Main, P.; Parsons, S.; Watkin, D. J. *Crystal structure analysis. Principles and practice.*, 2nd ed.; Oxford University Press/International Union of Crystallography, 2002.

[6] Warren, B. E. *X-ray Diffraction*; Dover Publications Inc., 1991.

[7] Davies, S.; Weller, M. *Inorganic Materials Chemistry*; Oxford University Press, 1995.

[8] Bain, G. A.; Berry, J. F. *J. Chem. Educ.* **2008**, *85*, 532.

[9] Tinkham, M. *Introduction to Superconductivity*; McGraw-Hill Education, 1995.

[10] Weil, J.; Bolton, J. *Electron Paramagnetic Resonance: Elementary Theory and Practical Applications*; Wiley, 2007.

[11] Davies, S. G.; Orchard, A. F. *Magnetochemistry*; Oxford University Press, 2003.

[12] Butcher, P. N. *Rep. Prog. Phys.* **1967**, *30*, 97.

[13] Griffiths, P.; De Haseth, J. A. *Fourier Transform Infrared Spectrometry*, 2nd ed.; Wiley, 2007.

[14] Wilson, E. B. *Molecular vibrations: The theory of infrared and Raman vibrational spectra*; Dover Publications Inc., 1980.

[15] Gibbs, S. J.; Jr., C. S. J. *J. Magn. Reson. (1969)* **1991**, *93*, 395.

[16] Hore, P. J. *Nuclear Magnetic Resonance*; Oxford Chemistry Primers; OUP Oxford, 1995.

[17] Long, G. J. *Mössbauer Spectroscopy Applied to Inorganic Chemistry*; Springer-Verlag New York, LCC, 1984.

[18] Frisch, M. J.; Trucks, G. W.; Schlegel, H. B.; Scuseria, G. E.; Robb, M. A.; Cheeseman, J. R.; Montgomery, J. A., Jr.; Vreven, T.; Kudin, K. N.; Burant, J. C.; Millam, J. M.; Iyengar, S. S.; Tomasi, J.; Barone, V.; Mennucci, B.; Cossi, M.; Scalmani, G.; Rega, N.; Petersson, G. A.; Nakatsuji, H.; Hada, M.; Ehara, M.; Toyota, K.; Fukuda, R.; Hasegawa, J.; Ishida, M.; Nakajima, T.; Honda, Y.; Kitao, O.; Nakai, H.; Klene, M.; Li, X.; Knox, J. E.; Hratchian, H. P.; Cross, J. B.; Bakken, V.; Adamo, C.; Jaramillo, J.; Gomperts, R.; Stratmann, R. E.; Yazyev, O.; Austin, A. J.; Cammi, R.; Pomelli, C.; Ochterski, J. W.; Ayala, P. Y.; Morokuma, K.; Voth, G. A.; Salvador, P.; Dannenberg, J. J.; Zakrzewski, V. G.; Dapprich, S.; Daniels, A. D.; Strain, M. C.; Farkas, O.; Malick, D. K.; Rabuck, A. D.; Raghavachari, K.; Foresman, J. B.; Ortiz, J. V.; Cui, Q.; Baboul, A. G.; Clifford, S.; Cioslowski, J.; Stefanov, B. B.; Liu, G.; Liashenko, A.; Piskorz, P.; Komaromi, I.; Martin, R. L.; Fox, D. J.; Keith, T.; Al-Laham, M. A.; Peng, C. Y.; Nanayakkara, A.; Challacombe, M.; Gill, P. M. W.; Johnson, B.; Chen, W.; Wong, M. W.; Gonzalez, C.; Pople, J. A. *Gaussian03, Revision D.01*; Gaussian Inc: Wallingford, CT, 2004.

[19] Becke, A. D. *J. Chem. Phys.* **1993**, *98*, 5648.

[20] Lee, C. T.; Yang, W. T.; Parr, R. G. *Phys. Rev. B: Condens. Matter* **1988**, *37*, 785.

[21] Miehlich, B.; Savin, A.; Stoll, H.; Preuss, H. *Chem. Phys. Lett.* **1989**, *157*, 200.

[22] Hay, P. J.; Wadt, W. R. *J. Chem. Phys.* **1985**, *82*, 270.

[23] Wadt, W. R.; Hay, P. J. *J. Chem. Phys.* **1985**, *82*, 284.

[24] Hay, P. J.; Wadt, W. R. *J. Chem. Phys.* **1985**, *82*, 299.

[25] Frisch, M. J.; Trucks, G. W.; Schlegel, H. B.; Scuseria, G. E.; Robb, M. A.; Cheeseman, J. R.; Scalmani, G.; Barone, V.; Mennucci, B.; Petersson, G. A.; Nakatsuji, H.; Caricato, M.; Li, X.; Hratchian, H. P.; Izmaylov, A. F.; Bloino, J.; Zheng, G.; Sonnenberg, J. L.; Hada, M.; Ehara, M.; Toyota, K.; Fukuda, R.; Hasegawa, J.; Ishida, M.; Nakajima, T.; Honda, Y.; Kitao, O.; Nakai, H.; Vreven, T.; Montgomery, J. A., Jr.; Peralta, J. E.; Ogliaro, F.; Bearpark, M.; Heyd, J. J.; Brothers, E.; Kudin, K. N.; Staroverov, V. N.; Kobayashi, R.; Normand, J.; Raghavachari, K.; Rendell, A.; Burant, J. C.; Iyengar, S. S.; Tomasi, J.; Cossi, M.; Rega, N.; Millam, J. M.; Klene, M.; Knox, J. E.; Cross, J. B.; Bakken, V.; Adamo, C.; Jaramillo, J.; Gomperts, R.; Stratmann, R. E.; Yazyev, O.; Austin, A. J.; Cammi, R.; Pomelli, C.; Ochterski, J. W.; Martin, R. L.; Morokuma, K.; Zakrzewski, V. G.; Voth, G. A.; Salvador, P.; Dannenberg, J. J.; Dapprich, S.; Daniels, A. D.; Farkas, Ö.; Foresman, J. B.; Ortiz, J. V.; Cioslowski, J.; Fox, D. J. *Gaussian09, Revision A.02*; Gaussian Inc: Wallingford, CT, 2004.

[26] Neese, F. *ORCA – an ab initio, Density Functional and Semiempirical program package*; Version 2.6. University of Bonn, 2008.

[27] Schafer, A.; Huber, C.; Ahlrichs, R. *J. Chem. Phys.* **1994**, *100*, 5829.

[28] Schafer, A.; Horn, H.; Ahlrichs, R. *J. Chem. Phys.* **1992**, *97*, 2571.

[29] Neese, F. *Inorg. Chim. Acta* **2002**, *337*, 181.

[30] Sinnecker, S.; Slep, L. D.; Bill, E.; Neese, F. *Inorg. Chem.* **2005**, *44*, 2245.

[31] Zhao, Y.; Schultz, N. E.; Truhlar, D. G. *J. Chem. Theory Comput.* **2006**, *2*, 364.

[32] Bader, R. F. W. *Atoms in Molecules: A Quantum Theory*; Clarendon Press, Oxford, 1990.

[33] Biegler-König, J., F.; Schönbohm *AIM2000, version 2.0*; Büro für Innovative Software: Bielefeld, Germany, 2002.

[34] Ditchfield, R. *Mol. Phys.* **1974**, *27*, 789.

[35] Wolinski, K.; Hinton, J. F.; Pulay, P. *J. Am. Chem. Soc.* **1990**, *112*, 8251.

[36] Vosko, S. H.; Wilk, L.; Nusair, M. *Can. J. Phys.* **1980**, *58*, 1200.

[37] Stephens, P. J.; Devlin, F. J.; Chabalowski, C. F.; Frisch, M. J. *J. Phys. Chem.* **1994**, *98*, 11623.

[38] Jensen, F. *J. Chem. Theory Comput.* **2008**, *4*, 719.

[39] Jiao, H.; Schleyer, P. R. *J. Phys. Org. Chem.* **1998**, *11*, 655.

[40] Schleyer, P. v. R.; Maerker, C.; Dransfeld, A.; Jiao, H.; Hommes, N. J. R. v. E. *J. Am. Chem. Soc.* **1996**, *118*, 6317.

[41] Beno, M. A.; Hope, H.; Olmstead, M. M.; Power, P. P. *Organometallics* **1985**, *4*, 2117.

[42] Lalancette, J.-M.; Rollin, G.; Dumas, P. *Can. J. Chem.* **1972**, *50*, 3058.

[43] Solari, E.; Musso, F.; Gallo, E.; Floriani, C.; Re, N.; Chiesi-Villa, A.; Rizzoli, C. *Organometallics* **1995**, *14*, 2265.

[44] Klose, A.; Solari, E.; Floriani, C.; Chiesivilla, A.; Rizzoli, C.; Re, N. *J. Am. Chem. Soc.* **1994**, *116*, 9123.

[45] Chatt, J.; Shaw, B. L. *J. Chem. Soc.* **1961**, 285.

[46] Seidel, W. *Z. Chem.* **1985**, *25*, 411.

[47] Klein, A. *Z. Anorg. Allg. Chem.* **2001**, *627*, 645.

[48] Seidel, W.; Burger, I. *Z. Anorg. Allg. Chem.* **1981**, *473*, 166.

[49] Gridnev, I. D.; Serafimov, J. M.; Quiney, H.; Brown, J. M. *Org. Biomol. Chem.* **2003**, *1*, 3811.

[50] Edema, J. J. H.; Gambarotta, S.; Vanbolhuis, F.; Smeets, W. J. J.; Spek, A. L.; Chiang, M. Y. *J. Organomet. Chem.* **1990**, *389*, 47–59.

# Appendix A

# X-ray Data Collection and Refinement Parameters

This appendix provides tabulated parameters from the collection and refinement of the crystal structures described in this thesis. Data is summarised using the notation: metal, bipyridine isomer, [bipyridine oxidation state]. For example, compound **8**: Cr(2,2´-bipy)$(mes)_2$, contains a neutral 2,2´-bipyridine ligand and would be written as "Cr 22 [0]" while its reduction product, compound **13**: [K(dibenzo-18-crown-6)][Cr(2,2´-bipy)$(mes)_2$], would be denoted "Cr 22 [–1]".

| Compound: | **1a** | **1b** | **2** | **3** | **4** | **5** |
|---|---|---|---|---|---|---|
| description | K 22 [–1] | K 22 [–1] | Rb 22 [–2] | K 24 [–1] | K 24 [–2] | Rb 24 [–1] |
| formula | $C_{12}H_{16}KN_4$ | $C_{48}H_{64}K_4N_{16}$ | $C_7H_{12}N_3Rb$ | $C_{12}H_{16}KN_4$ | $C_{27}H_{44}K_4N_{11}$ | $C_{27}H_{44}N_{11}Rb_4$ |
| crystal system | monoclinic | monoclinic | triclinic | orthorhombic | monoclinic | monoclinic |
| space group | $P2(1)/c$ | $P2(1)/c$ | $P\bar{1}$ | $P2(1)2(1)2(1)$ | $P2(1)/c$ | $P2(1)/c$ |
| $a$ / Å | 9.7584(2) | 14.7111(1) | 6.2046(3) | 6.9699(2) | 13.6287(1) | 14.0310(2) |
| $b$ / Å | 15.2777(4) | 18.6597(2) | 7.6321(3) | 9.3455(2) | 20.0334(3) | 20.3177(3) |
| $c$ / Å | 8.9523(2) | 21.5292(3) | 9.5740(5) | 19.0541(5) | 13.7395(2) | 13.5537(2) |
| $\alpha$ / degrees | 90.000 | 90.000 | 96.819(2) | 90.000 | 90.000 | 90.000 |
| $\beta$ / degrees | 104.000(1) | 118.910(1) | 99.593(2) | 90.000 | 118.718(1) | 117.447(1) |
| $\gamma$ / degrees | 90.000 | 90.000 | 104.053(2) | 90.000 | 90.000 | 90.000 |
| V / Å$^3$ | 1295.02(5) | 5173.4(1) | 427.60(4) | 1241.13(6) | 3289.86(7) | 3428.93(9) |
| $Z$ | 4 | 4 | 2 | 4 | 4 | 4 |
| radiation, $\lambda$ / Å | Mo K$\alpha$, 0.71073 | | | | | |
| $T$ / K | 200(2) | 150(2) | 150(2) | 150(2) | 150(2) | 150(2) |
| $\rho_{\mathrm{calcd}}$ / g cm$^{-3}$ | 1.310 | 1.312 | 1.737 | 1.367 | 1.371 | 1.675 |
| $\mu$ / mm$^{-1}$ | 0.394 | 0.395 | 5.728 | 0.411 | 0.578 | 5.711 |
| no. reflns collected | 4435 | 22852 | 3363 | 2811 | 14414 | 15302 |
| no. indep reflns | 2264 | 11654 | 1932 | 2811 | 7497 | 7795 |
| no. parameters | 162 | 613 | 117 | 155 | 403 | 403 |
| $R$(int) | 0.0164 | 0.0320 | 0.0420 | 0.0000 | 0.0303 | 0.0456 |
| R1/wR2, $I \geq 2\sigma_I$ / % | 4.24 / 11.38 | 4.00 / 9.25 | 3.98 / 10.22 | 4.00 / 9.70 | 4.02 / 9.55 | 3.92 / 9.30 |
| R1/wR2, all data / % | 5.15 / 12.12 | 7.54 / 10.43 | 4.16 / 10.41 | 4.70 / 10.25 | 6.52 / 10.66 | 5.65 / 10.08 |
| GOF | 1.058 | 1.028 | 1.029 | 1.098 | 1.049 | 1.025 |
| $A$ | 0.0708 | 0.0424 | 0.0603 | 0.0511 | 0.0493 | 0.0459 |
| $B$ | 0.5042 | 1.6659 | 0.3478 | 0.2496 | 1.3650 | 2.9749 |

Table A.1: X-ray data collection and refinement parameters for compounds **1a** to **5**. Description notation is explained at the start of this appendix. R1 $= \sum \mid\mid F_{\mathrm{O}} \mid - \mid F_{\mathrm{C}} \mid\mid / \sum \mid F_{\mathrm{O}} \mid$; wR2 $= \left\{ \sum w \left(F_{\mathrm{O}}^2 - F_{\mathrm{C}}^2\right)^2 / \sum w \left(F_{\mathrm{O}}^2\right)^2 \right\}^{1/2}$; $w = \left[\sigma^2 \left(F_{\mathrm{O}}\right)^2 + \left(AP\right)^2 + BP\right]^{-1}$ where $P = \left[\left(F_{\mathrm{O}}^2 - 2F_{\mathrm{C}}^2\right)/3\right]$ and the $A$ and $B$ values are as listed in the bottom two table rows.

| Compound: | **6a** | **6b** | **7a** | **7b** | **8** | **9** |
|---|---|---|---|---|---|---|
| description | Na 44 [–1] | Na 44 [–1] | Na 44 [–2] | Na 44 [–2] | Cr 22 [0] | Mn 22 [0] |
| formula | $C_{12}H_{16}N_4Na$ | $C_{24}H_{32}N_8Na_2$ | $C_7H_{12}N_3Na$ | $C_7H_{12}N_3Na$ | $C_{37}CrH_{39}N_2$ | $C_{28}H_{30}MnN_2$ |
| crystal system | monoclinic | monoclinic | orthorhombic | orthorhombic | monoclinic | monoclinic |
| space group | $C2/c$ | $P2(1)/c$ | $Pnma$ | $Cmca$ | $C2/c$ | $P2(1)/c$ |
| $a$ / Å | 13.4043(4) | 9.7528(1) | 15.1844(4) | 13.2652(7) | 27.8996(2) | 12.0845(5) |
| $b$ / Å | 9.7710(4) | 16.1943(2) | 13.0770(3) | 15.2401(8) | 13.1692(1) | 13.8358(6) |
| $c$ / Å | 10.3943(4) | 17.2751(3) | 8.3457(2) | 8.3637(5) | 18.3471(2) | 14.8944(6) |
| $\alpha$ / degrees | 90.000 | 90.000 | 90.000 | 90.000 | 90.000 | 90.000 |
| $\beta$ / degrees | 109.618(2) | 104.7626(6) | 90.000 | 90.000 | 110.830(1) | 102.445(2) |
| $\gamma$ / degrees | 90.000 | 90.000 | 90.000 | 90.000 | 90.000 | 90.000 |
| V / Å$^3$ | 1282.35(8) | 2638.63(6) | 1657.18(7) | 1690.8(2) | 6300.4(1) | 2431.8(2) |
| $Z$ | 4 | 4 | 8 | 8 | 8 | 4 |
| radiation, $\lambda$ / Å | Mo K$\alpha$, 0.71073 | | | | | |
| $T$ / K | 150(2) | 150(2) | 150(2) | 250(2) | 150(2) | 150(2) |
| $\rho_{\mathrm{calcd}}$ / g cm$^{-3}$ | 1.239 | 1.205 | 1.292 | 1.266 | 1.189 | 1.228 |
| $\mu$ / mm$^{-1}$ | 0.107 | 0.104 | 0.127 | 0.124 | 0.390 | 0.559 |
| no. reflns collected | 2814 | 11795 | 3550 | 1385 | 13529 | 7742 |
| no. indep reflns | 1464 | 6016 | 1945 | 766 | 7151 | 4207 |
| no. parameters | 78 | 358 | 109 | 55 | 387 | 280 |
| $R$(int) | 0.0280 | 0.0198 | 0.0159 | 0.0240 | 0.0226 | 0.0513 |
| R1/wR2, $I \geq 2\sigma_I$ / % | 4.29 / 10.75 | 4.36 / 11.30 | 4.29 / 11.66 | 6.88 / 19.53 | 4.68 / 12.53 | 5.16 / 13.20 |
| R1/wR2, all data / % | 6.80 / 11.91 | 6.11 / 12.40 | 5.69 / 12.74 | 8.74 / 20.74 | 5.85 / 13.46 | 7.40 / 14.34 |
| GOF | 1.016 | 1.024 | 1.061 | 1.086 | 1.037 | 1.032 |
| $A$ | 0.0603 | 0.0639 | 0.0673 | 0.1091 | 0.0711 | 0.0731 |
| $B$ | 0.3808 | 0.6408 | 0.6642 | 2.5572 | 3.8200 | 0.9199 |

Table A.2: X-ray data collection and refinement parameters for compounds **6a** to **9**. Description notation is explained at the start of this appendix. R1 $= \sum \mid\mid F_{\mathrm{O}} \mid - \mid F_{\mathrm{C}} \mid\mid / \sum \mid F_{\mathrm{O}} \mid$; wR2 $= \left\{ \sum w \left(F_{\mathrm{O}}^2 - F_{\mathrm{C}}^2\right)^2 / \sum w \left(F_{\mathrm{O}}^2\right)^2 \right\}^{1/2}$; $w = \left[\sigma^2 \left(F_{\mathrm{O}}\right)^2 + (AP)^2 + BP\right]^{-1}$ where $P = \left[\left(F_{\mathrm{O}}^2 - 2F_{\mathrm{C}}^2\right)/3\right]$ and the $A$ and $B$ values are as listed in the bottom two table rows.

| Compound: | **10** | **11** | **11 (RT)** | **12** | **13** | **14a** |
|---|---|---|---|---|---|---|
| description | Fe 22 [0] | Co 22 [0] | Co 22 [0] | Ni 22 [0] | Cr 22 [–1] | Mn 22 [–1] |
| formula | $C_{28}FeH_{30}N_2$ | $C_{32}CoH_{38}N_2O$ | $C_{32}CoH_{38}N_2O$ | $C_{28}H_{30}N_2Ni$ | $C_{60}CrH_{78}KN_2O_9$ | $C_{48}H_{70}KMnN_2O_8$ |
| crystal system | monoclinic | orthorhombic | orthorhombic | monoclinic | monoclinic | orthorhombic |
| space group | $P2(1)/c$ | $Pccn$ | $Pccn$ | $P2(1)/c$ | $P2(1)/c$ | $Fdd2$ |
| $a$ / Å | 11.9696(2) | 10.7358(1) | 11.4458(2) | 8.2789(1) | 14.2207(2) | 13.0840(2) |
| $b$ / Å | 13.7989(3) | 14.5102(1) | 14.2281(3) | 18.1865(2) | 13.7416(2) | 32.1910(4) |
| $c$ / Å | 14.9180(3) | 17.9942(1) | 18.1595(4) | 16.2600(2) | 29.9804(5) | 23.1510(3) |
| $\alpha$ / degrees | 90.000 | 90.000 | 90.000 | 90.000 | 90.000 | 90.000 |
| $\beta$ / degrees | 103.067(1) | 90.000 | 90.000 | 112.162(1) | 107.561(1) | 90.000 |
| $\gamma$ / degrees | 90.000 | 90.000 | 90.000 | 90.000 | 90.000 | 90.000 |
| V / Å$^3$ | 2400.16(8) | 2803.11(4) | 2957.3(1) | 2267.30(5) | 5585.6(2) | 9750.9(2) |
| $Z$ | 4 | 4 | 4 | 4 | 4 | 8 |
| radiation, $\lambda$ / Å | Mo K$\alpha$, 0.71073 | | | | | synchrotron, 0.68890 |
| $T$ / K | 150(2) | 150(2) | 293(2) | 150(2) | 150(2) | 150(2) |
| $\rho_{\mathrm{calcd}}$ / g cm$^{-3}$ | 1.246 | 1.245 | 1.180 | 1.328 | 1.263 | 1.222 |
| $\mu$ / mm$^{-1}$ | 0.645 | 0.638 | 0.605 | 0.873 | 0.337 | 0.407 |
| no. reflns collected | 10653 | 3192 | 4821 | 10116 | 18045 | 10294 |
| no. indep reflns | 5454 | 3192 | 2573 | 5153 | 9745 | 4039 |
| no. parameters | 280 | 174 | 155 | 280 | 695 | 300 |
| $R$(int) | 0.0302 | 0.0000 | 0.0198 | 0.0247 | 0.0399 | 0.0630 |
| R1/wR2, $I \geq 2\sigma_I$ / % | 4.10 / 10.14 | 4.37 / 12.50 | 5.66 / 16.68 | 3.88 / 9.16 | 5.04 / 11.28 | 4.32 / 10.89 |
| R1/wR2, all data / % | 6.36 / 11.30 | 5.04 / 13.16 | 6.79 / 17.66 | 5.49 / 9.95 | 8.89 / 12.46 | 5.06 / 11.56 |
| GOF | 1.040 | 1.064 | 1.050 | 1.055 | 0.996 | 1.060 |
| $A$ | 0.0580 | 0.0762 | 0.1171 | 0.0451 | 0.0556 | 0.0623 |
| $B$ | 0.6313 | 2.0748 | 0.2832 | 1.4576 | 2.9633 | 3.6430 |

Table A.3: X-ray data collection and refinement parameters for compounds **10** to **14a**. Description notation is explained at the start of this appendix. R1 $= \sum \mid\mid F_{\mathrm{O}} \mid - \mid F_{\mathrm{C}} \mid\mid / \sum \mid F_{\mathrm{O}} \mid$; wR2 $= \left\{ \sum w \left(F_{\mathrm{O}}^2 - F_{\mathrm{C}}^2\right)^2 / \sum w \left(F_{\mathrm{O}}^2\right)^2 \right\}^{1/2}$; $w = \left[\sigma^2 \left(F_{\mathrm{O}}\right)^2 + \left(AP\right)^2 + BP\right]^{-1}$ where $P = \left[\left(F_{\mathrm{O}}^2 - 2F_{\mathrm{C}}^2\right)/3\right]$ and the $A$ and $B$ values are as listed in the bottom two table rows.

| Compound: | **14b** | **15** | **16** | **17** | **18** |
|---|---|---|---|---|---|
| description | Mn 22 [–1] | Fe 22 [–1] | Co 22 [–1] | Ni 22 [–1] | $[Fe(mes)_3]^-$ |
| formula | $C_{48}H_{62.67}KMnN_{2.67}O_6$ | $C_{46}FeH_{66}KN_4O_6$ | $C_{46}CoH_{66}KN_4O_6$ | $C_{46}H_{66}KN_4NiO_6$ | $C_{51}FeH_{81}KN_2O_6$ |
| crystal system | monoclinic | orthorhombic | tetragonal | tetragonal | monoclinic |
| space group | $C2/c$ | $P2(1)2(1)2(1)$ | $P4(1)2(1)2$ | $P4(3)2(1)2$ | $C2/c$ |
| $a$ / Å | 13.3060(1) | 13.9644(1) | 12.8822(1) | 12.9305(2) | 24.2771(2) |
| $b$ / Å | 24.1421(2) | 14.5989(1) | 12.8822(1) | 12.9305(2) | 14.9508(1) |
| $c$ / Å | 43.8747(4) | 22.6777(2) | 27.3451(2) | 27.1526(8) | 28.5112(3) |
| $\alpha$ / degrees | 90.000 | 90.000 | 90.000 | 90.000 | 90.000 |
| $\beta$ / degrees | 94.833(1) | 90.000 | 90.000 | 90.000 | 97.664(1) |
| $\gamma$ / degrees | 90.000 | 90.000 | 90.000 | 90.000 | 90.000 |
| V / Å$^3$ | 14044.0(2) | 4623.19(6) | 4537.95(6) | 4539.9(2) | 10256.0(2) |
| $Z$ | 12 | 4 | 4 | 4 | 8 |
| radiation, $\lambda$ / Å | Mo K$\alpha$, 0.71073 | | | | |
| $T$ / K | 150(2) | 150(2) | 150(2) | 150(2) | 150(2) |
| $\rho_{calcd}$ / g cm$^{-3}$ | 1.230 | 1.244 | 1.272 | 1.271 | 1.183 |
| $\mu$ / mm$^{-1}$ | 0.419 | 0.466 | 0.520 | 0.569 | 0.422 |
| no. reflns collected | 20840 | 10530 | 10324 | 10334 | 17228 |
| no. indep reflns | 12268 | 10530 | 5171 | 5176 | 8901 |
| no. parameters | 794 | 523 | 263 | 263 | 564 |
| $R$(int) | 0.0246 | 0.053 | 0.0158 | 0.0228 | 0.0276 |
| R1/wR2, $I \geq 2\sigma_I$ / % | 4.44 / 9.31 | 3.00 / 6.67 | 2.81 / 7.18 | 3.38 / 7.98 | 5.53 / 14.80 |
| R1/wR2, all data / % | 7.52 / 10.40 | 3.77 / 7.03 | 3.29 / 7.38 | 4.23 / 8.39 | 6.88 / 15.52 |
| GOF | 1.017 | 1.043 | 1.025 | 1.027 | 1.042 |
| $A$ | 0.0387 | 0.0339 | 0.0427 | 0.0431 | 0.0775 |
| $B$ | 12.9335 | 0.9985 | 0.7856 | 0.9940 | 11.7064 |

Table A.4: X-ray data collection and refinement parameters for compounds **14b** to **18**. Description notation is explained at the start of this appendix. R1 $= \sum \mid\mid F_O \mid - \mid F_C \mid\mid / \sum \mid F_O \mid$; wR2 $= \left\{ \sum w \left(F_O^2 - F_C^2\right)^2 / \sum w \left(F_O^2\right)^2 \right\}^{1/2}$; $w = \left[\sigma^2 \left(F_O\right)^2 + \left(AP\right)^2 + BP\right]^{-1}$ where $P = \left[\left(F_O^2 - 2F_C^2\right)/3\right]$ and the $A$ and $B$ values are as listed in the bottom two table rows.

| Compound: | **19** | **20a** | **20b** | **21** | **22** |
|---|---|---|---|---|---|
| description | Zn 44 [0] | Zn 44 [–1] | Zn 44 [–1] | Zn 44 [–2] | $[Zn(mes)_3]^-$ |
| formula | $C_{46}H_{52}N_2Zn_2$ | $C_{66}H_{92}KN_2O_8Zn_2$ | $C_{66}H_{92}KN_2O_8Zn_2$ | $C_{70}H_{100}K_2N_2O_{12}Zn_2$ | $C_{43}H_{65}KO_7Zn$ |
| crystal system | triclinic | triclinic | triclinic | monoclinic | orthorhombic |
| space group | $P\bar{1}$ | $P\bar{1}$ | $P\bar{1}$ | $P2(1)/c$ | $Pbcn$ |
| $a$ / Å | 11.3857(1) | 19.7748(3) | 20.6965(1) | 11.7304(2) | 33.6475(2) |
| $b$ / Å | 19.2169(2) | 20.6378(3) | 20.8215(1) | 13.8528(2) | 10.7686(1) |
| $c$ / Å | 19.5817(2) | 21.1360(3) | 27.0298(1) | 22.4989(4) | 24.2059(1) |
| $\alpha$ / degrees | 83.461(1) | 118.439(1) | 76.111(1) | 90.000 | 90.000 |
| $\beta$ / degrees | 80.452(1) | 109.127(1) | 81.897(1) | 92.474(1) | 90.000 |
| $\gamma$ / degrees | 73.809(1) | 98.547(1) | 61.729(1) | 90.000 | 90.000 |
| V / Å$^3$ | 4047.15(7) | 6666.9(2) | 9953.6(1) | 3652.6(1) | 8770.7(1) |
| $Z$ | 4 | 4 | 6 | 2 | 8 |
| radiation, $\lambda$ / Å | Mo K$\alpha$, 0.71073 | | | | |
| $T$ / K | 150(2) | 150(2) | 150(2) | 150(2) | 150(2) |
| $\rho_{\mathrm{calcd}}$ / g cm$^{-3}$ | 1.253 | 1.207 | 1.212 | 1.246 | 1.209 |
| $\mu$ / mm$^{-1}$ | 1.218 | 0.833 | 0.837 | 0.828 | 0.700 |
| no. reflns collected | 35531 | 41137 | 89021 | 15136 | 19056 |
| no. indep reflns | 18473 | 23111 | 45306 | 8264 | 9975 |
| no. parameters | 901 | 1436 | 2134 | 554 | 488 |
| $R$(int) | 0.0286 | 0.0403 | 0.0261 | 0.0329 | 0.0250 |
| R1/wR2, $I \geq 2\sigma_I$ / % | 3.88 / 9.62 | 4.78 / 12.41 | 4.71 / 11.66 | 4.54 / 9.98 | 4.07 / 10.37 |
| R1/wR2, all data / % | 5.51 / 10.45 | 7.04 / 13.61 | 7.08 / 13.09 | 7.85 / 11.25 | 6.45 / 11.37 |
| GOF | 1.017 | 1.051 | 1.034 | 1.012 | 1.039 |
| $A$ | 0.0505 | 0.0674 | 0.0588 | 0.0476 | 0.0551 |
| $B$ | 1.6179 | 1.6237 | 6.4038 | 1.9513 | 4.6690 |

Table A.5: X-ray data collection and refinement parameters for compounds **19** to **22**. Description notation is explained at the start of this appendix. R1 $= \sum \mid\mid F_{\mathrm{O}} \mid - \mid F_{\mathrm{C}} \mid\mid / \sum \mid F_{\mathrm{O}} \mid$; wR2 $= \left\{ \sum w \left(F_{\mathrm{O}}^2 - F_{\mathrm{C}}^2\right)^2 / \sum w \left(F_{\mathrm{O}}^2\right)^2 \right\}^{1/2}$; $w = \left[\sigma^2 \left(F_{\mathrm{O}}\right)^2 + (AP)^2 + BP\right]^{-1}$ where $P = \left[\left(F_{\mathrm{O}}^2 - 2F_{\mathrm{C}}^2\right)/3\right]$ and the $A$ and $B$ values are as listed in the bottom two table rows.

# Appendix B

# List of Publications

Publications of research described in this thesis:

- "Synthesis and Characterization of the 4,4´-Bipyridyl Dianion and Radical Monoanion. A Structural Study." Denning, M. S.; Irwin, M.; Goicoechea, J. M. *Inorg. Chem.* **2008**, *47*, 6118.
- "Synthesis and Characterization of Alkali-Metal Salts of 2,2´- and 2,4´-Bipyridyl Radicals and Dianions." Gore-Randall, E.; Irwin, M.; Denning, M. S.; Goicoechea, J. M. *Inorg. Chem.* **2009**, *48*, 8304.
- "Experimental and Computational Study of the Structural and Electronic Properties of $Fe^{II}$(2,2´-bipyridine)$(mes)_2$ and [$Fe^{II}$(2,2´-bipyridine)$(mes)_2$]$^{-}$, a Complex Containing a 2,2´-Bipyridyl Radical Anion." Irwin, M.; Jenkins, R. K.; Denning, M. S.; Kramer, T.; Grandjean, F.; Long, G. J.; Herchel, R.; McGrady, J. E.; Goicoechea, J. M. *Inorg. Chem.* **2010**, *49*, 6160.
- "On the Structural and Electronic Properties of [$Zn_2$(4,4´-bipyridine)$(mes)_4$]n– (n = 0 – 2), a Homologous Series of Bimetallic Complexes Bridged by Neutral, Anionic, and Dianionic 4,4´-Bipyridine." Irwin, M.; Kraemer, T.; McGrady, J. E.; Goicoechea, J. M. *Inorg. Chem.* **2011**, *50*, 5006.
- "A Homologous Series of First-Row Transition-Metal Complexes of 2,2´-Bipyridine and their Ligand Radical Derivatives: Trends in Structure, Magnetism, and Bonding." Irwin, M.; Doyle, L. R.; Krämer, T.; Herchel, R.; McGrady, J. E.; Goicoechea, J. M. *Inorg. Chem.* **2012**, *51*, 12301.

Additional publications:

- "Covalency in the 4f Shell of tris-Cyclopentadienyl Ytterbium ($YbCp_3$) – A Spectroscopic Evaluation." Denning, R. G.; Harmer, J.; Green, J. C.; Irwin, M. *J. Am. Chem. Soc.* **2011** *133* 20644.
- "Transition Metal Complexes of Anionic N-Heterocyclic Dicarbene Ligands." Musgrave, R. A.; Turbervill, R. S. P.; Irwin, M.; Goicoechea, J. M. *Angew. Chem., Int. Ed.* **2012**, *51*, 10832.

# Appendix C

# Posters Presented at Conferences

High resolution copies of posters are included on the cd accompanying this thesis.

# Synthesis and Characterization of Highly Reduced Hetero-Aromatic Ligand Systems

Mark Irwin, Edward Gore-Randall, Rhiannon Jenkins, Mark S. Denning and Jose M. Goicoechea*

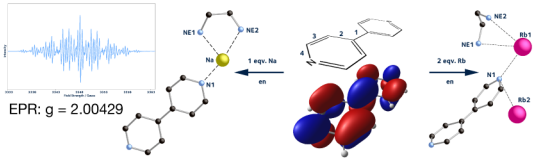
*Department of Chemistry, Chemistry Research Laboratory, University of Oxford, Mansfield Road, Oxford OX1 3TA, U.K.*

## 1. Introduction

The reduction of hetero-aromatic systems by alkali metals causes changes in bond lengths and influences electronic and bonding properties. This research aims to structurally characterize these reduced systems and to explore their interactions in coordination complexes and polymers.

## 2. Reduction of 4,4' -Bipyridine

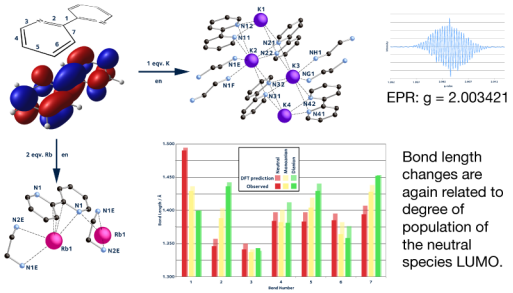
Addition of one equivalent of alkali metal to ethylenediamine (en) solutions of 4,4' -bipyridine (4,4' -bipy) forms an intense dark blue colour which yielded crystallized samples of $(M^{+})(4,4'\text{-bipy}^{-})(en)_x$ {M = Na, K, Rb, Cs; x = 0, 1}. Radical presence was confirmed by EPR. Reaction of two equivalents of alkali metal yielded crystals of $(M^{+})_2(4,4'\text{-bipy}^{2-})(en)_x$ {M = Na, Rb; x = 1, 2}.[1]




DFT calculations show the neutral species LUMO to contain bonding and anti-bonding components. As this orbital is incrementally populated, bonding areas cause shorter bonds and anti-bonding areas longer bonds, with bond 1 showing the greatest change.

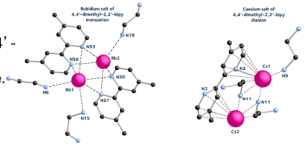
## 3. Reduction of 2,2'-bipyridine

Crystal structures of alkali metal salts of the singly and doubly reduced forms of 2,2'-bipyridine (2,2'-bipy) show a similar trend in bond lengths.[2]



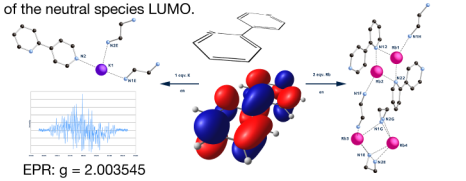

Bond length changes are again related to degree of population of the neutral species LUMO.

Two substituted forms were similarly reduced and are structurally characterised: 4,4' -dimethyl-2,2' -bipyridine and 5,5' -dimethyl-2,2' -bipyridine. Trends in bond lengths are similar to the unsubstituted species.

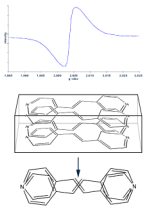


## 4. Reduction of 2,4'-bipyridine and trans-1,2'-bis(4-pyridyl) ethylene

Analogous reactions were performed with 2,4'-bipyridine (2,4'-bipy) and trans-1,2'-bis(4-pyridyl) ethylene (BPE). The bond lengths of the reduced forms of 2,4-bipy are again explained in terms of population of the neutral species LUMO.

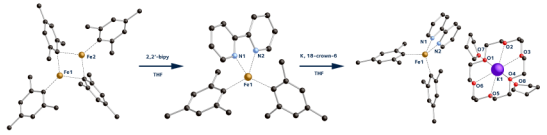



Despite unsuccessful attempts to form a BPE radial anion, dianionic salts of BPE have been found, all having a lustrous gold colour. SQUID and EPR experiments show these systems are metallic, with g = 2.003753 and a temperature independent positive molar susceptibility of 2.374´10-5 emu/mol after diamagnetic corrections. Disorder in the ligand has prevented a complete bond metric analysis, but the alkene bond appears to show greatest change. Due to an antibonding interaction in the neutral species LUMO, this bond elongates from 1.303(av) Å in the neutral species to 1434(10) Å in the dianion.

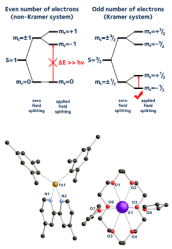


## 5. Reactions with $Fe_2(Mes)_4$

Tetrahydrofuran (THF) solutions of $Fe_2Mes_4$,[3] and 2,2'-bipy yielded crystals of $Fe(Mes)_2$2,2'-bipy that were isolated and subsequently reduced by K in the presence of 18-crown-6 to give $[K(18\text{-crown-6})(THF)_2]^{+}$ $[Fe(Mes)_2(2,2'\text{-bipy})]^{-}$.



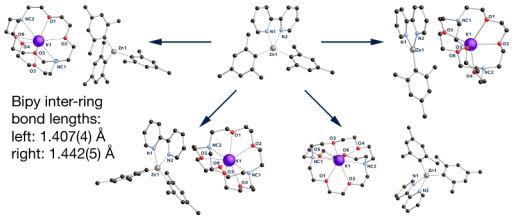

The 2,2' -bipy inter-ring distance shortens from 1.482(3) Å to 1.418(3) Å upon reduction, a value that is typical of the radical anions previously isolated. While Raman peaks also suggest radical presence, EPR experiments have been unable to prove this as this is a non-Kramers (even electron) system. Additionally, traces of a magnetic impurity not present in the neutral precursor, give unphysical $m_{eff}$ values despite repeated recrystallisations. Complexes of the earlier mentioned dimethylated forms of 2,2' -bipy were also synthesised to attempt to work round this problem.




To accurately determine the Fe oxidation state, samples are currently being prepared for Mössbauer spectroscopy.

## 6. Reactions with $Zn(Mes)_2$

$Zn(Mes)_2$(2,2'-bipy) was successfully crystallized as previously reported in the literature.[4] Subsequent reduction with K and 2,2,2-crypt gave rise to four novel products at once:



Bipy inter-ring bond lengths:
left: 1.407(4) Å
right: 1.442(5) Å

While the lower-left product inter-ring bond length is typical of a radical anion form of 2,2' -bipy, the lower-right product is midway between expected values for the neutral and radical species. The mixture of crystal products prevented immediate further characterisation but it is hoped the subtly different electronic properties of the dimethyl bipy analogues will favour formation of one structure above the other. To this end both the 4,4' -dimethyl- and 5,5' -dimethyl- 2,2' -bipy neutral species complexes have been synthesised and their reduction products are currently being researched.

## 7. Conclusions

Highly reducing forms of bipyridine and related ligands have been characterized both in alkali metal salts and in novel transition metal complexes. In addition to the work presented here, IR and Raman measurements have been made on all compounds, yielding diagnostic peaks for each level of reduction. It is hoped that this work will aid electronic assignments in future, more exotic coordination complexes and polymers.

## 8. Acknowledgements

We thank the EPSRC (EP/F00186X/1, PDRA MSD), the University of Oxford (studentship MI) and the Royal Society of Chemistry for financial support of this research. We also thank Stephen Boyer (London Metropolitan University) for elemental analyses and the University of Oxford for access to the CAESR, SQUID and Chemical Crystallography facilities.

EPSRC Engineering and Physical Sciences Research Council

RSC Advancing the Chemical Sciences

CÆSR Centre for Advanced Electron Spin Resonance, University of Oxford

## 9. References

1) Denning, M. S.; Irwin, M; Goicoechea, J. M. *Inorg. Chem.* **2008**, 47, 14, 6118-6120
2) Gore-Randall, E.; Irwin, M.; Denning, M. S.; Goicoechea, J. M. *Inorg. Chem.* **2009**, 48, 17, 8304-8316
3) Floriani, C. *et al. J. Am. Chem. Soc.* **1994**, 116, 20, 9123-9135
4) Seidel, W.; Burger, I. *Z. Anorg. Allg. Chem.* **1981**, 473, 2, 166-170

# Synthesis and Characterisation of Highly Reduced Hetero-Aromatic Ligand Systems

E. Gore-Randall,[1] R. Jenkins,[1] T. Krämer,[1] M. S. Denning,[1] F. Grandjean,[2] J. E. McGrady,[1] G. J. Long,[3]
R. Herchel,[4] J. M. Goicoechea,[1] and **Mark Irwin**[1]

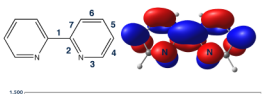
[1]*Department of Chemistry, Chemistry Research Laboratory, University of Oxford, Mansfield Road, Oxford OX1 3TA, U.K.*
[2]*Department of Physics, B5, University of Liège, B-4000, Sart-Tilman, Belgium*
[3]*Department of Chemistry, Missouri University of Science and Technology, University of Missouri, Rolla, Missouri, 65409-0010*
[4]*Department of Inorganic Chemistry, Faculty of Science, Palacký University, tr. 17. Listopadu 12, 77146 Olomouc, Czech Republic*

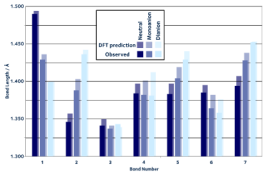
## 1. Introduction

Reduction of hetero-aromatic systems causes changes to their electronic and bonding properties. Crystalline samples containing alkali-metal salts of both singly and doubly reduced 2,2'- and 4,4'-bipyridine were synthesised.[1,2] DFT calculated LUMOs help rationalise observed trends in bond metrics. Upon population of the LUMO, the largest changes occur to the inter-ring bond in both cases. The changes in bond order due to population of this orbital are also visible in shifts of IR and Raman absorption peak positions. EPR studies have been used to confirm the presence of radical anionic species.

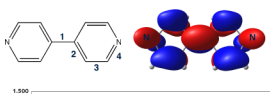
Together, these provide a set of diagnostic parameters that can be used to aid determination of charges in complexes incorporating these ligands where multiple valance tautomers could be hypothesised.

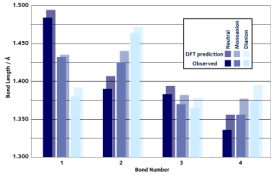
2,2'-bipyridine bonding:





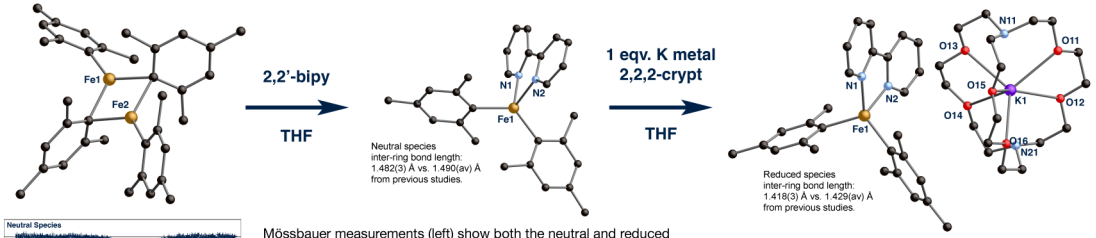

4,4'-bipyridine bonding:

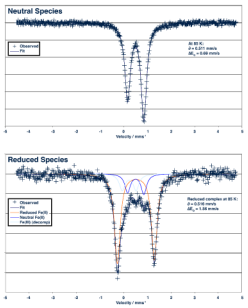





## 2. Fe(22bipy)(mes)$_2$ Systems: Non-innocent ligands

The reaction pathway below yielded crystals of a Fe complex with bond metric data indicative of substantial population of the bipy π* orbital.[3] This could be either an Fe(I) system with extensive π*-backbonding to a formally neutral ligand or, alternatively, a Fe(II) ion and a 'non-innocent' radical bipy ligand. Extensive studies strongly suggest that the latter is correct, making this the first structurally and electronically characterised example of a radical bipy ligand in a transition metal complex.

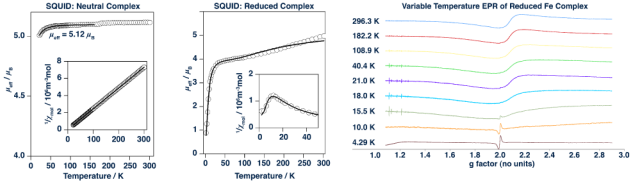



Mössbauer measurements (left) show both the neutral and reduced species contain tetrahedral Fe(II) sites and no Fe(I) sites are present. The reduced system contains a small Fe(III) contribution, attributed to slight decomposition while loading the highly air- and moisture-sensitive sample. Data shown was collected at 85 K.

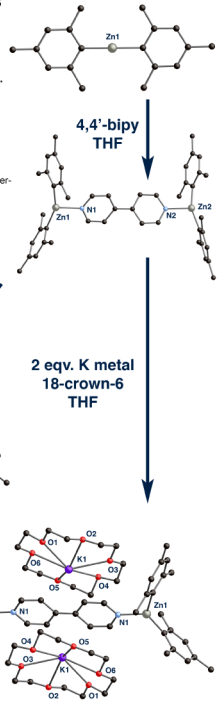
EPR experiments predictably show the neutral species has no signal since Fe(II) is a non-Kramer's (S = 2) ion. However variable temperature measurements (below) of a solid sample of the reduced complex show a resonance at room temperature (g = 2.086) which sharpens below 20 K (g = 1.994).

SQUID magnetometry (right) of the neutral species reveals a paramagnetic high-spin Fe(II) site exhibiting typical Curie-Weiss behaviour. The reduced species shows strong intramolecular antiferromagnetic coupling (S = $^3/_2$) between 30 and 100 K with deviations at higher temperatures due to population of a low-lying sextet state.




## 3. (Zn(mes)$_2$)$_2$(44bipy) Systems

Similar systems have recently been synthesised by the reaction of Zn(mes)$_2$ with 4,4'-bipyridine and subsequent reduction of the products. Variation in bond metrics provides early evidence of the formation of singly and doubly reduced bipyridyl anions. Isolation of a pure sample of the monoanionic ligand without impurities of either the neutral or dianionic forms has proved challenging and characterisation of these species is the subject ongoing investigation.




## 4. References and Acknowledgements

1) Denning, M. S. *et al. Inorg. Chem.* **2008**, 47, 6118.
2) Gore-Randall, E. *et al. Inorg. Chem.* **2009**, 48, 8304.
3) Irwin, M. *et al. Inorg. Chem.* **2010**, Awaiting publication.

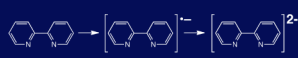
We thank the University of Oxford, the EPSRC (EP/F00186X/1, EP/G002789/2), the RSC, and the FNRS (9.456595, 1.5.064.05) for financial support of this research. We also thank the Oxford Crystallographic Service, the Oxford Supercomputing Centre, and CAESR for access to instrumentation and Prof. R. Cloots and Mr. G. Toussaint for the use of their dry box at the University of Liège.

# Synthesis and Characterisation of Metal Complexes of Highly Reduced Heteroaromatic Ligand Systems

Mark R. F. Irwin, Laurence R. Doyle, Rhiannon K. Jenkins, Tobias Krämer, John. E. McGrady, and Jose. M. Goicoechea
*Department of Chemistry, Chemistry Research Laboratory, University of Oxford, Mansfield Road, Oxford OX1 3TA, U.K.*

## INTRODUCTION

Over 50 years ago it was discovered that the *in situ* reduction of pyridine with alkali metals gave rise to intensely coloured solutions containing bipyridyl radicals. Cyclic voltammetry measurements revealed two accessible reduced states of both the 2,2'- and 4,4'-bipyridine isomers; the radical monoanions and dianions. Until recently, these systems had been characterised by in *situ IR*, Raman and UV-Vis measurements, with minimal structural data reported.

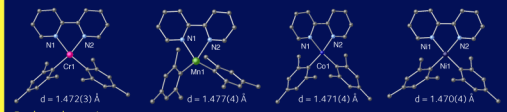


Crystalline samples containing alkali metal salts of both singly and doubly reduced 2,2'- and 4,4'-bipy have been synthesised.[1,2] DFT calculated LUMOs help rationalise variations in bond metrics upon reduction. More recently, transition metal complexes containing these reduced ligands have been synthesised; the exact electronic configurations of which are far less easily determined.

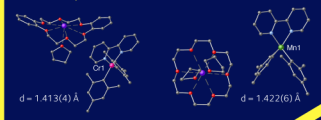
The Fe complex we describe here exhibits this intriguing behaviour.[3] $^{57}$Fe-Mössbauer shows the reduced complex contains Fe(II) meaning the metal is not reduced, while SQUID measurements suggest a temperature dependant mixing of $^3/_2$ and $^5/_2$ spin states.

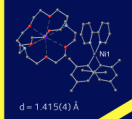
More recently, analogous Cr, Mn, Co and Ni neutral complexes and Cr, Mn and Ni reduced complexes have been isolated and crystallographically characterised. Investigations into their electronic structures are ongoing. Inter-ring bond distances are given below:

Neutral species:



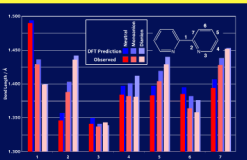

Reduced species:

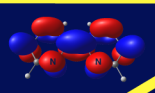


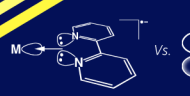

## COMPLEXES OF 2,2'-BIPYRIDINE: NON-INNOCENT LIGANDS

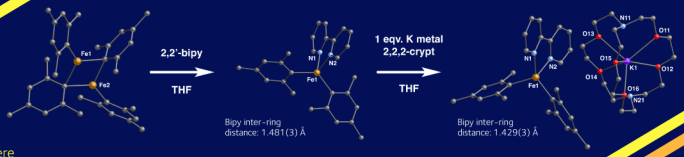
Bond metrics from alkali metal salts show systematic trends in bond lengths with bipy oxidation state (left). The diagnostic inter-ring bond contracts from 1.490(av) Å to 1.429(av) Å to 1.399(av) Å upon stepwise electron addition...

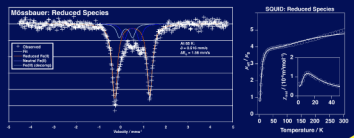




...but these changes in transition metal complexes may be caused by *either* ligand reduction, *or* by reduction of the metal and subsequent π-back bonding.

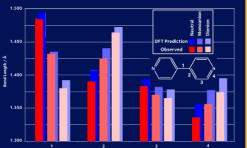


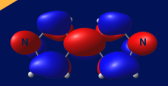


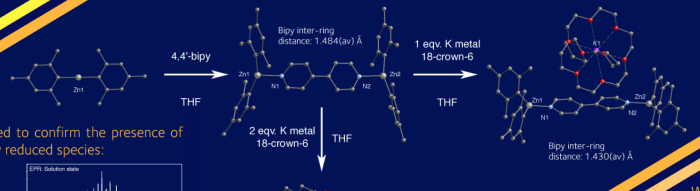

## COMPLEXES OF 4,4'-BIPYRIDINE

A similar trend is observed for 4,4'-bipy, where the inter-ring bond again shows the largest changes, from 1.484(av) Å to 1.432(av) Å to 1.380(av) Å upon each reduction.

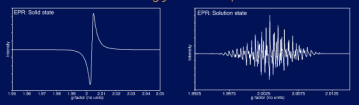




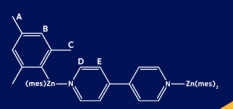
Analogous reactions to those with 2,2'-bipy have yielded three crystallographically characterised isostructural compounds of general formula $[[Zn(mes)_2]_2(4,4'\text{-bipy})]^{n-}$ (n = 0-2).[4]

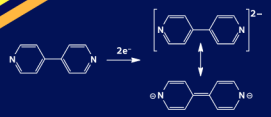


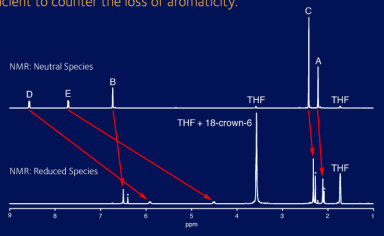

EPR has been used to confirm the presence of the radical in the singly reduced species:




$^1$H NMR studies of the neutral and doubly reduced species show the most striking result of the reductions, with chemical shift changes of 3 ppm for the bipy protons. The changes can be rationalised using the resonance canonical below, where the additional electrons lie as far apart as possible, on the most electronegative atoms, the benefit of which must be sufficient to counter the loss of aromaticity.






## ACKNOWLEDGEMENTS AND REFERENCES

We would like to thank the University of Oxford (studentship MI), the EPSRC (EP/G002789/2), and the RSC for financial support of this research. We thank the Oxford Supercomputing Centre and CAESR for access to instrumentation and the University of Oxford for access to Chemical Crystallography facilities.

1) Denning, M. S.; Irwin, M.; Goicoechea, J. M., *Inorg. Chem.* **2008**, *47*, 6118.
2) Gore-Randall, E.; Irwin, M.; Denning, M. S.; Goicoechea, J. M., *Inorg. Chem.* **2009**, *48*, 8304.
3) Irwin, M.; Jenkins, R. K.; Denning, M. S.; Krämer, T.; Grandjean, F.; Long, G. J.; Herchel, R.; McGrady, J. E.; Goicoechea, J. M., *Inorg. Chem.* **2010**, *49*, 6160.
4) Irwin, M.; Krämer, T.; McGrady, J. E.; Goicoechea, J. M., *Inorg. Chem.* **2011**, *50*, 5006.

EPSRC Engineering and Physical Sciences Research Council · RSC Advancing the Chemical Sciences · CAESR Centre for Advanced Electron Spin Resonance · OSC Oxford Supercomputing Centre

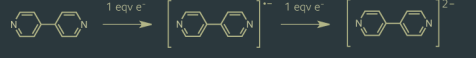
# IS BIPYRIDINE ALWAYS AS INNOCENT AS IT APPEARS?

Mark R. F. Irwin, Laurence R. Doyle, Rhiannon K. Jenkins, Tobias Krämer,
John E. McGrady, and Jose M. Goicoechea

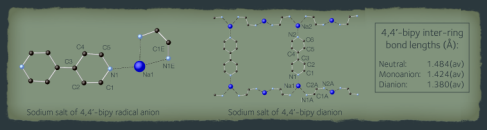
*Department of Chemistry, Chemistry Research Laboratory, University of Oxford, Mansfield Road, Oxford, OX1 3TA*

## INTRODUCTION

When a metal, capable of exhibiting multiple oxidation states, is complexed to a ligand that may also exhibit multiple oxidation states, precise determination of electronic structure is often challenging. In such situations, the ligand is deemed to be 'non-innocent'. Many examples of these ligands exist in both inorganic and biological chemistry. Here we consider the non-innocent properties of bipyridine.

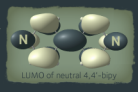



Bipy isomers may be reduced by sodium to form radical anions and dianions. In these alkali metal salts there is no ambiguity in oxidation state of the bipy moiety.

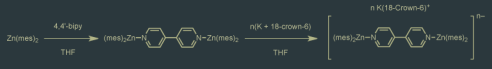



While many *in situ* measurements have been reported in the literature, little structural information about these species existed prior to this investigation.[1,2]

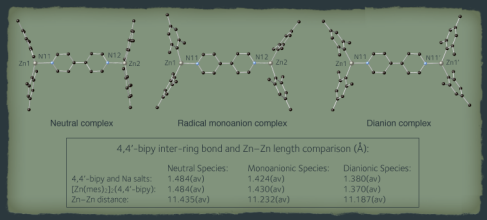
Statistically significant changes in bipy inter-ring bond lengths are observed upon step-wise reduction. This may be rationalised by examining the neutral species LUMO. The single lobe across the inter-ring bond implies a local bonding interaction, increased bond order and hence a decrease in bond length upon reduction. The converse argument is made for the immediately adjacent bonds where the presence of a node causes an anti-bonding interaction and thus shortening of the bonds.



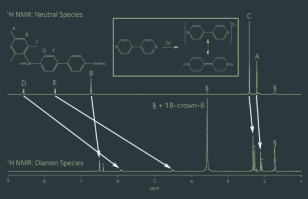

## 4,4'-BIPYRIDINE COMPLEXES




The above synthetic route (n = 0 – 2) yields three pseudo isostructural systems:



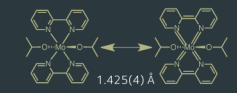

The paramagnetic radical anion was characterised by solid and solution EPR measurements and the diamagnetic neutral and dianionic forms by NMR studies.[4]



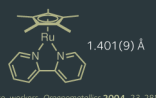

The dramatic change in chemical shift may be explained by considering the pictured resonance canonical, which separates the negative charges, placing them on the most electronegative sites, but at the cost of losing aromaticity and generation of significant alkene character around the ring.

## 2,2'-BIPYRIDINE TRANSITION METAL COMPLEXES

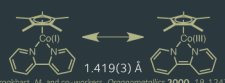
A typical unreduced 2,2'-bipy inter-ring bond length is 1.490 Å. Many examples exist in the literature that show an unusually short distance:




Chisholm, M and co-workers, *J. Am. Chem. Soc.* **1981**, *103*, 4945.

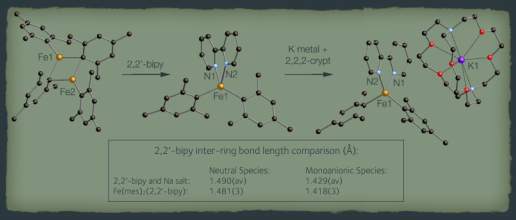



Tilley, T. D. and co-workers, *Organometallics* **2004**, *23*, 2855.

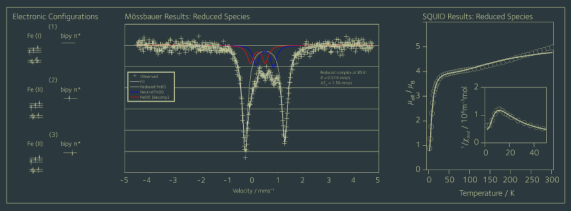



Brookhart, M. and co-workers, *Organometallics* **2000**, *19*, 1247.

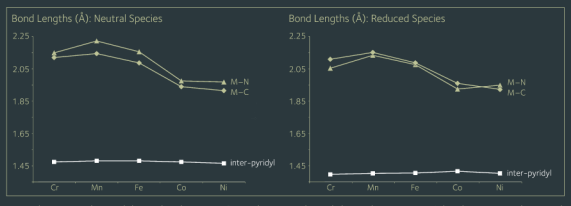
This is frequently explained by extensive π–backbonding from the electron rich metal center to the bipy π* orbital. However, more recently, Weighart and co-workers have questioned the π–acceptor ability of bipyridine and hence whether the above interpretations can be justified. Through a series of related first-row transition metal complexes we have explored this phenomenon, starting with an Fe system:




There are three potential electronic structures of the reduced species. Mössbauer measurements are consistent with the presence of an Fe(II) site, ruling out possibility (1) while SQUID magnetometry studies reveal a temperature dependent mixing of states (2) and (3).




This confirms the presence of a non-innocent bipyridyl ligand in the reduced Fe complex.[3]
Both neutral and reduced forms of analogous complexes containing Cr, Mn, Co and Ni have been synthesised and structurally and magnetically characterised, revealing the following trends:




We observe that although the M–C and M–N bond lengths vary with the central metal, bipyridine inter-ring bond lengths in a ligand of a given oxidation state remain constant. We believe this strongly makes the case for the use of single-crystal derived bond metrics as a diagnostic tool to probe oxidation states in bipyridine complexes.

## REFERENCES AND ACKNOWLEDGEMENTS

1) Denning, M. S.; Irwin, M.; Goicoechea, J. M., *Inorg. Chem.* **2008**, *47*, 6118.
2) Gore-Randall, E.; Irwin, M.; Denning, M. S.; Goicoechea, J. M., *Inorg. Chem.* **2009**, *48*, 8304.
3) Irwin, M.; Jenkins, R. K.; Denning, M. S.; Krämer, T.; Grandjean, F.; Long, G. J.; Herchel, R.; McGrady, J. E.; Goicoechea, J. M., *Inorg. Chem.* **2010**, *49*, 6160.
4) Irwin, M., Krämer, T.; McGrady, J. E.; Goicoechea, J. M., *Inorg. Chem.* **2011**, *50*, 5006.

We thank the University of Oxford (studentship MI), the EPSRC (EP/G002789/2) and the RSC for financial support of this research. We thank CAESR for access to instrumentation and the University of Oxford for access to Chemical Crystallography facilities.